Monophosphate tungsten bronzes and antimony : the interplay of framework instability and electron-phonon coupling

Arianna Minelli

Communauté
UNIVERSITÉ Grenoble Alpes

THÈSE

Pour obtenir le grade de

DOCTEUR DE LA COMMUNAUTE UNIVERSITE GRENOBLE ALPES

Spécialité : **Physique**

Arrêté ministériel : 25 mai 2016

Présentée par

Arianna MINELLI

Thèse dirigée par **Alexeï Bosak, Dr., ESRF**

préparée au sein du **European Synchrotron Radiation Facility**
dans **l'École Doctorale de Physique Grenoble, France**

Les bronzes monophosphate de tungstène et l'antimoine: l'interaction entre l'instabilité de "framework" et le couplage électron-phonon

Thèse soutenue publiquement le **20-12-2018**
devant le jury composé de :

Mr Didier MAYOU
Directeur de recherche CNRS, Institut Néel, Grenoble, Président
Mr Sylvain RAVY
Directeur de recherche CNRS, Université Paris Sud, Rapporteur
Mr Przemysław PIEKARZ
Maitre de conférences, Polish Academy of Sciences, Rapporteur
Mr Pierre MONCEAU
Directeur de recherche emérite, Institut Néel, Grenoble, Membre
Mme Marie-Hélène LEMÉE-CAILLEAU
Chercheure, ILL, Grenoble, Membre
Mr Philippe RABILLER
Professeur, Université de Rennes 1, Membre

Communauté
UNIVERSITÉ Grenoble Alpes

THÈSE

Pour obtenir le grade de

DOCTEUR DE LA COMMUNAUTE UNIVERSITE GRENOBLE ALPES

Spécialité : **Physique**

Arrêté ministériel : 25 mai 2016

Présentée par

Arianna MINELLI

Thèse dirigée par **Alexeï Bosak, Dr., ESRF**

préparée au sein du **European Synchrotron Radiation Facility**
dans **l'École Doctorale de Physique Grenoble, France**

Monophosphate tungsten bronzes and antimony: the interplay of framework instability and electron-phonon coupling

Thèse soutenue publiquement le **20-12-2018**
devant le jury composé de :

Mr Didier MAYOU
Directeur de recherche CNRS, Institut Néel, Grenoble, Président
Mr Sylvain RAVY
Directeur de recherche CNRS, Université Paris Sud, Rapporteur
Mr Przemysław PIEKARZ
Maitre de conférences, Polish Academy of Sciences, Rapporteur
Mr Pierre MONCEAU
Directeur de recherche emérite, Institut Néel, Grenoble, Membre
Mme Marie-Hélène LEMÉE-CAILLEAU
Chercheure, ILL, Grenoble, Membre
Mr Philippe RABILLER
Professeur, Université de Rennes 1, Membre

Alle mie nonne, cosi da obbligarle

a leggere la tesi seppur in inglese

“La vita di ogni artista e di ogni uomo è come quella dei popoli,
un incessante sforzo per ridurre a chiarezza i suoi miti.”

Cesare Pavese

Abstract

A large number of phase transitions can be interpreted as being driven by phonon softening and/or electron-phonon coupling. Thus, a full mechanistic description requires the understanding of structural transformation, changes in electronic structure and lattice dynamics. All together this represents an enormous, for many cases unrealisable, experimental and theoretical effort.

However, with the introduction of appropriate assumptions the problem may be simplified. Here we concentrate on two systems, where the interpretation of the phase transition may be split into an intrinsic instability of the building blocks combined with a superimposed electronic instability. We illustrate the interplay between the framework and electron-phonon-related instabilities using the seemingly heterogeneous examples of phosphate tungsten bronzes and elementary antimony. Based on the combined results from diffuse and inelastic X-ray scattering, we propose for the two systems a picture that explains the experimental observations. The similarities found between these two systems are deemed to be rather surprising.

Monophosphate tungsten bronzes are a family of quasi-2D-oxides, $(PO_2)_4(WO_3)_{2m}$, that exhibits charge density wave (CDW) instability. They contain empty perovskite WO_3 slabs with varying thickness between different members, characterised by the m value. This thickness defines the sequence of charge density wave phases that appear on cooling. The degenerate case of m=2, presenting a quasi-1D instability, was explored since the WO_3-octahedra zig-zag chain is isolated. A CDW phase (T_C=270K and $\mathbf{q}$=0.25$\mathbf{b^*}$) is found to be linked to a rigid-body motion, precisely, to a correlation in the tilting of the octahedra. For the others studied members, as m=6,7 and 8, we found another kind of structural instability. In this case the origin comes from the WO_3 slabs framework, realised as correlated displacements of tungsten atoms along the octahedral 4-fold axis direction (W-O-W-O direction). This leads to a strong x-ray diffuse scattering localised in specific planes, linked to relatively soft phonons modes. Specific Fermi surface nesting, close to the 2D case, gives rise to a freezing of the modulations at the specific momentum transfer, defined by the interplay of two instabilities, the structural and electronic one. Remarkably, the displacements of the tungsten atoms for m=8 are much superior than in m=6.

Elemental antimony at ambient condition has an A7 rhombohedral structure, obtained by small distortion from primitive cubic (PC) lattice through a Peierls transition. Under pressure, the distortion is reduced, but remains finite, as antimony transforms through a series of highly complex structures, before adopting as last the highest-symmetry body-centred cubic (BCC) phase. The main diffuse scattering features and to some extent the peculiarities in the lattice dynamics of the A7 phase − as above − can be explained by the instability of the primitive cubic network with respect to correlated displacements along the chains with <100> pseudo-cubic directions. Analysis of critical vectors for the BCC-PC transformation together with experimentally obtained phonon-energies pressure dependence provides further insights into the details of the phase transformation.

Abstract

Les phonons mous et le couplage électron-phonon sont considérés comme responsables d'un grand nombre de transition de phase. Pour en comprendre complétement les mécanismes, il est nécessaire d'étudier à la fois les modifications structurales, les changements de configuration électronique et les dynamiques de réseau cristallin. De toute évidence, cela représente une charge de travail expérimental et théorique considérable, voire même hors d'atteinte.

Néanmoins, il est parfois possible d'introduire certaines simplifications et d'ainsi rendre une telle étude réalisable. C'est le cas pour les deux systèmes au cœur de ce travail de thèse, pour lesquels la transition de phase peut être diviser en deux instabilités : l'une est structurale, intrinsèque aux éléments constitutifs du système et l'autre, superposée, provient de la configuration électronique. L'interaction entre ces instabilités est illustrée à travers l'exemple de deux systèmes à priori hétérogènes, la famille des bronzes monophosphate de tungstène d'une part et l'antimoine d'autre part, qui révèleront finalement posséder des similarités inattendues. La combinaison des techniques de diffusion diffuse et de diffusion inélastique de rayons X permet des observations qualitatives et une meilleure compréhension de la situation pour les deux systèmes.

Les bronzes monophosphate de tungstène font partie de la famille des oxydes quasi-2D, $(PO_2)_4(WO_3)_{2m}$, qui ont la particularité d'être sujet à des instabilités de type onde de densité de charges (ODC). Ces bronzes sont constitués d'une structure de perovskite vide composée par des couches octaédriques $(WO_3)_{2m}$. L'épaisseur de chacune de ces couches est définie par la valeur de m, qui mène ainsi à différents types de phase d'ODC. Le cas du terme m=2 a aussi été étudié car le fait que les chaînes zig-zag y soient isolées conduit à instabilité quasi-1D. La présence d'une phase d'ODC a été découverte à T_C=270K avec $\mathbf{q}$=0.25$\mathbf{b^*}$. Cette phase est engendrée par le mouvement à corps rigide, plus exactement, par les basculements corrélés des octaèdres. Pour les autres termes (m=6,7 et 8), l'instabilité structurale a une origine différente et est liée à l'agencement en couches de WO_3, plus particulièrement aux déplacements corrélés des chaînes W-O-W-O. Ces derniers sont la cause d'une forte diffusion diffuse sur des plans spécifiques, résultant de la présence de phonons "relativement" mous localisés dans la même région. Ensuite, l'emboitement de la surface de Fermi quasi-2D est à l'origine

de l'ancrage du vecteur de modulation sur une valeur spécifique de transfert de moment, définit par l'interaction de deux instabilités, structural et électronique. De façon remarquable, l'amplitude des déplacements des atomes de tungstène dans le terme m=8 est beaucoup plus élevée que dans le m=6.

L'antimoine à température ambiante possède une structure rhomboédrique, dérivant d'une légère distorsion de la structure cubique primitive (CP) par transition de Peierls. Sous pression, la distorsion se réduit sans toutefois disparaître complétement, puisque l'antimoine se transforme dans un premier temps en une série de structures complexes, pour finalement adopter celle possédant la plus grande symétrie, la structure cubique centrée (CC). De la même façon que pour les bronzes, les caractéristiques de la diffusion diffuse ainsi que, dans une certaine mesure, les particularités de la dynamique du réseau rhomboédrique, s'expliquent à travers de l'instabilité du réseau cubique primitif. Cette dernière est liée aux déplacements corrélés dans les chaînes avec direction pseudo-cubique <100>. En outre, les détails de la transition de phase peuvent être explicités par l'association de l'analyse des vecteurs critiques de la transformation CC-CP avec les résultats expérimentaux obtenus sur la dépendance en pression de l'énergie des phonons.

Résumé

Introduction

L'étude des transitions de phase est un problème complexe pour lequel plusieurs points de vue peuvent être adoptés : notamment la thermodynamique, les théories phénoménologiques et les changements de symétrie des phases ou l'aspect atomistique. La théorie de Landau, qui est une théorie phénoménologique très générale, permet de décrire les transitions du deuxième ordre à partir de la définition d'un paramètre d'ordre et des considérations de symétrie. Elle a été appliquée avec succès dans de très nombreux cas, ainsi que pour certaines transitions du premier ordre. Lorsque l'on souhaite effectuer une description microscopique de ces mécanismes il est nécessaire d'étudier les changements dans la structure cristallographique, la structure électronique et la dynamique du réseau. C'est un problème difficile car il est en général compliqué d'accéder à toutes ces informations et on a recours à des simplifications supplémentaires.

Nous avons choisi d'étudier dans cette thèse deux systèmes qui, bien que très différents, présentent des anomalies dans les transitions de phases très similaires. Le premier système est la famille des bronzes de monophosphate de tungstène et le deuxième système est l'antimoine élémentaire. Les deux systèmes sont caractérisés par une compétition entre deux instabilités : la première est structurale, avec l'instabilité du réseau d'unité rigides (comme les octaèdres de la structure pérovskite), qui est intrinsèque aux éléments constitutifs du système. La deuxième est une instabilité donnée par la structure électronique qui se superpose à l'instabilité structurale. Dans une première analyse il faut étudier ces deux instabilités séparément, puis comprendre leur interaction qui est un facteur important pour la compréhension de l'aspect atomistique de la transition.

Méthode expérimental

Dans ce travail pour étudier les transitions de phases et aborder le problème des mécanismes microscopiques, nous avons utilisé de manière conjointe la mesure de

la diffusion diffuse (DS) des rayons x, la mesure de la diffusion inélastique des rayons X (IXS) et les calculs *ab initio* [1, 2]. La mesure de diffusion diffuse des rayons X permet une collecte rapide de la distribution d'intensité dans tout l'espace réciproque et d'identifier ainsi les régions de l'espace réciproque présentant un intérêt : maxima d'intensité, asymétries etc. Les mesures de diffusion inélastique des rayons x sont ensuite menées sur ces régions spécifiques afin de déterminer si la DS est de caractère inélastique ou élastique. Les calculs *ab initio* sur la structure et/ou sur la dynamique de réseau sont utilisés de manière complémentaire pour la compréhension des mécanismes. Cette étude conjointe a été utilisée avec succès pour l'étude des transition de phase d'autres systèmes [3–5]. Avec ce travail, nous montrons tout l'intérêt de cette approche conjointe. De plus, la difficulté d'effectuer des calculs de la dynamique de réseau pour la famille des bronzes de monophosphate de tungstène, a validé la possibilité d'utiliser une interprétation semi-quantitative de la diffusion diffuse pour comprendre le mécanisme.

Les deux systèmes en étude

Nos avons choisi d'étudier deux systèmes différents pour aborder ce problème des transitions de phases.

Le premier système présenté dans la thèse est la famille des bronzes monophosphate de tungstène à tunnels pentagonaux ($MPTB_p$), de formule chimique $(PO_2)_4(WO_3)_{2m}$. Cette famille de composés, résulte de l'intercroissance régulière de tranche d'octaèdres (WO_6) liés par les sommets, dont l'épaisseur est fonction de m et de tétraèdres (PO_4). Les $MPTB_p$ présentent des instabilités électroniques, comme les ondes de densité de charge (ODC) et de la supraconductivité. En fonction de la valeur de m différents types de phase d'ODC sont observés. On peut observer des transitions au premier ou deuxième ordre, des modulations commensurables ou incommensurables, des satellites très fortes ou faibles, en fonction de la valeur de m et donc du nombre de plans d'octaèdres. La dynamique du réseau n'avait pas encore été étudiée pour cette famille. Nous avons concentré l'étude de l'ODC et de la dynamique de réseau associée sur trois membres de la famille (m=2, 6 et 8) qui sont représentatifs des différentes caractéristiques observées. Le premier terme, un cas dégénéré de la famille, est le terme m=2. Dans ce particulier, les octaèdres de tungstène WO_6 ne forment pas de plan mais seulement des chaînes en zig-zag entourés par les groupes de phosphates. Pour les termes d'ordre supérieur, il a été observé que le comportement de l'ensemble des membres se classe en deux catégories, avec pour les faibles valeurs de m, un couplage électron-phonon qui est faible, et des satellites dont l'intensité est également faible, alors que pour les fortes

valeurs de m le couplage électron-phonon est fort donnant lieu à des satellites de forte intensité. Nous avons choisi d'étudier le terme m=6 caractéristique des faible valeurs de m et le terme m=8 caractéristique des fortes valeurs de m.

Le deuxième système étudié et présenté dans ce travail est l'antimoine. Il a une structure rhomboédrique, appelé A7, qui est dérivé d'une distorsion de Peierls de la structure cubique primitive (CP) et qui est donc stabilisé par l'ouverture d'un gap dans la structure électronique. Cette structure est similaire à celle des éléments du groupe Va, mais sous pression les structures finales obtenues sont différentes. L'arsenic et le phosphore noir ont une structure cubique primitive, alors que l'antimoine réduit la distorsion, avec un chemin de transition plus complexe et plusieurs transitions de phase. Il passe de deux structures incommensurables pour se transformer à plus haute pression dans une phase de de symétrie plus grande, comme la structure cubique centrée (CC). L'évolution de la dynamique du réseau avec la pression est l'étude clé pour comprendre ce chemin de transition dans le système.

Résultats

Avec les trois termes choisis dans la famille des bronzes, on est capable de faire une description générale des comportements dans la famille. Le terme le plus bas peut être considéré comme la base constitutive de couche d'octaèdres. Il présente un système électroniques quasi-1D qui amène à une instabilité d'ODC. La présence d'une phase d'ODC a été découverte à T_C=270K avec $\mathbf{q}$=0.25$\mathbf{b^*}$. Cette phase est engendrée par le mouvement à corps rigide, plus exactement, par les basculements corrélés des octaèdres. Le mécanisme de la transition a été compris grâce aux simulations de dynamique moléculaire.

Pour les autres termes (m=6,7 et 8), l'instabilité structurale a une origine différente et est liée à l'agencement en couches de WO_3, plus particulièrement aux déplacements corrélés des chaînes W-O-W-O. Ces derniers sont la cause d'une forte diffusion diffuse sur des plans spécifiques de l'espace réciproque. Deux famille de plans sont reconnaissables : la direction "long" et la direction "court" des chaînes correspondant aux chaînes parallèles ou perpendiculaires à la couche de phosphates. Cette instabilité est normalement présente dans les pérovskites ou pérovskite vides. L'instabilité structurale est liée à des phonons mous localisés dans la même région, qui pourrait être décrit avec la théorie des bipolarons d'Aubry. Ensuite, l'emboitement de la surface de Fermi quasi-2D est à l'origine de l'ancrage du vecteur de modulation sur une valeur spécifique de transfert de moment, définit par l'interaction de deux instabilités, structurale et électronique. La théorie de

Aubry considère que pour les couplage électron-phonon forte, le phonon donnant lieu à l'ancrage n'est pas seulement celui du vecteur de modulation d'ODC mais aussi tous les phonons proches de basse énergie et qui forment une vallée.

Des différences sont visibles lorsque on étudie le membre m=6 et emphm=8. Pour le bas terme la diminution de la température change la distribution de la diffusion diffuse , une structure fine est révélé qui est liée à l'emboitement de la surface de Fermi " caché". L'intensité faible des satellites révèle un déplacement des atomes de tungstène très modeste lors de la transition de phase. Dans le même temps, l'énergie de phonon sur $\mathbf{q}_{CDW}$ a aussi une faible dépendance avec la température lorsqu'on s'approche de la transition. Dans le cas du terme haut, le m=8, un déplacement important des atomes de tungstène qui sont long la chaine W-O-W-O appelé long est observé, avec une amplitude de déplacement maximum de 0.4 Å. L'ODC correspondant présente des satellites beaucoup plus intenses. Pour cette raison, la dynamique de réseau était beaucoup plus difficile à étudier pour ce terme. La composante élastique à $\mathbf{q}_{CDW}$ reste présente dans la phase à haute température. Deux phonons reliés à la transition ont été identifiés: l'un de basse énergie, mais également un mode optique.

Une étude de la dynamique de réseau sur pression a également été réalisée sur le bronzes MPBT, pour les hauts termes de la série. Avec le terme m=8, une nouvelle transition de phase a été découverte à 1.2 GPa donnant une phase avec $\mathbf{q}$=0.5$\mathbf{a}$*, *i.e.* un doublement de la maille sur a. Quand nous avons abordé le problème de comment la dynamique de réseau répondait à la transition, nous avons trouvé qu'elle n'est pas responsable de la transition et elle subisse pas de changement proche de la transition sur le vecteur de modulation.

La même instabilité de la structure est visible dans l'antimoine. Dans ce système, la distorsion de Peierls amène à une distribution de la diffusion diffuse qui est une signature claire de la brisure de symétrie. De plus, l'instabilité est visible avec des plans de diffusion perpendiculaire à la direction pseudo-cubique $< 100 >$. Grâce à l'étude phénoménologique des vecteurs critiques présent dans les différentes transitions de phase et aux calculs *ab initio*, nous avons pu déterminer les directions importantes qui ont ensuite été investiguées par IXS. Les résultats montrent que lorsqu'on exerce une pression sur le système, la distorsion de Peierls diminue, ce qui donne une tendance pour une transition vers la structure CP. Au contraire, le couplage entre électron et phonon favorise un chemin plus complexe avec des structures incommensurables. En fait, la diminution de l'énergie de phonon dans la direction du vecteur critique pour la transition A7-structure-incommensurables-BCC est plus forte que dans la direction liée à la transition A7-CP.

En conclusion, cette étude a montré la compétition entre des mécanismes d'instabilité intrinsèque et le couplage électron-phonon. Les résultats expérimentaux ont permis de comprendre le mécanisme à l'origine des transitions de phase dans ces systèmes.

Plan de la thèse

Le plan de la thèse s'organise autour de 6 chapitres. Le travail étant articulé autour de deux systèmes très différents, il y aura une introduction sur chacun des systèmes dans le chapitre correspondant.

- Le première chapitre est une introduction générale de la thèse, avec les points en commun pour les deux systèmes. Il présente la motivation de cette étude;
- Le deuxième chapitre est consacré aux aspects théoriques nécessaires pour la compréhension de la thèse. Des concepts de base concernant la dynamique de réseau, l'instabilité structurale de " framework" et les formules clés pour la théorie sur les ondes de densité de charge y sont présentées;
- Le troisième chapitre va introduire le concept base sur la diffusion élastique et inélastique des rayons X, avec la description des deux techniques expérimentales utilisées dans cette thèse, DS et IXS. Ces deux techniques ont été utilisés sur la ligne ID28 a l'ESRF, où la première a été récemment développé. Les méthodes expérimentales pour la préparation des expériences synchrotron, et en particulier pour les études sous haute pression sont également introduites.
- Le quatrième chapitre est dévolu à l'étude faite sur les bronzes de monophosphate de tungstène. Une première introduction sur le système et les principaux résultats théoriques et expérimentaux existant seront présentés. Ensuite, les principaux résultats expérimentaux sont comparés pour trois différentes membres, m=2,6,8, en cherchant à comprendre les différences avec l'augmentation de la largeur des couches de WO3 avec m. Le premier membre est présenté dans une section séparée, car des simulations de dynamique moléculaire ont été possible. Les résultats DS et IXS pour les deux autres membres m=6 et 8 sont ensuite présentés. Une dernière section est dédiée aux changements structuraux dans les différents termes avec la transition de phase ODC.
- Le cinquième chapitre est consacré à l'antimoine. La structuration du chapitre est similaire au chapitre précédent. L'instabilité de "framework" dans cette structure distordue et la réponse de la dynamique de réseau seront présentés. Une introduction de la structure cristallographique de l'antimoine est présentée pour comprendre la distorsion de Peierls. Une section est dédiée aux

méthodes phénoménologiques utilisées pour étudier les transitions de type reconstructive. Les résultats expérimentaux sont comparés avec les deux modèles théoriques utilisés pour cette étude: le modèle phénoménologique basé sur le changement de symétrie dans les transitions de phase et les calculs *ab initio*.

- La conclusion générale est présentée dans le sixième chapitre. Nous présentons les principaux résultats, qui concernent l'explication microscopique des transitions des phases quand l'instabilité structurale du "framework" et le couplage électron-phonon sont les deux forces d'entraînement qui amènent aux nouvelles phases. Les similarités dans les deux systèmes y sont aussi expliquées. Une partie de ce chapitre est dédiée aux perspectives d'avenir avec des suggestions pour des expériences futures possible sur ces systèmes et sur ses homologues.

Contents

1. Introduction

The phase transitions can be studied from different points of view: atomistic models, thermodynamics, symmetry changes. One of the successful theories is a phenomenological interpretation given by Lev Landau, later named after him. Without considering the mechanism at the microscopic level, frequently phase transitions may be described *via* Landau free energy and order parameter [6]. However, such a description can be completely detached from the microscopic mechanism. Getting a full mechanistic description requires the understanding of changes in crystallographic structure, electronic structure and lattice dynamics, which is generally impossible without further simplifications.

In this thesis, we approach this problem for two types of system through the combination of diffuse x-ray scattering (DS), inelastic x-ray scattering (IXS) and *ab initio* calculation [1–5]. DS allows relatively fast localisation of the regions of interest in the reciprocal space (*i.e.* strong diffuse features, asymmetry, regular attenuation, etc.). The results then can be analysed through slow IXS experiment, which allows identifying the origin of diffuse features, namely inelastic or elastic or quasielastic or the combinations of those. Alternatively, or in the complementary way, *ab initio* calculations of structure and/or lattice dynamics can be employed.

The first system explored is a family of quasi-2D-oxides, the monophosphate tungsten bronzes, which exhibits electronic instabilities leading to the formation of charge density waves (CDW) ground state. Index m in the general formula $(PO_2)_4(WO_3)_{2m}$, gives the thickness of WO_3 perovskite building blocks, interconnected by a layer of phosphate groups. Vast range of CDW phases with different characteristics (*e.g.* commensurate/
incommensurate modulation, weak/strong satellite peaks, 1^{st} and 2^{nd} order transitions) is observed, depending on the family member. The information on the lattice dynamics for this system remained practically nonexistent and rather extensive study is required both in terms of diffuse scattering and inelastic scattering.

The second system is the elemental antimony, which presents a rhombohedral structure of so-called A7 type. It arises from a Peierls distortion of the primitive cubic (PC) structure, linked to the opening of an energy gap in the electronic density of state. This structure is common to other group Va elements, however some of them, as arsenic and black phosphorus under pressure adopts the PC

structure. Antimony, although decreasing the distortion under pressure, prefers to follow a more complicated series of phase transitions, passing two incommensurate host-guest structures and reaching at the highest pressure a body-centre cubic (BCC) structure. The evolution of the lattice dynamics with pressure is expected to explain the structural path chosen by this system.

This PhD Thesis is composed as follows. Chapter 1 provides an introduction to the project. Chapter 2 presents an overview of the theoretical foundations, fundamentals for the understanding of the subsequent chapters. Chapter 3 provides an introduction to the theory behind the scattering experiments and the two techniques used at the ID28 ESRF beamline. A subsection is devoted to the high-pressure measurements and the presentation of the experimental methods, *e.g.* samples and experiments preparation. In Chapter 4 and Chapter 5, respectively, the systems are presented through a general introduction and the state of art. The results obtained for the monophosphate tungsten bronzes and elemental antimony, respectively, will follow. An extensive explanation of the instabilities linked to the underlying lattice and to the electronic subsystem are discussed. The experimental findings are accompanied by *ab initio* calculations. Chapter 6 discusses the general conclusions and explores potential directions for future studies.

2. Lattice dynamics and electron-phonon coupling: theoretical foundation

In this chapter, the theoretical foundations of lattice dynamics and electron-phonon coupling are presented. The concepts of framework instability and sliding chains are shown and the basic theory regarding the charge density wave system is described.

2.1. Lattice dynamics

The lattice cannot be considered as a rigid model, where the atoms are fixed in their equilibrium positions. In fact, the atom vibrates around their equilibrium position due to two contributions. The first contribution has a quantum origin due to the uncertainty principal, which is independent by the temperature. It is called *zero-point fluctuation* since it is present also at absolute zero temperature. The second has a thermal origin, which is associated with the atoms increasing the vibrations amplitude as a function of temperature. This vibration is normally referred to as *thermally excited vibration*, also called *phonon*. It is associated to a finite temperature and corresponds to the normal mode vibrations of atoms in the crystal. One can describe such vibrations as quasiparticles in condensed matter physics and characterise them by their momentum transfer, energy and displacement pattern [7]. In a crystal, two types of vibrations are possible. The first are in-phase vibrations in the low-q limit, which are three branches called acoustic phonons. The second vibrations are the optic phonons, which are 3N-3 branches with polarization different from the acoustic ones. Considering the direction of phonon propagation, the phonon can be longitudinal or transverse. The lattice dynamics is treated in different papers and books [8–17].

The simplest model to describe the lattice dynamics is a linear chain of N atoms of mass m, separated from each other by a distance a. We allow each atom to

interact only with its nearest neighbours. We follow here the formalism of Dove [10] to extract the equations of motion for this model.

For such a chain of N atoms, the total energy of the system at rest is considered as a sum over all the contribution of the atom-atom interaction:

$$E(\mathbf{u} = \mathbf{0}) = N\varphi(a), \tag{2.1}$$

where $\varphi(r)$ is the energy of interaction between neighbour atoms separated by a distance r and $\mathbf{u}$ is a vector representing all the atoms displacement from their rest position. If we consider that each atom k is displaced along the chain by $u_k << a$, the total energy should take this effect into consideration, as follows:

$$E(\mathbf{u}) = \sum_k \varphi(a + u_k). \tag{2.2}$$

The energy above can be expanded in a Taylor series of φ around the position a. This is useful, as we assume that the displacements u_k are only small perturbations, $u_k << a$. With this ansatz, the equation above can be rewritten as:

$$E(\mathbf{u}) = N\varphi(a) + \sum_{s\geq 1} \frac{1}{s!} \frac{\partial^s \varphi}{\partial u^s}\Big|_{r=a} \sum_k (u_k - u_{k+1})^s. \tag{2.3}$$

Note that the distance between two atoms can be written as $r = a + (u_n - u_{n+1})$ and the derivatives of ϕ relative to u_k or r are the same. The first derivative of φ is zero, considering that a is the equilibrium position. The term where $s = 2$ in the sum above is referred to as the *harmonic* term and the higher-order terms as *anharmonic*. The latter terms are frequently neglected. Considering a more complex system, where all the interactions are considered, φ becomes the interaction energy between any pair of atoms with j atom in the l-th unit cell. In this case, the lattice energy at rest is:

$$E = \frac{1}{2} \sum_{jj',ll'} \varphi \begin{pmatrix} jj' \\ ll' \end{pmatrix} \tag{2.4}$$

where the interaction energy (potential energy) φ is for the pair of atoms (jl) and $(j'l')$. Note that the factor of $\frac{1}{2}$ has been added to avoid double counting. The *harmonic* term in this case is:

$$E^{harm} = \frac{1}{2} \sum_{jj',ll'} \mathbf{u}^T(jl) \cdot \mathbf{\Phi} \cdot \mathbf{u}(j'l') = \frac{1}{2} \sum_{jj',ll'} \sum_{\alpha,\beta} u_\alpha(jl) \Phi_{\alpha\beta} u_\beta(j'l') \tag{2.5}$$

where α and β corresponds to the cartesian vector components x,y and z. The 3x1 displacement matrix $\mathbf{u}$(jl) is defined as:

$$\mathbf{u}(jl) = \begin{pmatrix} u_x(jl) \\ u_y(jl) \\ u_z(jl) \end{pmatrix}, \tag{2.6}$$

and the 3x3 force constant matrix $\mathbf{\Phi}$ has elements:

$$\Phi_{\alpha,\beta} = \frac{\partial^2 E}{\partial u_\alpha(jl) \partial u_\beta(j'l')}. \tag{2.7}$$

At this point, the equation of motion for a j-th atom in the l-th cell can be written as:

$$m_j \ddot{\mathbf{u}}(jl,t) = -\sum_{j',l'} \mathbf{\Phi} \begin{pmatrix} jj' \\ ll' \end{pmatrix} \cdot \mathbf{u}(j'l',t), \tag{2.8}$$

where m is the mass and now the dependence of the displacement vector on the time t has been made explicit.

The wave in a crystal can be seen as travelling wave, that in one dimension is $\mathbf{u}(x,t) = \tilde{u} \exp(\mathrm{i}[\mathbf{k}x - \omega t])$, where $\tilde{u}$,$\mathbf{k}$ and ω are the amplitude, the wave vector and the angular frequency, respectively. In the *Born-von Kármán* periodic condition, the solution for $\mathbf{u}$(jl,t) is a linear superposition of travelling harmonic waves as:

$$\mathbf{u}(jl,t) = \sum_{\mathbf{k},\nu} \mathbf{U}(j,\mathbf{k},\nu) \exp(\mathrm{i}[\mathbf{k} \cdot \mathbf{r}(jl) - \omega(\mathbf{k},\nu)t]), \tag{2.9}$$

where ν is the mode of the wave and $\mathbf{U}$ is the amplitude vector or *displacement* vector. We will use the notation $r(jl)$ to refer to the equilibrium position of the atom (jl), or to the origin of the unit cell l, when convenient. With respect to the choice, the phase of $\mathbf{U}$(j,$\mathbf{k}$,l) changes. If we substitute the wave equation in Eq. 2.9 in Eq. 2.8, we obtain the following condition:

$$m_j\omega^2(\mathbf{k},\nu)\mathbf{U}(j,\mathbf{k},\nu) = \sum_{j'l'} \mathbf{\Phi}\begin{pmatrix} jj' \\ ll' \end{pmatrix} \cdot \mathbf{U}(j',\mathbf{k},\nu)\exp(\mathbf{i}\mathbf{k}\cdot[\mathbf{r}(j'l') - \mathbf{r}(j0)]) \quad (2.10)$$

where the reference atom in the exponential has been taken to be in the 0-th cell. This is referred to as standard equation of motion.

The equation of motion for a single solution, ν, is written:

$$\omega^2(\mathbf{k},\nu)\mathbf{e}(\mathbf{k},\nu) = \mathbf{D}(\mathbf{k})\cdot\mathbf{e}(\mathbf{k},\nu) \quad (2.11)$$

where $\mathbf{D}(\mathbf{k})$ is the $3n\times 3n$ dynamical matrix for n atoms per unit cell. The column vector $\mathbf{e}$ of $3n$ elements is the result of the displacement vector weighted by the atomic mass, *e.g.* $(m_1)^{1/2}U_x(1,\mathbf{k},\nu)$. It is also called *polarisation* vector, since it is related to the polarisation of the wave.

The dynamical matrix can be considered as formed by blocks of 3×3 matrices, where each block corresponds to pair of atoms (j and j') and the elements of each block have labels α,β=1,2,3, which represents x,y,z. The elements of the 3×3 blocks are given:

$$D_{\alpha\beta}(jj',\mathbf{k}) = (m_j m_{j'})^{-\frac{1}{2}}\sum_{l'}\Phi_{\alpha\beta}\begin{pmatrix} jj' \\ 0l' \end{pmatrix}\exp(i\mathbf{k}\cdot[\mathbf{r}(j'l') - \mathbf{r}(j0)]). \quad (2.12)$$

Note that, as $l = 0$ in the argument of $\Phi_{\alpha\beta}$, this uses the 0-th unit cell as a reference.

If we consider a new matrix, as the eigenvalue frequency matrix $\mathbf{\Omega}(\mathbf{k})$ which is made as the diagonal matrix of the squares of the angular frequencies, we can write in compact form the dynamical matrix:

$$\mathbf{e}(\mathbf{k})\cdot\mathbf{\Omega}(\mathbf{k}) = \mathbf{D}(\mathbf{k})\cdot\mathbf{e}(\mathbf{k}). \quad (2.13)$$

An important property of the dynamical matrix is that is *Hermitian*:

$$\mathbf{D}(\mathbf{k}) = (\mathbf{D}^*(\mathbf{k}))^T \quad , \tag{2.14}$$

so the eigenvalues are real and the eigenvectors are orthogonal. The eigenvalues give the squares of the angular frequencies for each vibrational mode, whereas the eigenvectors are linked to the relative displacements of the atom for each vibrational mode. As a result, the dynamical matrix contains all the information about the lattice dynamics. The equation 2.11 creates a set of motions associated with each wave. The eigenvectors identify *normal* modes and they are linearly independent (orthogonal). The orthonormality condition for the eigenvectors is further enforced:

$$(\mathbf{e}(\mathbf{k}, \nu))^T \cdot \mathbf{e}(-\mathbf{k}, \nu') = \delta_{\nu\nu'} \quad . \tag{2.15}$$

2.2. Framework instability

In this thesis, we will use the term framework instability in order to describe some instabilities and distortions in the structure either of bronzes, either of antimony. Since the distortion should be connected to low-energy phonon, the lattice dynamics can help to understand the origin behind the structural instability [18, 19].

The framework structure is normally composed by an infinite framework of corner-linked polyhedral group of atoms. Often, those structures are associated with instability due to the imperfect rigidity. In fact, there are some internal degrees of freedom for the distortion. An example is the quartz, corner-linked SiO_4 tetrahedra. In this case, the rigid body distortion was defined as the zero-frequency solutions to the dynamical equation. The distortion was related to a displacive phase transition. A parent structure (higher symmetry structure) easily distorts coupled/driven by a soft phonon. Thus, the phase transition is associated with an easy-mechanical instability [20].

The Rigid Unit Modes (RUMs) theory connects the instability to low-energy phonon modes [21–23]. This theory is based on two, apparently opposite, characteristics of the polyhedra: the stiff and the floppy forces. The stiff force refers to the rigid body motion of the polyhedron, whereas the floppy force refers to the flexible linkage and bonding between two polyhedra, Fig. 2.1. A software to simulate the dynamical equations and their solutions was developed and it was able to

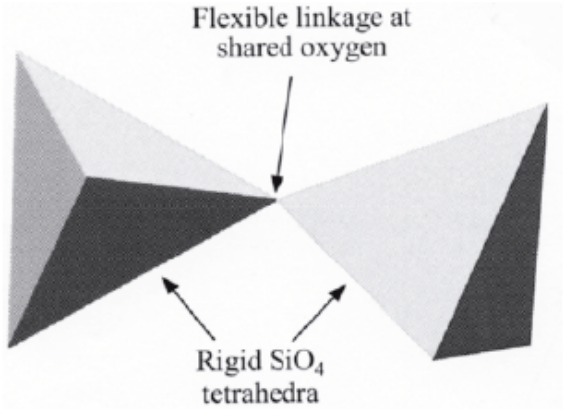

Figure 2.1.: The two types of forces and related distortions in the rigid unit mode.

simulate the intensity of the thermal diffuse scattering [22]. From this, an array of diffuse patterns were found for framework structures. From a simple plane, like in SiO_2 trymidite, to an undulating web of lines for the β-quartz.

In a similar way, atomic chains can be intrinsically disordered in some crystalline structures. Such a disorder gives rise to reciprocal diffuse sheets, having (quasi)elastic nature in case of true disorder, and inelastic in case of phonon-associated displacement, e.g. for KNb_3O [24–27]. Distinction between those cases frequently produced controversies.

2.3. Peierls transition and charge density wave

Moving on from a simple structural distortion, discussed above, the basic principles describing the Peierls transition and CDWs are introduced. Similarities between the dynamical response of the lattice due to CDW and framework instabilities will be explored.

Peierls predicted for the first time the transition that took its name in 1955 [28]. The 1D metals consisting of linear chains are intrinsically unstable with respect to a gap opening at the Fermi level. As a result, this would lead to a metal-insulator transition. For the higher dimensionality, the electrons are "condensing" in momentum space so-called charge density wave, which is characterised by a q-vector related to the specific topology of the Fermi surface.

To introduce the problem, the electronic instability should be presented. The subject is described in great details in books or reviews dedicated to the topic [29–

38] and in chapter of wide-ranging books [39–43]. In our summary, the formalism of Grüner is used [35].

The electrons in a metal can be considered by the free electron gas model, in which the ions are inert and uniformly charged. In a perfect metal, the distribution of the electrons follows the Bloch function, which is periodic with the lattice. Thus, the electrons should not interfere with the crystal cell. However, in the real metal, some interactions due to impurity, holes and thermal vibration appear. If an external potential, V_{ext}, is introduced, the electron density, ρ_{ind}, can be linearly approximated as follows [11]:

$$\rho_{ind}(\mathbf{q}) = \chi(\mathbf{q}) V_{ext}(\mathbf{q}) \quad , \tag{2.16}$$

where $\mathbf{q}$ is the reciprocal space vector and χ, is the Lindhard response function, which is given by:

$$\chi(\mathbf{q}) = \int \frac{d\mathbf{k}}{(2\pi)^d} \frac{f(\mathbf{k}) - f(\mathbf{k}+\mathbf{q})}{\epsilon(\mathbf{k}) - \epsilon(\mathbf{k}+\mathbf{q})} \quad , \tag{2.17}$$

where $f(\mathbf{q})$ is the Fermi-Dirac function, $\epsilon(\mathbf{k})$ is the energy of the electronic state in $\mathbf{k}$ and d is the dimension of the system. For a 1-D electronic gas, a linear dispersion relation around the Fermi energy can be assumed, through $\epsilon_k - \epsilon_F = \hbar v_F (k - k_F)$ where the velocity v is given by the relation $m_e v = \hbar k$. The integral of the susceptibility is given by:

$$\chi(\mathbf{q}) = \frac{-e^2}{\pi \hbar v_F} \ln \left| \frac{\mathbf{q} + 2\mathbf{k}_F}{\mathbf{q} - 2\mathbf{k}_F} \right| = -e^2 n(\epsilon_F) \ln \left| \frac{\mathbf{q} + 2\mathbf{k}_F}{\mathbf{q} - 2\mathbf{k}_F} \right| \tag{2.18}$$

where $\mathbf{k}_F$ corresponds to the Fermi wavevector. When $\mathbf{q}$=$2\mathbf{k}_F$, the occupied $\mathbf{k}$ state and the unoccupied $\mathbf{k}$+$\mathbf{q}$ gives a divergent contribution to the Lindhard function. If one considers a 3D-sphere, the susceptibility becomes [44]:

$$\chi(\mathbf{q}) = \chi(x) = -e^2 n(\epsilon_F) \left[1 + \frac{1-x^2}{2x} \ln \left| \frac{1+x}{1-x} \right| \right], \quad \text{with} \quad x = \mathbf{q}/2\mathbf{k}_F \tag{2.19}$$

where $n(\epsilon_F)$ is the density of states at the Fermi level, considering the spin direction. From this equation, we notice that x decreases decreasing $\mathbf{q}$. Also in this

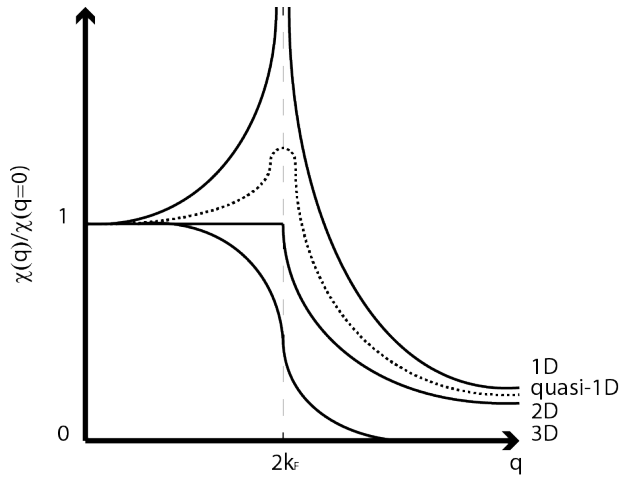

Figure 2.2.: Lindhard response fuction for 1D, quasi-1D, 2D and 3D free electron gas at zero temperature

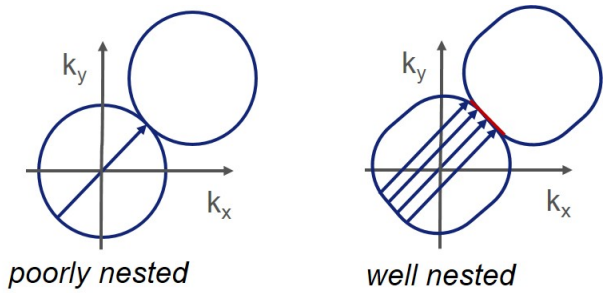

Figure 2.3.: Different 2D Fermi surfaces and their related nesting vectors.

case, a logarithmic singularity is present at $\mathbf{q} = 2\mathbf{k}_F$. This instability takes the name of Peierls and the Fig. 2.2 summarises the results. More vectors are related to this instability, the more the divergence is evident, so the Lindhard function is actually sensitive to the Fermi surface topology. In fact, the perfect divergence of the 1D dimension case due to the higher amount of possible vectors starts to decrease as the dimension increases, together with the number of *nesting* vectors. Qualitatively, the nesting of the Fermi surface is possible when a piece of it can be superposed on another piece by the translation q-vector. An example on the Fermi surface dimensionality and how it affects the nesting can be seen in Fig. 2.3.

For some systems, the concept of the geometric Fermi surface nesting is not sufficient to explain the electronic instability. In fact, for metals in lower dimension, the different partially filled electronic dispersions should be studied. Moreover, their combined Fermi surfaces give as a results a nested superposed surface, Fig. 2.4. Those nestings are related to the subsequent CDW phase, which removes the

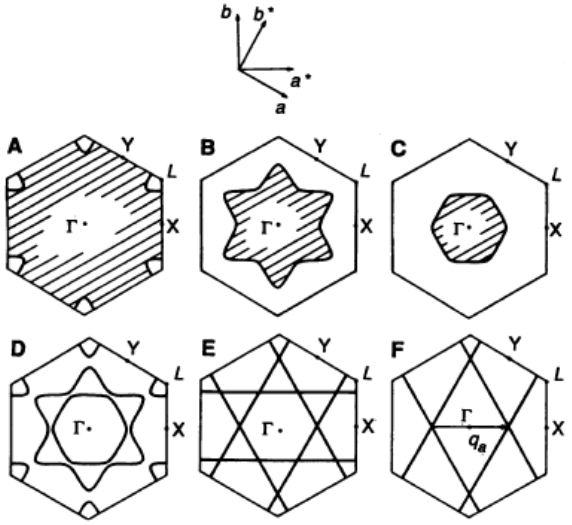

Figure 2.4.: Example of hidden nesting for the purple bronze $KMo_{16}O_{17}$. The three calculated Fermi surfaces of the partially filled *d*-blocks, A, B and C, are superposed, D, and the nesting vector related to the superposition is visible in F. From *M.-H. Whangbo, E. Canadell, P. Foury, J.-P. Pouget, Science* ***252*** *96-98 (1991).* Reprinted with permission from AAAS.

nested regions [45–47]. Apparently, the same or better result can be obtained considering the Lindhard function instead of geometric constructions.

2.4. Kohn anomaly

As already mentioned, the lattice is affected by the Peierls instability. Thus, when we describe the free electron in a periodic potential, the thermal vibration of the lattice should be taken into account. To introduce the concept, the 1D-linear chain example will be used as an example. In order to take into account the coupling, the Fröhlich Hamiltonian can be used as a model in the context of the mean field theory:

$$H = H_{el} + H_{ph} + H_{el-ph} = \sum_k \epsilon_k a_k^\dagger a_k + \sum_q \hbar\omega_q b_q^\dagger b_q + \sum_{k,q} g_q a_{k+q}^\dagger a_k (b_{-q}^\dagger + b_q). \quad (2.20)$$

In the first Hamiltonian, which corresponds to the electronic part, the electron state has an energy of $\epsilon_k = \hbar^2 k^2/2m$ and $a_k^\dagger$ and a_k correspond to the creation

and annihilation operators. The second Hamiltonian refers to the lattice vibrations, where $b_q^\dagger$ and b_q are the creation and annihilation operators for the phonon characterised by the wavevector $\mathbf{q}$. The latter term is the Hamiltonian for the electron-phonon coupling described using the rigid ion approximation, where the ionic potential V at any point is just dependent to the distance from the center of the ion. The electron-phonon coupling in the equation is expressed by:

$$g_q = i\sqrt{\frac{\hbar}{2M\omega_q}}|q|V_q \tag{2.21}$$

where M is the ionic mass. The mean field theory of the CDW formation is mathematically analogous to that of the BCS theory of a superconductor.

The electron-phonon interaction should be described in an equation of motion with small amplitude displacements. This leads to renormalised frequencies for the lattice motion. The frequency $\omega(\mathbf{q})$ becomes:

$$\omega^2(\mathbf{q}) = \omega_0^2 + \frac{2g_q^2\omega_0}{\hbar}\chi(\mathbf{q}) \tag{2.22}$$

where g_q is the electron-phonon coupling, and ω_0 is referred to the unrenormalised phonon frequency. The anomaly in the phonon spectrum is similar to χ, especially following its dimension. Since the maximum value of χ is $\sim \mathbf{q} = 2\mathbf{k}_F$, a related decreasing intensity or softening is expected in $\mathbf{q} = 2\mathbf{k}_F$. The anomaly in the phonon spectrum is normally referred to as Kohn anomaly [48, 49], Fig. 2.5a. An equation gives the temperature dependence for the frequency for $T > T_{CDW}$:

$$\omega(2\mathbf{k_F}) = \omega_0(2\mathbf{k_F})\sqrt{\frac{T - T_{CDW}^{MF}}{T_{CDW}^{MF}}}, \tag{2.23}$$

where T_{CDW}^{MF} is referred to the transition temperature calculated in the mean field theory.

The phase transition with a subsequent freezing of the lattice vibration is observed for a 1D metal. The effect of the renormalisation, relative to the dimensionality of the system is shown in Fig. 2.5b. If the phonon freezes (with $\omega = 0$), we have what is called a "frozen-in" lattice distortion. This causes a periodic distortion in the lattice due to the CDW phase. A soft phonon anomaly is observed above the transition, as a precursor of the condensation into the Bragg peak. In the case of CDW, this phonon anomaly condenses into a pattern of static displacement at the transition, which produces a modulated structure of period $2\pi/2k_F$.

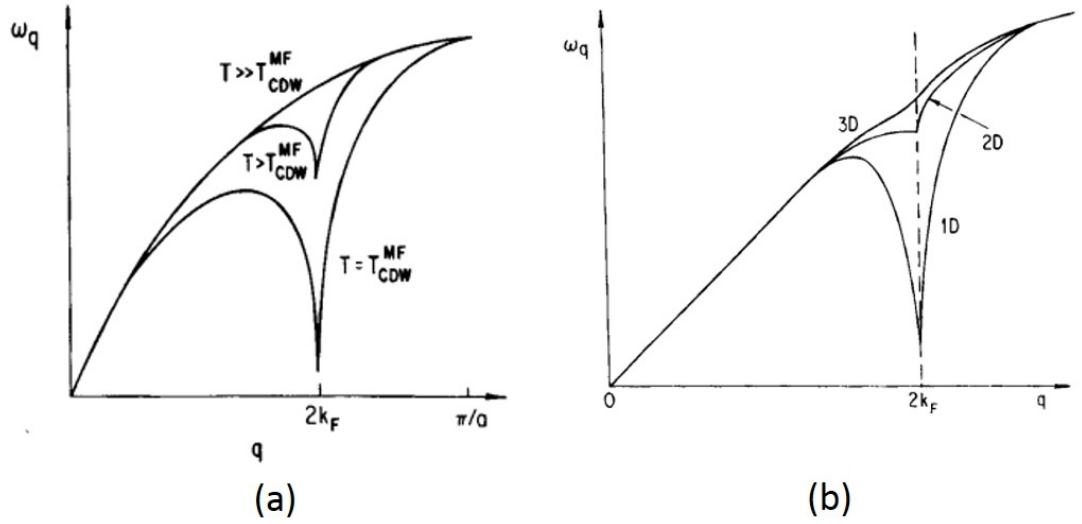

Figure 2.5.: In figure (a) the phonon dispersion at different temperatures above the transition and in figure (b) the dependence of the phonon dispersion respect the dimensionality of the system. The figures are taken from Ref. [35].

2.5. Peierls distortion

Although the transition is normally referred to as "the Peierls transition", the thermodynamics of the CDW state has been studied by Kuper. Furthermore Fröhlich, independently, suggested that the ground state can carry an electric current under an applied electric field.

When Peierls describes for the first time the intrinsic instability of a 1D chain [28], he though that it was a mathematical result with no connection with reality, since in nature there are no a strictly example of 1-dimensional system. However, this kind of instability was found in many crystals, constitute by a series of linear chains correlations [40]. In order to describe the Peierls distortion, we should use the structure and electronic dynamics. In fact, starting from the idea of the partly filled band, the energy of the electrons decreases with a gap opening. The occupied states are in a lower-energy band and the higher-energy band has just empty states, changing the material's behaviour to that of an insulator. To open a gap at the vector k_F, a structural distortion is needed, where the k_F corresponds to the Brillouin zone border of the insulator. This transition happens if the gain in the electron kinetic energy compensates the loss in elastic energy due to the distortion. The gap is expected at temperatures enough low to avoid the thermal excitations of the electrons, which will cancel the gain in the kinetic energy, Fig. 2.6.

This gap in the electronic dispersion can also be seen as a parameter of order in the charge density wave phase [35]. It is actually used also in the superconductor phase and the spin density wave [50, 51]. It is written as:

$$\Delta = |\Delta| e^{i\phi} \quad . \tag{2.24}$$

If it is added to the Fröhlich Hamiltonian, shows the development of a gap in the electric dispersion relation. The opening of the gap lowers the electronic energy, whereas the lattice distortions lead to an increase elastic energy. The total energy is given by the two contributions:

$$E_{tot} = E_{el} + E_{latt} = n(\epsilon_F) \left[-\frac{\Delta^2}{2} - \Delta^2 \log\left(\frac{2\epsilon_F}{\Delta}\right) + \frac{\Delta^2}{2\lambda} \right] \quad , \tag{2.25}$$

where λ is the dimensionless electron-phonon coupling constant:

$$\lambda = \frac{g^2 n(\epsilon_F)}{\hbar \omega_{2k_F}} \quad . \tag{2.26}$$

The Peierls distortion phase is stable when the gain in the electronic energy is larger than the elastic energy of the distortion. Considering the ground state wave function and the integration over the occupied states, in the limit of weak coupling limit ($\epsilon_F >> \Delta$), the periodic charge density variation is found as:

$$\rho(x) = \rho_0 \left[1 + \frac{\Delta}{\hbar v_F k_F} \cos(2k_F x + \phi) \right] \quad . \tag{2.27}$$

In the real system, the perfect nesting of the Fermi surface is almost impossible. However, if the Fermi surface is destroyed by the gap, the transition will be metal-semiconductor or metal-insulator. Whereas, if electron and hole pockets still remain in the Fermi surface after the transition, there would be a metal to metal transition [43].

Another consideration is the inter-correlation, as the inter-chain interaction of the 1D chain. The Peierls instability appears in the regions where pre-transitional fluctuations in the high-symmetry phase were visible. The PLD (Periodic lattice

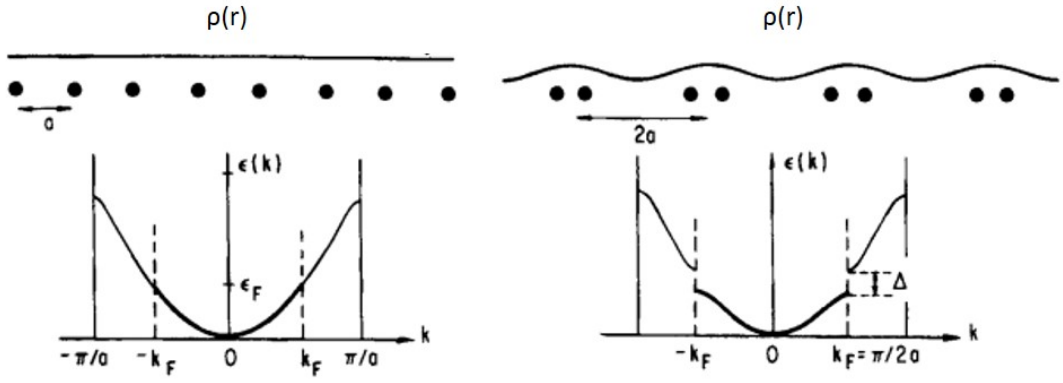

Figure 2.6.: The electron density for a 1D metallic chain above the transition, on the left, and in the CDW phase, on the right, where the PLD and the gap opening, Δ, are visible. The figures were modified from Ref. [35].

distortion) and CDW are correlated along the chain directions with a parallel *correlation length*, $\xi_{//}$, whereas between chain a perpendicular *correlation length*, $\xi_{\perp}$, should be considered. The correlation lengths depend on the temperature. In fact, the fluctuation in the *direct* space of the high-symmetry phase shows diffuse sheets in the reciprocal space, meaning a short-range order. Decreasing the temperature, the correlation order is increasing faster in the intra-chain correlation and a long-range order is defined at the transition temperature, where the 3D Peierls transition is visible with the satellite reflections. The temperature dependence of the correlation lengths is visible in Fig. 2.7 [52].

2.6. Beyond the weak electron-phonon coupling: the strong case

The Peierls transition related to the CDW transition is usually explained by a weak electron-phonon coupling. However, not all the systems can be explained only with this approximation. The first criticism comes with a paper of Migdal [53, 54]. He showed that a many electrons system, when coupled with the phonons, is unstable above a critical value of electron-phonon coupling, considering the Fröhlich interaction. In order to describe the strong-electron phonon coupling, a Ginzburg-Landau-phenomenological model by McMillan was presented [55]. His approach is based on considering the electron-phonon coupling based on a short-order range. In fact, in the weak coupling approach, the mode associated to $q = 2k_F$ is the only one considered and for this reason, we are artificially considering an infinite coherence length. With this consideration for the strong coupling, the

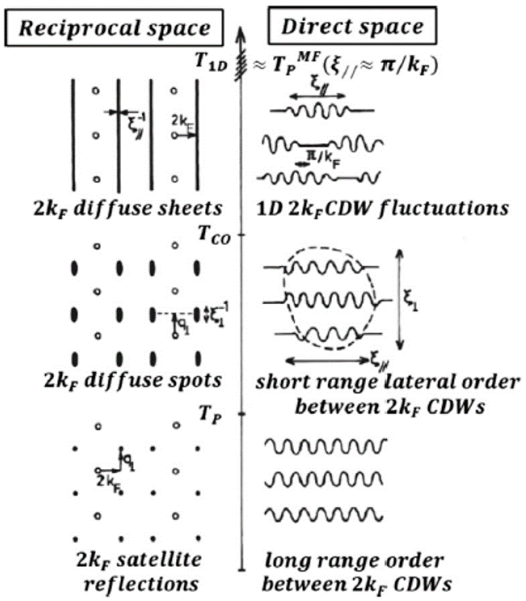

Figure 2.7.: The passage from a pre-transitional fluctuation phase to the Peierls transition with $2\mathbf{k}_F$ satellite reflections [52].

Mean Field model is no longer valid and the harmonic frequencies of the nesting vectors should be added. The interaction becomes more localised in the real space that in the reciprocal space. The Kohn anomaly associated with the instability is not longer exclusively at $q = 2k_F$. A softening in a larger part of the q-space is expected, as found already experimentally in different cases [56, 57].

Aubry and Quémerais [58–60] proposed a model using the bipolaron as quasiparticle. The polaron is an electron, which has a renormalised mass, considering the strong connection with the phonons surround it. A bipolar is a bound pair of polarons. Above T_C, the bipolaron are disordered and below the transition they are ordered, separated by a $1/(2k_F)$ distance. Also for this case, the short-range of the lattice deformation is present and the transition is considered as an order-disorder type transition. With this model, the CDW wave is not described as a sinusoidal *cos*-wave, but it is described by different Fourier terms where the first harmonic is in $2k_F$, Fig. 2.8. Recently, Gor'kov proposed a two-step mechanism [61]. At first, the strong electron-phonon coupling forms the polaron-type where ions and electrons are closer. At this point, the potential becomes anharmonic and, due to the strong coupling, it can be described by the Ising spin concept. The CDW phase originates from an order-disorder transition.

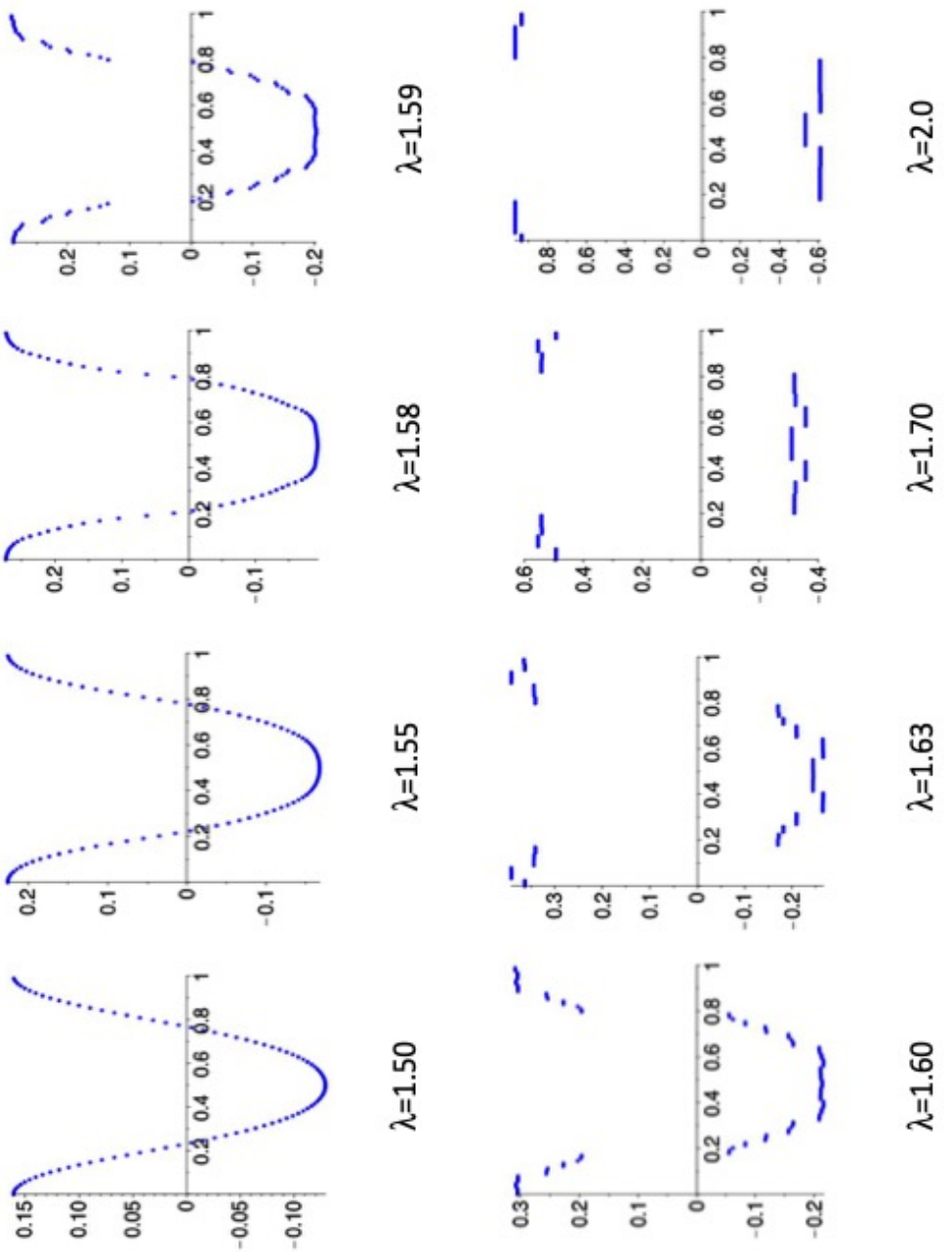

Figure 2.8.: Dimensionless enveloppe function $g(x)$ of the distortion u_n related to the charge density wave in the Holstein model [62, 63]. It is defined as $u_n = g(nc + \alpha \mod 1)$, where α is a phase, n the lattice site and $c = R/S$ is the concentration of pairs of electrons (here $R/S = 55/89$, $c \approx 0.618$). The function $g(x + 1) = g(x)$ is periodic. The different figures correspond to different dimensionless electron-phonon coupling λ. The Aubry transition for this incommensurate system occurs at $\lambda_c \approx 1.57$, above which the bipolaron regime appears, see Ref. [58] [a].

[a] This model was made by Pascal Quèmerais, who gently offered to redone a figure of Raimbault thesis [60].

3. Experimental methods and data analysis

In order to understand the experimental methods used to study the lattice dynamics, the array of techniques used is presented with an introduction to the theory behind. At the end of the chapter, the experimental details for each studied system are described.

3.1. Scattering process and theoretical formalism

The geometry of the general inelastic process is shown in Fig. 3.1, where for the momentum and energy conservation laws, the scattering vector, $\mathbf{Q}$ and the energy transferred to the system in order to create/annihilate a phonon can be written as:

$$\mathbf{Q} = \mathbf{k_i} - \mathbf{k_f} \tag{3.1}$$

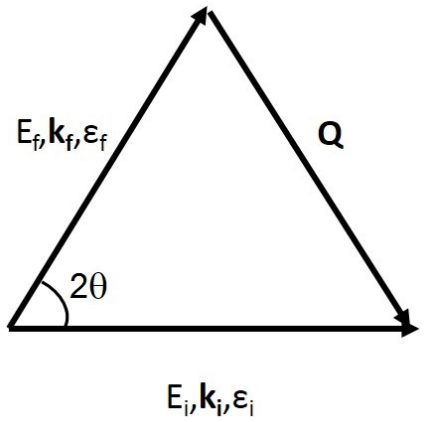

Figure 3.1.: Schematic of a scattering process. The incident and the scattered photons are characterised by their E, ϵ and $\mathbf{k}$. More details in the text.

$$E = E_i - E_f \tag{3.2}$$

$\mathbf{k}_i$ and $\mathbf{k}_f$ are the wave vectors of the initial and final states, respectively, while E_i and E_f are the energies of the initial and final states. For a phonon, the exchange energy in the scattering process of X-ray photons is just on the order of magnitude of meV ($E << Ei$) , therefore one obtains:

$$Q = 2k_i \sin(\theta) \tag{3.3}$$

where 2θ is the angle between k_i and k_f, the scattering angle.

In a scattering process, the physical property that can be measured is the double-differential cross section, $\frac{d^2\sigma}{d\Omega\, dE_f}$, which is proportional to the number of incident photons scattered into a solid angle, Ω, in a range of energy. In order to write a model on the electron-phonon interaction, the weak relativistic limit is used [64]. Additionally, one should neglect the phenomena near the X-ray absorption threshold and related to the magnetic coupling. The Hamiltonian describing the interaction can just contain the Thomson part [65]:

$$H_{Th} = \frac{1}{2} r_0 \sum_j \mathbf{A}^2(\mathbf{r}_j, t) \qquad , \tag{3.4}$$

where $\mathbf{r}$ is the coordinate in space, r_0 is the classical electron radius and $\mathbf{A}$ is the electromagnetic field vector potential. Starting from the general term of the scattering from an incoming beam with uniform *luminosity*, $\mathscr{L}$, as $\sigma = \mathscr{L} * | < F|S|I > |^2$, given the S-matrix from perturbation theory for the perturbation Hamiltonian above, and $|I >$, $|F >$ as initial and final states and expressed by the Fermi's "golden rule" [66], one can write for the double-differential cross section [67]:

$$\frac{d^2\sigma}{d\Omega\, dE_f} = r_0^2 (\epsilon_\mathbf{i} \cdot \epsilon_\mathbf{f})^2 \frac{k_i}{k_f} \sum_{I,F} P_I \left| < F| \sum_j e^{i\mathbf{Q}\mathbf{r_j}} |I > \right|^2 \delta(E - E_f - E_i), \tag{3.5}$$

where the Dirac delta only enforces energy conservation. As considered before, some approximations can be made considering that the exchange energy is very small for the scattering process regarding the phonon. The first is the validity of

the adiabatic approximation, which leads to the separation of the system quantum state $|S>$ in two separate contributions, from the electronic and nuclear part. The second is related to the electronic part of the total wave function, in this case, it is not changed by the scattering. Thus, the initial and final state present differences due to the excitations of the ion system. One obtains:

$$\frac{d^2\sigma}{d\Omega dE_f} = r_0^2(\epsilon_\mathbf{i}\cdot\epsilon_\mathbf{f})^2\frac{k_i}{k_f}\left\{\sum_{I_n,F_n} P_{I_n}\left|< F_n|\sum_j f_k(\mathbf{Q})e^{i\mathbf{QR_k}}|I_n>\right|^2 \delta(E-E_f-E_i)\right\}. \tag{3.6}$$

where $f_k(\mathbf{Q})$ is the atomic form factor (in general $f(\mathbf{Q}) = \int \rho(\mathbf{r})e^{\mathbf{iQr}}\mathrm{d}^3\mathbf{r}$) and $\mathbf{R}_k$ is its position vector. Here, we can define the scattering factor, $S(\mathbf{Q},E)$, as the expression in the bracket.

We will consider now the case of a single-phonon scattering process in a crystal sample. For this part, we will follow the formalism of Xu and Chang [68]. A crystal with N unit cells containing n atoms labelled as k, where the position of the k-th atom in the m-th cell is written as $\mathbf{r}_{m,k}$=$\mathbf{R}_m$+τ_k, with the lattice vector as $\mathbf{R}_m$ and the atomic basis vector in unit cell as τ_k. Assuming the harmonic approximation [69], the scattering function can be given by:

$$S(\mathbf{Q},E) = \sum_\nu G(\mathbf{Q},\nu)F(E,T,\mathbf{Q},\nu) \qquad , \tag{3.7}$$

which is divided in two factors:

$$G(\mathbf{Q},\nu) = \left|\sum_k \frac{1}{\sqrt{M_k}} f_k(Q)[\mathbf{e}_k^\nu(\mathbf{q})\cdot\mathbf{Q}]e^{\mathbf{iQr}_k}\exp^{-W_k}\right|^2 \qquad , \tag{3.8}$$

$$F(E,T,\mathbf{Q},\nu) = \frac{< n(E_\nu(\mathbf{Q},T)+\frac{1}{2}\pm\frac{1}{2}>}{E_\nu(\mathbf{Q})}\delta(E\mp E_\nu(\mathbf{Q})). \tag{3.9}$$

The first is the dynamical structure factor, G, where we introduce the M_k as the mass of the atoms, e^{-W_k} as the Debye-Waller factor and ν as the mode with

ν=1,...,3n. The phonon eigenvector $e_k^\nu(\mathbf{q})$, presented in Chapter 2, of the wavevector $\mathbf{q}$ for the scalar product with $\mathbf{Q}$ imposes selection rules in the detection of the phonons. The Debye-Waller factor is:

$$W_k = \frac{1}{4M_k}\sum_{k,\nu}\left|\frac{\hbar}{N\omega_k^\nu}\coth\left(\frac{\hbar\omega_k^\nu}{2k_BT}\right)\right|^2 |\mathbf{Q}\cdot\mathbf{e}_k^\nu(\mathbf{q})|^2\,. \tag{3.10}$$

The second term is the thermal factor and it specifies the probability of creation/annihilation of a vibration. The term $< n(E,T) >$ is the thermal occupation factor that is the *Bose* factor:

$$< n(E,T) >= \frac{1}{e^{E/(k_BT)}-1} \quad . \tag{3.11}$$

Finally, the X-ray intensity is determined by eigenfrequencies $\omega_{\mathbf{k}}^\nu$ and eigenvectors, $\mathbf{e}_k^\nu$, of the dynamical matrix, eq. 2.13.

For computational purposes, the intensity formulae are not simple. In order to resolve and find the intensity for X-ray inelastic scattering and diffuse scattering, a simplification can be made, as considering the factor G as a small quantity. The Taylor expansion results:

$$I_0 \propto \sum_{k,k',m} f_k f_{k'} e^{-W_k - W_{k'}} e^{-\mathrm{i}\mathbf{Q}(\mathbf{R}_m+\tau_{k,k'})}. \tag{3.12}$$

This term corresponds to the Bragg diffraction and there is a dependence of the intensity, in fact, it decreases due to the Debye-Waller factor.

In order to write the higher term, we use an identity:

$$\sum_{m=1}^{N} e^{\mathrm{i}\mathbf{k}\mathbf{R}_m} = N\sum_{l=1}^{N}\delta_{\mathbf{k},\mathbf{K_l}}, \tag{3.13}$$

where $\mathbf{K_l}$ is the reciprocal lattice vectors. The second term, which corresponds to the single phonon scattering and gives the scattering intensity of IXS, is:

$$I_1(\mathbf{Q},E) \propto \sum_\nu \left[\frac{1}{\omega_{\mathbf{Q}}^\nu} coth(\frac{\hbar\omega_{\mathbf{Q}}^\nu}{2k_BT})\right]_{\mathbf{k}=\mathbf{Q}-\mathbf{K_Q}} \left|\sum_k \frac{f_k}{\sqrt{M_k}} e^{-W_k}(\mathbf{Q}\mathbf{e}_{\mathbf{Q}}^{\nu,k}) e^{-\mathrm{i}\mathbf{K_Q}\tau_k}\right|^2_{\mathbf{k}=\mathbf{Q}-\mathbf{K_Q}} \delta(E-E_f-E_i),$$

(3.14)

where $\mathbf{K_Q}$ is the nearest reciprocal lattice vector to $\mathbf{Q}$ and $\mathbf{k}$ is the reduced wavevector of $\mathbf{Q}$ in the 1st Brillouin zone. This term can be considered also for the DS. In fact, the DS is the sum of I($\mathbf{Q}$,E) on all energies: $I_{DS}(\mathbf{Q})=\int(\mathbf{Q},E)dE$. We can notice that in both cases, the intensity is strongly influenced by the thermal population factor in the *coth* function. For this reason, the acoustic phonons are normally stronger. For DS, the acoustic phonons contribute more in the proximity of Bragg nodes.

3.2. Diffuse scattering

Further information about the diffuse scattering theory and technique can be found in Ref. [2, 17, 70–72].

The diffuse scattering technique is a useful tool in order to determine the static or dynamic deviations from the long-range ordered structure, normally detected by conventional X-ray diffraction experiment. In fact, the short-range order, as defects, can be studied, as well as inelastic components, such as low energy phonons and the related elastic constants. The DS can be collected relatively quickly and can be analysed in order to identify the region of interest in the reciprocal space.

Experimental set-up

At ID28 beamline, two branches can work at the same time. The sketch of the beamline shows the two techniques: diffuse scattering and inelastic X-ray scattering, Fig. 3.2.

The source consists of linear undulators with a synchrotron radiation of $\Delta E/E$ $\approx 10^{-2}$ and an integrated power $\approx$ 200 W. To extract the beam, a Laue-Bragg monochromator (LBM) is used and it has two components. The first is a diamond (311) which divides the primary beam for the two branches (Laue). The beam that is passing in the DS branch is reflected from a second Si(422) crystal (Bragg). The work wavelengths are in the range 0.5-1.0 Å (energy range 12.4-24.8 keV). The upper limit of flux on the sample is $2.7 \cdot 10^{12}$ ph/s/100 mA at the energy 17.8 keV. The X-ray beam is focused by the combination of a transfocator equipped with cylindrical Be refractive lenses, in the vertical direction, and a multilayer mirror, in the horizontal direction. The beam can have a focus with a range between 30-100 μm of FWMH.

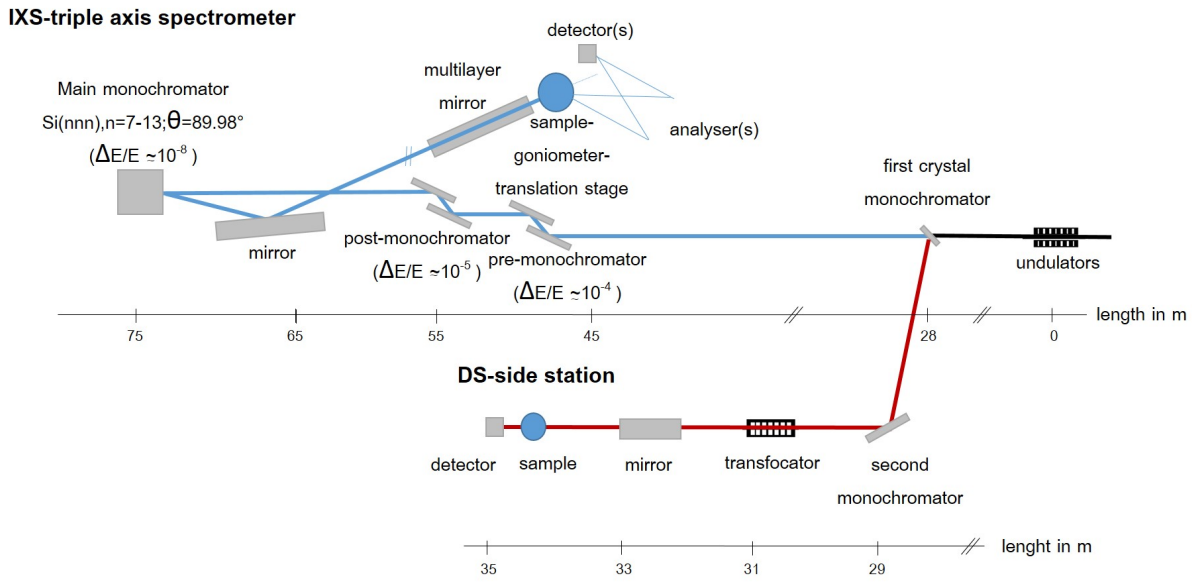

Figure 3.2.: Schematic layout of ID28 beamline at the ESRF, with the IXS-triple axis spectrometer and the side station for DS and diffraction measurements.

At the sample stage, the set-up is identical to x-ray diffraction, Fig. 3.3. The transmission geometry is preferred, while the geometry in reflection is used for thin film. To avoid the air scattering signal a collimator before the sample and a beamstop behind it are used. The 5-circles Huber goniometer is used with a load translation for the pixel detector in order to provide a variable detector-sample distance from 244 mm to 414 mm. Scattering angles up to 130 degrees can be covered with multiple exposures. A silicon hybrid pixel detector, PILATUS3 1M X with no dark noise, is used. It has an active area of 168.7x179.4 mm^2 with a pixel size of 172x172 μ m^2 [73]. Each pixel is reading out individually and the detector has a single-photon counting mode. Frames are collected on the detector with a maximum of 2° step/0.5 sec. In the case of diffraction measurements, different absorbers before the collimator can be applied if the fastest collection is not enough to decrease the intensity and avoid the saturation of the Bragg peaks.

The heavy load stage of the Huber goniostat allows hosting a variety of sample environment options: Huber goniometer heads, closed-cyrcle cryostat, cryostream (Oxford Cryostream 700/700+), heat blower (mini blower and eurotherm), uni-axial strain device and high-temperature electric field set-up. Collections with high-pressure equipment are also possible. Indeed, the Diamond anvil cell (DAC) can be mounted on the goniostat, as shown in Fig. 3.3b.

In this thesis, the first measurements on bronzes were done in ID23-1 MX beam-

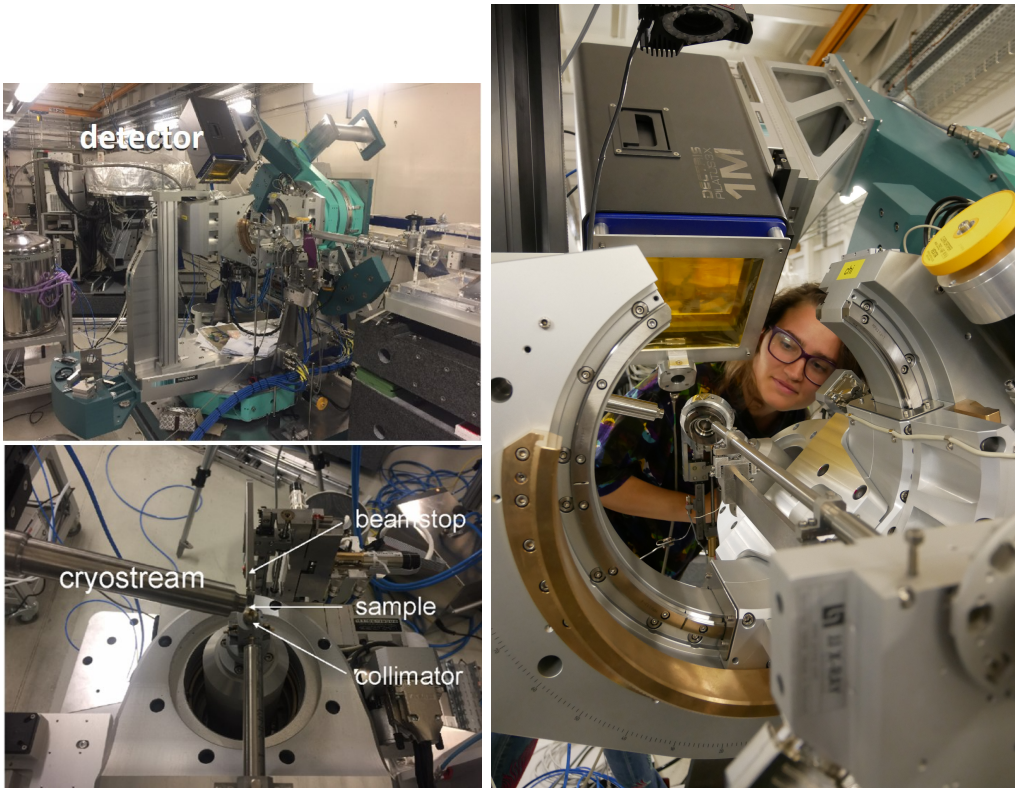

(a) (b)

Figure 3.3.: Sample stage on the side station for DS and diffraction measurements. (a) On the top, the Pilatus detector with 1M pixels and on the bottom, the collimator and the beamstop are visible before and after the sample holder. On the sample stage, the sample is mounted on a goniometer head, in this picture, at the position χ=0. (b) The mounting of the DAC cell on the goniostat.

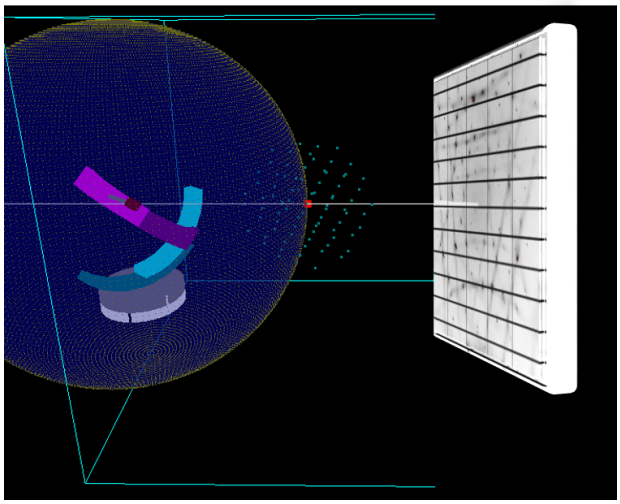

Figure 3.4.: Diffraction geometry of the side station in transmission. The frame collected is the result of the projection of the Ewald sphere onto the detector.

line. The PILATUS detector, in this case, is of 6M pixels with an active area of 423.6x424.6 mm^2.

3.2.1. Data collection

In transmission geometry, the beam passes through the sample and the primary part goes on the beam stop. The scattered intensity is detected by the detector. A beam with incident wave vector, $\mathbf{k}_i$=$2\pi/\lambda$, is diffracted by the sample and if the difference of the two is equal to a vector of the reciprocal space, there is a constructive interference. The point in the reciprocal space which will be detected lies on the related Ewald sphere (with $2\pi/\lambda$), Fig. 3.4. This sphere has a certain thickness coming from the energy uncertainty: $\Delta E/E=\Delta\mathbf{k}/\mathbf{k}$. Area detectors usually are flat, and for this reason, it collects a projection of the Ewald sphere. The sample is then rotated of 360° around a perpendicular axis with respect to the incoming beam, meanwhile frames are collecting with an angular step. In ID28 to access large Q-vectors, the angle of the sample, χ, and the position of the detector, Γ, can vary.

In the beamline, a program of the Swiss Norwegian Beam line (SNBL) at the ESRF [74] called Pylatus can be used as control software to run the frames collection. It is an easy interface where the desired geometry and the acquisition details can be chosen (deg-step, time acquisition, position/distance detector, goniostat geometry, etc.). Plug-ins driving the experimental environment equipment are available.

Series of measurements for different angular combinations, sample translations and temperatures can be added to the sequence with the estimated measurement time, which is automatically provided. Alternatively, Python syntax is used for the fast generation of sequences.

The data collected can be inspected by Albula software, provided by Dectris. The analysis is done by CrysAlis [75], where the basic built-in geometry is in kappa instead of the Euler one used in the beamline. In order to reconstruct the reciprocal space, some corrections should be taken into account. The planar projection of the scattered beam to the detector requires a geometrical correction factor, $D = (1/cos^3(2\theta))$. Another correction to apply at the image to the detector is the parallax, the distortion caused by the absorption properties of the sensor array. A correction should be applied considering the polarisation of the incident beam, $P = sin^2(\Phi) + cos^2(\Phi)cos^2(2\theta)$, considering the synchrotron light. The last correction is called Lorentz and it is related to the rotation of the sample irradiated with the beam. In fact, the reciprocal space points with small momentum transfer stay a longer time in the scattering geometry with respect to the points with a large momentum transfer. It is normally important for diffraction measurements with sharp Bragg peaks. For slowly changing DS Lorentz correction should not be applied. The three corrections are implemented directly in CrysAlis.

Another software locally developed in ID28 (Project X) provides the possibility to reconstruct with high-quality the reciprocal space. Additionally to the 2D reconstructions, it can provide 3D reconstruction, generating a CCP4 file. Examples will be shown in Chapter 4.

3.3. Inelastic X-ray scattering

Inelastic x-ray scattering can conclude on the static or dynamic nature of the fluctuations found in the diffuse scattering. In fact, measuring longitudinally/ transversally on the observed diffuse scattering, the coupling with phonon can be perhaps found. There could be a phonon with a low-energy and wave-vectors ending in the same plane, line or point.

The energy resolution is both the most important and most demanding element of the inelastic x-ray scattering experimental apparatus. In fact, in order to have photons of the wavelength compatible to the inter-particle distances, around $\sim$ λ=0.1 nm, their energy is quite high, *i.e.* 12 keV. The latter is not comparable to the energy of collective excitations as phonon (on the order of meV). For this reason, the energy resolution should be at least $\Delta E/E \approx 10^{-7}$. This latter is technically challenging, especially compared to the neutron scattering. In that case

the resolution necessary is just $\Delta E/E \approx 10^{-2}$ since the energy of neutrons with that wavelengths is ~ 100 meV. However, IXS can probe materials with small size (μm) and/or under high pressure. Additionally, it can access Q-E regions, which are not accessible by neutron measurements, since it has not kinematic limitations. For our case, the samples were too small for neutron study, and the situation is even worse for our pressure study.

In order to obtain the challenging energy resolution, a perfect crystal should be used as monochromator. The resolving power ($E/\Delta E$) is given by [76]:

$$\left(\frac{\Delta E}{E}\right) = \frac{d_{hkl}}{\pi \Lambda_{ext}} \tag{3.15}$$

where d_{hkl} is the lattice spacing of (hkl) reflection order and Λ_{ext} is the primary extinction length, which increases with increasing reflection order. High order Bragg reflections and highly perfect crystals are necessary. The choice of the crystal becomes really strict, which almost constrains us to use Si crystals. In fact, the crystal should have the capability to induce relative variations of d, the lattice spacing, larger than the desired energy resolution: $\Delta d/d \ll (\Delta E/E) \approx 10^{-8}$. Geometrical conditions as the angular divergence of the beam ($\Delta\theta$) should be taken in account, in fact in order to reach the desired energy resolution, the angular contribution has to be comparable or smaller. As result, the divergence should be in the order of magnitude of $nrad$, the choice of the extreme backscattering geometry allows a $\Delta\theta$ of ~ 20 μrad.

The layout of the ID28 beamline at the ESRF is presented in Fig. 3.2, based on a triple-axis spectrometer. The beam is pre-monochromated from two channel-cut single crystals, Si(111) and Si(400), until $\Delta E/E$=10^{-5} and their use is to prevent the over-heat loading of the main monochromator. The main monochromator works with a Bragg angle of 89.98°. The chosen reflections can vary from Si(777) to Si(13 13 13) providing from a 7 ΔE meV until a 1.0 ΔE meV. This highly monochromised beam is focused by different kind of mirror, from a platinum-coated toroidal mirror at 25 m, which focuses the beam at 250 x 80 μm (HxV), until a focusing of 25 x 12 μm (HxV) with the combined use of Kirkpatrick-Baez (KB), which focuses the vertical part, and a multilayer mirror, for the horizontal part of the beam. The Tab. 3.1 contains the details of the two most used energy resolutions and the different mirror set-up that determines the working beam dimension on the sample.

No effects from parasitic scattering are observed before the beam reaches the sample, due to the usage of sample slits. The scattered photons are collected at the end of a 7-meter spectrometer arm by 9 silicon analysers, which are arranged in

Reflection	**Energy**	ΔE
Si(nnn)	keV	meV
9 9 9	17.79	3
12 12 12	23.72	1.3

Mirrors	**Focusing** [a]
	(HxV)μm
Toroidal	270x70
Cylindrical + ML	14x60 (25x60)
Toroidal + KB	270x7 (270x12)
KB + ML	14x7 (25x12)

Table 3.1.: Key parameters of the IXS branch of ID28; in the left table, the two most used reflections of the main monochromator and its related beam energy and energy resolution; in the right table, the focusing of the beam on the sample with different set-ups.

[a]The expected focus is reported and, additionally, the averaged one obtained during the experiments is in parenthesis.

the horizontal plane with a fixed angular offset of ~ 0.75 °. The arm can rotate with a range of 0-45° and 9 momentum-transfer spectra are collected at the same time, since the radiation from the analyser is collected by CdTe detectors by Bragg reflection. The analysers must be spherical and sliced, with a radius equals to the distance between sample and analyser. It ensures an identical Bragg angle for each photon entering the device [77]. This is known as Rowland condition.

To measure at one particular momentum transfer, the scattering angle 2-θ and the orientation of the sample (two angles) should be calculated. The geometry of the scattering can be transformed in (HKL) coordinates, normally done by the UB matrix [78]. In order to perform an energy scan with the backscattering geometry, the energy difference cannot be done by varying the Bragg angle between the analysers and the monochromator. Instead, the temperature T of the main monochromator is changed, producing a change in its lattice parameters d, while the analysers temperature is kept constant [79]:

$$\frac{\Delta T}{T} = \alpha(T)\Delta T; \qquad \text{where} \qquad \alpha(T) = \alpha_0 + \beta(T - T_0) \quad , \tag{3.16}$$

where $\alpha(T)$ is the expansion coefficient, considering T_0=22.5 °C and the constant are α_0=(2.581±0.002)x10^{-6}K^{-1} and β=(0.016±0.004)x10^{-6}K^{-2} [80]. The variation in the lattice parameter corresponds to a variation in the scattered energy,

looking at the Bragg law:

$$\frac{nhc}{E} = 2d\sin\theta. \tag{3.17}$$

Then, the variation of the lattice parameter Δd corresponds with $\Delta E/E$= -$\Delta d/d$ and looking at Equation 3.16 becomes:

$$\frac{\Delta E}{E} = -\int_{T_0}^{T} \alpha_0 + \beta(T' - T_0)dT' = -(\alpha_0 - \beta T_0)\Delta T + \frac{1}{2}\beta(T^2 - T_0^2). \tag{3.18}$$

Thus, the temperature of the monochromator should be controlled with a precision of mK. In the same way, the analysers should have a stable temperature with the same precision. In order to accurately control the stability, a temperature bath is controlled by an active feedback system [81]. For further information about the theory and the instrumentation, the reader is encouraged to read Ref. [1, 65, 82–84]

3.3.1. IXS spectra

The IXS scans are the intensity collected in the detectors in function of the temperature of the monochromator, or better the energy loss. An example is shown in Fig. 3.5. The collecting time can vary between 30 seconds up to a few minutes for each point of the scan. The count rate varies considering the scattering cross-section, the incoming flux, the illuminated volume and the efficiency of the analysers.

One should take in account the instrumental resolution when measuring the intensity, adding it to the single phonon scattering intensity derived in the first part of the chapter, Eq. 3.14:

$$I(\mathbf{Q}, E) = A(\mathbf{Q})[I_1(\mathbf{Q}, E) \bigotimes R(E)] + B(Q, E) \tag{3.19}$$

where $A(\mathbf{Q})$ is the intensity factor taking into account the experimental set-up and the scattering geometry, $R(E)$ the instrumental resolution function and $B(\mathbf{Q}, E)$ is related to the background of the electronics and the environment [1]. In the case of ID28, the contribution of the background can be neglected, since it is of the

[1] The $\bigotimes$ denotes the convolution operator.

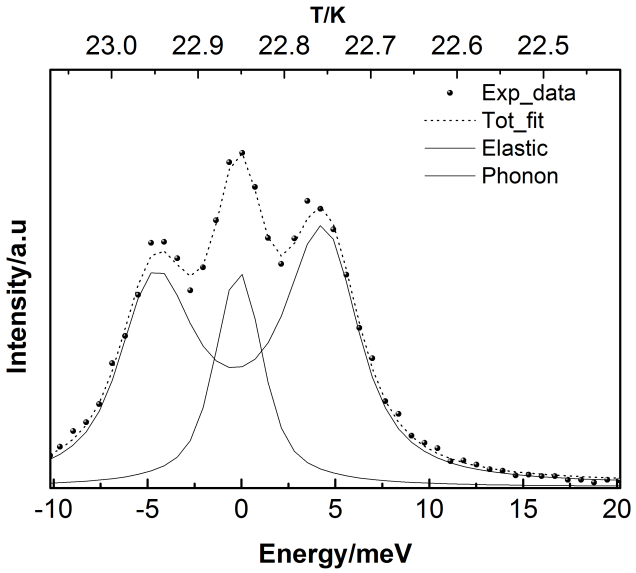

Figure 3.5.: Example of IXS scan with a resolution in energy of 3 meV and a resolution in Q of 0.076 Å. In this particular scan, the horizontal slits had a gap of 56 mm, normally they are opened at 20 mm, giving a resolution in Q of 0.025 Å. The scan is taken at 250 K for the sample m=6 in **Q**=(2.62 2 0). The dots correspond to the experimental data. The total fit is in dotted line whereas the fitted elastic peak and phonon are drawn by black lines.

order of one count per 30 minutes. Whereas the instrumental resolution function is normally measured by the scattering of a plexiglass sample at T=10 K and at the position of q=10 nm^{-1}, where the inelastic contribution is minimised. The resolution has, for example, FWHM of 3.0 meV with the reflection Si(999), fitted by a pseudo-Voigt function.

In the scan, Fig. 3.5, a central peak at zero energy corresponds to the elastic peak and it is fitted by a Lorentzian considering the instrumental resolution. On the other hand, the peaks at a certain energy transfer are related to the phonons which are created or annihilated, $E > 0$ and $E < 0$, respectively. Thus, two symmetric peaks at negative and positive energies are visible. However, the amplitude is different and the difference on intensity is related to the temperature for the Bose-Einstein factor. In order to fit the phonon profile, obviously considering the instrumental resolution, the Damped harmonic oscillator (DHO) or a Lorentzian profile are normally chosen. In the DHO case [85]:

$$I(\mathbf{Q},E) = \frac{2}{\pi}|A(\mathbf{Q})|\frac{E-E_0}{1-\mathrm{e}^{-(E-E_0)/k_BT}}\frac{|2\Gamma_{\mathbf{Q}}|}{\left[(E-E_0)^2-\hbar^2\omega_{\mathbf{Q}}^2\right]^2+(2\Gamma_{\mathbf{Q}})^2(E-E_0)^2}, \tag{3.20}$$

where $\hbar\omega_{\mathbf{Q}}$ is the phonon energy, $\Gamma_{\mathbf{Q}}$ is FWHM of the peak, E the loss energy and E_0 the compensation for a change in the zero energy.

3.4. High pressure measurements

The high-pressure measurements to reach very high pressure is normally done in two ways: with a piston-cylinder vessel or by anvils which compress the sample in the middle. The Diamond anvil cell (DAC) is the most used achieving until 400 GPa, an example in Fig. 3.6.

The sample is positioned in between the two gem-quality single crystal diamonds with a flat surface and a conic shape. From the area of the anvil faces, the pressure into the DAC can change applying the same amount of force (P=F/A). In order to apply the pressure on the sample, the faces must have a high degree of concentricity and parallelism. One of the anvils is mounted at the end of a sliding piston and it is guided to the other anvil in two ways: or mechanically by screws, or by gas loading. In order to protect the diamonds and to produce an isotropic pressure distribution on the sample, the latter should be confined in a pressure medium softer than the sample. To do that, a metallic gasket is used. Normally, an indentation of the

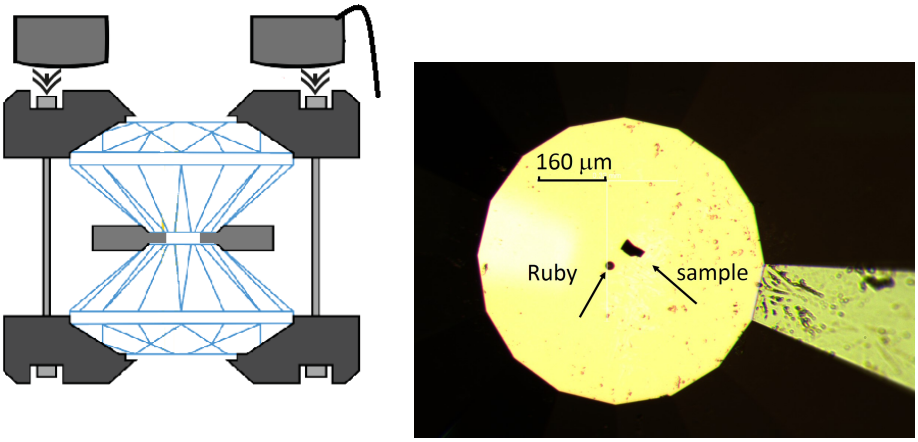

(a) (b)

Figure 3.6.: (a) A sketch of a DAC with the two diamonds separated by a gasket. The pressure applied by the membrane is also shown. In (b) an example of the sample m=8 (black platelet) on a 600 μm-culet diamond facet. A ruby crystal is also positioned near the sample.

gasket to leave a thickness of 3 times the sample one is used to avoiding instability and deformation in the hole. The hole is made in the middle of the gasket by laser-cut or electro-erosion. Also in this case, the hole diameter should be 3 times the sample size. The hole can be loaded with gas, *e.g.* helium and neon, liquid mixture, *e.g.* alcohol and silicon oil, or soft and hard solids such as NaCl or MgO.

To measure the pressure the most used method is the ruby fluorescence [86]. Tiny ruby crystals (5-30 μm), an example is visible in Fig. 3.6b, are positioned inside the DAC together with the sample and their luminescence is excited by a laser, showing a double peak that shifts linearly with hydrostatic pressure. The pressure calibration is done on the most intense peak, whose pressure dependence is well established by different experiments [87–90].

3.5. Experimental details

Here the experimental details for the two systems are presented.

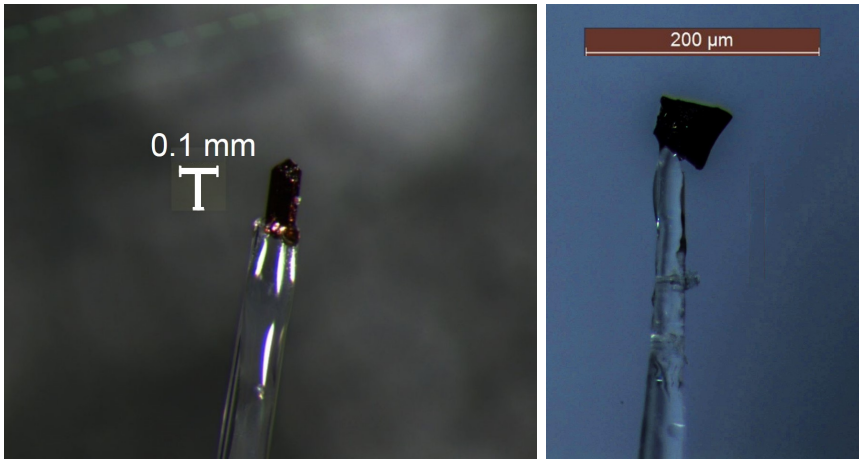

(a) (b)

Figure 3.7.: Example of samples mounted on a capillary: m=2 in figure (a) and m=7 in figure (b). The platelet-like shape and surface colour are similar. The c-axis is normal to the platelet for both.

$\mathbf{MPTB}_p$

High-quality samples were prepared in EnsiCaen by Elen Duverger-Nedellec of the CRISMAT group. The samples are platelet-like with a thickness of $\sim$ 20-40 μm and a maximum surface of 120x120 μm^2. The samples are too fragile to be cleaved or etched. For this reason, no chemical/physical treatment was done. The samples are mounted on a capillary, as it is shown in Fig. 3.7.

The DS measurements were made with a wavelength of 0.689 Å in ID23-1 and of 0.6968 Å in ID28. The frames were collected with an angular slicing of 0.1°/1sec in ID28 and in 0.1 sec in ID23-1. The IXS measurements were done using an energy resolution of 3 meV or 1.5 meV depending on necessity. In the Chapter 4 is specified in the text which resolution was used for the specific experiment or scan.

Pressure measurements were performed on two samples with a DAC of 600 μm culet, using neon as a pressure transmitting medium. Rhenium and stainless steel were used as gaskets, respectively, for m=10 and m=8 samples. In both cases, the orientation of the platelet (c-axis) is the one perpendicular to the diamond facets. Example of the sample m=8 positioned on the facet of the diamond with a ruby crystal is in Fig. 3.6b.

Antimony

Crystals of antimony were commercially available with a high quality from SurfaceNet GMBH [91]. The sample was etched using an HCl/HNO_3 mixture to remove surface damage. A rocking curve of $\backsim 0.1^\circ$ confirmed a high crystalline quality. A platelet-like sample of $\sim$50 μm thickness was used for ambient pressure measurements. For the high-pressure study, cylinders of $\sim$150 μm diameter and $\sim$50 μm thickness were laser cut with subsequent etching.

The pressure measurements were performed at room temperature with compressed helium used as a pressure transmitting medium. The sample was cut in order to be oriented with the hexagonal c-axis perpendicular to the diamond anvils.

The wavelength of 0.689 Å was used for the DS measurements in ID23. The frames were collected with an angular slicing of 0.1°. The IXS measurements were performed with an energy resolution of 3 meV. The beam had a spot size of 15x13μm^2.

4. Lattice dynamics and CDW phases in the monophosphate tungsten bronze family

The study of the several CDW phases in the monophosphate tungsten bronze family is presented and discussed in this chapter. An introduction is necessary to understand the entire family, their electronic instabilities and the difference between family members, showing in details the state of the art for the specific ones studied in this work. The experimental results and the simulations will be extensively presented and examined. The family members will be compared with each other in this chapter's conclusion, in order to summarise the findings. In particular, the dimensionality of the system, as well as the structural and electronic instability characteristics will help to understand the differences between members of the family.

4.1. W-bronze family introduction

In the broad field of the low dimensional metals, peculiar electronic phases, such as superconductivity, charge and spin density waves (C-SDW), are investigated. Particular interest was dedicated to the "bronzes". This term was given to a large variety of ternary metal oxides with general formula $A_x(MO_y)_z$, where A is a monovalent cation or an elemental group. The A species change the occupation of the electrons in the $d - t_{2g}$ level of the transition metal (M). In fact, the MO_y parent oxides normally have those levels unoccupied. Thus, those new systems have a charge transfer that transforms them into conductors, giving a metallic surface recalling the Cu-Sn alloy of the same name.

The first electronic instabilities in this kind of oxides were found in the blue bronzes, in particular $K_{0.3}MoO_3$, and just a year later in the violet bronzes, such as AMo_6O_{17}, with A as K and Na [92–94]. In fact among the bronzes, the most studied are the molybdenum derivatives [58].

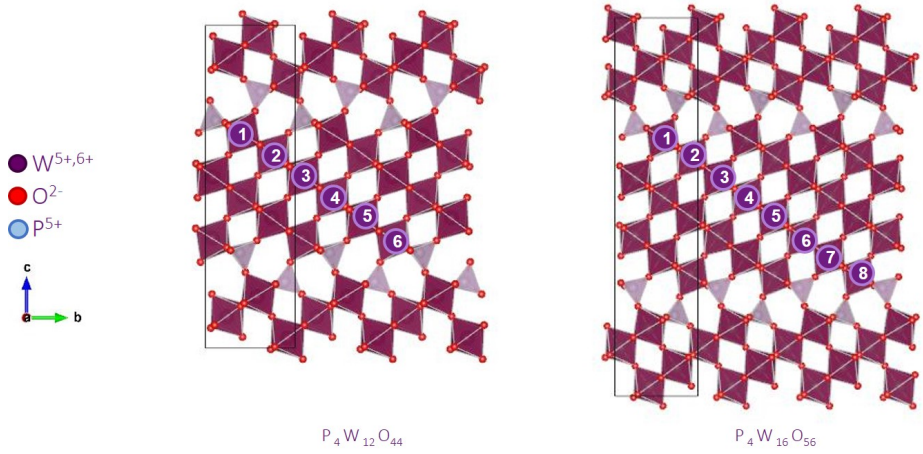

Figure 4.1.: The structure of the monophosphate tungsten bronze family. On the left, the member m=6 with formula $P_4W_{12}O_{44}$ and on the right, the member m=8 with formula $P_4W_{16}O_{56}$. The thickness of the W-block is the element that defines the different members and it is linked with the m index.

This chapter focuses on the monophosphate tungsten bronze family. A family of quasi-2D oxides with CDW instabilities. They were synthesised in the late 70s by mistake at the CRISMAT laboratory, in Caen (France), as an unsuccessfully synthesis of Rb_xWO_3 [95]. The general formula is $A_x(PO_2)_4(WO_3)_{2m}$, and the phosphorus was the spurious element that appeared in the silica ampoule where the oxides were synthesised [96].

The crystal structure

The bronzes have a framework structure similar to the Magnéli phase γ-Mo_4O_{11}, with stacking layers of octahedra and tetrahedra [97, 98]. The structure can be described as a ReO_3-type layered structure, composed by blocks of W-octahedra and monolayers of PO_4 tetrahedra. The m index, which defines the specific member and also the thickness of the W-block, can be seen in the structure in Fig. 4.1.

The family is divided into two varieties of structure. The first group is formed by the members with a pentagonal tunnel between the monolayer of phosphates and the W-block. The group is called $MPTB_p$, the subscript p is referred to pentagonal, and the blocks are linked by a rotation axis of order 2 plus translation. When an A cation is added to the general formula, the tunnel becomes hexagonal in order to let the cation enter in the tunnel. In this case, the blocks have the

same orientation and they are related only by translation. This is the $MPTB_h$ group, where the subscript h stands for hexagonal [99, 100]. This latter layered structure has been studied for technological applications due to the electrochemical, optical and mechanical properties [101–103]. Some materials can be used as Li-ion batteries cathode material, solid electrolytes in fuel cells and others, thanks to the hexagonal tunnels, which vary their shape thank to A_x.

In this Thesis, the $MPTB_p$ group will be studied. The thickness of the tungsten slabs varies with m, whereas the a, b cell parameters weakly differ. The c dependence can be described as:

$$c = \frac{ma\cos 35^\circ}{\sqrt{2}} + 4.90\text{Å} \quad .$$

A way to described this group by a single superstructure was formulated by Pérez *et al.* [104]. They summarised the high-temperature structures with the (3+1) mode. This model works for all the known members in their high-symmetry phases with the exception of m=9, defined by a ≈5.30 Å, b ≈6.58 Å, c ≈2.95 Å where the modulation vector is $q=\frac{1}{m+2}c$ and the supergroup is Pnnm(00σ_3)0s0. This example is referred to as an orthorhombic group for the even member. The odd members are described by a monoclinic structure, with a slight deviation from 90° for the β angle.

The empty perovskite cubic structure is the base of this system. However, the substitution of one octahedron with a P-tetrahedra which has a shorter distance gives rise to some possible distortions in the structure:

(i) a distortion in the W-octahedra neighbours, i.e. their O-O distances;

(ii) a possible tilting in the octahedra;

(iii) a possible displacement in the W atoms inside the octahedra, with an off-centred W position.

Earlier diffraction studies confirmed the tilting of ∼ 8° in the same direction for the same segment and in mirror position with respect to the others. The segments are along the [100] and [010] axes of the perovskites [96].

This family is of particular interest, since several properties depend on m. Looking at the thickness of the W-block, the system behaves similarly to WO_3 with increasing m($m \to \infty$). The oxide has an anti-ferroelectric (AFE) behaviour [105] and the high-term members seem to follow it, such as the example of the case of m=10 [106]. Whereas the members with $m < 6$ are reported as classical Peierls systems with a weak electron-phonon coupling.

Another parameter influenced by m is the oxidation state (OS) of the cell, which is constant for each member, whereas the single tungsten OS is dependent of m, giving as result that W OS will evolve to reach 6, W OS $\rightarrow$6 with $m \rightarrow \infty$. For this reason, the electronic properties are tuned by m and the electronic density decreases in the higher term members. It leads to a smaller screening of the long-range Coulomb interactions, and a possible Wigner localization of charges through a Mott transition [107] in the higher term members [108, 109]. Thus, the parameter m can tune the properties of the system. This family is clearly a good use-case to study the change in the dimensionality, electron-phonon coupling and other properties, as well as the subsequent CDW phase.

Charge density wave phases in the family

This family shows quasi-2D electronic properties and a quasi-cylindrical Fermi surface, since the *5d* conduction electrons are located in the empty perovskite-like WO_3 slabs. Additionally, there are directions where the W-chains have a strong overlap of the d-t_{2g} orbitals in the block. Due to this specific directionality, the chains are considered as quasi-1D chains which form quasi-2D oxides. This is at the basis of the "hidden" Fermi surface nesting and the correlated CDW instability [46, 110–112].

Thus, the distortions due to the change in the basic empty perovskite cubic structure and the particular electronic structure give rise to the CDW instabilities. In general, the CDW transition temperature increases with m, thus a better nesting of the Fermi surface is achieved [113]. In literature, tables with all the members information as cell parameters, temperatures of transition, T_{CDW}, modulation vectors, were reported multiple times. They can be consulted in the publications of Roussel and Duverger-Nedellec [96, 114, 115]. We report the essential information for the studied members in Sec. 4.2.

The structure in the CDW phases and their modulation vectors are less known with respect to the high-symmetry phase. The first refinements were done in the 2000s for m=4 and 10 [106, 116]. After that, one had to wait almost 20 years in order to add the refinement structures of the different phases for m=6, 8 and the missed ones of m=10 by Duverger-Nedellec [115]. Thanks to her last work, the differences found between low- and high-term members, predicted in the literature, are confirmed. In fact, the CDW phases create a difference between members with a low-term, until m=6, and the high-term members, $m\geq$8.

In fact, the low-term members undergo a Peierls transition towards a CDW state characterised by a sinusoidal modulation, where the hole and electron pockets

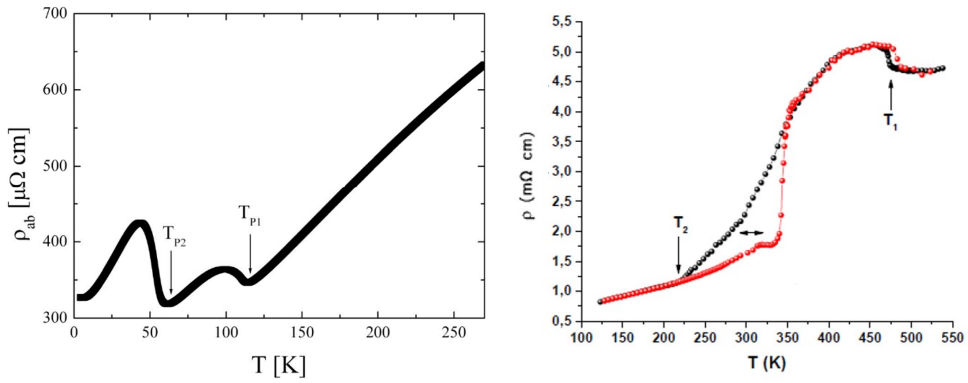

(a) (b)

Figure 4.2.: In (a) the temperature dependence of the resistivity for the low-term member m=6. In (b) an example of temperature dependence of the resistivity for a high-term member, m=10. In black the decreasing temperature slope, in red the increasing temperature one. The pictures are taken from the PhD thesis work of Kolincio and Duverger-Nedellec [115, 119], respectively .

stayed on Fermi surface due to the CDW gap openings [117, 118]. The low-term members present CDW with incommensurate vectors and weak satellite reflections.

For high-term members, the transitions are at higher temperatures and they have commensurate CDW **q**-vectors. In some members, the vectors correspond to the cell doubling with a **q**-vector along **a*** and **a*+c***, as for m=9,10,12, 13,14 [115, 120, 121]. In addition, the intensities of the satellites are around an order of magnitude higher than the low-term members ones and second order satellites are visible [115]. For the latter, a huge improvement in their detection due to the synchrotron measurements is shown in the PhD thesis work of Duverger-Nedellec, since she performed some experiments in ID23 at the ESRF [115] and from our measurement, *vide infra*. There is not yet an understanding on the mechanism which underlies those CDW instabilities for the high-term members. It could be given by an enhanced electron-electron interaction and a strong electron-phonon coupling (considering the bipolaron-type model) or a competition between CDW and the antiferroelectric instability found in the parent oxide WO_3 ($m \to \infty$) [58, 121, 122]. The cell doubling seems to confirm the presence of the antiferroelectric-type distortion [106].

When the structural displacement is analysed, also in this case, the low- and high-term members present some differences. The displacement for the low-term members is related to some large displacement of the oxygen, whereas the tungsten is slightly moving. The high-term members present the same distortions, but the

displacement of the tungsten is bigger, between 0.19-0.4 Å [106, 115, 116]. An in-depth analysis of the structural deformation is presented in Sec. 4.7.

The structural displacements and the CDW phases differences are reflected in the physical properties. In fact, a "classic" example of resistivity increasing below the T_{CDW} is shown for the low-term member m=6, which is a general feature of the Peierls gap opening and the correlated change in the charge mobility, as it can be seen in Fig. 4.2a [117, 119]. As example of the behaviour for the high-term member, the m=10 is shown in Fig. 4.2b. At high temperature, they normally present a bad metal behaviour (increasing m, the system is going to the insulator behaviour of WO_3), with an abrupt change in the slope due to a first order transition. They normally also present hysteresis between the increasing/decreasing slope [115, 121].

Electronic structure and its calculation

Since this family has a quasi-2D electronic structure with instabilities, a section dedicated to the electronic structure and its calculation is necessary.

For every member of the family, there are two 5d electrons for m WO_6 octahedra that contribute to the conduction band. Those electrons are uniformly distributed in the tungstens. For each W-atom, there is an average of $2/m$ conduction electrons. They will cover the t_{2g} just in the lower energy part. The band was calculated for the first time with a tight binding method using the extended Hückel in a 2D approximation by Canadell and Whangbo for m=2,4,5,6,7,8 [110, 111, 123, 124]. They took as base the zig-zag chain as shown in Fig. 4.3 and they start from the single W-block where they use the a, b and c parameters oriented with the block. Three directions are necessary to describe the entire W-block by the zig-zag chains. Those directions create three bands and the resulting electronic dispersion is shown in Fig. 4.4 on the left, for the case of m=6. The directions are $\mathbf{a}^*$, $(\mathbf{a}^* + \mathbf{b}^*)$ and $(\mathbf{a}^* - \mathbf{b}^*)$. It can be seen that there is a band confined along the $\mathbf{a}^*$ axis, which is a 1D-band. The other two are 2D bands, dispersive along the $\mathbf{a}^*$ and $\mathbf{b}^*$ axes. When those results are combined and the three Fermi surfaces are superimposed, their nesting is visible, shown in Fig. 4.4 on the right. Different combined Fermi surfaces can be drawn from the electronic band, depending on the Fermi energy. For this family, the result is in Fig. 4.4a, when there are two electrons in the t_{2g}. The Fermi surface combination of the three bands for the m=8 is also represented in Fig. 4.5a, where the decomposition in the 1D and the 2D bands are also represented in (b) and (c) figures [111].

Also *ab initio* calculations were performed with the generalized gradient approximation (GGA), used for the exchange energy specifically [125]. From the calculation, it has been found that the energy bands along c* are flat ($\Gamma - Z$), meaning

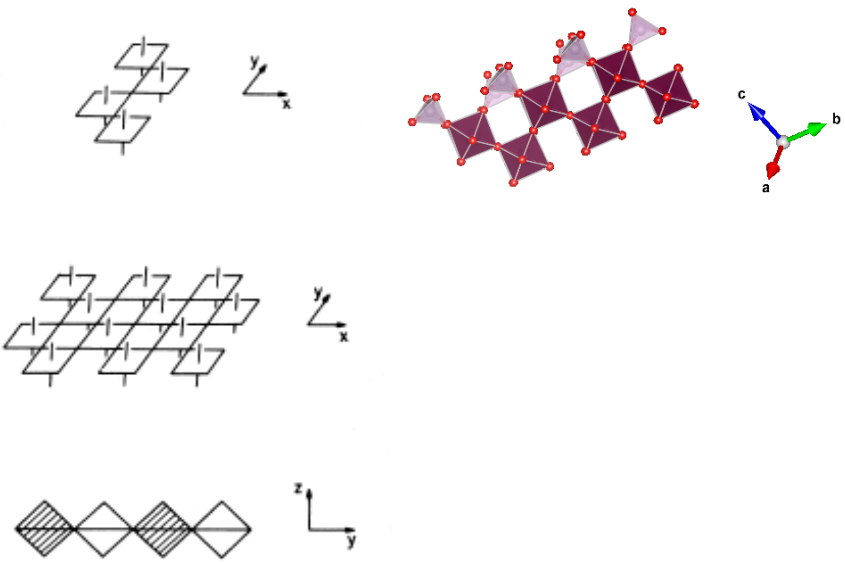

(a) (b)

Figure 4.3.: (a) The zig-zag chains with the unit W_4O_{21} along different projection. *E. Canadell, M.-H. Whangbo, Phys. Rev. B* ***43*** *1894 (1991).* Copyright 2018 by the American Physical Society. (b) Example of zig-zag chain in the monophosphate tungsten bronzes structure (m=8).

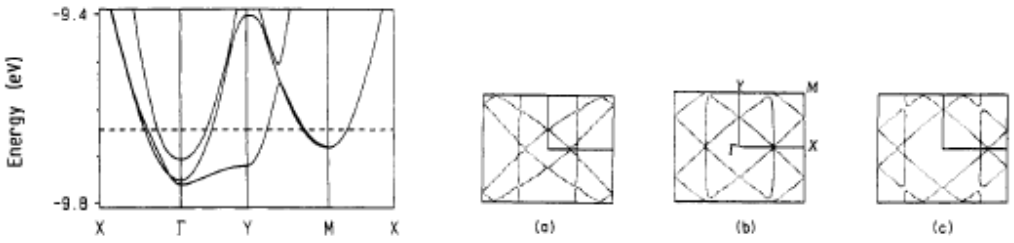

Figure 4.4.: The dispersion relations calculated by Canadell and Whangbo for m=6, on the left. On the right the figure (a), (b) and (c) correspond to the combined Fermi surfaces choosing a different E_F. Reprinted with permission from *E. Canadell, M.-H. Whangbo, Chem. Rev.* ***91*** *965-1034 (1991).* Copyright 2018 by Academic Chemical Society

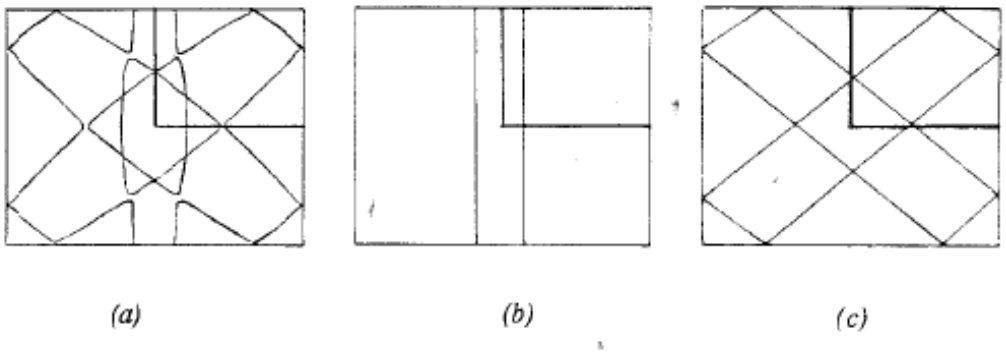

Figure 4.5.: The combination of the Fermi surfaces for m=8. Reprinted with permission from *E. Canadell, M.-H. Whangbo, Chem. Rev.* ***91*** *965-1034 (1991).* Copyright 2018 by Academic Chemical Society

that the interaction along the layered direction is weak in m=6. This result provides evidence that supports the hypothesis that the tungsten bronze family has a 2D character. However, the EHTB method provides more convincing evidence, since it agrees very well with the experimental results obtained, *vide infra*. In the last years, the Fermi surface was studied experimentally twice through ARPES measurements, in both cases the impossibility to cleave properly the surface of the sample lead to partial studies [109, 125, 126].

Below the transition, those instabilities give rise to a gap opening in the electronic structure with either a metal-semiconductor transition, the 1D system, or a metal-metal transition if electron and hole pockets are left on the FS, which happens in the 2D case [108]. The tungsten bronzes family generally follows the second case. In fact, in 2D with the metal-metal transitions, the CDW gap is just partially open [127]. However, it is really difficult to trace the left part of the Fermi surface. Some example can be found for η-Mo_4O_{11} and for m=6 [117, 128].

4.2. State of art for *m*=2, *m*=6 and *m*=8

Degenerate case, m=2

The lowest member, m=2, can be taken as a degenerate case since the W-block becomes a single zig-zag chain, which is isolated by phosphate groups that surround it, Fig. 4.6.

A hypothesis has been raised that if the layered structure is not anymore present, the synthesis could lead to a bad quality crystal. This hypothesis has been found to

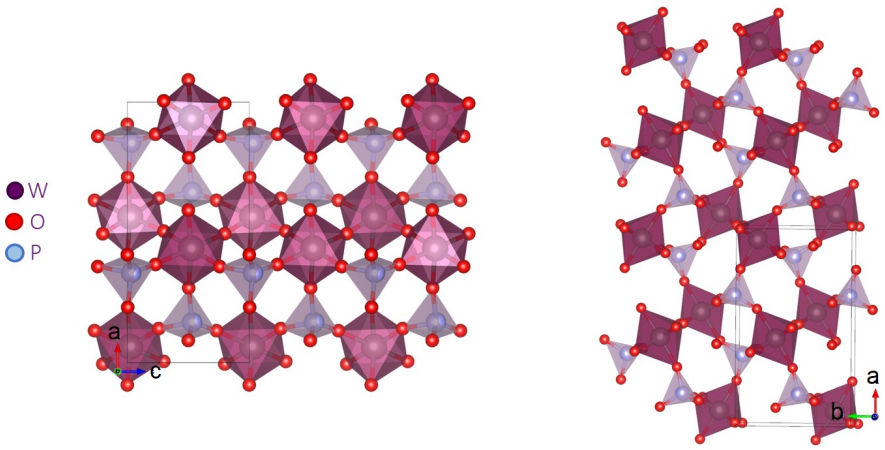

Figure 4.6.: The structure of m=2. The zig-zag chains of the W-octahedra, well visible on the left, are isolated from each other by the phosphate groups, shown on the right.

be misleading and this member was considered unstable, as it can be seen reported in Ref. [129].

Nevertheless, the member was successfully synthesised by two different groups [130, 131]. Initially, two different polymorphs were synthesised without and under pressure. The first, synthesised under pressure, has a tetragonal cell (a=6.250(1) Å and c=4.066(1) Å). The second crystallises with a monoclinic cell (a=5.235(1) Å, b=6.566(1) Å, c=11.19(1) Å and α=90.34(4)°) [131]. For the latter structure, a simplified system was proposed: an orthorhombic cell with space group $Pna2_1$ [130]. The structural analysis of this member shows a strong distortion of the octahedron and tetrahedron [130].

A theoretical paper by Canadell *et al.* examined the system through tight-binding model, as they did for the other members, and they predicted a possible electronic instability due to the localised and delocalised electrons present in W_2O_{10} chains [123], as it can be seen in Fig. 4.7a. They first calculated the dispersion for the single corner-shared octahedra chain. The dispersions show dispersive and flat bands along Γ-Z, which corresponds to **a***, considering our cell parameter. They are related to the δ-orbital, x^2-y^2 orbital, and to the π-orbitals, xz and yz orbitals, respectively, as one can see in Fig. 4.7b. When the calculation is enlarged to the real cell, the result is similar.

The member m=2 presents a rare oxidation state for the tungsten of V and not an averaged one, as for the other members. Considering the d^1 configuration and the two tungsten atoms per cell, two electrons fill the t_{2g}. The lowest energy band is half filled, corresponding to the dispersive band. Whereas the two nearly

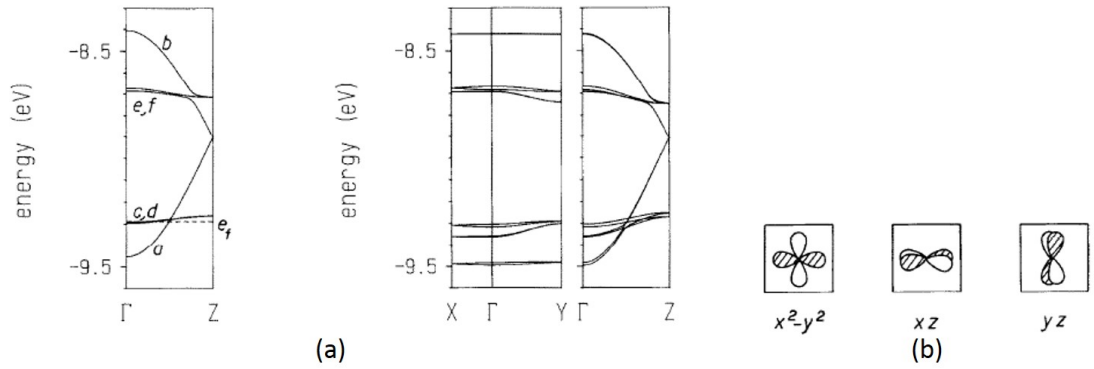

Figure 4.7.: (a) The calculated dispersions of the t_{2g} bands of m=2. On the left, the calculation related to the single zig-zag chains. On the right, the calculated dispersion relations of the three-dimensional lattice. (b) The schemes of the different orbitals that play a role in the dispersion. Reprinted with permission from *E. Canadell, M.-H. Whangbo, J. Solid State Chem.* ***86*** *131-134 (1990).* Copyright 2018 by Academic Press. Inc.

degenerate flat bands are quarter-filled. In the flat bands, the electrons will be localised [132–134], while they would be delocalised in the dispersive band. The latter has a 1D metallic behaviour that may lead to an electronic instability as a CDW one [123].

Teweldemedhin *et al.* studied the system through electrical resistivity measurements, checking for the probable instability found by calculation. The study did not show any CDW transition and the m=2 was observed to have a semiconductor behaviour, as one can see in Fig. 4.8. However, there is a quasi-one-dimensional character along the direction of the W-octahedra zig-zag chain. In fact, the resistivity is about one to two orders of magnitude lower than along the other directions [135].

Low-term member, *m*=6

Amongst all family members, the m=6 has probably been studied the most, due to a successful synthesis and to the fact that it is isostructural with the Magnéli molybdenum phase. For this member, diffuse scattering was already measured in the 90s, using Cu-α X-ray beam with the fixed-crystal, fixed-film method [128], as it can be seen in Fig. 4.9. The authors of [128] described the diffuse patterns as composed of diffuse lines "constituted by the superposition of slightly split diffuse segments" parallel to the **a*-b*** and **a*+b*** directions [128]. For them, those

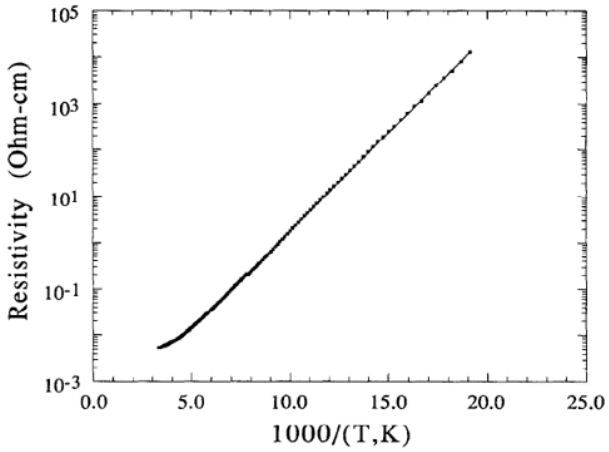

Figure 4.8.: The temperature dependence of the resistivity of m=2. A semiconductor behaviour is shown and no particular instabilities are visible. Reprinted with permission from *Z. S. Teweldemeghin, K. V. Ramanujachary, M. Greenblatt, J. Solid State Chem.* ***95*** *21-28 (1991).* Copyright 2018 by Academic Press. Inc.

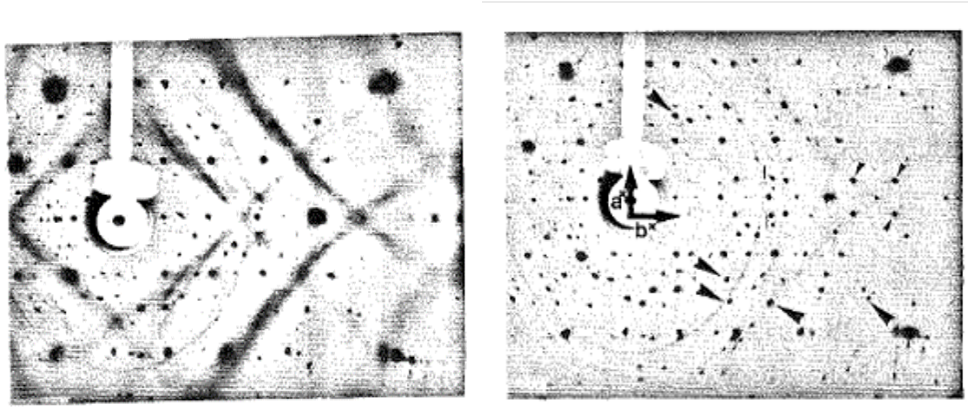

(a) (b)

Figure 4.9.: Diffuse scattering on m=6 at (a) 300 K and (b) 20 K, showing the transition to the CDW phase. The figure is taken from the PhD thesis work of Foury [117, 128].

diffuse lines in the reciprocal space correspond in the direct space to the directions of the WO_6 chains that are connected in a staircase manner by their axial oxygen atoms [111], as already explained in Sec. 4.1. Upon cooling, interchain critical correlations developed, looking at the modulation of the diffuse line intensity. Later, other diffuse scattering studies showed the low-frequency modes of the family, and in a study by Foury *et al.* [136] those modes were described as derived from a displacements of the tungsten atoms away from the octahedra centre. The correlation is inside the segment of the m octahedra. No correlation is found between neighbours, showing a ferroelectric-type displacement [136].

Three different CDW phases were found, the **q**-vector and the temperatures of transition are summarised in Tab. 4.1 [137]. The resistivity measurement shows the first two transitions, however the third one at 30 K is not visible, as can be seen in Fig. 4.2a. Nevertheless, the anomaly is visible through thermoelectric power and Hall effect measurements [138].

There were other experiments done on m=6, on which the magnetoresistance shows a large anisotropy in the lowest CDW phase, where small carrier pockets are left on the Fermi surface by the gap opening. Those pockets are described with cylindrical shape along c^*, thus leading to an anisotropy [113]. Reflectance spectra shows strong vibrational features when light is polarized along the interlayer direction (**c**) [139]. The 2D character was confirmed, with a semiconducting behaviour along **c**, while it is metallic in the other directions. These results confirm the prediction found by *ab-initio* calculations [125].

High-term member, *m*=8

One of the first studies made on m=8 was of Foury and Pouget in 1993. They claimed that this member was already in a distorted structure at room temperature [140]. From there, it was studied through diffraction and through its physical properties (resistivity, magnetoresistivity, thermoelectric power) [122, 127, 141–144]. This member has two transitions with associated CDW-vectors. In earlier studies the CDW spots were not condensing into distinct satellites neither in the 1^{st} phase at 220 K, neither in the 2^{nd} one at 200 K. Since the condensation was not achieved by cooling down at very low temperatures (until $\sim$ 35 K), as it can be seen in Fig. 4.10a, the CDWs were considered having a correlation of short-range only [120, 121]. At the two CDW phases, incommensurate modulations were assigned: $\mathbf{q}_1 \sim 0.47\mathbf{a^*}$ and $q_2 \sim 0.19\mathbf{a^*}$ [121]. The resistivity measured by Hess shows a metallic behaviour ($d\rho/dT > 0$) at high temperature (T > 300 K) and a very weak change in the slope corresponding to the first transition, Fig. 4.11a. At lower temperatures, the resistivity increases, perhaps due to a weak localisation which is created from the disorder of the system [144].

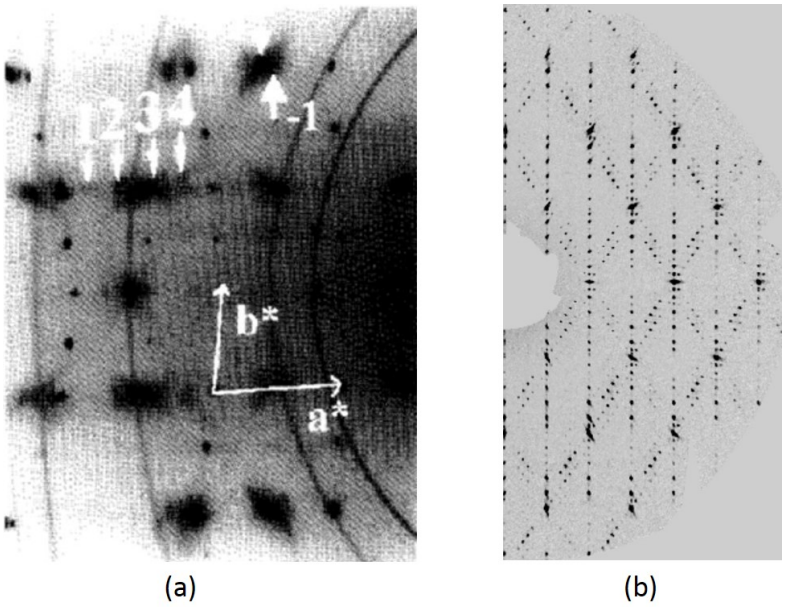

Figure 4.10.: (a) The diffuse scattering results at 37 K obtained by Ottolenghi *et al.*. Reprinted with permission from *A. Ottolenghi, P. Foury, J.P. Pouget, Z.S. Teweldemedhin, M. Greenblatt, D. Groult, J. Marcus and C. Schlenker, Synth. Met.* ***70*** *1301-1302 (1995).* Copyright 2018 by Elsevier Science S.A. In figure (b) the H0L planes obtained by Duverger-Nedellec, with a condensation of the CDW spots in a long-range correlation [115].

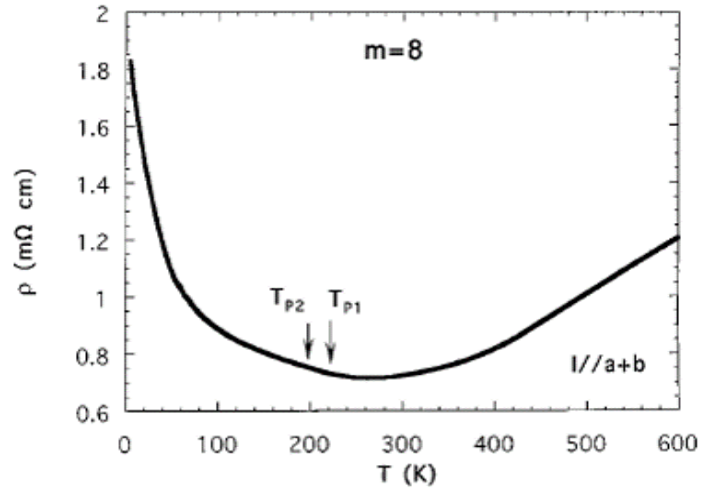

(a)

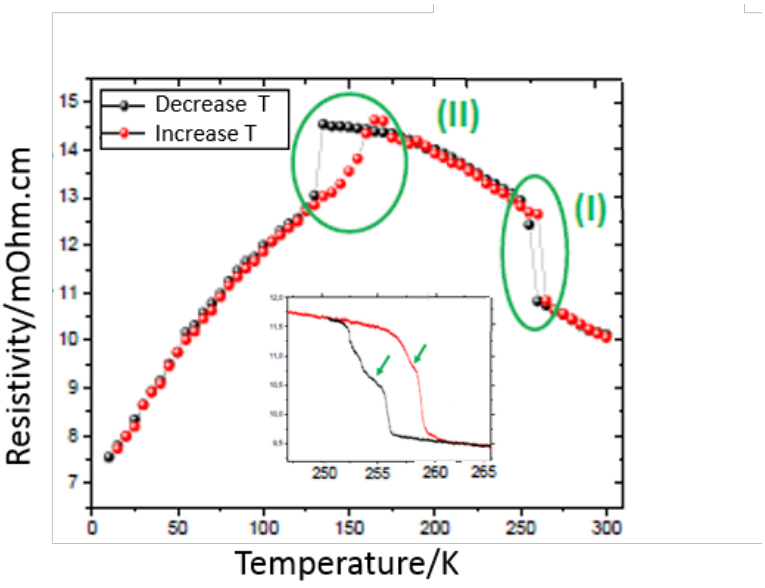

(b)

Figure 4.11.: (a) The temperature dependence of the resistivity measured by Hess [143] and (b) the resistivity measured by Duverger-Nedellec, where two transitions of the 1st order are clearly visible [115].

A new synthesised sample leads the group in Caen to find the long-range correlation for m=8 through diffraction measurement, Fig. 4.10. By resistivity, the clear evidence of three transitions, as it can be seen in Fig. 4.11b, shows the difference between the samples quality. The two already known are transitions of the 1st order. In addition, a new phase with a tiny range of temperatures is found before the 1st phase and it was called phase 0 (258–250 K). This new result presents a member that can be defined as high-term member [145]. The refinement of the CDW phases found commensurate vectors for the two strong transitions with components in **a*** and **c***, as it can be seen in Tab. 4.1. The intensity of the satellites is one order of magnitude higher with respect to the low-term members.

While this member has been considered to be between the low- and high-term members [121], the latest results suggest it belongs to the group of high-term members. This can be better understood by studying the refinement of the CDW phases. It shows strong W-atoms displacements with respect to the octahedra center, oriented in different directions suggesting an antiferroelectric (AFE)-like order as for another high-term member [106]. Those displacements are a result of collective movements of atoms in the direction of the chains with a total ferroelectric (FE) order for the 2nd CDW phase and only partial for the 1st phase [115].

Finally, a summary of the space group, cell parameters and CDW instabilities reported in the literature for the different members is shown in Tab. 4.1. An important difference regarding the m=6 and m=8 CDW phases should be emphasized. In m=6, the modulation vectors are added after each transition. In fact, the $\mathbf{q}_{CDW}$ of the 1st phase can be found also in the 2nd and 3nd and so on. In the latter member, there are separate modulation vectors for each phase.

4.3. Experimental method

The samples were prepared in Caen [1] with a refined synthesis for high-quality crystals. The diffuse scattering demonstrates the difference with respect to the quality of the crystals used until now.

The synthesis in a three-step process is well explained in the PhD thesis work of Duverger-Nedellec. She provided, together with her collaborators, all the sample used in this study [115]. The first two steps allow one to obtain powders of MPTB$_p$,

[1] This project was possible thanks to a close collaboration with a group in Caen; Dr. Olivier Perez, Dr. Alain Pautrat and, at the time, the PhD student assigned to the synthesis, diffraction characterization and physicals analysis, Dr. Elen Duverger-Nedellec, and Dr. Marc de Boissieu from the Université de Grenoble Alpes.

member	space group and cell parameters at RT	T_C	modulation vector	Ref.
2	$P2_1cn$			[130]
	a=5.23 Å b=6.55 Å			
	c=11.17 Å			
6	$P2_12_12_1$	T_1 = 120 K	q_1=[0.385,0,0]	[115, 128]
	a=5.29 Å b=6.56 Å	T_2 = 62 K	q_2=[0.310,0.295,0]	[115, 128]
	c=23.55 Å	T_3 = 30 K	q_3=[0.29,0.11,0]	[115]
8	$P2_12_12_1$	$T_0 \sim$ 258 K	q_0=[0.446,0,0]	[115]
	a=5.29 Å b=6.55 Å	T_1 = 250 K	q_1=[4/9,0,-4/9]	[115]
	c=29.70 Å	T_2 = 125 K	q_{21}=[1/2,0,-1/2]	[115]
			q_{22}=[1/6,0,-1/6]	[115]

Table 4.1.: Space groups and cell parameters of m=2, 6 and 8 and the critical temperatures and modulation wave vectors for m=6 and 8.

and they take in total some days, whereas the last step is the growing process into a single crystal. The powder should stay in a quartz tube with a temperature gradient (from 1000° to 1200°) for a month. The total reaction can be described as:

$$2P_2O_5 + (2m - \frac{2}{3})WO_3 + \frac{2}{3}W \rightarrow (PO_2)_4(WO_3)_{2m}$$

The sample has normally a platelet-like shape where c is perpendicular to the plate. The best quality samples are normally grown in the cold part of the quartz tube. However, the quality is first confirmed by an optic exam and, later, with the diffraction. The crystal quality is essential for the CDW presence and for the fundamental diffuse scattering features, that can become blurry in case of defects, i.e. stacking faults. Some examples are shown in our results but also in precedent works [115].

4.4. Member *m*=2

The member m=2 was initially synthesised for another purpose. In fact, it is the only one in the family with oxidation state, W^V. Some RIXS measurements were under preparation and they are based on the differences in the d states [2]. Thus, m=2 was the perfect example of a d^1 state. Running some preliminary test on the crystal quality by DS, we noticed some diffuse intensities that could correspond to CDW satellites. As already anticipated in Sec. 4.2, this member is the only one without an electronic instability according to the literature. Through thorough IXS measurements, the CDW phase was confirmed at surprisingly high temperature ($\sim$ 270K). In this work, DS and IXS measurements are reported. In addition, the results obtained by the group in Caen that are important for the understanding of this work will be mentioned and presented. For more information about the synthesis and the crystallographic and physics results, the reader is advised to consult the PhD thesis of Duverger-Nedellec [115].

4.4.1. Experimental study of a new CDW phase (*m*=2)

This member is expected to present different characteristics with respect to the other members of the family as already explained in the introduction, due to its

[2] The analysis of the RIXS data is ongoing.

peculiar structure. The W-octahedra do not form a block with a certain thickness, they are rather positioned in a single zig-zag chain which is completely isolated from the others due to the P-tetrahedra that surround the chain. This particularity gives to this member a quasi-1D-character, lowering the dimensionality with respect to the others. There are good reasons to expect an electronic instability, however, as already mentioned, in an earlier study no interesting features were noticed through resistivity measurements [135]. On the other hand, an electronic instability was predicted in a theoretical paper by Canadell and Whangbo along the octahedra chain direction [123].

The diffuse scattering, made to evaluate the quality of the crystals, revealed some diffuse patterns concentrated around specific **q** in the reciprocal space. Diffuse rods, or pre-transitional fluctuations as planes and lines were not observed, as the 3D reconstruction shows in Fig. 4.12b. The only observable is an isotropically-distributed diffuse pattern around what could be a satellite. A temperature study of the system revealed a possible CDW transition, Fig. 4.12. The 0KL reconstructed maps at different temperatures show the development of the transition, starting from a diffuse cloud which condenses in a CDW satellite. The temperature of transition is quite high($\sim$ 270 K), considering the trend in the bronze family. The q-vector has a **b*** component and from the diffuse scattering measurement it can be evaluated as **q**(0,0.25,0). From the figure, a focus on the interesting zone shows the (01$\overline{6}$) Bragg peak and a satellite at (0 1+ξ $\overline{6}$),with ξ=-0.25, which were chosen for the inelastic measurements, *vide infra*.

In order to check the assumptions made about a CDW transition, the rocking curves were recorded with IXS spectrometer ($\Delta E = 0$) at different temperatures on the diffuse spots near the Bragg peak. The satellite at **Q**(0, 0.75, $\overline{6}$) shows the development of an elastic peak at the transition, as seen in Fig. 4.13. In Fig. 4.13b, the intensity starts to increase at room temperature and the satellite is completely formed at around 270 K. The latter measurement confirms the CDW phase for this member with the same temperature transition observed by DS. Diffraction studies and transport measurements made in Caen corroborated our results, Fig. 4.14. In the earlier works found in literature in which no CDW transition was found, probably the quality of the samples or the synthesis were different [135].

The high temperature phase can be indexed by an orthorhombic cell with parameters: a=5.223 Å, b= 6.548 Å and c=11.91 Å. It has been confirmed, using diffraction measurements, that the commensurate modulation vector is of $\mathbf{q} = \frac{1}{4}\mathbf{b}^*$ [115]. The CDW phase in the superspace can be described as orthorhombic $P2_1cn(0\sigma_1 0)00s$, due to the structural refinement. Through resistivity measurements, three instabilities were found, at 285 K, 180 K and 120 K, as shown in Fig. 4.14 [115]. Additionally, the CDW depinning has been observed. This is the first observation of this effect in a member of the monophosphate tungsten bronzes.

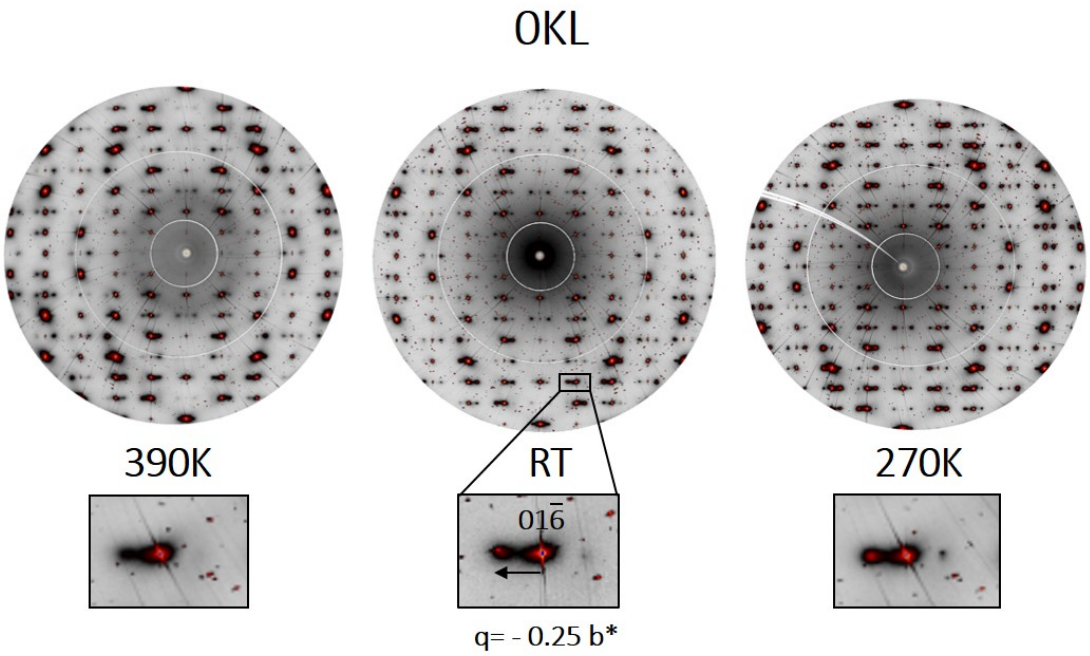

(a)

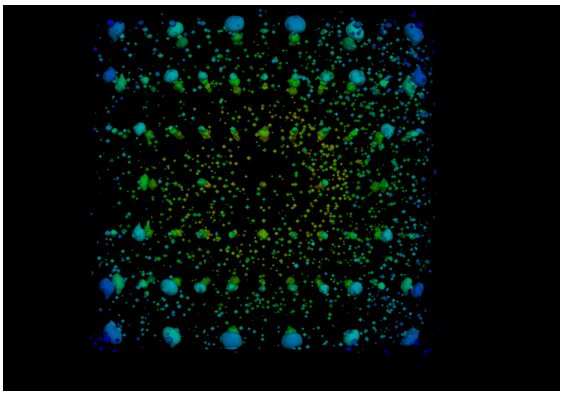

(b)

Figure 4.12.: In figure (a) the reconstructed 0KL diffuse maps of m=2 at 390 K, RT and T_{CDW}=270 K. A focus on (01$\bar{6}$) shows the part of the reciprocal space where IXS measurements were performed, following the **b** direction. It also visualises better the diffuse and subsequent Bragg satellite at **q**=-0.25**b*** and its evolution by temperature. In figure (b) the 3D reconstruction of the reciprocal space with the layer parallel to 0KL plane. The pretransitional diffuse scattering around the satellite is roughly isotropic.

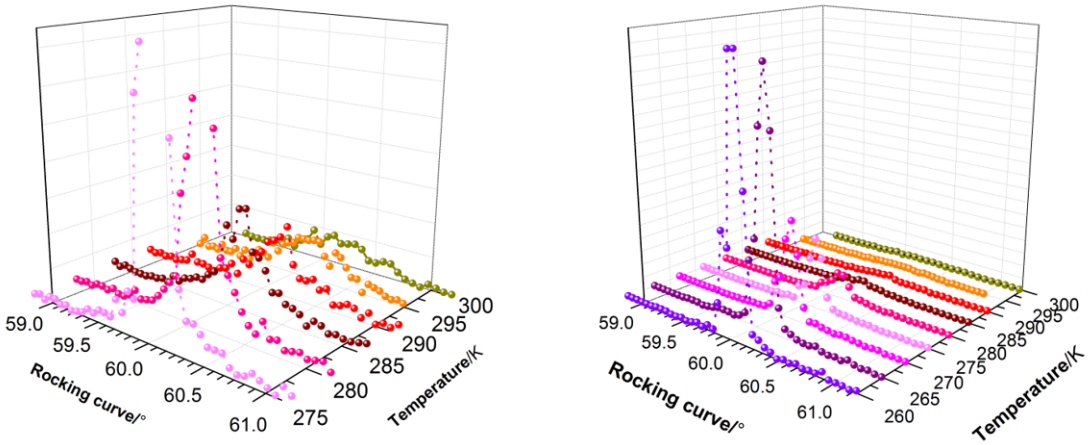

(a)

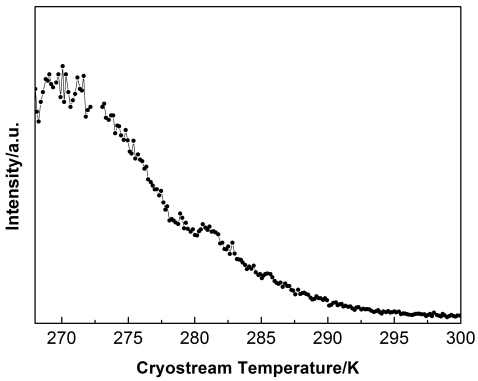

(b)

Figure 4.13.: In figure (a) the rocking curves made by IXS on the CDW satellite, **q**=-0.25**b***, at the reciprocal position Q(0 -0.75 6), from 300 K to 275 K, on the left, and until the transition, on the right, where the intensity increases and the Bragg peak is formed. In figure (b) the intensity recorded on the detector with the IXS spectrometer on cooling temperature is consistent with the transition temperature around 270 K.

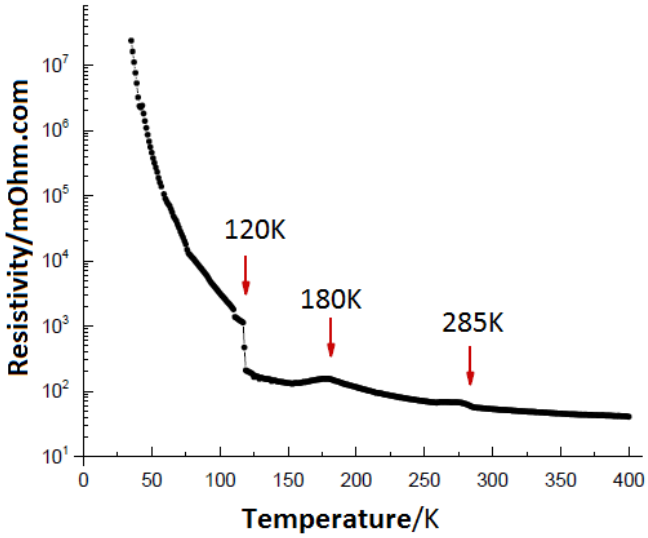

Figure 4.14.: Temperature dependence of the resistivity in m=2. Three anomalies are observed at 285 K, 180 K and 120 K. The first one is related to the CDW phase. The figure is modified from the PhD thesis work of Duverger-Nedellec [115].

This phenomenon can be responsible for the instabilities below 250 K found by the resistivity measurement [115].

In order to find the response of the lattice dynamics to the electronic instability caused by the CDW phase, inelastic scans were performed along the **b*** direction from the $(01\bar{6})$ Bragg peak. Since the satellite is strong in negative direction and less evident in the opposite direction, the positive direction helps to uncover the phonon dispersion without the huge anomaly that the satellite peaks cause, as shown in the phonon maps at different temperatures in **??**. Furthermore, the IXS scans of the dispersion taken at room temperature show the acoustic-like phonon dispersion, the related phonon peaks are highlighted by their area in Fig. 4.16a. In addition, a low energy peak corresponding to the soft phonon mode is clearly visible for ξ>0.30 near the elastic scattering. The evidence of the existence was given by the extremely large elastic peak, which could not be fitted considering just the resolution of the elastic peak. However, the real position in energy was very difficult to fit. One can evaluate a range of energies (2-4 meV). In order to decrease the elastic peak on the satellite, the temperature was increased, however, also in this case no significant change is observed. The temperature dependence of the elastic component is observed in Fig. 4.16b, where the IXS scans at ξ=0.25 show a progressively decreasing intensity of the elastic peak by increasing temperature. At the same time, the increasing temperature reveals the soft phonon at $\sim$ 2.5

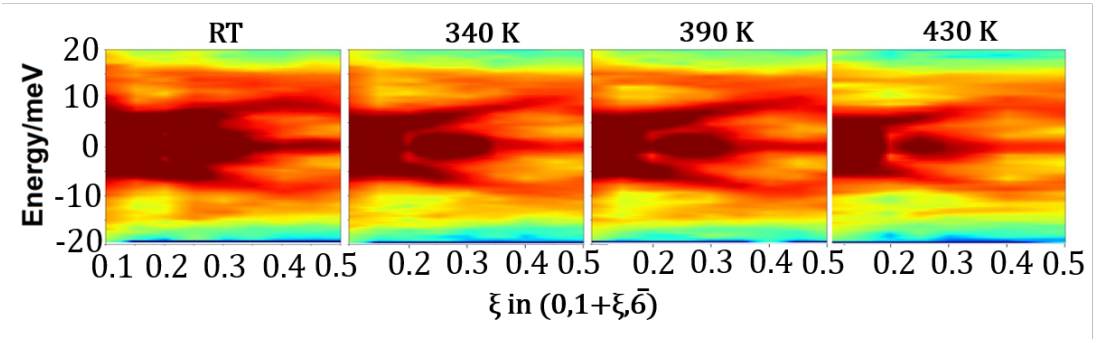

Figure 4.15.: Phonon dispersion map made by IXS scans at different temperatures: RT, 340 K, 390 K and 430 K from the left to the right in the direction [010], where the satellite is less visible. However, an elastic component is neverthless present at x=0.25. The scans were obtained with a resolution of 3 meV.

meV.

In the negative direction, where the satellite is condensing, the related phonon dispersion shows a clear softening, Fig. 4.17a. From 430 K to room temperature, the dispersion has a softening at **q**=1/4**b***. However, the resolution of 3 meV is not sufficient to study the phonon softening, due to the very low energy of the phonon. For this reason, the Si (12 12 12) reflection was chosen with a resolution of 1.5 meV. In order to follow the softening, more inelastic scans on the satellite were recorded. An example of the fit done on the IXS scans is presented in Fig. 4.18. The first scan at 390 K shows just an inelastic contribution and gives easy access to the position of the phonon (E=(1.66±0.05)meV). Inevitably, the elastic peak increases, as one moves closer to the transition temperature, covering the phonon contribution. The fit was possible until 290 K (E=(0.80±0.15)meV), after which the phonon position was impossible to determine. The fit results are shown in Fig. 4.17b, in which a softening is visible and the phonon progressively goes to zero as one reaches the transition region. It is possible to fit the temperature dependency of the phonon energy by the power law that is normally used for second order transitions:

$$E = E_0(1 - T_{CDW}/T)^{\gamma}$$

,

where E_0 corresponds to the high-T limit, γ is the critical exponent and normally is equal to 0.5 within the mean-field theory for second order transitions [146, 147]. The temperature transition was chosen as 270 K, looking at the IXS results.

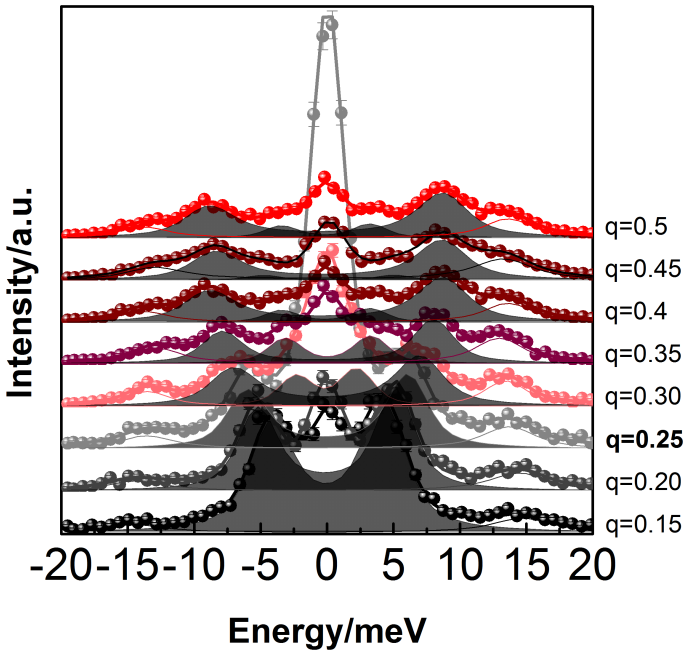

(a)

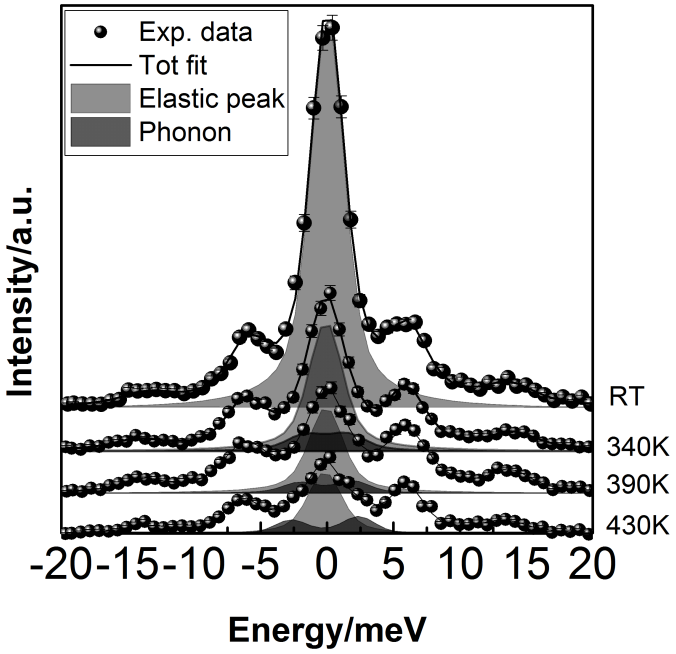

(b)

Figure 4.16.: (a) The IXS scans of the dispersion along **q**=(0ξ0) at room temperature. The areas of the acoustic-like phonons are highlighted. (b) The temperature dependence of the elastic and phonon contribution, highlighted by their area, on the satellite Q(0 1.25 $\overline{6}$) through IXS measurement.

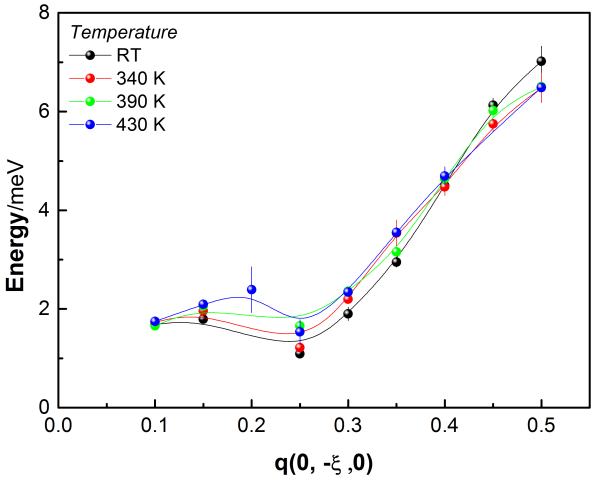

(a)

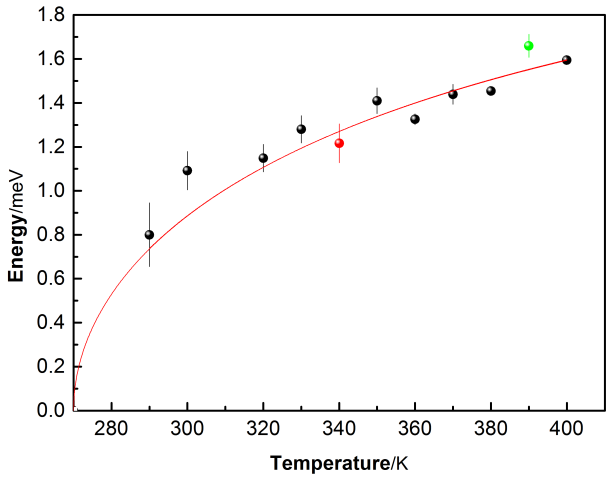

(b)

Figure 4.17.: (a) The phonon dispersion curve in the **b*** direction for negative ξ values from the Bragg $(01\bar{6})$. The solid lines are only guide for the eyes. (b) The temperature dependence of the phonon energy at ξ=0.25, which is the satellite position. The phonon seems to freeze at zero-energy reaching T_{CDW}, the fitting follows the power law, which is shown as a red line. The coloured points are referred to the temperature where the total dispersion was performed.

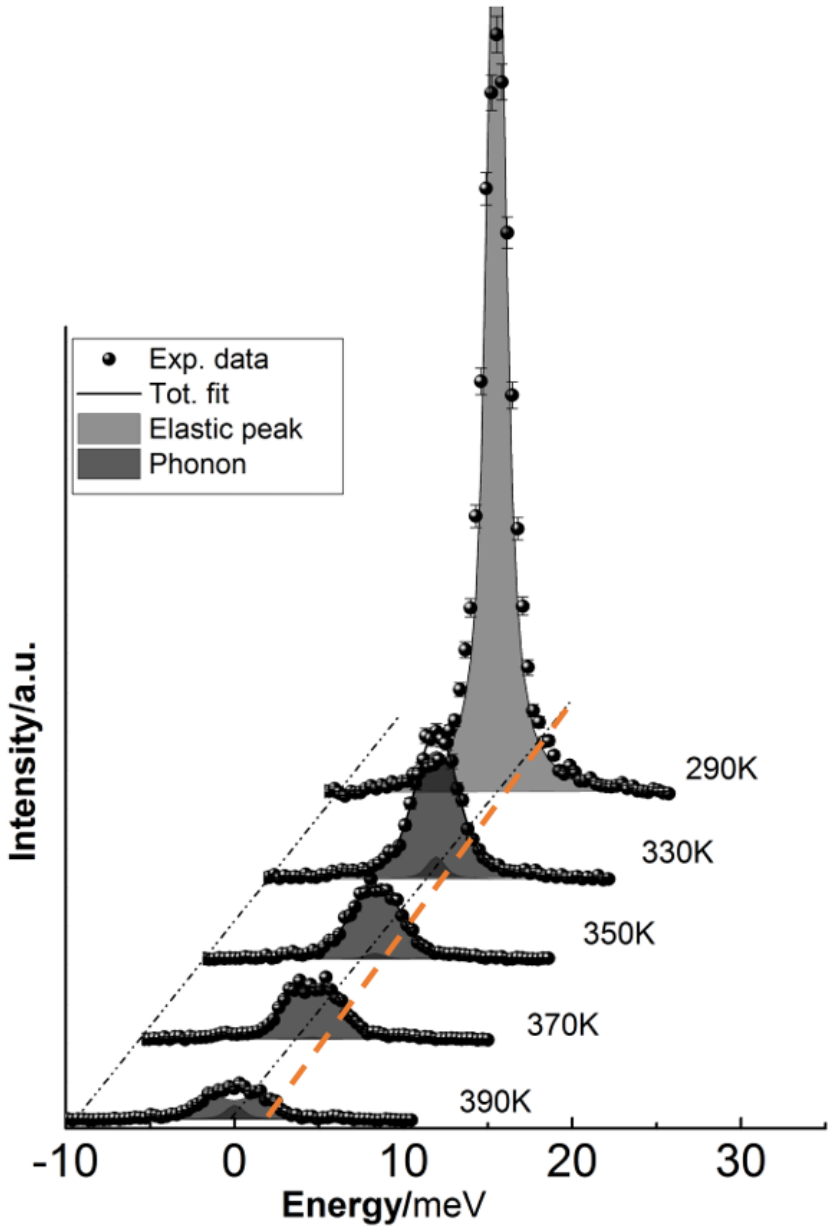

Figure 4.18.: The inelastic scans at the satellite position Q(0 0.75 $\overline{6}$) as a function of temperature. The evolution by temperature of the phonon energy can be followed by eyes through the orange dotted line. A black dotted line shows the position at each scan of the zero-energy point. The area of the phonon and elastic peaks are highlighted by strong and light grey, respectively.

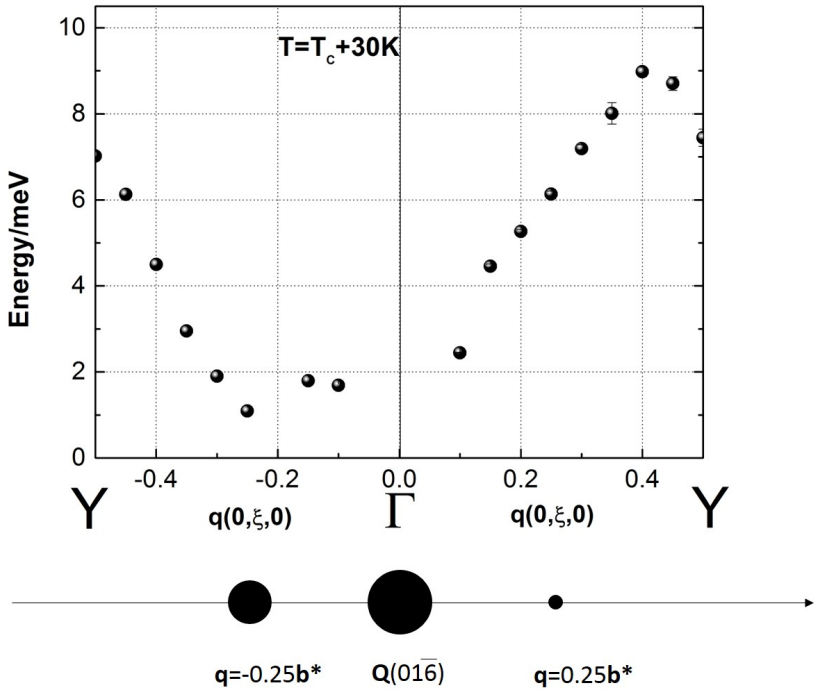

Figure 4.19.: The two phonon dispersion curves at [0ξ0] and [0−ξ0] showing the difference in the phonon response for a strong or weak elastic satellite peak at room temperature. A scheme of the related intensities of the peak is visible on the bottom. In the direction for negative ξ values, the phonon softens near the satellite with a stronger intensity. In the direction for positive ξ values, the normal acoustic-like dispersion is visible, since the intensity of the satellite is weaker.

This parameter was fixed since there are no points very near to the transition temperature. The fit result finds the value of E_0 as (2.8±0.2) meV and γ is near the prediction, 0.49±0.06.

The phonon dispersion in the two directions along <0x0>, from the same Bragg peak, should be analysed and confronted. In Fig. 4.19 the two dispersions at room temperature are shown. The negative direction shows the dispersion which is coupled at ξ=0.25, due to the CDW phase. In the positive direction, the same dispersion at low energies is present, however, the major intensity in this direction comes from a higher energy phonon. The dispersions are not just different on the satellite position, but the coupling with the CDW phase enhances the phonon which is with a very low signal in the other direction.

The behaviour of m=2 is clearly a good example of Peierls transition, where the W-octahedra zig-zag chains form a quasi-1D-electronic structure which gives rise to an electronic instability. The phonon dispersion shows a classic Kohn anomaly with a phonon at $\mathbf{q}_{CDW}$ which tends to a 0-energy when the temperature approaches T_C.

Other dispersion were taken during the experiments. For example, the longitudinal phonon dispersion was measured and the result can be consulted in the Appendix A.

4.4.2. Molecular dynamics calculation

The calculations are important tools in order to distinguish and study the phonon behaviour. This part of the project was done with the help of Dr Marek Mihalkovic, based in Bratislava (Slovakia) at the Slovak Academy of Sciences. The first idea was to run some calculations which could resolve the lattice dynamics of the smallest member, m=2. Since it has a little cell compared to the other members (with 28 atoms), it is the best candidate. Unfortunately, the calculations were not sufficient to reproduce the lattice dynamics. On the other hand, it gives a clear view of the structural distortion connected to the CDW instability.

First attempts with DFT code, searching for new solutions

The package used to run the simulations is the Vienna Ab initio simulation package (VASP) [148–151]. In order to run some *ab initio* phonon calculations, the first step is to optimise the structures, the "high-symmetry" and the "superstructure", with the CDW phase, ones. For the latter, the structure is 4 times bigger in **b** direction, in order to describe the satellite. The first attempt was done with the density functional theory (DFT) framework code. In this case, numerical convergence was not reached and the results were not accurate enough to perform subsequent calculations. Different approaches were used in order to improve the convergence of the numerical method, but without success. For instance, a magnetic or non-magnetic phase and the smearing factor were added, and also different potentials were tried.

The fact that the numerical method did not converge can be explained by the high-symmetry phase of the system, which cannot be properly relaxed within the DFT framework, since the calculations are done at zero temperature. Furthermore, the *ab initio* approach cannot describe the occupation probability of the electronic states for temperatures different from zero. However, this was not the only issue. The system seems to not have a single basic cell. The high-symmetry structure

seems to have averaged positions for the atoms, with a spatial correlation that exceed the cell. It is remarkable to notice that the best setting reached by DFT is to quadruplicate the cell in **b**, following the modulation of the CDW phase. As a result of this change, the energy was lower than observed (~ 3 meV/atom). As a consequence, the simulation of the modulated structure did not converge either. In the latter case, the only analysis possible was to confront the experimental structure with the optimized structure by DFT. The experimental structure has a modulation that distorts the octahedra, with a displacement of the tungsten atoms. This differs from the DFT, where the software normally just rigidly rotates the octahedra, with a final less significant distortion.

In order to continue the analysis, the following steps could be taken, based on the assertions just presented:

- Running again the DFT code and retrying the so-called smearing factor, that is usually used as a technical tool to achieve convergence for metallic systems in DFT calculations and used in different CDW systems [152–155]. The smearing factor reaches a physical meaning, considering the Fermi-Dirac distribution: it could be seen as the electronic temperature of the system;
- Running a molecular dynamics (MD) simulation where the calculation is done choosing the temperature of the system and it can be useful in order to understand the movement of the atoms. If the supposition of an averaged structure is true, this method could show the distortion in the structure.

The latter possibility was our choice. It is the best option for an averaged structure since molecular dynamics can leave atomic positions to split. The only problem is that it requires a long processing time.

Successful attempt with MD

The MD simulations took several (10 – 15) days. We start from the VASP-relaxed superstructure already obtained by DFT and the simulation was performed at different temperatures settings: 200K, 250K, 300K and 350 K. A study of the orientations and rotations of the octahedra and tetrahedra in the system shows the distortion for this member, in particular, the rigid body movements.

The optimised set-up was reached using a **k**-point grid of 5x1x3. The PBE+GGA (Perdew-Burke-Ernzerhof and generalized gradient approximation) functional was used to run the simulation, where a spin-polarization was also considered. The number of steps for single simulation were 1500 with a timestep of 5 fs. The simulations were continued more than one time, depending on the temperature.

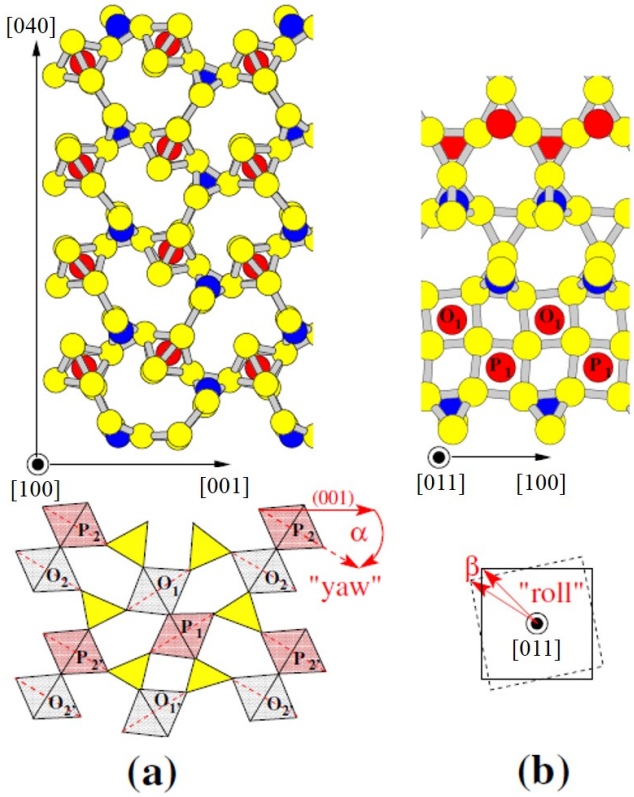

Figure 4.20.: The description of the yaw and roll axes, which are necessary to describe the rigid-body rotations in the octahedra, are on the bottom. In figure (a) the yaw axis on the [100] direction, with a big α-angle of libration. The octahedra have different colours for the different layers (grey the lower layer and pink the upper layer). In figure (b) the roll axis on [110] direction with a little angle, β. On the top, the orientations of the structure for the two axes. The yellow corresponds to oxygen atoms, blue to the phosphorus and in red are the tungsten atoms.

The most interesting result comes from the librations of the different axes in the zig-zag chains of tungsten octahedra. The libration is the real position of the axes of rotation by an inclination angle from the "normal" axes. In order to describe the octahedra librations, three rotational axes are used: yaw, roll and pitch. Those angles normally define the axes in the aircraft[3]. The yaw axis runs parallel to [100] direction, whereas the pitch and roll axes are in the YZ plane. The pitch axis is parallel to [110] axis and the roll axis is perpendicular to it. The yaw axis is describing the superstructure modulation and its libration last 3-4 ps with a magnitude of ~ 12 °. It corresponds to the slowest mode. In fact, the roll axis is a few times faster with a short-range correlation and the β angle is small with respect to the huge amplitude of the yaw axis. Finally, the libration of the pitch axis has a frequency very high, probably due to thermal noise. For the octahedra, the yaw and roll are shown, respectively, in Fig. 4.57 a and b, where the orientations of the cell along those axes are also drawn for clarification.

The yaw axis shows a space-time dependence on the octahedra position that is clearly referred to the supercell modulation. In fact, the octahedron rotation around the [100] axis has a 12 °of magnitude with a change of phase by $2\pi/4$ with respect to the neighbour W-octahedron in the [010] direction. This result explains perfectly the 4-fold supercell that is observed experimentally with the CDW at $\mathbf{q}=1/4\mathbf{b}^*$. Furthermore, the MD simulations show that the principal degree of freedom is based on the rigid-body rotations of octahedra. The rotations in time are shown in Fig. 4.21 for the simulation at room temperature, where at the top the structure is projected along the [100] axis and each octahedron has assigned a number. Lower (upper) layer octahedra are in red (blue). The two schemes at the top show the correlation between yaw angles of octahedra related by (020) translation, the 107 and 105 octahedra. The fluctuation of the yaw angle is about $\pm$ 12 degrees on the average angle, which is about 62 degrees in the [001] direction. The scheme on the left shows a perfect anti-correlation model, the right figure shows that the correlation is obtained with a shifting in time of one of the two of 1.6 ps. The two schemes in the middle show a similar correlation for octahedra which are related by a (010) translation. In the same way, the scheme on the right shows that the correlation is obtained with a 0.8 ps shifting, exactly half of the time of the above one. The time shift shows that there is an angular time dependency. It demonstrates that the yaw axis vibrations break the (010) translation period: for the (010) translation with a phase shift of $2\pi/4$ and for the (020) translation with a phase shift of $2\pi/2$. The fact that the time dependency can be correlated by shifting quarter or half period means that the octahedra librations are highly correlated and they can be described as plane waves. Since those results come from the 300 K MD simulation, the correlation between yaw-

[3] https://en.wikipedia.org/wiki/Aircraft_principal_axes

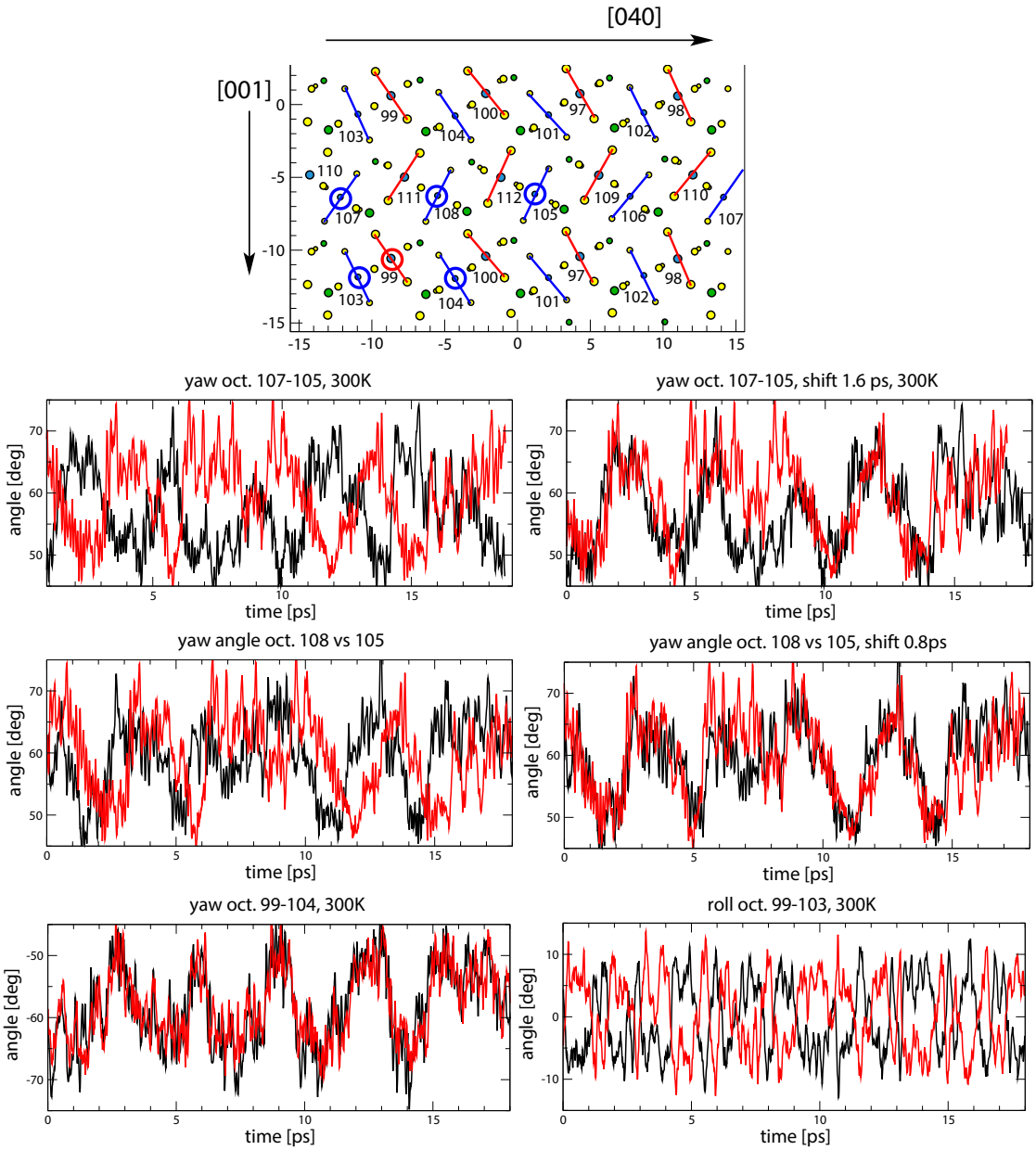

Figure 4.21.: On the top, the view of the structure projected along the [100] direction. The octahedra highlighted with blue/red line correspond to the upper/lower layer and each of them has an assigned number. The lower figures show the time dependence of the yaw angle values for two octahedra, the octahedra numbers are written on the top for each scheme. For the first two, a time shift was applied and shown on the right, the shift applied is written on the top of the figures. The scheme on the bottom and right is referred to the anti-correlation between the roll angles. The results come from the MD simulations at 300 K.

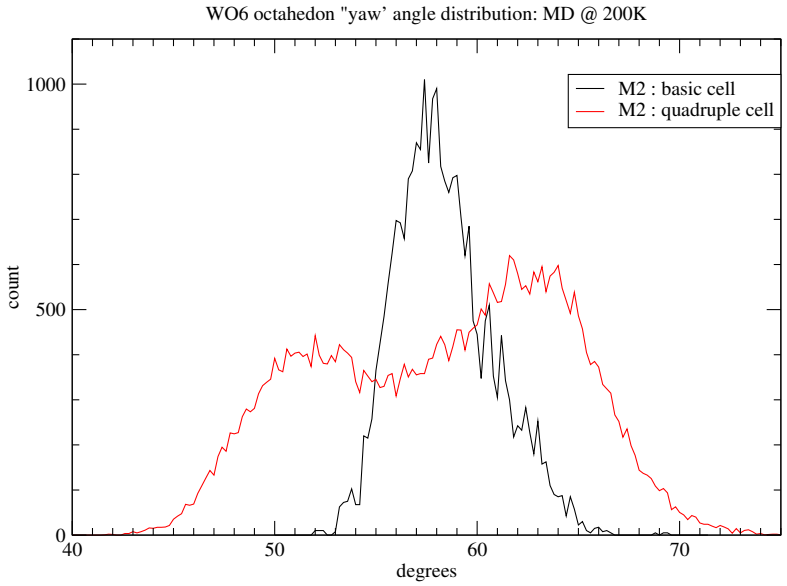

Figure 4.22.: The yaw-angle distribution. In red the one obtained for the supercell used in MD simulations and in black the one referred to the basic cell.

angle causing the modulation is not disappearing at high temperature. The phase transition should remove this correlation, which actually holds until 350 K.

It is worth to mention other strong correlations that do not affect the translation periodicity, shown at the bottom of the figure: on the right, the correlation between an octahedron in the upper layer and one in the lower layer (99 and 104); on the left, the anti-correlation of the roll angles between the nearest octahedra, again on the upper and lower layer (99 and 103).

Since the yaw angle seems to be responsible for the large libration of octahedra, an analysis of the distribution of this angle could be interesting. In fact, the MD supercell shows at 200K an average angle with a splitting into two separate peaks at 52 and 63 degrees, as shown in Fig. 4.22. Whereas, the basic cell with 28 atoms, normally used, shows a Gaussian smeared distribution around 58 degrees. The splitting in the distribution should be reflected in a splitting also of the Wyckoff sites. It is not trivial to refine the structure with this consideration, since the atoms are not vibrating around some equilibrium position. Instead, the atoms have a more complex movement. In fact, the displacive modulation is described with the librations of the axes which were described above in this section. Thus, one cannot extract a time averaged structure and the modulation wave should be subtracted.

From the MD simulation, the phonon-DOS at 200 K, 250 K and 300 K using the quadruple supercell were calculated and the results can be seen in Fig. 4.23.

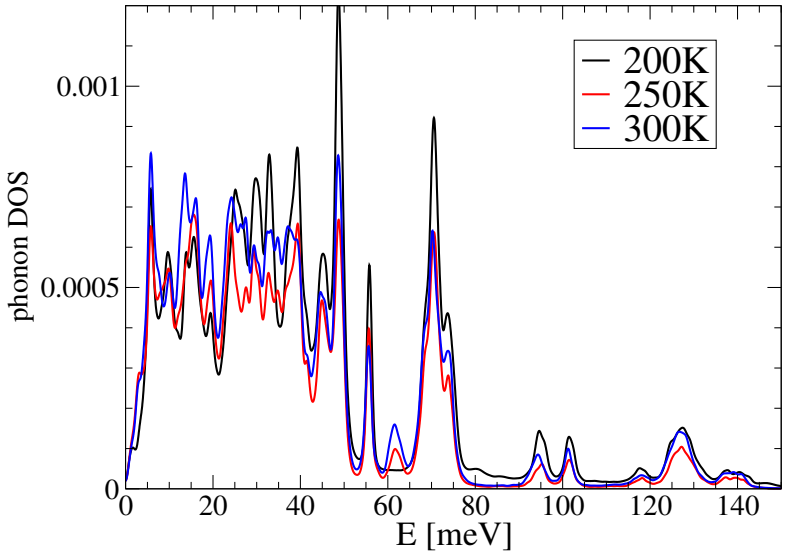

Figure 4.23.: The phonon-DOS extracted from the MD simulations at 200K (black line), 250K (red line) and 300K (blue line) of m=2. The lower temperature DOS shows some differences already in the first curve.

The program used to simulate the density of states is nMoldyn [156]. In order to perform the phonon-DOS simulation, the calculation took two weeks in the supercomputer at the Slovak Academy. From the figure, a difference between the low temperature (200 K) with respect to the other two temperatures phonon-DOS is visible. In order to simulate the specific phonon dispersion, especially the [010] direction, the single structure factor for each **q** point is necessary. However, this simulation is not enough resolved in the **k**-space. Thus, in order to run simulations on the lattice dynamics, a bigger supercell is necessary. In the future, those results should be confronted with the experimental phonon dispersions.

In conclusion, until 300 K the system has rigid body rotations and the principal displacement in the averaged structure is referred to the oxygen atoms around the W-center. They are vibrating around the tungsten atom in a highly correlated manner with rigid-body motion. This latter result is important to show that those movements are at the basis of the low energy phonon. Furthermore, in the phonon-DOS the lower energy part corresponds to the octahedron libration modes. However, in order to confirm this conclusion, further investigations with nMoldyn are necessary to analyse the rigid-body motion. In addition, an attempts with a bigger superstructure should be done in order to confirm that the 4-fold-superstructure is the ground state.

4.5. Family members with W-blocks

In this section the results of the diffuse scattering and inelastic x-ray scattering for the other members of the bronze family are presented. Since m=2 is a degenerate case, presenting a lower electronic dimensionality, the other members are grouped in this section. However, as already explained before, normally there is a separation between low-term members, until m=6, and high-term members. In this section, we will compare the m=6 and m=8 diffuse scattering patterns and lattice dynamics response.

4.5.1. Diffuse scattering

The diffuse scattering data collection allows us to see possible structural defects (as stacking faults) and potentially the precursor effects of the CDW. The evolution of the cell parameters, the change in the diffuse patterns and the condensation on the CDW spots can be followed with an experimental temperature study. In fact, there is a possibility to find some pretransitional fluctuations, more precisely, along the W-chain, where the electronic and framework instabilities could be present. In the high-symmetry phase above the T_{CDW}, stripes and lines were found for different members by diffuse scattering [117], suggesting that the CDW instability is caused by the quasi-1D character of the electronic structure. Foury *et al.* suggested that the diffuse pattern was generated by the zig-zag chains that are in the W-block along the **a***, **a*** ± **b*** directions and their relation. The directions of the chains were in connection with the "hidden" Fermi surface and its nesting, as already explained in the introduction of the chapter. This analysis was reported for the member m=6.

The earlier diffuse scattering results were obtained in a laboratory with a long time of acquisition. Thanks to the synchrotron light, which produces a revival of DS studies, and the evolved synthesis, new measurements on different members should be done in order to re-evaluate the reciprocal space distribution of scattered intensity. In order to compare the results, the member m=6 is redone. To complete and evaluate the behaviour of the family an odd and even members were added to the list. In addition, since the m=6 is a low-term member, the m= 7 and 8 were chosen as part of the high-term members.

Room temperature experimental results

The members studied (m=6,7,8) have different temperatures of transition, which increase with m. The low-term member shows the first transition at 120 K, m=7 at

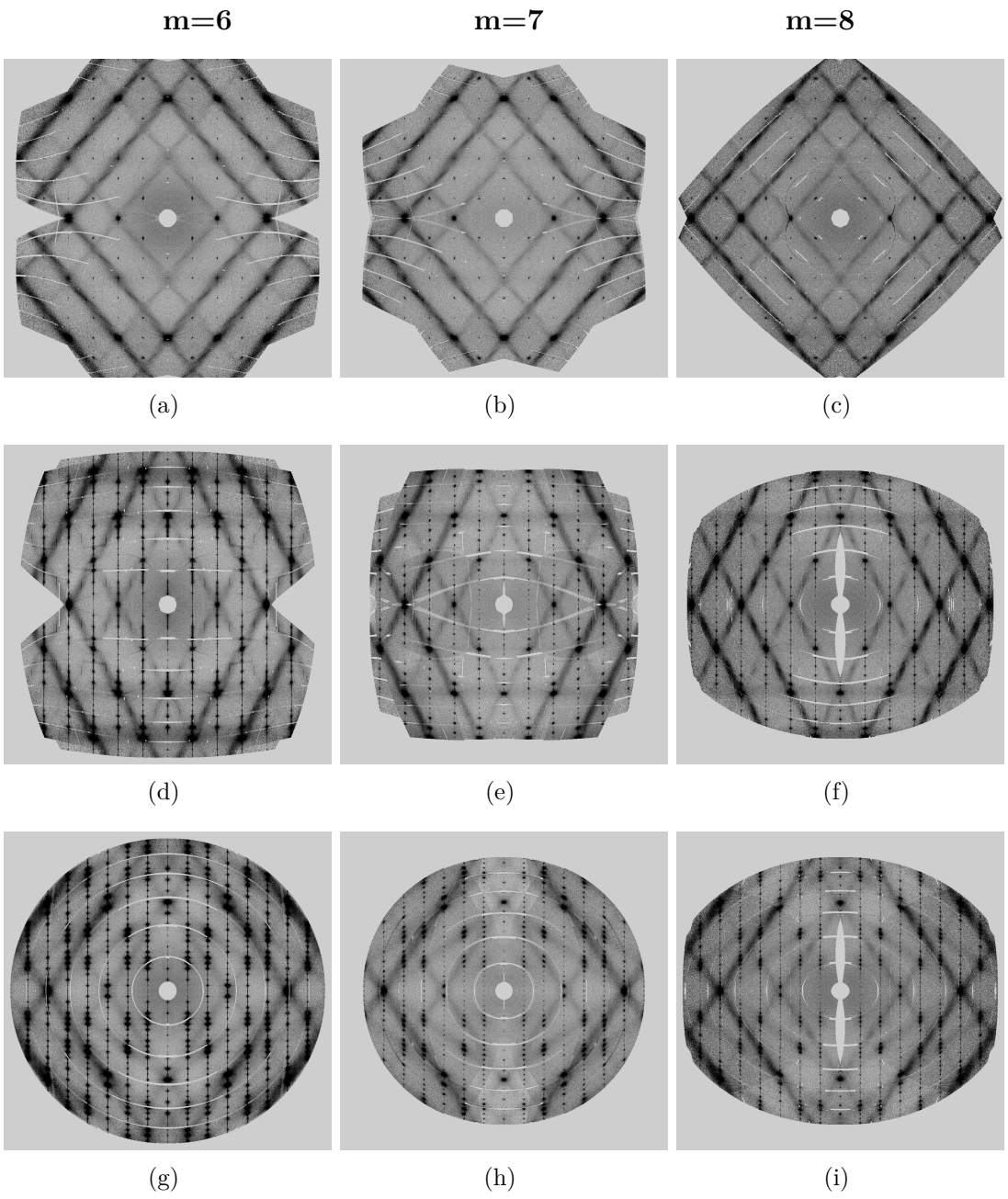

Figure 4.24.: The DS maps of the three members at room temperature: on the top line, the HK0 maps of (a) m=6, (b) m=7 and (c) m=8; on the middle line, the H0L maps of (d) m=6, (e) m=7 and (f) m=8; on the bottom line, the 0KL maps of (g) m=6, (h) m=7 and (i) m=8. Laue symmetry is applied to the RS reconstructions.

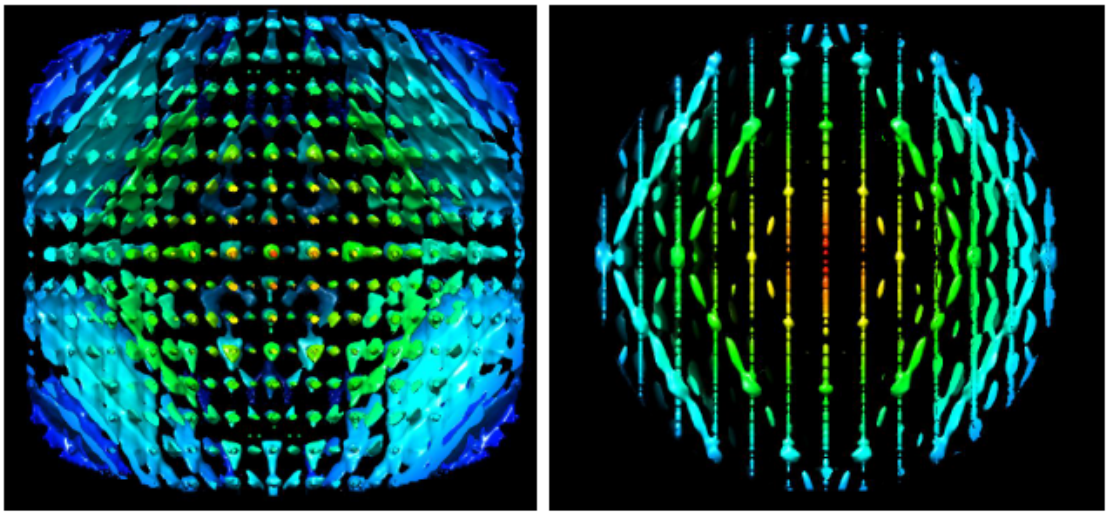

(a) (b)

Figure 4.25.: The 3D reconstruction of the reciprocal space from the diffuse scattering measured in $P_4W_{16}O_{56}$, m=8: a) layer parallel to HK0 plane and b) layer parallel to H0L plane.

188 K and the latter has the transition at a quite high temperature, 250 K. Thus, at room temperature all the three are in the high-symmetry phase. The DS maps in Fig. 4.24 shows that, for the three members, diffuse rods along **c*** are present and they correspond to planar defects - stacking faults and or/and twin boundaries. The diffuse scattering measurements are valuable tools to check the quality before any experiments in IXS. For this reason, different samples were analysed of each member and the less twinned were chosen for the IXS experiments, *vide infra*.

The diffuse scattering is very similar for the three members as shown in Fig. 4.24. The maps show diffuse planes, which have low symmetry normals with 2 or 3 non-trivial components in the main axes. A 3D reconstruction [4] of the diffuse scattering helps to understand the diffuse planes orientation, Fig. 4.25.

The origin of the diffuse planes can be understood considering the *direct* space. In fact, the direction in the structure of the family will allow us to understand which atoms, chains, etc. contribute to the instability of the system. In order to pass from *reciprocal* and *direct* space, the normal way to calculate the directions in the *real* space is to check the normal at the diffuse plane. However, a trick can be used to simplify. The method used to describe the direction (HKL) starting from the

[4] 3D reconstruction of the reciprocal space is visualised with the UCSF Chimera package. Chimera is developed by the Resource for Biocomputing, Visualization, and Informatics at the University of California, San Francisco (supported by NIGMS P41-GM103311) [157].

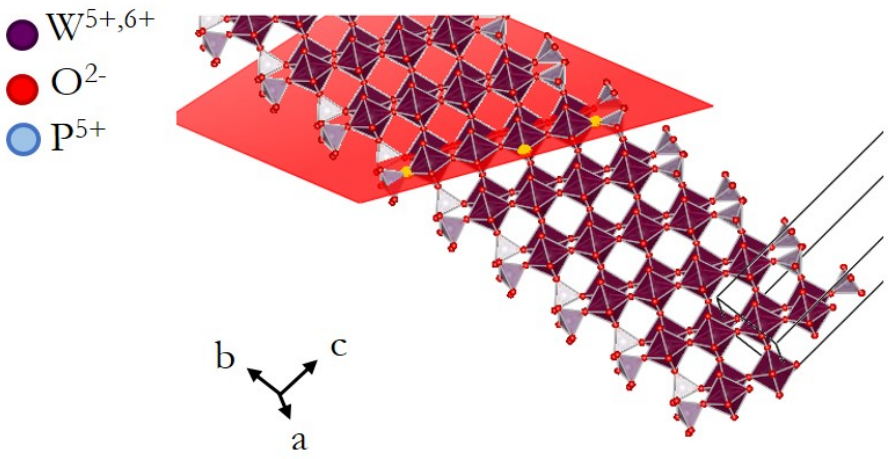

(a)

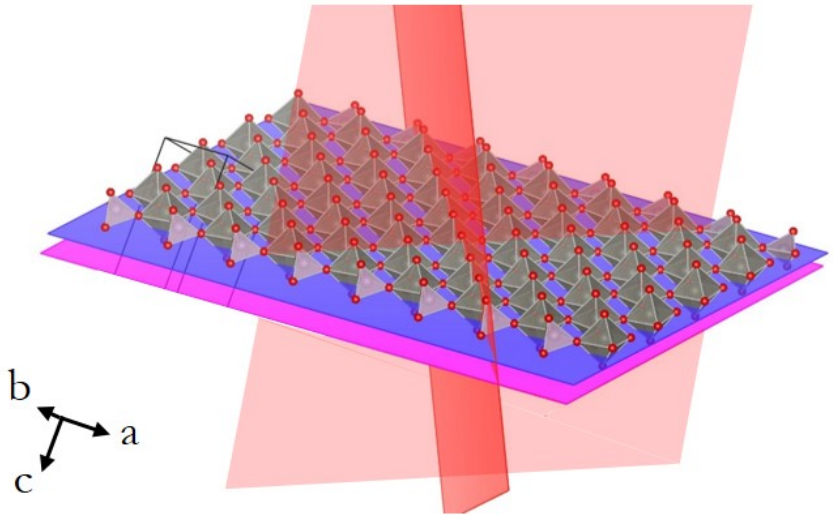

(b)

Figure 4.26.: Examples of short and long chains for the m=8 structure. In figure (a) the direction along the "short" W-O-W-O chain related to the diffuse planes in the reciprocal space, the length is $m/2$ octahedra for even member, as m=8, and $m/2\pm1$ for odd members.(b) The two "long" W-O-W-O chain directions for m=8 are highlighted by the two pink planes which intersect the octahedra plane in violet and strong pink. They have a length corresponding to m.

Identification of the diffuse planes					
m=6		**m=7**		**m=8**	
HKL	$u,\ v,\ w$	HKL	$u,\ v,\ w$	HKL	$u,\ v,\ w$
2 3 16	$\frac{1}{2}u + \frac{1}{3}v + \frac{1}{16}w$	2 3 18	$\frac{1}{2}u + \frac{1}{3}v + \frac{1}{18}w$	2 3 20	$\frac{1}{2}u + \frac{1}{3}v + \frac{1}{20}w$
∞ 6 16	$\frac{1}{6}v + \frac{1}{16}w$	∞ 6 18	$\frac{1}{6}v + \frac{1}{18}w$	∞ 6 20	$\frac{1}{6}v + \frac{1}{20}w$

Table 4.2.: Diffuse planes in m=6,7,8. In the same lines, we reported the same kind of planes, they come from the same 4-fold octahedron axis, however since the thickness of the block changes by m, the orientation in the cell change in each member.

plane in the *real* space can be used in a "reverse" mode. The intersection of the planes is found in the reciprocal space and rewritten with the *real* space vectors. The results are summarised in Tab. 4.2. In the table, a different intersection in L is found for the different members. The change is due to the different thickness of the WO_3-slab. However, it is the same orientation in Cartesian space, recalling the same chains.

There are two families of planes, which describe two kinds of W-octahedra chains. The two families of planes correspond in the *real* space to the W-octahedra 4-fold axis directions. Fig. 4.26 shows the structures projected along the two types of W-O-W-O chains. The first family is shown in figure (a). It is called "short" chain since its length is $m/2$ octahedra for the even member and $m/2\pm1$ for the odd one. In the figure (b) the two "long" chains directions are related to the second family of planes. In this case, the length of the chains is equal to m.

In general, the instability of what is called the framework is normally related to the perovskite blocks. For the empty perovskites and for some filled perovskites, the octahedral framework is unstable along the B-O-B-O chains in the corresponding channels along (pseudo) 4-fold axis. Fig. 4.27 is made in order to simplify the passage between the *direct* and *reciprocal* space, where the simple cubic structure of WO_6 without the adding of the phosphate tetrahedra shows the directions of the diffuse planes corresponding to the instabilities of the W-O-W-O chains. The diffuse scattering intensity distribution of the "basic" structure should be taken in account. Earlier experiments in ID28 were made by Stekiel *et al.* on the tungsten trioxide, WO_3, which has the same empty-perovskite structure made

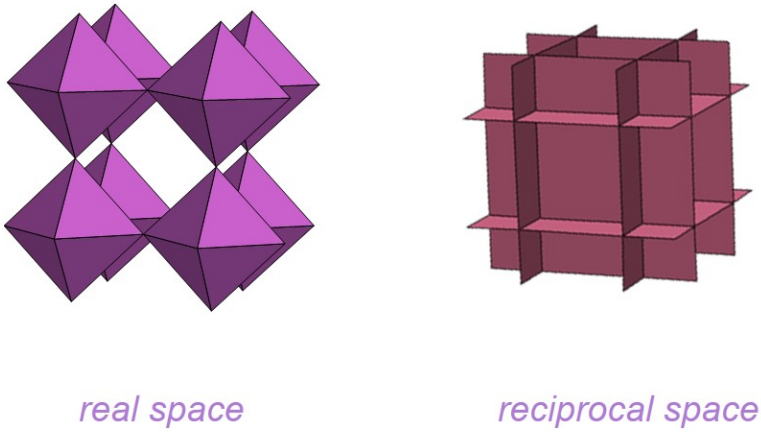

Figure 4.27.: The basic representation of the perovskite structure and the sketch of diffuse planes related to the instability of the B-O-B-O chains.

by W-octahedra[5]. We compare the results with the WO_3 phase at room temperature in the monoclinic phase, P-1, Fig. 4.28. The resemblance confirms our assumption. The plane in this case are perpendicular to the W-O-W-O chains. The monophosphate tungsten bronzes have a more complicated system and directions. The planes are not in a simple symmetry because the basic cell presents two blocks that have different orientations due to the bonding with the monolayer of phosphates.

The scheme of the diffuse planes repartition in reciprocal space of the $MPTB_p$ family is given in Fig. 4.29. In the reconstruction in 3D of the diffuse planes, the different colours correspond to the two types of W-block orientations, which give rise to the final outcome. In the same figure, the intersections with the high-symmetry planes, *i.e.* HK0, H0L and 0KL, are presented. In this latter, the two different intersections are given from diffuse planes derived from the "short" and "long" chains. The drawn is made isolating the experimental diffuse planes of m=6 and represents our analysis.

Now that the repartitions of the families is more clear, one can look more deeply to the diffuse maps of this family, Fig. 4.24. Two interesting features regarding the intensity are visible. In fact, the intensity of the planes coming from the "long" chains do not grow linearly with **Q**. The first plane is really weak with respect to the second, which is almost of the same intensity as the third. This result comes from

[5]The results were taken by M. Stekiel and collaborators during an experiment at ID28. They kindly accepted to show their results, Fig. 4.28 and Fig. 4.44

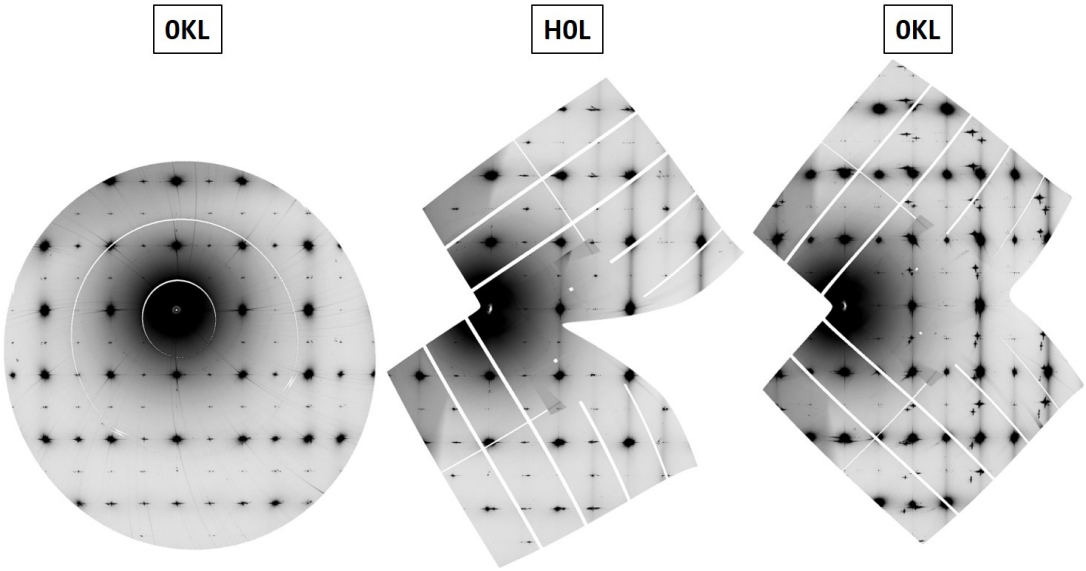

Figure 4.28.: Reconstruction of DS high-symmetry planes for WO_3. The same diffuse planes are visible.

a complicated correlation between the W-octahedra chain. If the correlation was just intra-chain, the intensity would be proportional to $\mathbf{Q}$. In this particular case, the intensity follows a more complicated pattern since an inter-chain correlation is probably also in place. There are other systems presenting similar diffuse behaviour as $KNbO_3$, also studied by DS and IXS in this beamline [26, 27, 158]. In addition to the discussion, also the intensities of the two families are different. One can understand the origin of the latter due to the CDW transition and the structural distortions, *vide infra*.

The final outcome of this part of the study shows the resemblance and the affinity of all the members at the high-symmetry phase. At high temperature, all the members that possess a W-octahedra slab have a framework instability. It is due to the empty-perovskite structure and it is revealed to the diffuse planes divided in two families derived from the different orientations of the W-block and the division on one short chain and two long chains. The differences in the members with respect to the CDW phases, strong/weak electron-phonon coupling, etc. seem not to be present at this point.

CDW phase experimental results

The temperature study of two members (m=6 and 8) was done in order to follow the evolution of the diffuse scattering intensity distribution. By decreasing temper-

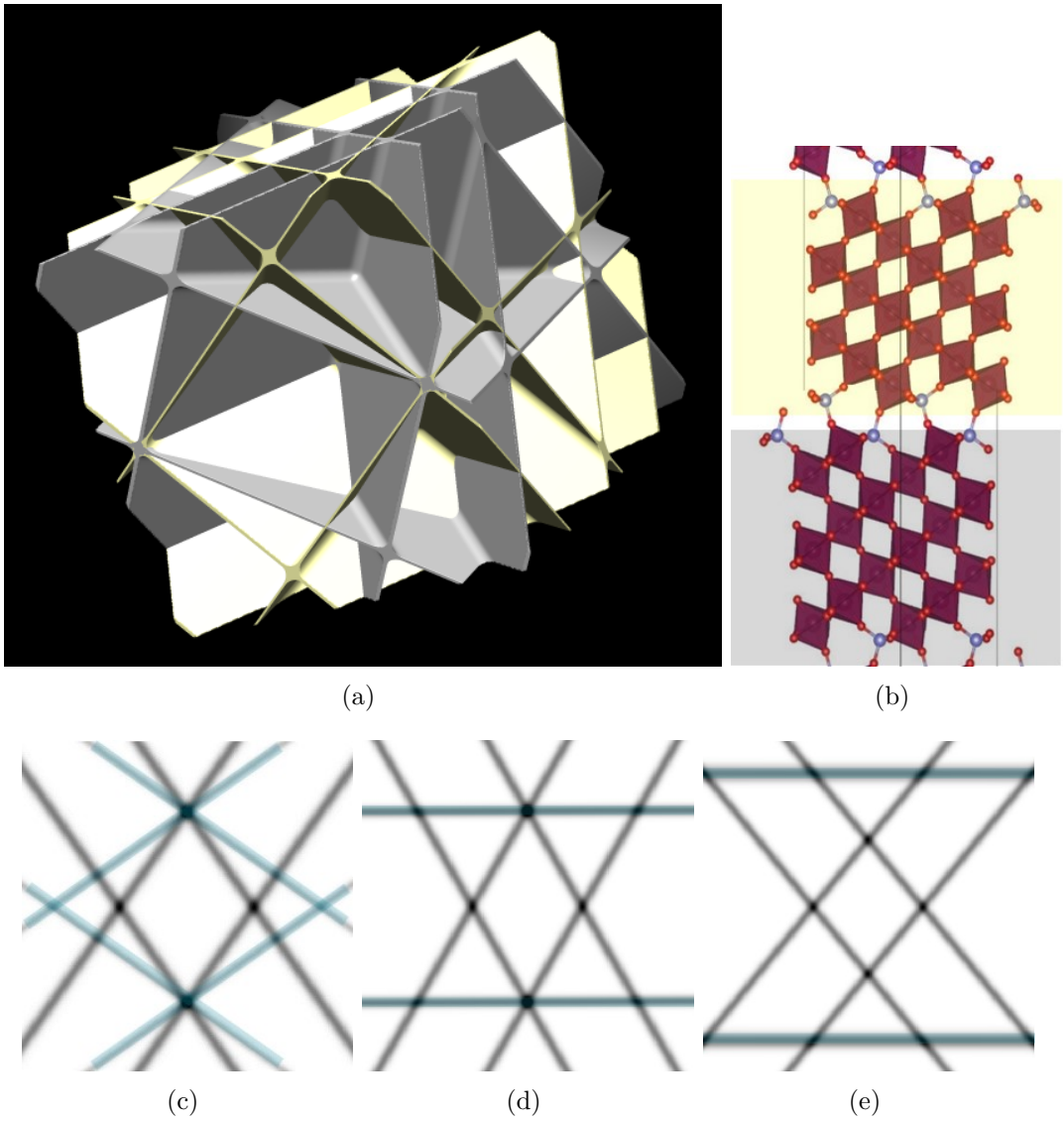

Figure 4.29.: Scheme of (a) 3D repartition of the diffuse linked to the perovskite slabs, the grey and yellow shows the planes coming from the two different orientation of the blocks in the structure, shown on the right in figure (b). The scheme of the intersections of the diffuse planes on (c) 0KL (d) H0L and (e) HK0 are also shown, to be compared to the experimental data of Fig. 4.24. In those scheme the blue and black correspond to the planes related to the "short" and "long" chains, respectively. Only first observable planes are shown.

ature, the condensation of diffuse intensity into the CDW-modulation spots with incommensurate propagation vector should be observed. The transition for the low-term member, m=6, is around 120 K. The results of the DS study are shown in Fig. 4.30. The diffuse planes evolve going into a finer structure, more evident in the HK0 plane. The formation of satellite Bragg peak expected at T_{CDW1}=120 K is not present, neither at 80 K, as it is evident in the H0L and HK0 planes at the lowest reached temperature. A cryostream was used for this experiment, which has the low temperature limit at $\sim$ 80 K.

The HK1 planes show clearly the directions of the fine structure. To make a correlation between the diffuse scattering intensity distribution and the CDW satellite, the nesting of the Fermi surface can be analysed. For this family, we should consider the superimposed Fermi surfaces, made by three different layers. When the three are superimposed, the result is shown in Fig. 4.31. In order to make a comparison, the Fermi surface has been stretched by a factor two, which would give some feeling on the distribution of diametral Kohn anomalies. In the PhD thesis of Foury [117], the crossing between the different sheets can eb seen as the maximum probability for the nesting vectors. It is explained that the maximum nesting is reached when the nesting vector is connecting two different sheets. In this case, the gain in energy is two times bigger, considering that the cost in elastic energy lost is just referred to a single modulation.

For this member, this theory seems to correspond perfectly with the spot of maximum intensities, as it was confirmed also by Foury [117]. In fact, it is possible to describe the spots as the three different vectors related to the CDW phases of m=6. The first transition at 120 K with a $\mathbf{q}_1$=0.38$\mathbf{a^*}$, the second transition at 62 K with the vector with two components $\mathbf{q}_2$=0.31$\mathbf{a^*}$+0.29$\mathbf{b^*}$. The last transition is at very low temperature (30 K) with the vector $\mathbf{q}_3$=0.29$\mathbf{a^*}$+0.11$\mathbf{b^*}$. The latter with a strong diffuse scattering intensity already at 80 K. The three modulation vectors are drawn in the HK0 plane of Fig. 4.30.

In order to understand the evolution of the diffuse lines along $\mathbf{a^*}\pm\mathbf{b^*}$, reconstructed planes on different of them were done, Fig. 4.32. In fact, the planes are done considering the $[1\bar{1}0]$ and [001] axes and with an offset equal to the distance where the diffuse lines are visible. Those maps permit to visualise the condensation. At room temperature, there are strong clouds which start to condense at lower temperature. However, the condensation is still not reached at $\sim$ 80 K and diffuse stripes are visible with a length of $\sim 2\mathbf{c^*}$. The reason can be due to the heating of the sample by the X-ray beam, with a real temperature on the sample different from 80 K. Another possibility is the quality of the sample. Some samples, for different reasons, as quality/synthesis/etc. do not reach the CDW phases although if they present a pre-condensation of the diffuse intensity. In earlier study, the same kind of behaviour of the diffuse intensity was found for m=8

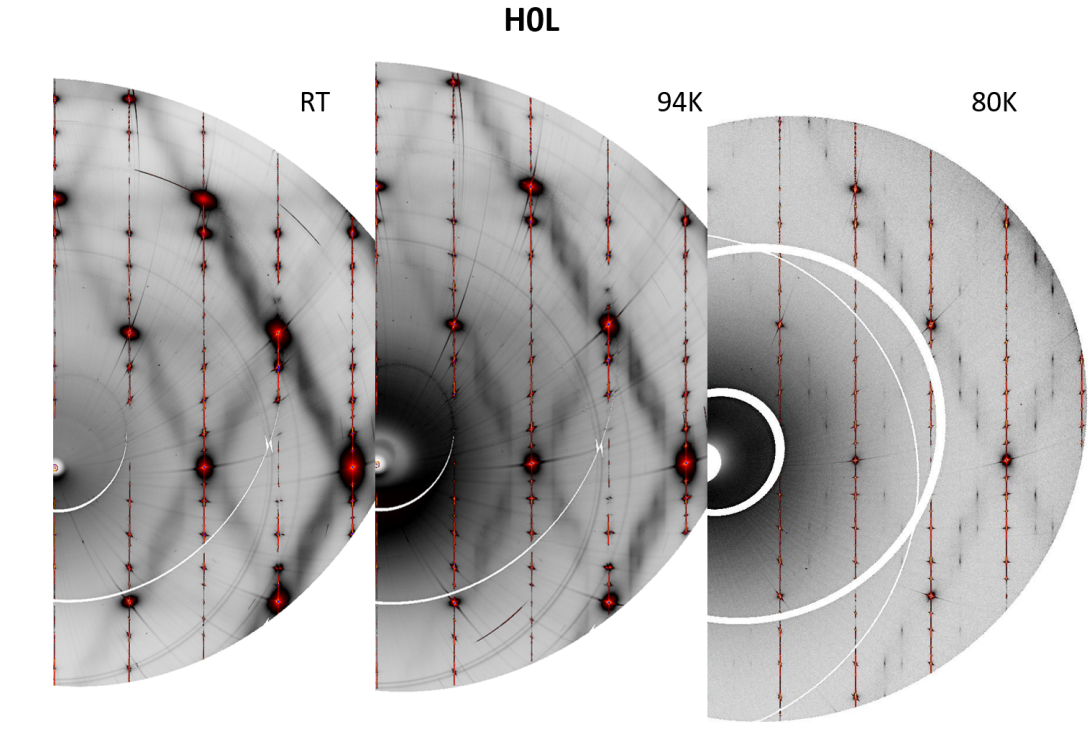

(a)

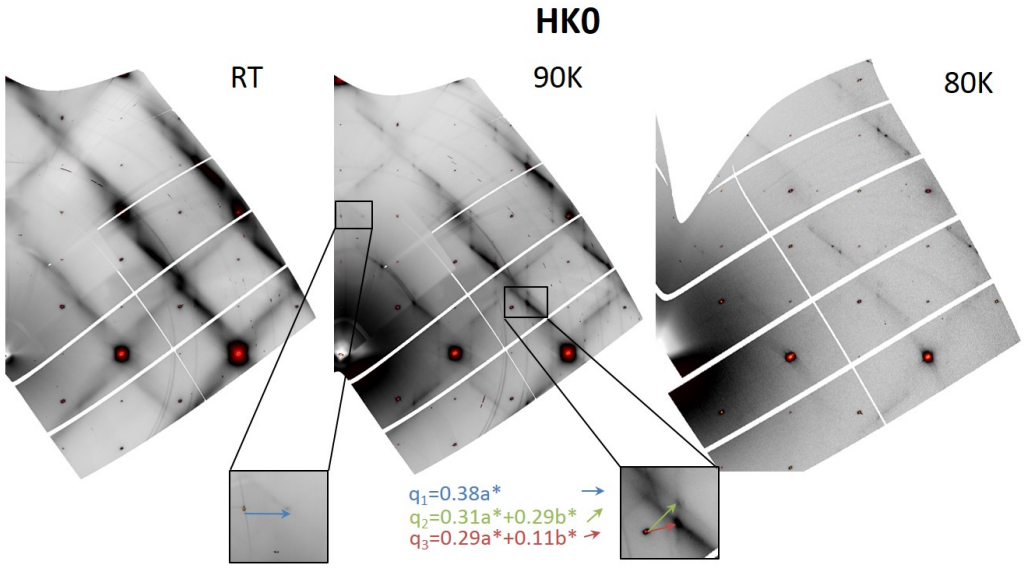

(b)

Figure 4.30.: The H0L and HK0 diffuse maps at different temperatures for m=6. The diffuse planes evolve in a finer structure that starts to condensate at low temperature. The three incommensurate vectors related to the different CDW phases are drawn in different colors. Here for 80 K the setting parameters were different with respect to the others; *i.e.* slits aperture and a less numbers of lenses, which means a less focused beam.

by Ottolenghi *et al.*. They claimed this member had just short-range correlations and no CDW phase was reached [120, 121].

In the case of m=8, the diffuse scattering shows that the diffuse planes at above T_{CDW1} condense in satellite reflections below the first transition, as can be seen in Fig. 4.33a. It is worth to mention that the measurement in temperature was made starting from the 100 K where the sample was already on the CDW phase [6]. This member has a very strong hysteresis in the T transition, already noticed in the resistivity measurement seen in Fig. 4.11b. This can be the cause of the visible difference from 280 K and the RT measurements in Fig. 4.24f and Fig. 4.33a.

The H0L map at 240 K shows the complete condensation of the satellite of the 1st transition, Fig. 4.33b. The most intense satellites are related to the diffuse planes, which seem still present in the CDW phase. In order to describe the CDW phase, the cell parameters found by CrysAlis are shown in the figure. Diffraction studies show that the phase is slightly monoclinic with β=(90.221±0.013)° [115]. The CDW vector of the first phase is $\mathbf{q}_{11}$=4/9**a***-4/9**c***. This member, a high-term member, has a commensurate vector, while the m=6, a low-term member, has incommensurate vectors. In theory, those differences could result in a different response in the lattice dynamics.

In earlier studies, as already explained before, the m=8 was considered not having a CDW phase since only a short-range order was achieved [120, 121]. The group in Caen synthesised samples with very different physical properties. The m=8 passes from a normal metal to a bad metal with two transitions of the first order, Fig. 4.11b. They found the transition with a long-range order and, in the same way, the result is confirmed by our study.

At lower temperature, a monoclinic distortion starts to be visible before reaching the second transition. In fact, the two vectors of the two phases are already present before the transition. An extensive structural analysis was done by diffraction and presented in the PhD thesis work of Duverger-Nedellec [115].

The differences noticed between the low-term and the high-term member are that a finer structure is a precursor of the condensation around the modulation vectors for m=6. Whereas, in m=8, the diffuse planes condense directly in the satellite spots without going through finely modulated DS. A structural analysis and the study of the lattice dynamics will help to understand those differences.

[6] The DS maps at every measured temperature are reported in Appendix A

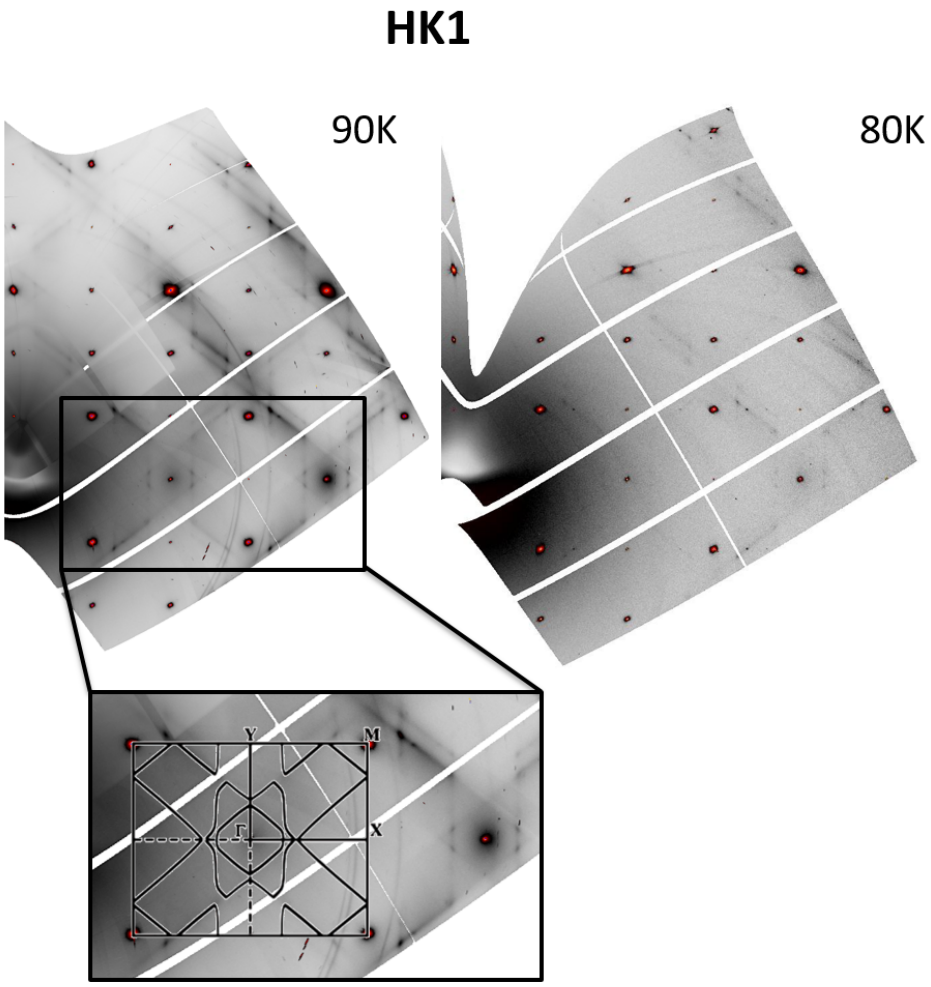

Figure 4.31.: The HK1 planes at 90 K and 80 K of m=6. In the insert, the Fermi surface calculated by Whangbo and Canadell [110, 117] has been stretched by a factor two and superimposed to the X-ray pattern.

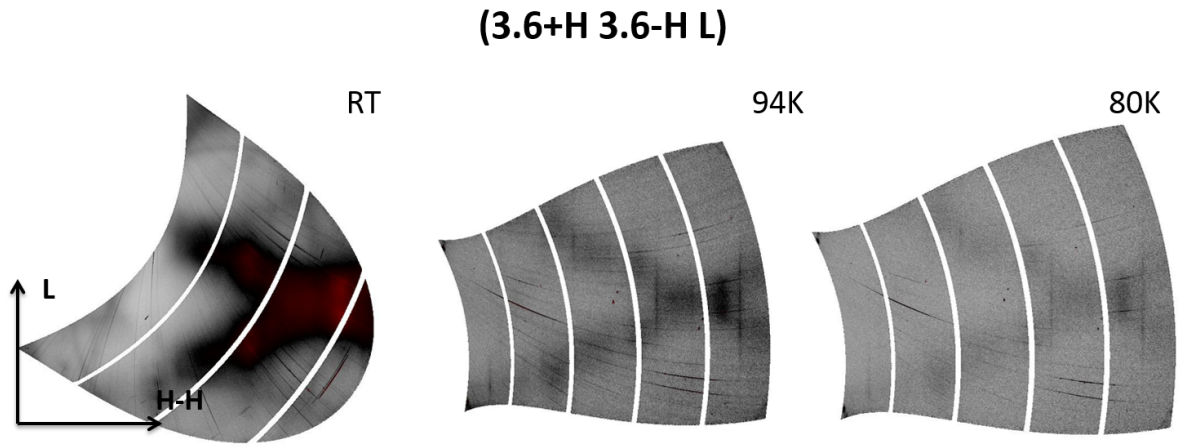

(a)

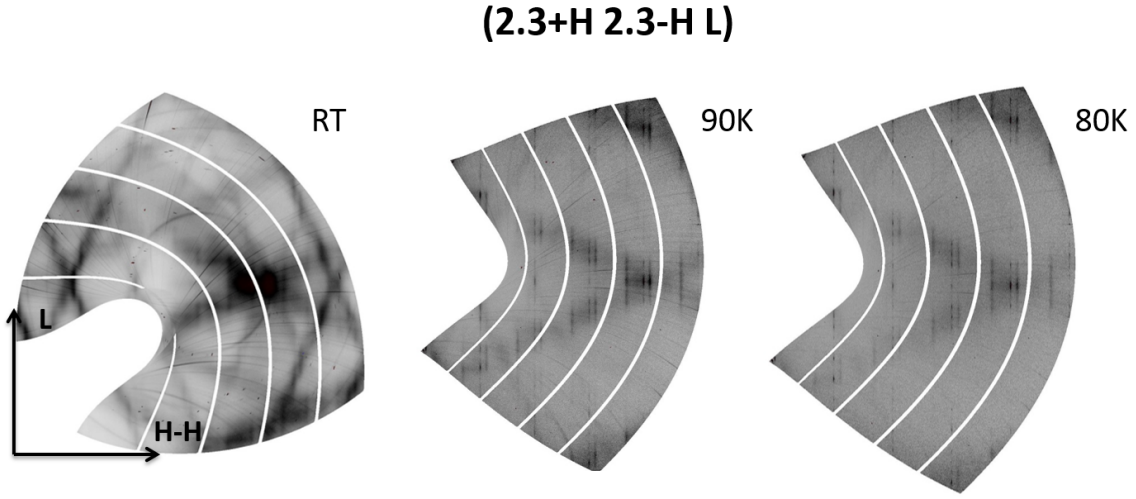

(b)

Figure 4.32.: Temperature dependence of the DS intensity for the specified planes on the finer structure of m=6. At the lowest temperature the condensation is not visible, a stripe of lenght $2c^*$ is still visible

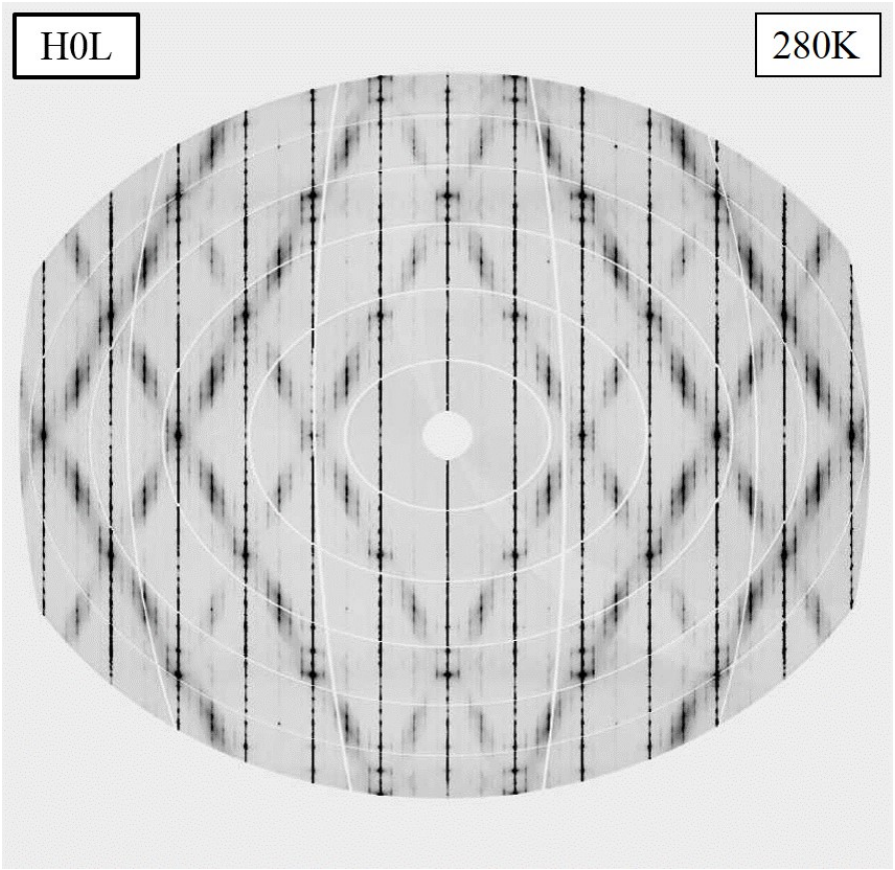

(a)

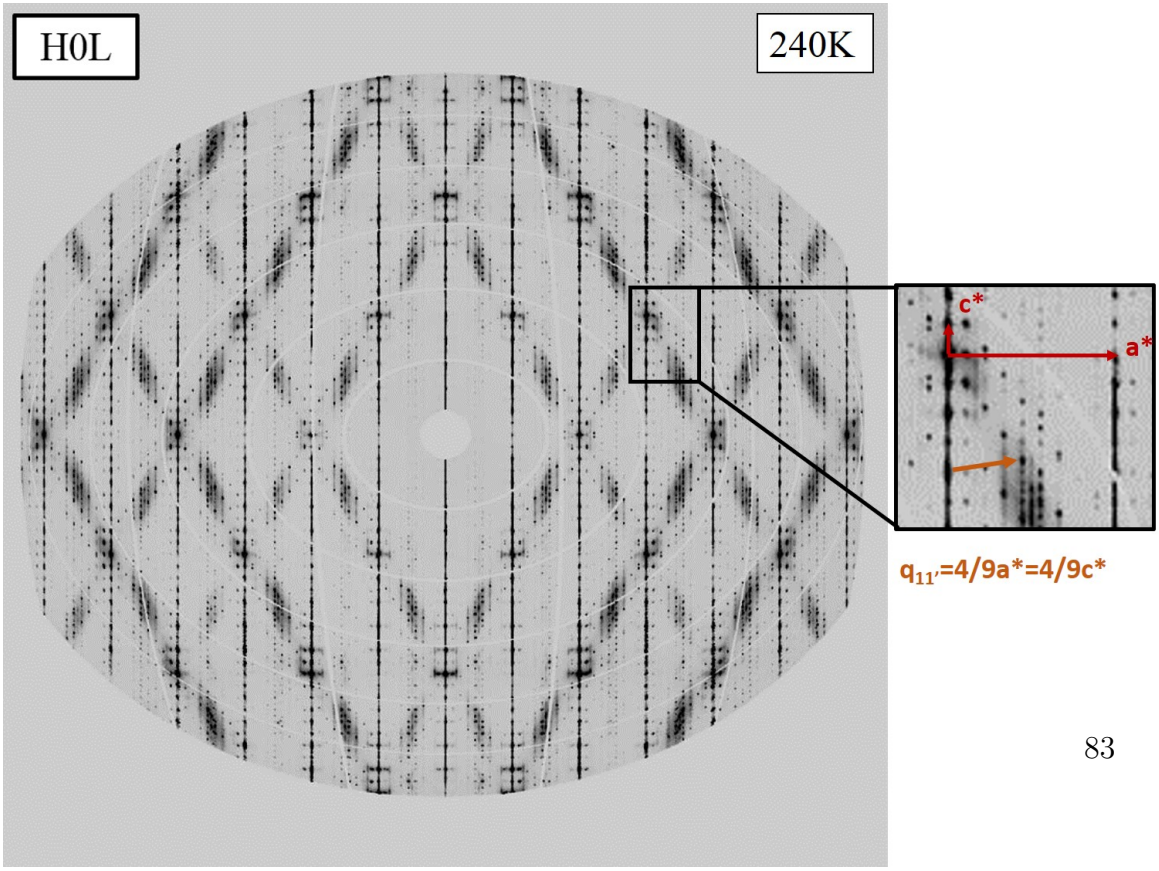

(b)

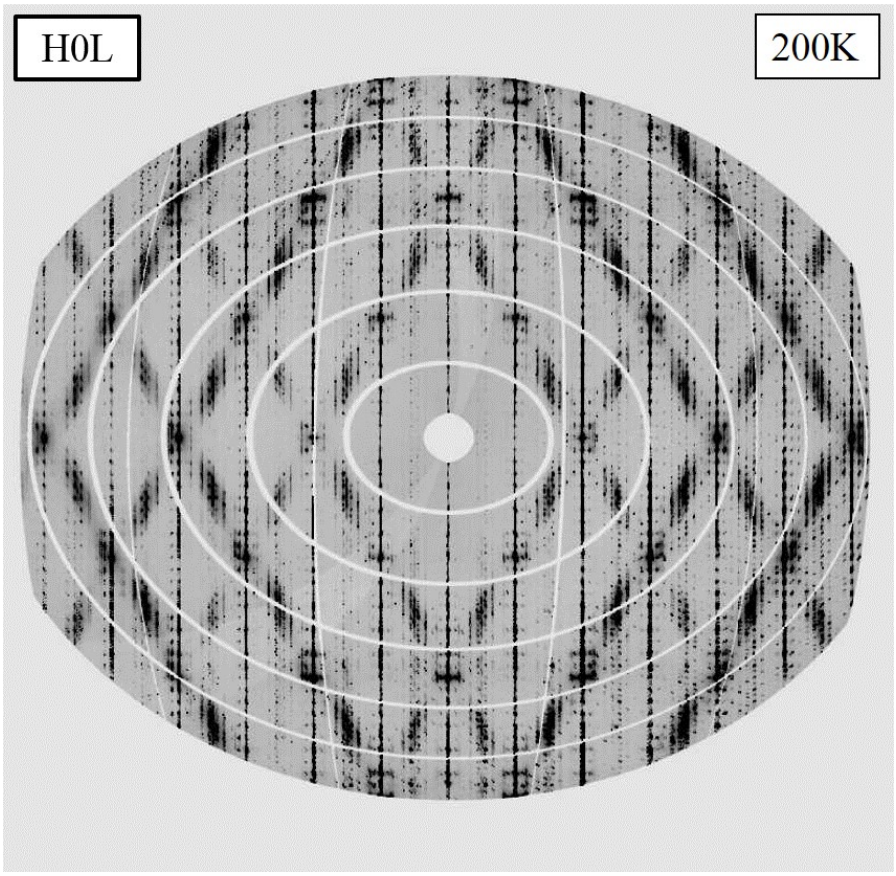

(c)

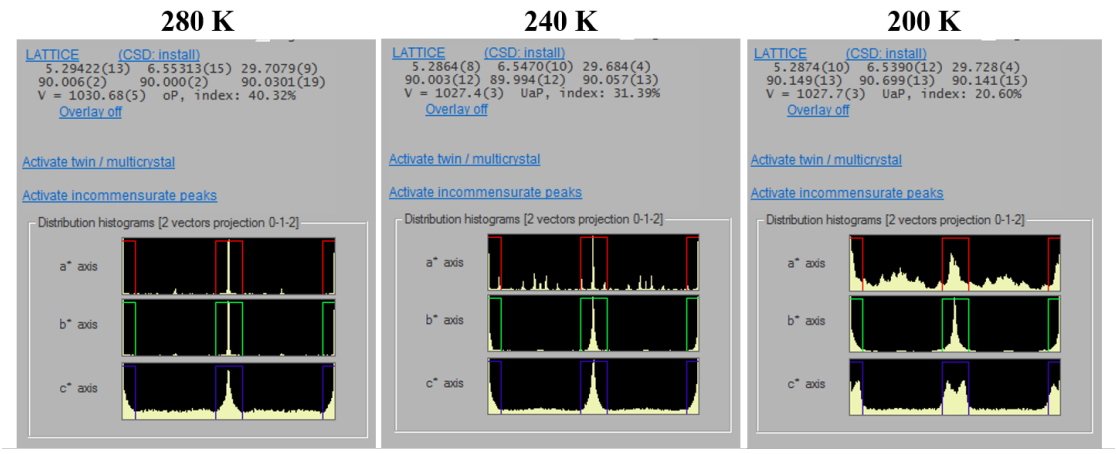

(d)

Figure 4.33.: Temperature dependence of intensity distribution in H0L plane for m=8 at (a) 280 K, (b) 240 K and (c) 200 K. The cell parameters of parent cell found with CrysAlis are included in figure (d) together with the histograms of RS vectors.

4.5.2. Inelastic x-ray scattering of *m*=6 and *m*=8.

As already explained in Chapter 3, this second technique is notably time consuming. Thus, a few representative cases were chosen. The m=2 scenario has a quasi-1D tungsten chain, already presented in the section above, and the members with a W-block can be divided into low-term and high-term members. Some differences can be found in the diffuse patterns already presented in Sec. 4.5.1. However, the inelastic scattering is expected to show a definitively different result in the lattice dynamics response. For the low-term members, a classical Peierls transition should give a phonon freezing at the transition temperature with a constant decrease of the phonon energy at the q_{CDW}. The high-term members should follow the bipolaronic theory of Aubry *et al.* [59], where a larger part of the reciprocal space present a phonon softening and no freezing is expected at the transition, as found for $TbTe_3$ and $ErTe_3$ [56, 159] and theoretical explained by Quémerais [160]. The difference is expected since the low-term members present CDW phases which are normally linked with a weak electron-phonon coupling, as the weak intensities of the satellite peaks and the incommensurate $\mathbf{q}_{CDW}$. Whereas, the high-term member shows the strong electron-coupling scenario, where the intensities of the satellite peaks are almost comparable to the principal Bragg peaks and the $\mathbf{q}_{CDW}$ is commensurate. The m=6 is the low-term member, whereas the m=8 is representative of the high-term member.

Low-term member: m=6

The inelastic measurements were made with a high-quality platelet sample of 120x60 μm and the 3 meV resolution set-up was chosen.

As already discussed in the previous section, the DS measurements show the diffuse patterns decreasing and almost condensing around the satellite. However, the satellites never completely condensate and diffuse stripes along **c*** and in the HK0 plane still appear at very low temperature, below the expected transition. The inelastic scans should be done in the region around the satellite in order to understand the phonon contribution and behaviour. The satellite was chosen observing the refined structure proposed by Dr. Olivier Pérez. The (2.62 2 0) satellite is the most intense in the measurable part of the reciprocal space.

Since the IXS spectrometer can be used also as a high-resolution diffraction tool with its 7-meter analyser arm, elastic scans were performed in function of temperature on the CDW satellite (2.62 2 0), similar to the analysis done for m=2. The correlation lengths, ξ, and the behaviour of the transition can be understood through those scans. In the literature, the transition is assigned as of the second

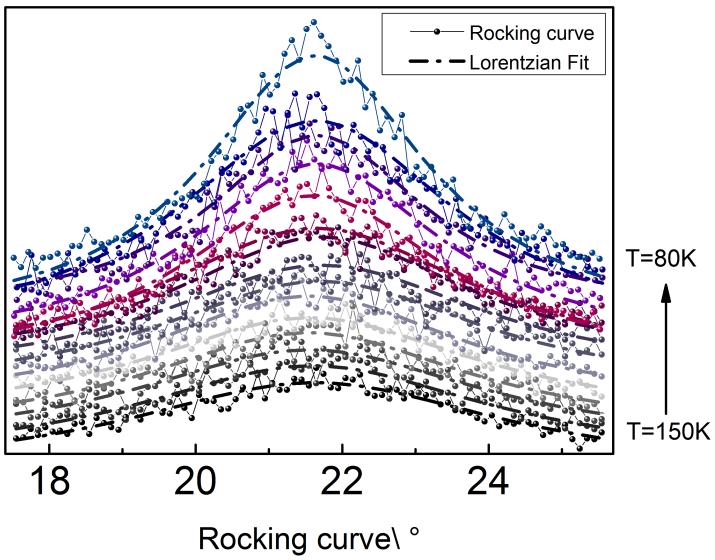

Figure 4.34.: The rocking curve scans on the satellite, (2.62 2 0), from 150K to 80K for m=6. They are transverse scans along **c***, starting from (2.62 2 0.9) until (2.62 2 -0.9).

order at 120K. Normally, for this particular case, a microregion of a critical fluctuation with a *correlation length* that tends to infinity is expected at the critical point. More information about the 2nd order transition theory can be found in Ref. [161]. The rocking curves and θ-2θ elastic scans cut in transverse and longitudinal the CDW satellite peak, along [001] and [230] directions, respectively. The rocking curve was a transverse scan through **c*** going from (2.62 2 0.9) to (2.62 2 -0.9), as it can be seen in Fig. 4.34. The length was chosen based on the diffuse stripes, however, the higher temperature scans are cut. The scans were not taken in a proper way, since the peak is not reaching zero intensity with its tails. Despite this error, a qualitative analysis of the *correlation length* along **c***, $\xi_\perp$, can still be done. The correlation length is obtained from the ΔQ and Δq_l which are the width of the elastic scan in term of reciprocal space and reciprocal length, extracted from the fit:

$$\xi_\perp = \frac{2\pi}{\Delta Q}; \qquad \text{where} \qquad \Delta Q = \Delta q_l \cdot c^*$$

From the FWHM (Full width half maximum) of the large Lorentzian peak as a function of the temperature, shown in Fig.4.35, and the rocking curve, which is in

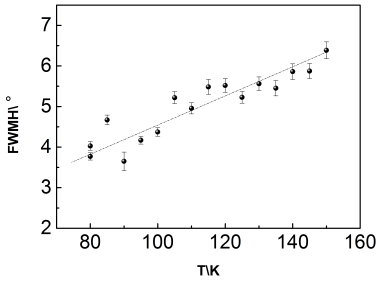

Figure 4.35.: The temperature dependence of the Lorentzian FWHM of the rocking curve.

FWHM (rad)	T (K)	$\xi_\perp$ (Å)
0.112±0.003	150	16.1 ± 0.5
0.096±0.003	120	18.3 ± 0.6
0.0681±0.0017	80	26.9 ± 0.4

Table 4.3.: Correlation length along **c*** for different temperatures, calculated from the Lorentzian FWHM of the rocking curve.

total 8 ° corresponding to 1.8 c*, a simple proportion was applied to calculate $\xi_\perp$. The results for three temperatures: before, on and after the transition, are given in Tab.4.3. An increase of the correlation lengths from 16 Å to 27 Å is shown, around the length of the cell parameter c (23.575 Å). Nonetheless, the long-range order seems to be not present in the transverse scan at low temperature, as it was already visible in the reconstructed plane on the satellite, Fig. 4.32, where the formation of a 3D peak is missing, especially in the **c*** direction.

On the other hand, the longitudinal scans, θ-2θ, have a more enhanced elastic peak and the two components are evident, as seen in **??**. The longitudinal scan cuts the satellite and the diffuse stripe (a focus on the surrounding of the CDW satellite in Fig. 4.41 can help to visualize it) from (2.12 1.55 0) to (3.12 2.45 0). The central peak is related to the formation of the Bragg peak. The second peak, if it is related to the microregion of fluctuations explained before, should be visible near the critical point and disappears after the transition. The sample seems to present the two components in all the temperature range, from 130 K to 80 K, with no change in the FWHM for the large peak ($\sim$ 2.4 °) and a tiny dependence for the central one, Fig.4.37. The parallel correlation length along [2.62 2 0] direction, $\xi_\parallel$, can be calculated using:

$$\xi_\parallel = \frac{2\pi}{\Delta Q}; \qquad \text{where} \qquad \Delta Q = \frac{4\pi}{\lambda}\cos\theta d\theta$$

where ΔQ has a different formula since the scans are longitudinal. The Bragg scattering angle 2θ is equal to the FWHM, $\cos\theta$ can be approximate to 1 and λ corresponds to the wavelengths of the beam, in this case 0.6968 Å. The results are

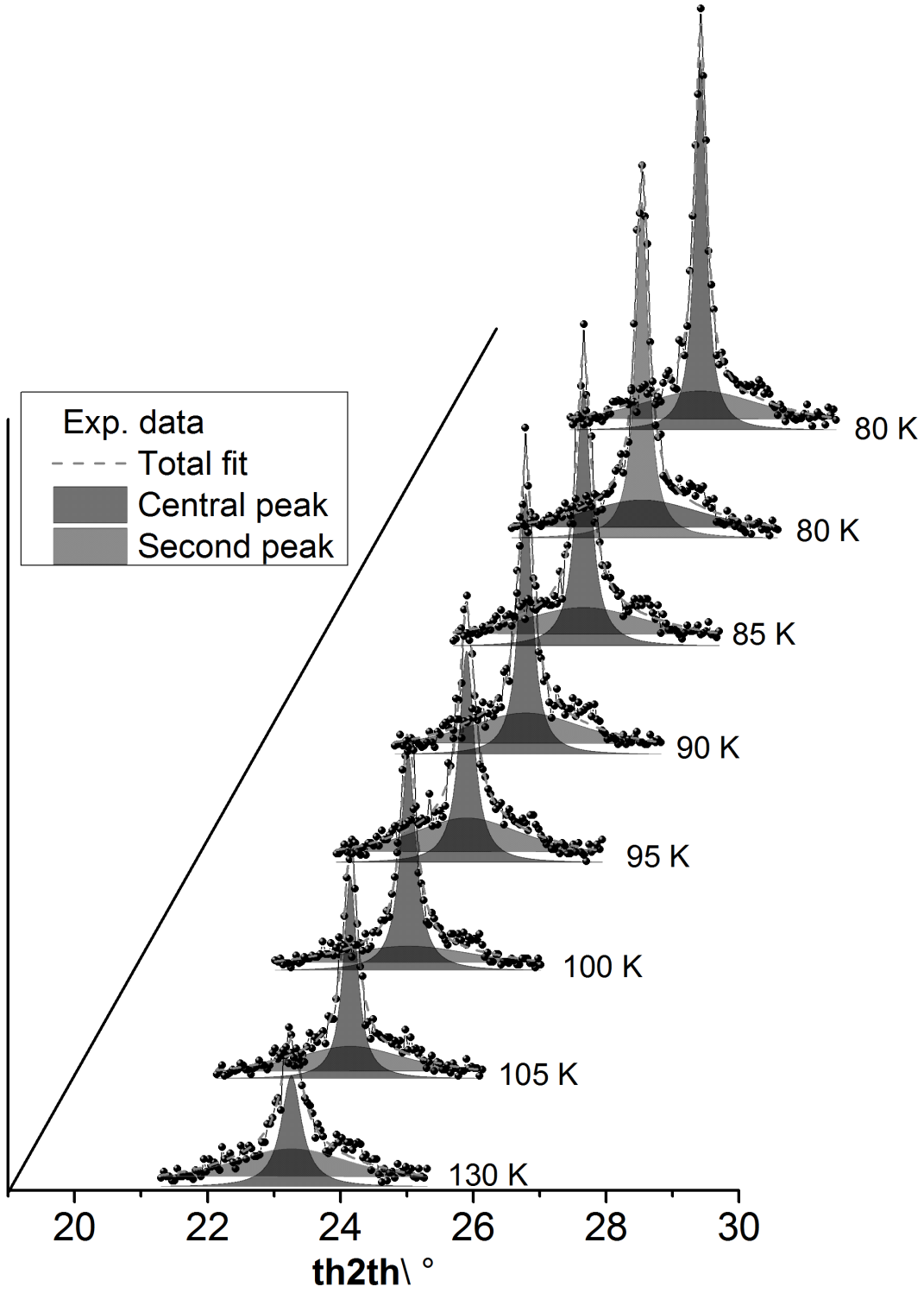

Figure 4.36.: The θ-2θ scans from 130K until 80K of m=6. At 80K the scan was repeated twice. They correspond to a longitudinal scan. There are two contributions which are both visible until very low temperatures.

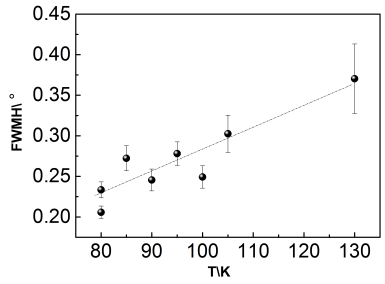

Figure 4.37.: The temperature dependence of the Lorentzian FWHM of the central peak in the longitudinal scan, θ-2θ.

FWHM (rad)	T (K)	$\xi_{\parallel}$ (Å)
0.0065±0.0007	130	107± 11
0.0053±0.0004	105	131± 9
0.00383±0.00015	80	182±7

Table 4.4.: Parallel *correlation length* for different temperatures, calculated from the Lorentzian FWHM of the central peak in θ-2θ scans.

summarised in Tab.4.4. The elastic peak seems already formed in the longitudinal scan and the $\xi_{\parallel}$ confirm a longer range.

The second peak of the longitudinal scan does not have temperature dependence. Thus, it is probably not related to a second order transition behaviour but to a frozen-in disorder.

The temperature dependence of the inelastic scattering intensity on the satellite at $\mathbf{Q}$(2.62 2 0) exhibits a soft phonon behaviour different to the one observed on the m=2 compound. The IXS scans were performed from 400 K to 80 K as seen in Fig. 4.38. The softening is visible at the nominal transition (T_{CDW}=120K), however the phonon does not disappear and goes to 0-energy at $\mathbf{q}_{CDW}$ at the transition as expected. Since the elastic contribution after the transition becomes more and more important, it was difficult to estimate the real position and contribution of the phonon. However, with a certain approximation, the phonon has a stable energy around 3.7 meV. The phonon softening can be seen more clearly with just two example of IXS scans at high temperature, 400K, and low temperature, 90K, in Fig. 4.39c and the phonon energy dependence is shown in detail in Fig. 4.39b. The area of the fitted elastic contribution using a Lorentzian peak is increasing constantly with a change in the slope after the transition, as it can be seen in Fig. 4.39a. The area does not have the same behaviour as reported by Foury [117] for the same member. Since the study was performed in one single crystal, the different quality could be the reason for this behaviour. As already pointed out, the system was studied down to 80 K due to the usage of the cryostream. Thus, the "plateau" of the elastic contribution, normally necessary to describe the behaviour of the transition, was not reached.

Looking at the diffuse planes and their condensation in stripes by temperature, one should study the intensity dependence of the phonon on the satellite. In fact,

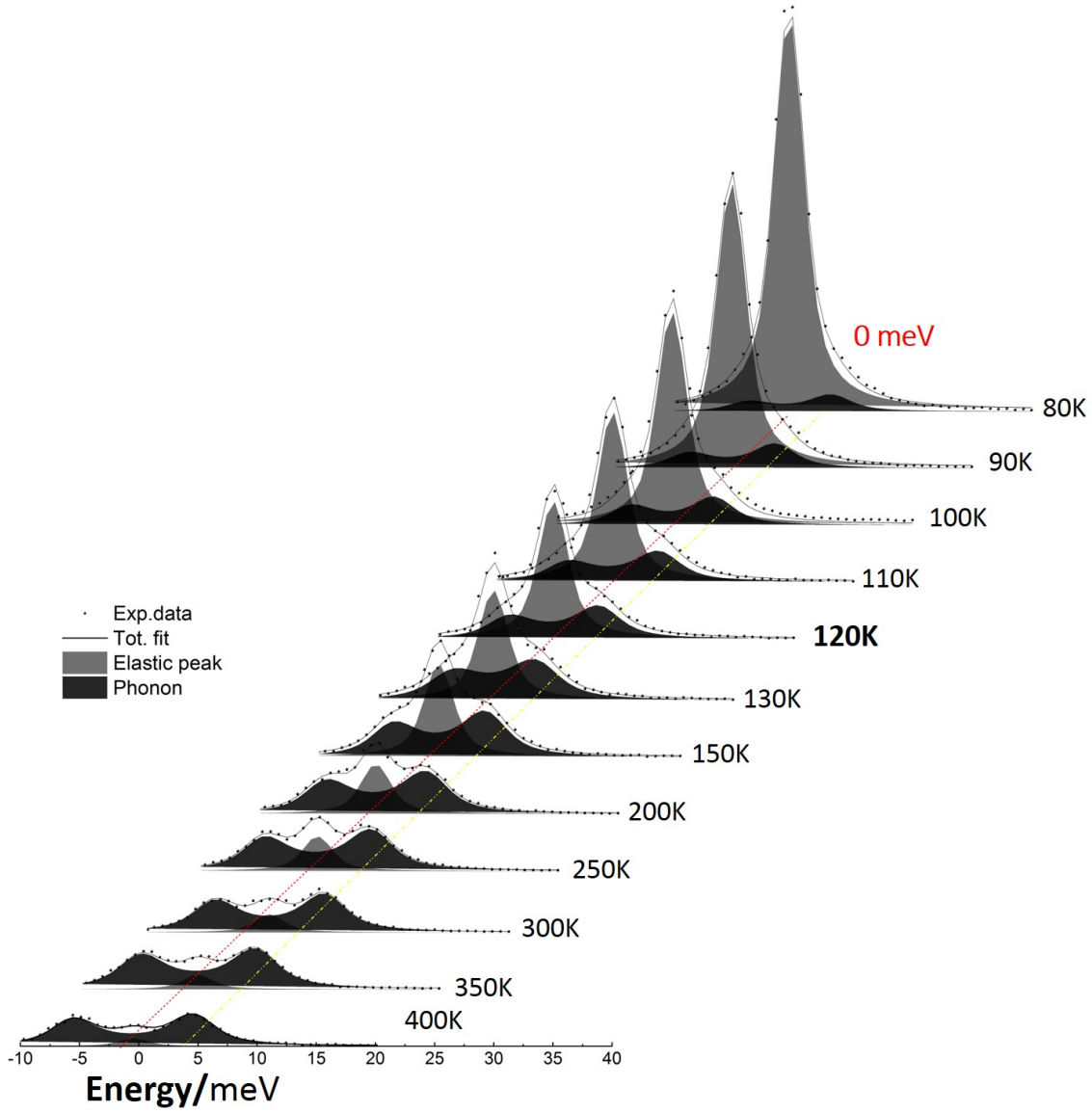

Figure 4.38.: The IXS scans in the (2.62 2 0) satellite position at different temperatures above and below the nominal transition temperature. It is visible the phonon softening and the increasing of the elastic contribution. The red line shows the zero energy, whereas the yellow dotted line follows the phonon energy. The effect is propagating also below the expected transition.

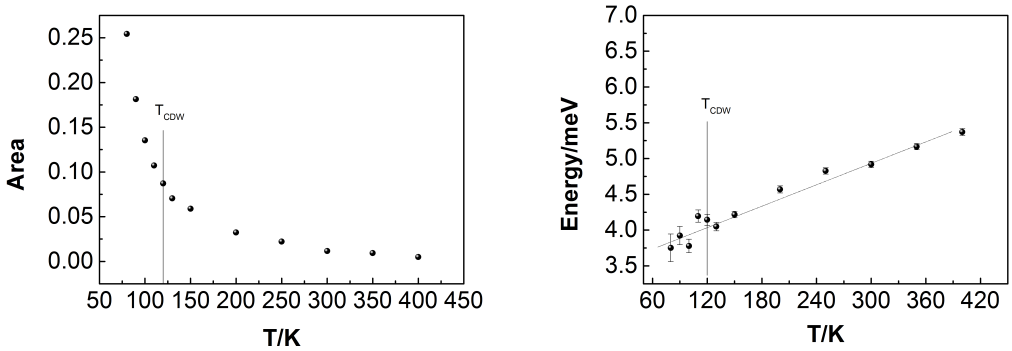

(a) (b)

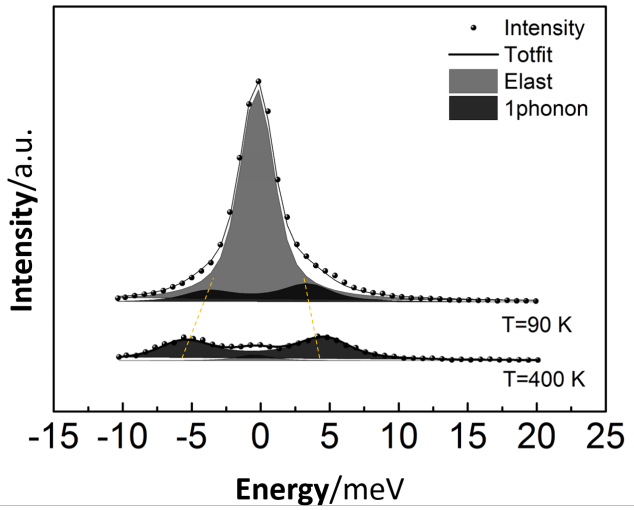

(c)

Figure 4.39.: (a) The area of the elastic peaks at different temperatures in the (2.62 2 0) satellite position for m=6; (b) The temperature dependence of the phonon energy, showing a continuous softening. After the transition at 120 K, the elastic peak prevents to clearly see the phonon contribution and its position; (c) Two IXS scans in the satellite position at 400K and 90K. The yellow dotted line is used as help for eyes to show the softening. The fitted phonon and elastic contributions are highlighted by their areas strong and light gray, respectively.

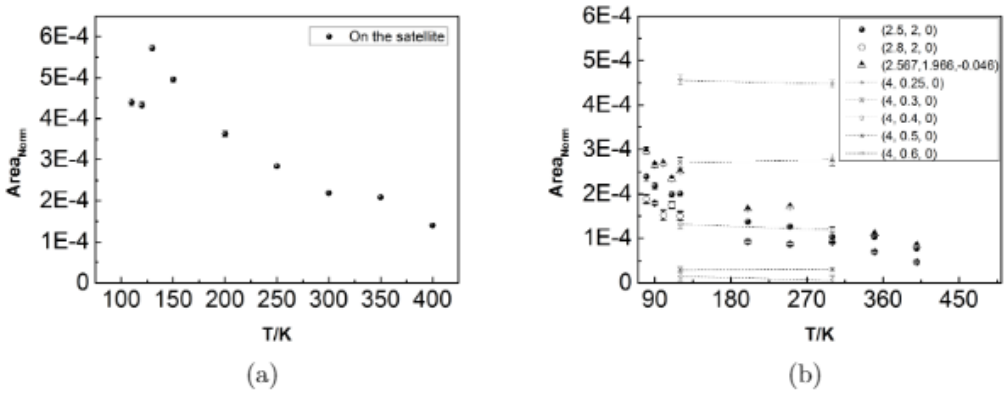

Figure 4.40.: (a)The area of the fitted phonons at **Q**(2.62 2 0) reported for all the temperatures; (b) The area for two points of the reciprocal space near the satellite: (2.8 2 0) and (2.5 2 0) and on the tail of the peak, (2.567 1.966 -0.05). The acoustic phonon in the [010] direction at RT and 130K show the normal behaviour of the area. The areas were normalized considering the Bose factor.

the phonon integrated intensity at a specific q-vector is constant with temperature when normalized considering the Bose factor. The area of the phonon peak is shown in Fig. 4.40a, where an anomalous behaviour is observed. The area increases until the temperature transition, probably related to the condensation of the diffuse region. One can argue that this analysis is not sufficient since the scans are cutting just in one particular part without taking into account all the directions around the satellite. However, in support of our analysis, the area of the phonon peaks at different **q** points around the satellite were studied. The same behaviour is found for two points along the **a*** direction: (2.8 2 0) and at the border of the Brillouin zone (2.5 2 0). In a third point on the tail of the CDW peak, the phonon integrated intensity was also analysed, (2.567 1.966 -0.05), Fig. 4.40b. Thus, the diffuse scattering intensity is dynamical in nature. The experimental results seems to show a trend in "increased" diffuse scattering intensity with decreasing temperature and thus increased signal. This phenomenon could be related to the very small change in turn in the frequency. To confirm the irregular trend around the satellite, in the same figure, the phonon peak area at different points of the acoustic branch in the [010] direction are reported. They present the standard tendency of the phonon on temperature.

The inelastic measurement was extended to the region around the satellite, crossing the diffuse stripes and along them. In general, all the directions show a region of low-energy phonons. From ambient conditions to 130 K, the results of the fit along different directions are shown in Fig. 4.41. Three directions are along H,

Phonon dispersions around the (2.62 2 0) satellite

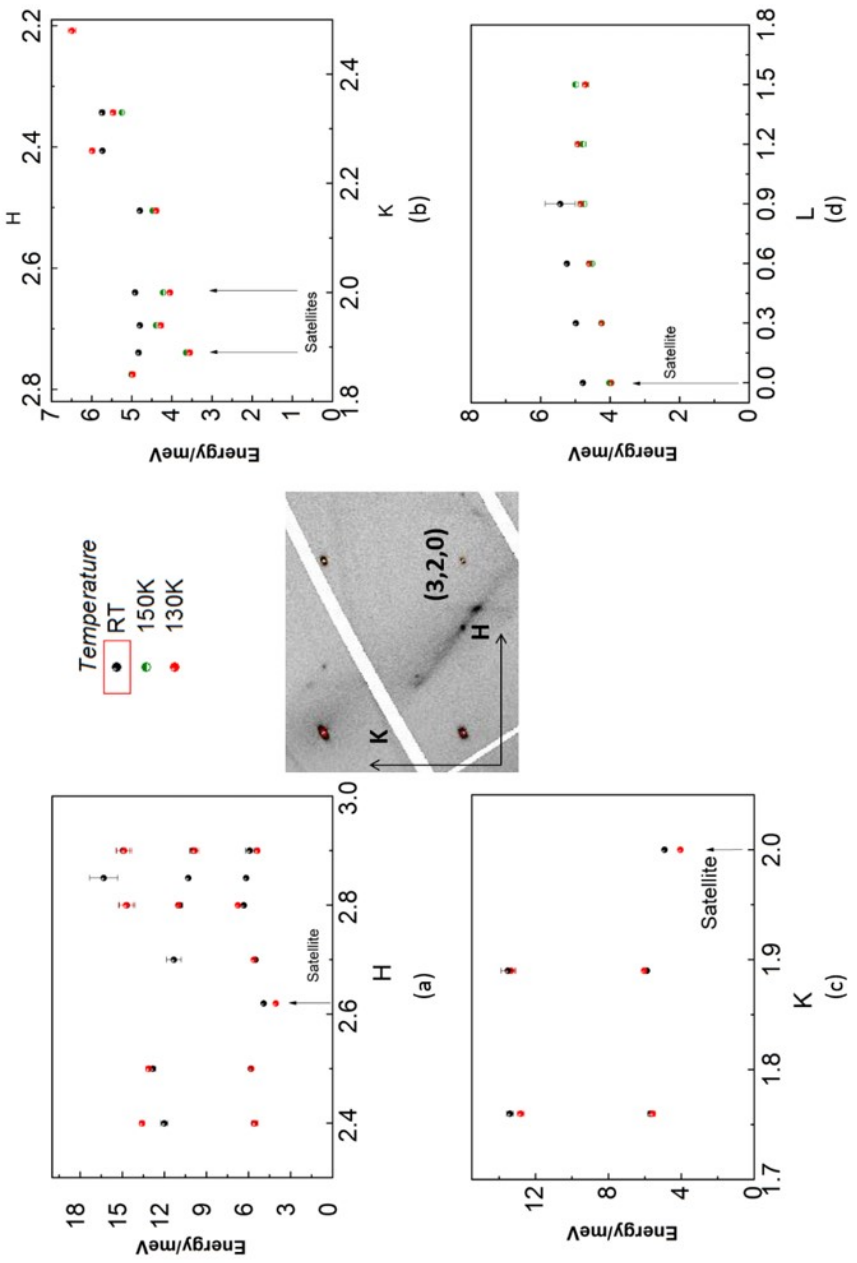

Figure 4.41.: Phonon dispersions around (2.62 2 0) satellite: (a) along H, (b) along the diffuse stripe with (**a***-**b***) direction, (c) along K and (d) along L at three temperatures, RT, 150 K and 130 K in black, green and red dots, respectively. In the middle, a focused HK0 map around the satellite, in order to better visualise the diffuse pattern.

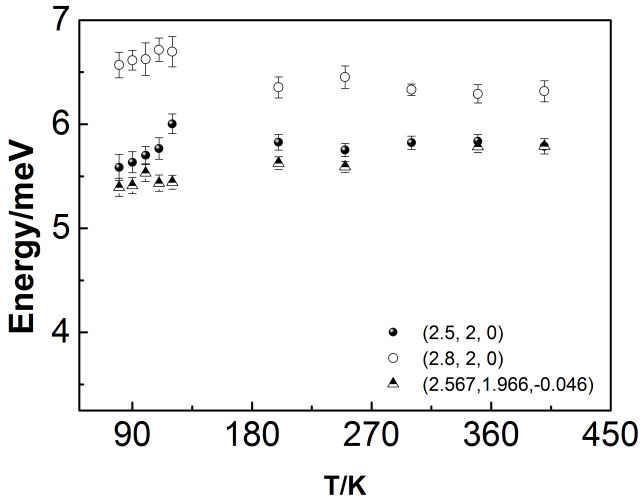

Figure 4.42.: The temperature dependence of the phonon energy for (2.5 2 0), (2.8 2 0) and (2.567 1.966 -0.046) Q-points. Only the phonon at the BZ border shows a softening below the T_{CDW}, less pronounced in respect to the phonon on the satellite. The same range in energy of Fig. 4.39b is used to have a better comparison.

K, L and the fourth one is along the diffuse stripe, (**a***-**b***). The phonons have a common trend in the energy, showing a general constant value around 5 meV. A heterogeneity start to be visible with the temperature response. The temperature dependence of the phonon energy is more visible on the satellite and the directions where the diffuse intensity is present, as [001] and [1$\bar{1}$0]. Additionally, on the satellites ($\mathbf{q}_1$=-0.38**a*** and $\mathbf{q}_3$=-0.29**a***-0.11**b***) is more pronounced with the softest phonon. The second position is referred to a satellite of the 3^{rd} CDW phase at 30K, however, the phonon seems already to have a strong coupling with the instability at lower temperature. The last direction, **c***, as shown in the diffuse scattering, has a diffuse stripe until 80K with a length of $\sim$2c*. For this reason, at each temperature, each point in the dispersion soften. Also in this case, the softening is more accentuated on the satellite. Whereas the phonon energies in the points out of the diffuse are constants (along [100] and [010] directions).

Other than the satellite, a more complete inelastic scan study by temperature was done for the 3 points already described before: (2.8 2 0) and (2.5 0 2) along **a*** and (2.567 1.966 -0.05) at the tail of the satellite. From Fig. 4.42, no softening is visible. The only point showing a very weak dependency is the phonon at the BZ border, that has a softening after the expected T_{CDW}.

The phonon dispersions around a strong Bragg peak, (400), were done in order

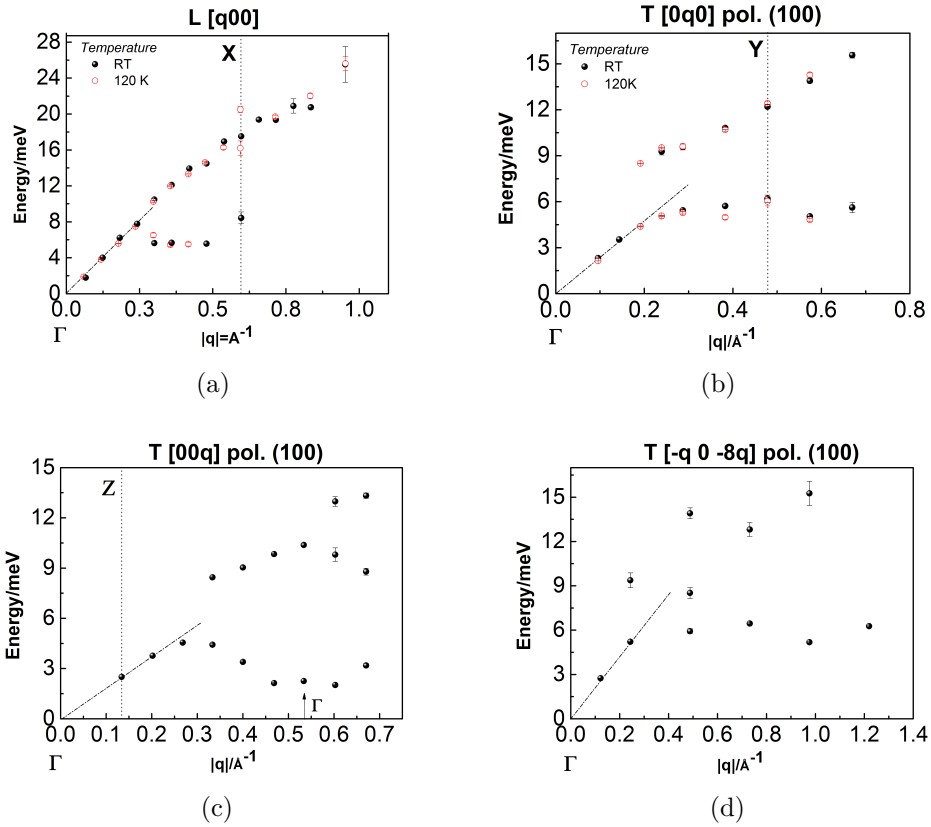

Figure 4.43.: Three phonon dispersions at ambient conditions and 120 K of m=6 on the high symmetry axes starting from (400) Bragg peak: (a) along the [100], (b) [010] and (c) [001] directions; (d) the dispersion along the diffuse planes on the H0L intersection, $[\bar{1}0\bar{8}]$ direction. In all the cases an anticrossing in the dispersion is visible.

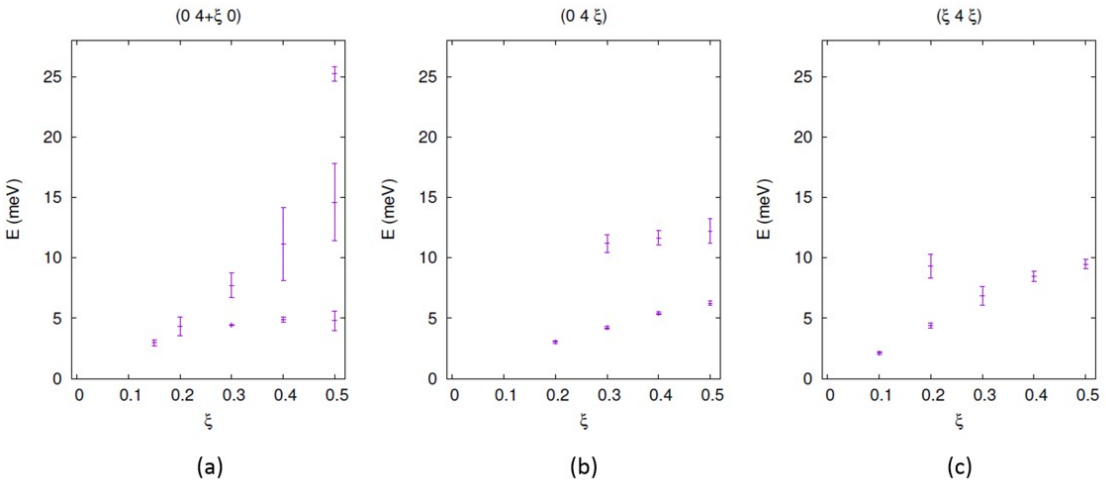

Figure 4.44.: Phonon dispersions along (a) [010], (b) [001] and (c) [101] directions for WO_3 in the monoclinic phase, P-1, at room temperature [162].

to have the general behaviour of the lattice dynamics without the anomaly that a satellite causes. The main directions in H, K and L and along the intersection of the diffuse plane, $[\bar{1}0\bar{8}]$ are shown in Fig. 4.43. Since the Brillouin zone is very small in **c***, we present an extended scheme. For this reason, at |q|=0.55 in Fig. 4.43c, the low energy phonon is an acoustic phonon resulting from the near (420) Bragg, which has a medium intensity.

The first direction going to X shows the longitudinal phonon dispersion, whereas in the other directions going to Y and Z, the phonons are of transverse type and a mix-type is present in the diffuse direction, $[0\bar{1}0]$, [001] and $[\bar{1}0\bar{8}]$ directions, respectively, with (100) polarization. An anticrossing is visible with a energy gap of $\sim$ 3 meV between the acoustic-like phonon and low-energy optic phonon. The longitudinal branch presents a optic phonon with a higher energy and the gap is of $\sim$ 6 meV.

The tungsten trioxide, WO_3 is constituted by the same base of the W-block in the monophosphate tungsten bronze members. As we see earlier, the diffuse intensity distribution is very similar, with diffuse planes corresponding to the instability of the W-O-W-O chains. For this reason, the lattice dynamics of the simple oxide can be useful to understand this family. In fact, in our system the heavier atoms are the tungsten so, the low-energy phonons should be driven by them. One can notice the same anticrossing in the three directions found in the tungsten bronzes in Fig. 4.44, confirming our prediction and showing the link between the low-energy phonons and the diffuse planes.

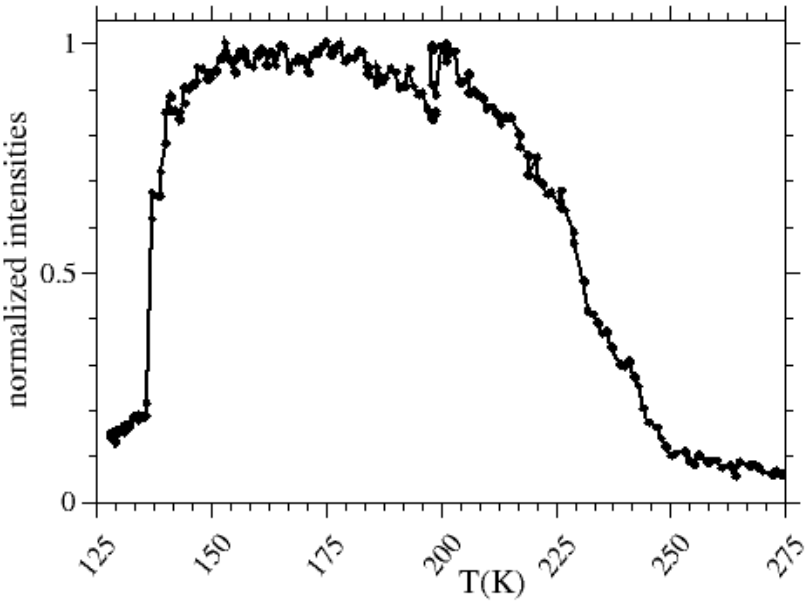

Figure 4.45.: Temperature dependence of the intensity detected in analyser 2 near q_{CDW1}, **Q**(3.53 0 3.46), for m=8.

High-term member: *m*=8

Already in the diffuse scattering results, some differences between the members were found and how this are reflected on the lattice dynamics can help to clarify the family behaviour. The quite high temperature of the first transition with commensurate CDW instabilities at 250K (T_{CDW1}) and a second one at 140 K (T_{CDW2}), both having different modulation vectors, $\mathbf{q}_{11}$=4/9**a***-4/9**c*** and $\mathbf{q}_{21}$=1/2**a***-1/2**c***, $\mathbf{q}_{23}$=1/6**a***-1/6**c***, will oblige to study at high temperature in order to avoid the elastic contribution of the satellites.

The high-quality of the sample was already confirmed by DS and a bigger sample was possible to measure, contrary to m=6. Since in the diffuse scattering measurement, the beam shows to heat the sample of m=8 and the transition is a setpoint temperature, a check on the transition temperatures for the two phases was done. In the same way that we have done with m=2, a temperature dependence of the intensity on the $\mathbf{q}_{CDW1}$ was recorded. The transitions were found at 250 K and 140 K, since the intensity increases gradually until reaching the "plateau" at T_{CDW1} and drops significantly when the second phase is reached, as seen in Fig. 4.45. The slope on the first transition shows an intermediate phase between the first transi-

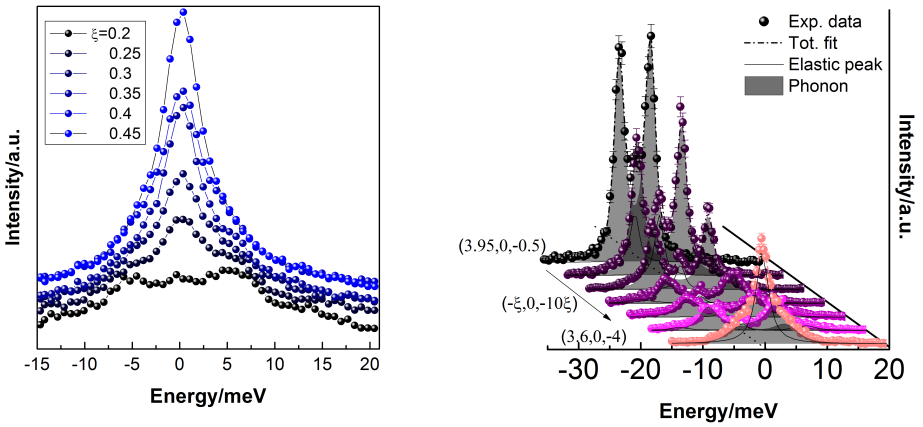

(a) (b)

Figure 4.46.: In figure (a) the IXS scans along the direction in the diffuse scattering, [-1 0 -10], at RT with a resolution of 3 meV, whereas in figure (b) the same direction at 350 K with a resolution of 1.5 meV.

tion and the high-symmetry phase. It is normally called "phase zero" since it was discovered just recently by the group in Caen [115], with a modulated vector of **q**=0.5**a***. It resembles the first condensation in stripes around 0.5**a*** found in the diffuse scattering, a focus on the diffuse part is in Fig. 4.47b.

In order to study the response of the phonon, the temperature dependence of the phonon dispersion in different directions of the reciprocal space was done. The experiment started with the lower energy-resolution of 3 meV. However, the elastic contribution forced us to change to the high energy resolution, an example of the difference between low and high resolution can be seen in Fig. 4.46, which shows the phonon dispersion on the same direction. In (a), the phonon dispersion along the direction in the diffuse plane taken with low resolution, [-1 0 -10], measured at room temperature (in the high-symmetry phase) shows the elastic peak which covers the phonon contribution. Whereas in (b) the resolution of 1.5 meV is shown, the IXS scans become more clear and it is possible to find the energy of the phonon without a large error. However, also for the dispersion at a higher temperature (400 K) and higher resolution, the elastic peak has still a strong contribution in the IXS scan, as shown at the q-point near the border of the BZ, **Q**(3.6 0 -4).

The direction in the strong diffuse plane should be studied, since it is where the CDW satellite reflections are condensing and a related phonon softening is expected. The phonon dispersion at three different temperatures was recorded,

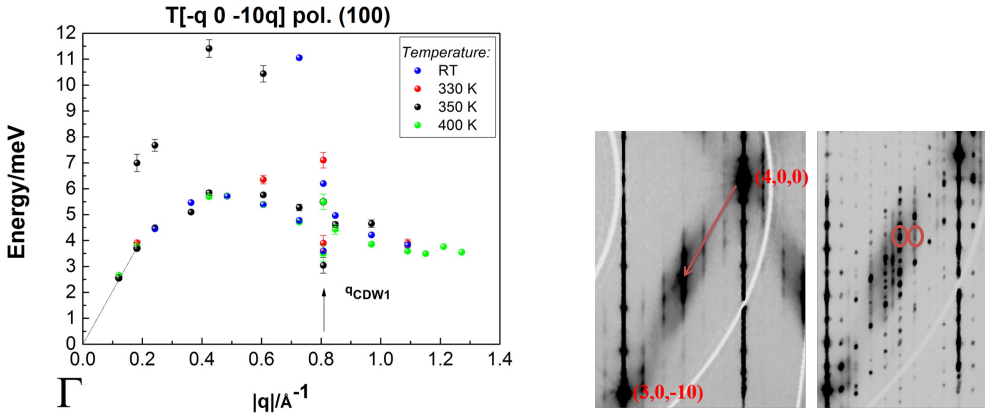

(a) (b)

Figure 4.47.: In figure (a) the phonon dispersion along the diffuse line in the high-symmetry phase at different temperatures for m=8. In figure (b) the H0L plane at RT, on the left, and 240 K, on the right. The measured direction is shown by the red arrow and the two satellites, **Q**(3.53 0 -3.46) and **Q**(3.67 0 -3.33), are in the circles.

Fig. 4.47. The dispersion shows a large valley of soft phonons, from |q|=0.5 Å^{-1} until the border of the BZ with a minimum energy equal to roughly 3.8 meV. However, there is no significant energy evolution of the soft phonon by temperature. One can argue that what we call soft valley is present also in the m=6 after the anticrossing in different directions of the reciprocal space. However, the energy range is different. The low-term member presents the low energy phonon around $\sim$ 6 meV, whereas the softening in m=8 is stronger, around $\sim$ 3.5 meV, just half of the energy is required to excite that particular vibration. At |q|=0.8 Å^{-1}, corresponding to a 1st CDW satellite of the first order, an additional softening seems to be present. The |q|=1.2 Å^{-1} is the position of the lowest phonon energy of the soft valley, corresponding to **Q**(3.5 0 $\bar{5}$). It is actually in the position of the first strong condensation found through DS. For each point in the dispersion, the fit was very difficult and the error in the energy is large.

In the measured signal, there are two inelastic contributions. In fact, a phonon of higher energy (range 8-10 meV) is visible. It has a weaker intensity and the real energy position is estimated. Comparing the scans obtained at two different points at 350 K, as **Q**(3.67 0 -3.33), corresponding to |q|=0.8 Å, and **Q**(3.75 0 -2.5), a point in the dispersion near the satellite corresponding to |q|=0.6 Å^{-1}, a particular behaviour is visible, Fig. 4.48. In fact, the inelastic contribution on the satellite cannot be fitted with just one phonon. Looking at the figure, we

notice two highlighted areas, which are referred to two phonons with FWMH of $\sim$ 3 meV. The adjacent position, |q|=0.6 $Å^{-1}$, shows the second phonon at higher energy. However, it is difficult to predict the softening, if the two are related to the instability and they are soft phonon or just the optical phonon at higher energy is approaching the energy of the lower one. Thus, the elastic signal is not the only issue. The complicated phonon contribution and their superposition should be added. In this case, the only statement that can be made, is that in the satellite position there are two phonons with a low energy and the optical one manifests strong softening.

In order to better understand the two phonon contributions and the soft valley region, different IXS scans were taken around the satellite (3.67 0 -3.33), as seen in Fig. 4.49. Two directions: [010] and [-1 -1.5 0] were chosen and, as for the IXS scans on the satellite, all of them present more than one phonon contribution. The phonon at higher energy moving away from the satellite increase its energy until $\sim$ 10 meV, especially along the [010] direction. The phonon at low energy is stable around 3.5 meV. This latter result confirms the soft valley region. In addition, this average energy confirms a further softening on the satellite with respect to the soft valley along the diffuse plane.

Additional studies at the satellite positions (3.67 0 -3.33) and (3.555 0 -3.444) were made in temperature, the first was previously showed. The second satellite presents a higher intensity and to avoid the strong elastic peak, the IXS scans were taken near the satellite position at **Q**(3.53 0 -3.46), shown in Fig. 4.50. Their positions are highlighted in the DS map at low temperature in Fig. 4.47b.

In the first case, the elastic contribution passes from the huge contribution at 263 K to almost disappears at 400 K. However, as already explained, also without the issue of the elastic component, the two phonons at low energy complicate the fit. The real energies of the two contributions are difficult to disentangle. Thus, the fit was possible, considering a significant error in the energy estimation. For the latter satellite, the IXS scans show a big elastic contribution, which is decreasing at high temperatures. However, the only observation is a change in the tail of the elastic peak from 290 K to 400 K, suggesting the presence of a phonon at low energy.

The Tab. 4.5 summarises the phonon energies from 290 K for the two satellites. At lower energy the intensity of the elastic peak is predominant. For the first satellite, the energy is just given almost in a qualitative way, due to the error in the estimation of the real position in the IXS scans. However, the energies are around $\sim$ 3 meV and $\sim$ 6.5 meV, respectively, for the two phonons. The phonon frequency in the position of the 2^{nd} satellite is $\sim$2.7 meV. No significant temperature dependency on the phonon energy is found.

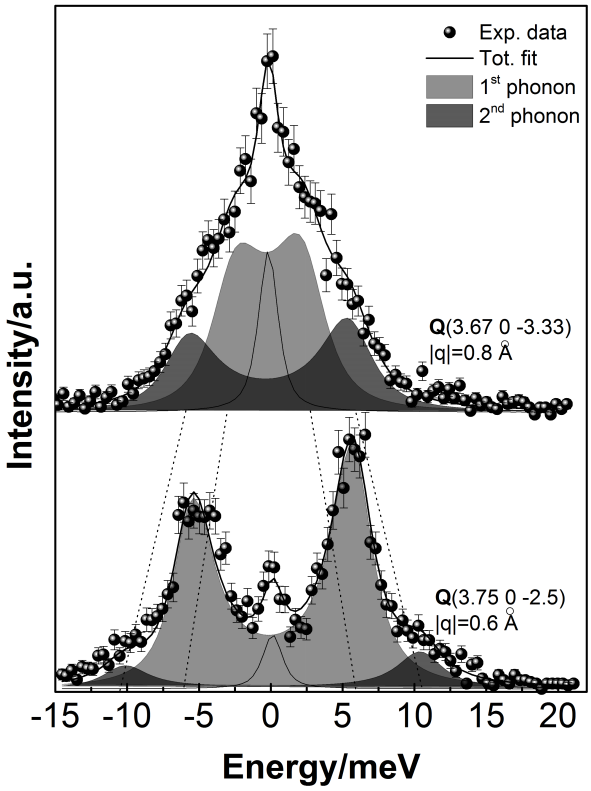

Figure 4.48.: IXS scans with the fitted phonons highlighted by their area at 350 K for m=8. On the upper figure the satellite **Q**(3.67 0 -3.33). On the lower figure a point near the satellite on the diffuse direction, **Q**(3.75 0 -2.5). The two scans are compared in order to show the phonon softening in the satellite position and the possible presence of two phonons.

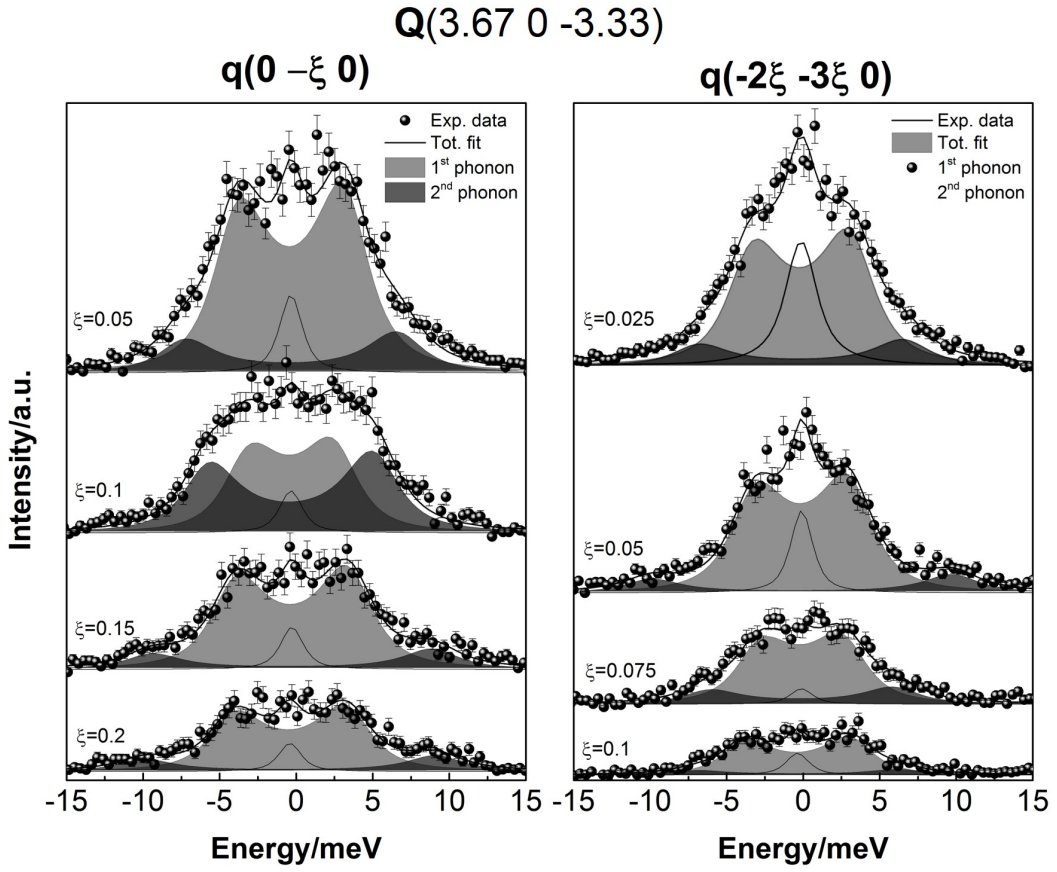

Figure 4.49.: IXS scans with the fitted phonon and elastic contribution at 400 K, along [0-ξ0] direction , on the left, and [-2ξ -3ξ 0] direction, on the right, starting from the satellite **Q**(3.67 0 -3.33) for m=8. The two phonon peaks have their area highlighted using strong and light gray colors.

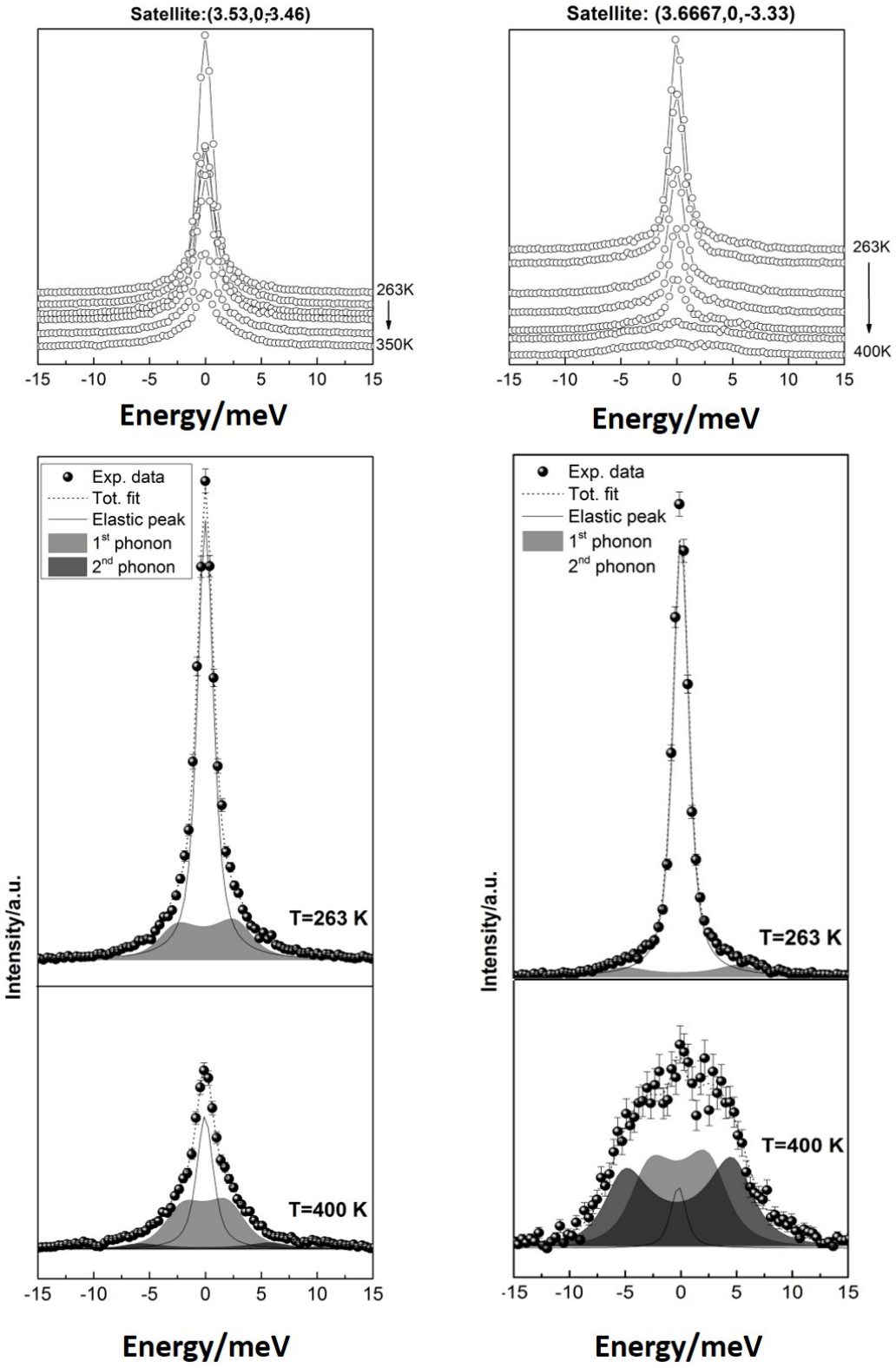

Figure 4.50.: Temperature dependence of the IXS scans at the satellites (3.555 0 -3.444) and (3.67 0 -3.33) positions of the first CDW phase of m=8. On the left column, the scans related to (3.555 0 -3.444) satellite. On the right, the ones related to (3.67 0 -3.33) satellite. The single scans at 400 K and 267 K with the fitting functions, show the decreasing at high temperature of the satellite intensity. At 400 K the phonon contribution starts to be visible.

T (K)	Phonon energy on Q(3.53 0 -3.46) (meV)	1st phonon energy on Q(3.67 0 -3.33) (meV)	2nd phonon energy on Q(3.67 0 -3.33) (meV)
400	2.89 ± 0.13	3.5 ± 0.3	5.5 ± 0.3
350	2.68 ± 0.11	3.04 ± 0.14	5.9 ± 0.2
330		3.9 ± 0.3	7.1 ± 0.3
310	2.77 ± 0.13	3.8 ± 0.9	6.4 ± 0.7
290	2.7 ± 0.3	3.6 ± 0.3	6.2 ± 0.3

Table 4.5.: The phonon energy on the **q**-points of the two satellites of m=8, for the satellite at **Q**(3.53 0 -3.46) one contribution is present, in the contrary at the satellite **Q**(3.67 0 -3.33) the scans were fitted considering two phonons contribution. No visible softening is present in the two points.

Dispersions along other directions were measured, Fig. 4.51. On the figure (a), the [00$\bar{1}$] direction shows the same dispersion found for the member m=6. In this case, the opening is just of $\sim$ 2.5 meV, rather than $\sim$ 3.5 meV as for the low-term member. However, the anticrossing point is in the same position, **Q**(4 0 -1.25), for both members. On the other hand, the linear dispersion along [100] shows one contribution, whereas in m=6 the anticrossing is visible with a low energy phonon around 4 meV.

This high-term member, m=8, presents a rather complicated lattice dynamics. The high-temperature measurements and the high energy-resolution help to decrease the elastic contribution, from one side, and show better the phonon contribution, from the other. However, it was not sufficient to understand completely the system. Calculations will be useful to disentangle the phonon response. As it was already reported, the calculations for this large cell and complex electronic system are complicated.

In conclusion, the high-term member presents a lattice dynamics response that seems to be the signature of a strong electron-phonon coupling, with the proposed polaronic model by Aubry *et al.* [59]. In the context of strong coupling theory, the softening covers a larger part of the reciprocal space [160], rather than in the "classical" displacive soft phonon mode as in a Peierls transition, where the phonon goes to zero energy at T_C. Indeed in the case of strong coupling one expects an elastic contribution to remain above T_{CDW1} with a hardening of the soft phonon mode when the temperature increases. The phonon dispersion along the diffuse

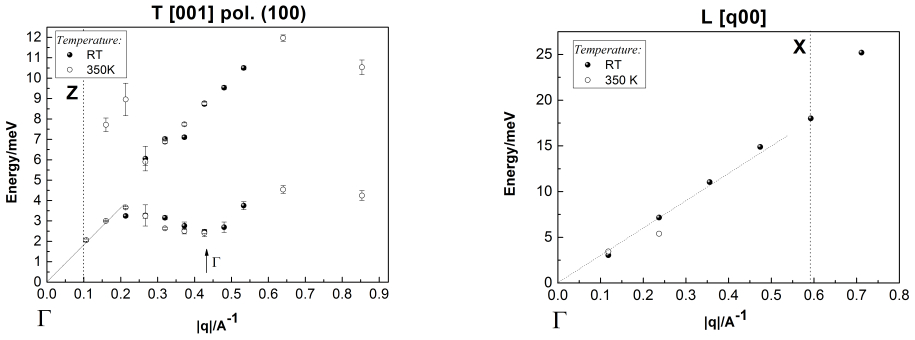

(a) (b)

Figure 4.51.: The phonon dispersions of m=8 from (400) Bragg peak along (a) $[00\bar{1}]$ and (b)[100] directions.

direction, $[\bar{1}0\bar{1}0]$, at higher temperature should show this behaviour. In addition to the soft phonon valley in this direction, a major softening is found in the satellite position, which has an energy lower of $\sim$ 1 meV with respect to its neighbours along the diffuse plane direction. A more significant softening is oberved for the higher energy phonon, an optic phonon that is around $\sim$ 10 meV and decreases its energy to $\sim$ 6.5 meV at the satellite position.

4.6. Pressure effect on bronzes

The temperature is the easier trigger to study fascinating physical properties as Peierls transition towards CDW/SDW phases and superconducting instability, and the competition between these two phases. Further study of the charge density wave under pressure can give valuable information to understand the phenomenon of electronic instabilities in low-dimensional conductors. In addition, in case of perovskite structure and their instabilities, the pressure is an essential tool in order to study the phase transitions [163, 164].

The isotropic pressure can suppress or enhance the CDW phase. More commonly, a hardening of the phonon due to the lattice compression is found [165]. This behaviour can be explained considering the mean field expression for the critical temperature valid in the 1D case (the fluctuations are neglected) [166]:

$$k_B T_{CDW} = 2.28 E_F \exp(-\eta\omega_0(2k_F)/g^2 N(E_F)), \tag{4.1}$$

where $\omega_0(2k_F)$ is the phonon frequency at the wavevector $2k_F$, $N(E_F)$ is the density of states at the Fermi level and g is the electron-phonon coupling constant [167, 168]. The phonon frequency related to the electronic instability at $\mathbf{q}_{CDW}$ should increase, due to two factors: the hardening of the lattice under pressure that increases the strain energy and the gain of the electronic free energy by the gap opening at the Fermi level [167, 169]. The first, in other words, is related to the compression of the volume that increases the inter and intra chains coupling and the 3D character of the system. The second is related to the cost in elastic energy at the Fermi surface, which is larger when the pressure increases. Both factors cause a final suppression of the 1D thermal fluctuations. In fact, for $NbSe_3$ and η-Mo_4O_{11}, the Shubnikov-de Haas oscillations show that the Fermi surface is strongly affected by the pressure [170, 171]. Thus, the general behaviour is the decrease of the CDW temperature transition, which is found in different compounds. Examples are $NbSe_3$, layered di-trichalcogenides, etc. [170, 172–175]. Since the CDW phase is not favoured from the pressure, the latter becomes an important tool when there is a competition between superconductivity and CDW phase. In fact, in the already cited case of $NbSe_3$, the superconductivity phase emerges when the CDW phase disappears, around 0.55 GPa [170, 176]. In the same way, in the dichalcogenides and $Li_{0.9}Mo_6O_{17}$ purple bronze, the T_C [7] increases under pressure[174, 177, 178]. In this list, the Magnéli η-Mo_4O_{11} as isostructural of m=6 should be added. Pressure studies show an opposite behaviour. In fact, T_{CDW1} increases with pressure while T_C decreases [171, 179].

Obviously, there are multiple exceptions with opposite behaviour which can be found in different ranges of pressure. In the purple bronzes, the two behaviours can be found, e.g. $Na_{0.9}Mo_6O_{17}$, $K_{0.9}Mo_6O_{17}$ [168, 169, 178, 180, 181], or in VSe_2 [182]. In this case, the intra-chain coupling and a more favourable Fermi surface nesting are induced by the pressure [168, 169, 179].

In the same system, there can be a competition of all those characters, as in the bromide and chloride-bridged platinum. Under pressure, they reveal an initial hardening and a final softening of the mode connected to the CDW phase [165]. As a final example, also more complicated sequences can be found under pressure. In $ZrTe_3$, the modulation vector, $\mathbf{q}_{CDW}$, has a pressure dependence [183].

For the monophosphate tungsten bronze family, different behaviours are reported for the members as m=4,(4/6),6 and 10 [115, 167], summarised in Tab. 4.6, where the Magnéli phase η-Mo_4O_{11} is also reported. Resistivity measurements were made for the low-term members by Beille *et al.*, whereas the high-term member was studied by the group in Caen by diffraction [115, 167]. The member m=4 has at

[7] In this section we use T_C to describe the critical temperature of the superconductor, whereas T_{CDW} is referred to the CDW phase transition.

Member	**Exp. study**	**dT$_1$/dP** [a] K/GPa	**dT$_2$/dP** [a] K/GPa	**Max. P** GPa	**Ref.**
4	Resistivity	-36	9 (P<0.5 GPa) -28 (P>0.5 GPa)	1.8	[167]
4/6	Resistivity	-33.5	03	1.8	[167]
6	Resistivity	-9	-5	1.8	[167]([184])
10	Diffraction	n/a	-177	0.68	[115]
η-Mo_4O_{11}	Resistivity	$\sim$ 8	$\sim$ -11.5	1.3-1.2	[167, 171]

[a] they are referred to the pressure dependence of T_{CDW} of the 1st and 2nd phase.

Table 4.6.: Pressure study on the monophosphate tungsten bronzes, with the results related to the CDW phase and a comparison with the similar system Mo_4O_{11}. The papers and thesis works are reported on the right.

ambient conditions two transitions, under pressure the first transition is decreasing linearly, whereas the second transition has a different behaviour, increasing with pressure. At 1 GPa, the two transitions completely disappear. The member 4/6 follows exactly m=4, with the same pressure dependence of the transition (-33.5 K/GPa). One can establish the connection between the two members since they have the same nesting vectors. The m=6 has two transition temperatures that decrease with pressure.

The high-term member was studied differently by Duverger-Nedellec [115]. Diffraction studies at room temperature were made for m=10. This member is easier to study, since it is already in the 1^{st} CDW phase at room temperature. The **q**-vector is at 3/7**a*** at room temperature. This member has two different CDW phases, the first phase is stable in the range 450 K-220 K and the second phase below 220 K. When a pressure of 0.32 GPa is applied to the system, it seems to pass to the second CDW phase at room temperature, in which the modulation vectors are $\mathbf{q}_{21}$=1/2**a*** and $\mathbf{q}_{22}$=2/5**a***. The measurement has been performed up to 0.68 GPa and it confirms the stabilisation of this phase. An extremely high dT_{CDW}/dP, with a value around 177K/GPa, was found and it was linked to a strong electron-phonon coupling. Thus, the system needs just a little variation of pressure to reduce the thermal fluctuations and favour the second CDW phase.

In this section of the thesis, the study through diffraction and inelastic scattering

measurements was performed for two members of the family. The first is the member m=10, in order to continue the study of Duverger-Nedellec and reach a higher pressure. The second member is m=8, which was never studied under pressure. The reason for this choice comes from its specific lattice dynamics response. The pressure can affect the soft valley region. In this case, the strong electron-phonon coupling should be affected by the pressure, resulting in some change in the lattice dynamics. However opposite behaviours are shown in the family, where the low-term members show a negative dT_{CDW}/dP, and the high-term member a positive one.

4.6.1. Structural study on m=8 and m=10

Diffuse scattering studies in ID28 were done. The maximum aperture angle of measurement is defined by the angular aperture of the DAC, ± 30 °. A characteristic of this family is the big c parameters, so the DS reconstructed maps have still a significant amount of Bragg peaks, permitting some important results.

For the member m=10, a DAC with 600 μm diameter culet was chosen and the rhenium gasket was prepared. The gas loading was at 0.3 GPa and the first run of measure with this pressure was made, showing nice DS reconstructions, Fig. 4.52. The phase at 0.3 GPa has a component in **a***, visible in HK0 and H0L planes. Specifically, on the H0L plane, the satellite divides the a^* parameter cell in 10, confirming the two vectors of the second CDW phase. The two **q**-vector are shown in the H0L map. In addition, an earlier experiment in ID23 made by our collaborators shows some similar stripes in the direction 0.2**a***-**c***, that starts from the first vector of this phase, $\mathbf{q}_{21}$=1/2**a*** [115]. For this member, we performed a DS study just at this pressure point.

For the DAC cell of m=8, a stainless steel gasket was chosen and the cell was gas loaded at the pressure of 0.31 GPa. Different pressures were achieved: 0.3 GPa, 1.1 GPa and 2.8 GPa. The m=8 has a stable phase until 1.2 GPa, after a new structural phase is observed at 2.8 GPa. A step-by-step pressure study on the Bragg peak and satellites were made in decreasing ramp using the diffraction resolution of the IXS arm, *vide infra*. The new phase was found at 2.8 GPa, showing the doubling in the a parameter, as seen in Fig. 4.53. From our preliminary analysis, the vector of this phase is **q**=1/2**a*** and the cell has a monoclinic distortion. The new phase can be described with: a= 10.4315(18) Å, b= 6.467(3) Å, c=29.329(15) Å and $\beta \sim 90.6°$. This member, then, does not stabilise or enhance one of its CDW phases already found in the temperature study. The system prefers to go thought a new CDW transition. This new phase is similar to the one found in m=10 under pressure. Both have the cell doubling along **a***. More significantly, this vector is the one that characterised almost all the high-term members.

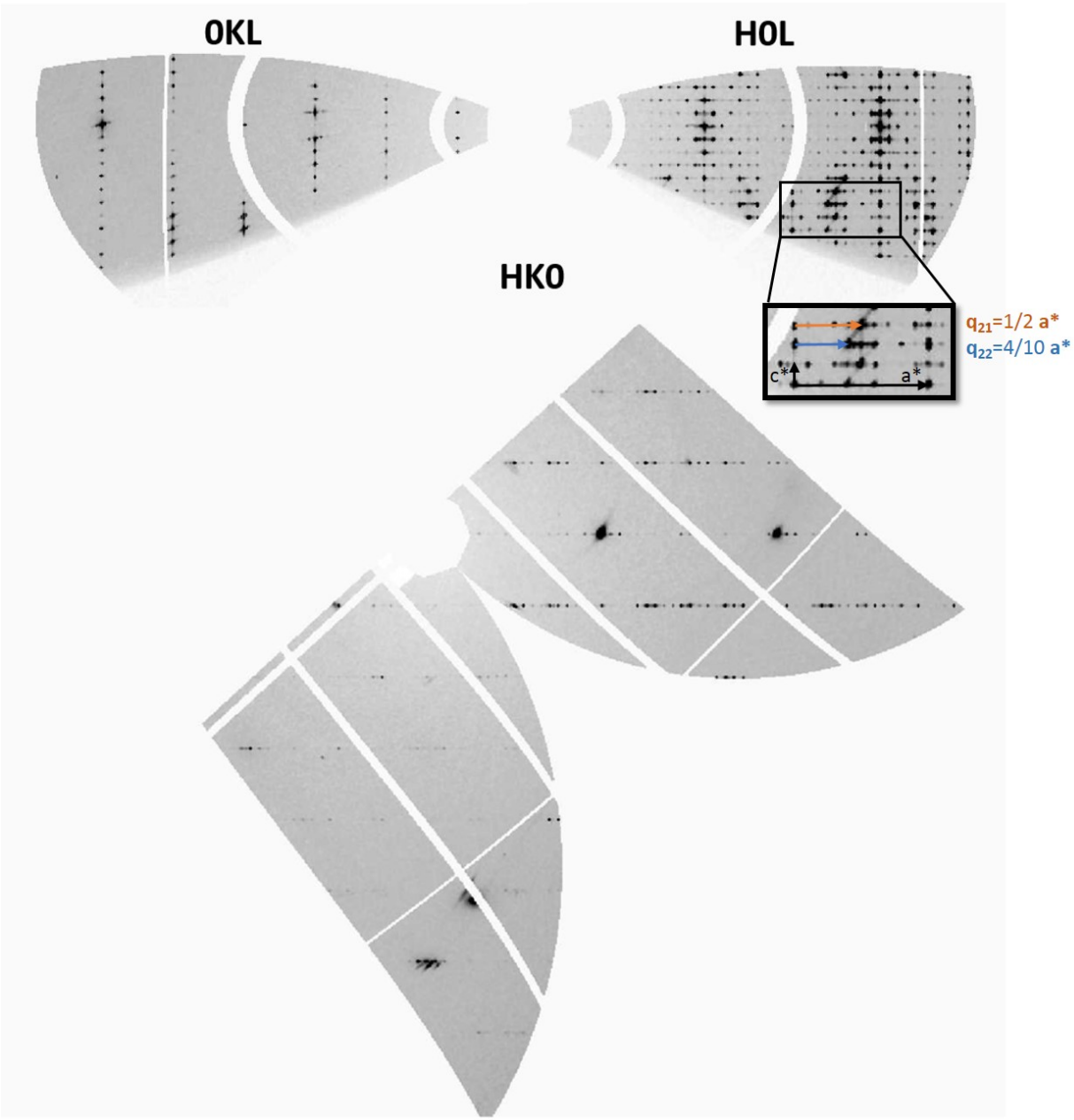

Figure 4.52.: The diffuse scattering maps of m=10 at 0.3 GPa. The system is in the second CDW phase, normally stable at lower temperatures. The blue and orange arrows show on the focused part of the H0L plane the two **q**-vectors of the phase: $\mathbf{q}_{21}=1/2\mathbf{a}^*$ and $\mathbf{q}_{21}=4/10\mathbf{a}^*$, respectively. Diffuse lines connect the two Bragg satellites.

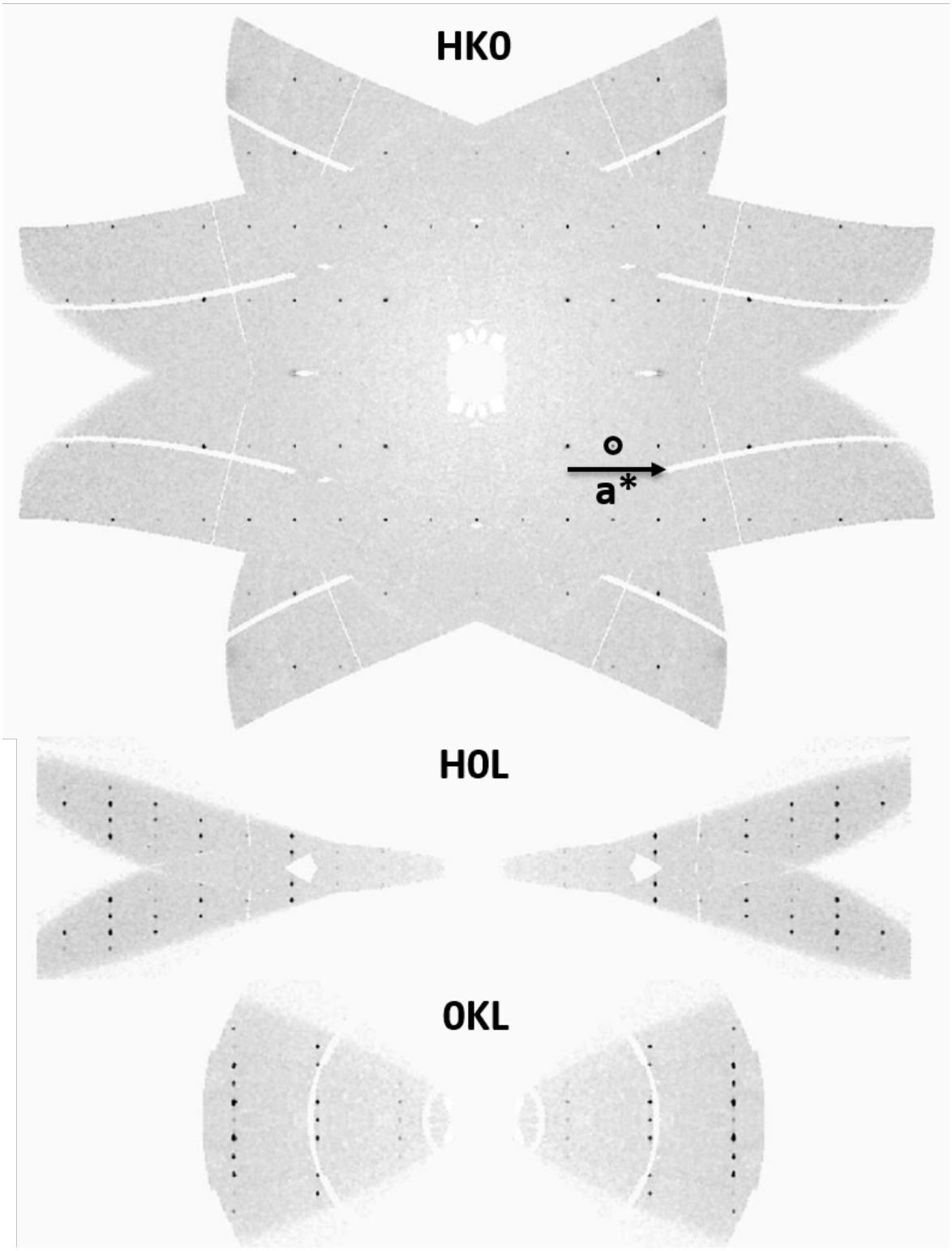

Figure 4.53.: The diffuse scattering maps of m=8 at 2.8 GPa. A new CDW phase is stabilised by pressure. A doubling of the a parameter is visible. Laue symmetry is applied to the RS reconstructions.

This is the first time that a study of this member is performed as a function of the applied pressure. For this reason, an accurate diffraction study was done on this new CDW phase, the refinement of the structure is in progress.

The high-resolution in the reciprocal space on the IXS branch permits, as already shown multiple time, to follow by pressure one specific Bragg peak. The transition was studied by increasing pressure on the (400) Bragg peak for 1.1, 2.67 and 2.8 GPa pressures, Fig. 4.54a. The splitting due to the monoclinic distortion is evident. In Fig. 4.54b, the satellite (3.5 0 0) was followed by decreasing the pressure. The satellite starts to be strongly modified by the pressure at 1.37 GPa and it completely disappears at 1.16 GPa. In addition, the monoclinic distortion starts to decrease before the transition to the high-symmetry phase. An example is the peak in violet at 1.65 GPa which does not show clearly the monoclinic distortion, however, the intensity of the CDW satellite is still strong. The transition pressure can be predicted $\sim$ 1.2 GPa.

4.6.2. Lattice dynamics of m=8 under pressure

This new phase adds a new parameter on the lattice dynamics study. Not only the directions presented earlier at ambient conditions, related to the classic CDW phase of this member, should be inspected, but also the direction where the new phase is present, i.e. **a***. The effect of the pressure on the phonon softening of bronzes has never been reported up to now.

Regarding the region of soft valley that is present at ambient condition, the direction along the diffuse pattern is taken also at different pressures, as seen in Fig. 4.55. Different kind of hardening are present under pressure. The first is along the phonon dispersion until |q|=0.5 Å relative to the dispersion at ambient conditions. The second is at satellite position of the 1st CDW phase. However, the predicted hardening of the entire valley is not present neither below or above the phase transition. The lattice dynamics is not visibly affected by the pressure, in this particular direction.

In order to study the dynamical response of the lattice in the new phase, the phonon energy at **q**=0.5**a*** is studied at two pressure configurations, below and above the transition. The phonon dispersion is shown in Fig. 4.56a, where the points derived from the fitting made on the IXS scans in Fig. 4.56c. The longitudinal phonon dispersion does not show any pressure dependency, especially at the **q** of the CDW satellite. The IXS scan on $\mathbf{q}_{CDW}$ at 2.8 GPa does not show any phonon contribution, just a slight increase on the elastic component. The acoustic phonon does not seem to be correlated to the new phase, however the transverse phonons should be also analysed.

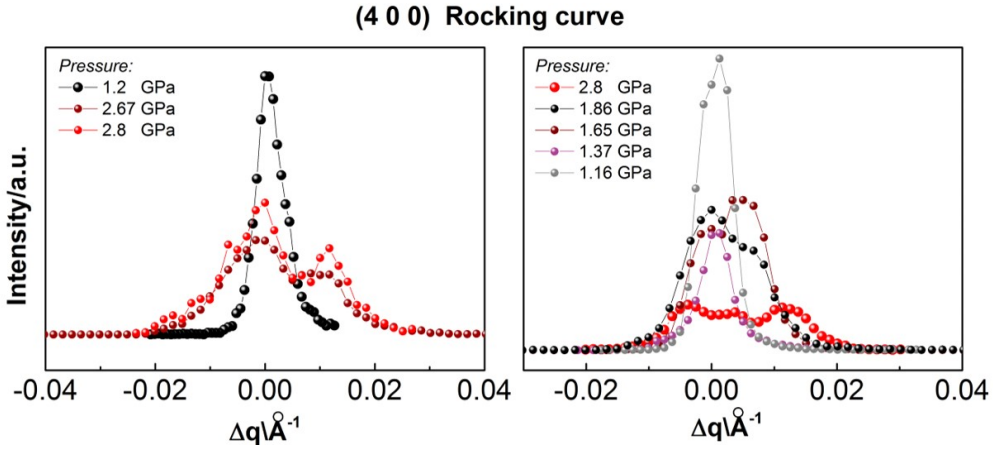

(a)

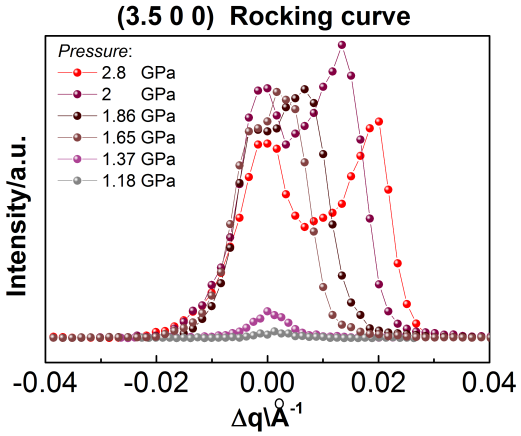

(b)

Figure 4.54.: (a) The pressure dependence of the (400) Bragg-peak rocking curve of m=8 when increasing P, on the left; on the right, the rocking curve of the same Bragg peak on decreasing pressure. (b) The rocking curve of the satellite, **Q**(3.5 0 0), decreasing pressure. The last two pressures, in yellow and brown dots at 1.37 GPa and 1.16 GPa, respectively, show the disappearance of the satellite peak and the transition to the high symmetry phase.

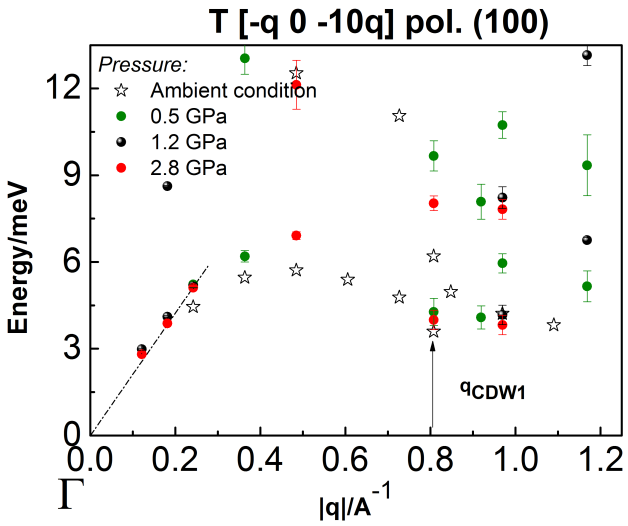

Figure 4.55.: The phonon dispersion along the diffuse, [-1 0 -10] direction, starting from the Bragg (400), as for the study at ambient condition for m=8 at different pressures. The pressures are above and below the transition. With the start symbol, the phonon dispersion at ambient conditions is reported to compare.

Pressure dependence of the phonon dispersion along [001] direction was studied only at some specific points. The pressure dependence on the anticrossing shows a softening on the lower phonon. This study in pressure on the lattice dynamics is obviously not sufficient, further analysis and measurements are necessary in order to confirm and expand our work.

To conclude, the results on m=10 confirm the analysis already obtained in Caen. Under pressure, the system passes to the 2^{nd} CDW phase. In m=8, a new CDW phase is present applying pressure at $\sim$ 1.2 GPa and the transition is found reversible. This new phase seems not to be related to any of the CDW phases stabilised by temperature. It has a monoclinic distortion and a CDW vector corresponding to $\mathbf{q}$=1/2$\mathbf{a^*}$. The IXS study along $\mathbf{a^*}$ shows that the lattice dynamics are probably not linked to the phase transition. The dispersion along the diffuse plane, characteristic of the high-symmetry phase, shows a hardening in the first part of the dispersion. Whereas, the soft valley does not harden and it is still present in the high pressure phase (2.8 GPa).

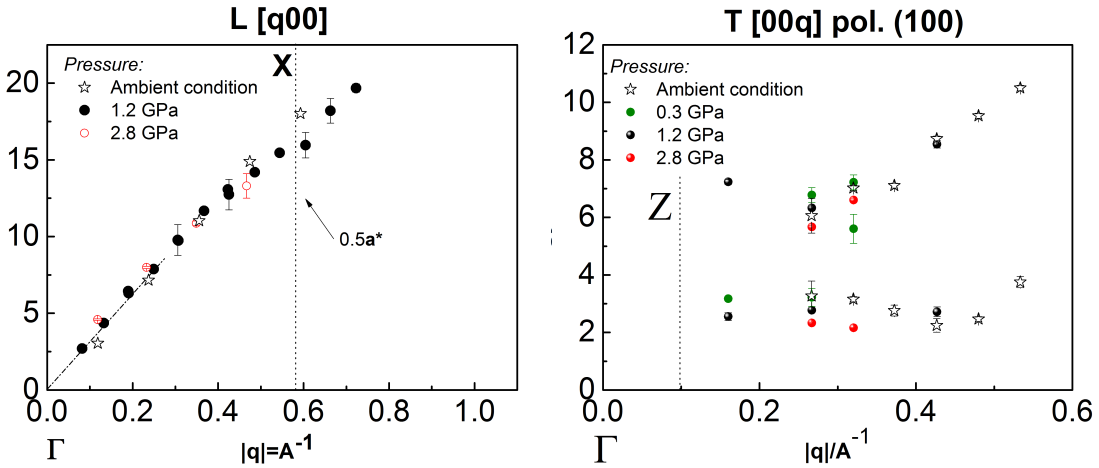

(a) (b)

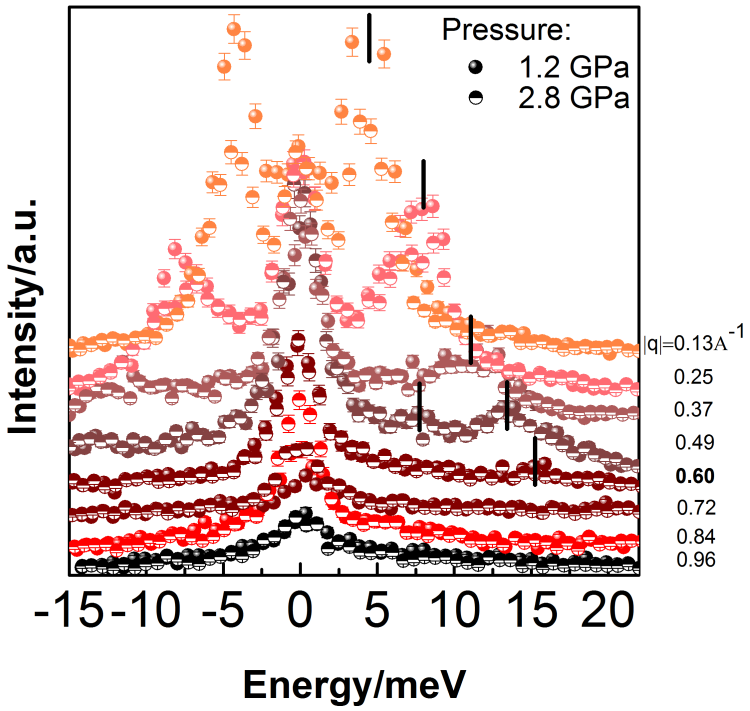

(c)

Figure 4.56.: (a) The longitudinal acoustic-like phonon dispersion along [100] direction; (b) The phonon dispersion along [001] direction. In all the directions, the dispersion recorded at ambient condition is shown (star symbol). (c) The IXS scans are shown for the direction [100] at 1.2 and 2.8 GPa. The vertical black line is an help for the eyes in order to see the phonon energy obtained from the fitting.

4.7. Structural transformation

An analysis on the structural phase transitions and the related instabilities through the family members could help in order to understand the origin behind the differences found in the lattice dynamics. The CDW phases were refined in details by Elen Duverger-Nedellec [115].

The degenerate case of the member m=2 presents a classical example of Peierls instability. It has a quasi-1D-electronic system, where a W-double chain is isolated by phosphate-groups and the lattice dynamics shows a continuous softening in $\mathbf{q}_{CDW}$, until the phonon freezing at T_{CDW}. Those chains are related to the electronic instability at lower temperature. Two analysis can help us to understand the CDW phase of this member. Firstly, the molecular dynamics simulation shows a rigid-body motion of the octahedra where the bigger libration was referred to the yaw angle (see Sec. 4.4.2 for more information). The correlation between W-octahedra neighbours corresponds to the CDW **q**-vector along the **b*** direction. The second analysis is based on the refinement of the structure in the CDW phase and the transformation that occurs from the high-symmetry phase. In this case, every atom is rearranged in the transformation, however, the bigger displacement is related to the oxygen atoms. The oxygen atoms can displace up to 0.444(1) Å, whereas the tungsten and phosphorus atoms just 0.095(1) Å and 0.1101(1) Å, respectively. On the overall structure, the distortion can be seen as a tilting of the octahedra and tetrahedra [115]. In Fig. 4.57 the reconstruction of the CDW structure is shown. The figure also shows clearly that not all the oxygen atoms move with the same amplitude. In fact, the oxygen atoms bonding with the phosphate groups have more freedom of movement. Whereas the oxygen shared between two octahedra are less displaced and it follows a different direction, [011], perpendicular in respect of the oxygen shared between a octahedron and a tetrahedron.

For m>2 the W-block starts to appear, the system passes to a quasi-2D-electronic structure. In addition to the octahedra rotations and the displacement of the oxygen, the tungsten moves relative to the centre of the octahedron. The kind of distortion is the same for the two members (m=6 and 8), however, the magnitude differs significantly. In the low-term member, the maximum displacement of the tungsten atoms is 0.04 Å. The general displacements for m=6 are shown in Fig. 4.58. For the high-term member, the displacement is one order of magnitude bigger. In fact, the tungsten atoms can move until 0.4 Å, Fig. 4.59.

In order to understand the connection between the structural transformation and the instability revealed by the diffuse scattering, the displacement of the tungsten atoms is analysed for m=8. The choice of the high-term member derives from the huge displacement of the W-atoms and their easier visualisation. In Fig. 4.59

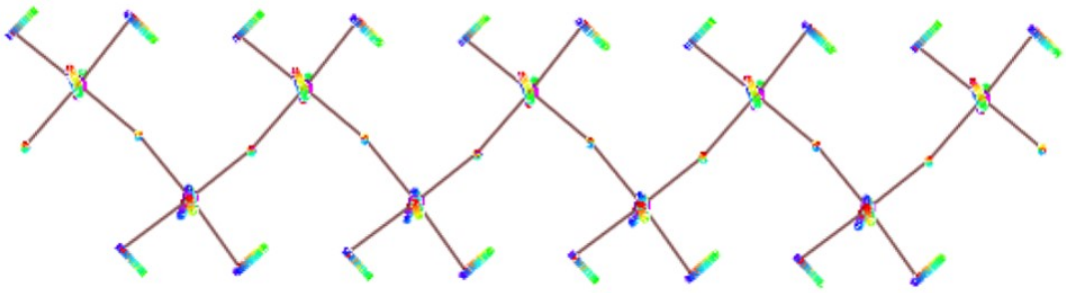

Figure 4.57.: The CDW structure of m=2 along [011] direction, in which the zig-zag chain of W-octahedra is visible. In green the phosphate, in red the oxygen and the tungsten in violet. The displacement of the atoms are represented by the Lissajous curves and they are two times the real one. The rainbow colour represents the displacements of the atoms related to the same region of the crystal. This figure is taken from the thesis of Duverger-Nedellec [115].

the refinement of the 1st CDW structure reveals that the displacements are clearly along the 4-fold axis of octahedra and more specifically, along the "long" W-O-W-O chain. Thus, the CDW phase with its structural phase transition is linked to the framework instability found in the high-symmetry phase. Furthermore, thanks to this analysis, it is possible to explain the reason for the stronger intensities for the diffuse planes related to the long chains.

A synoptic table of the different distortions due to the structural transformation demonstrates the changing due to m, Tab. 4.7. From a double chain to a W-block with m thickness, the distortion on the structure passes from a rigid-body tilting to a displacement of the central atom of the octahedron.

4.8. Conclusion

A summary of the obtained results for each member can help trace a general behaviour of the family and the evolution of the properties as a function of m.

The degenerate case m=2 with zig-zag octahedral chains exhibits quasi-1D-electronic behaviour. A new CDW phase with T_{CDW} is found at $\sim$ 270 K, the q-vector is at 0.25 **b***. A soft phonon mechanism was revealed by the combination of DS and IXS studies, with a classical Peierls distortion and the freezing of the phonon at the transition in $\mathbf{q}_{CDW}$. MD simulation provides the distortion pattern which is correlated to the libration angle of the octahedron (100) axis (magnitude of $\pm 12°$).

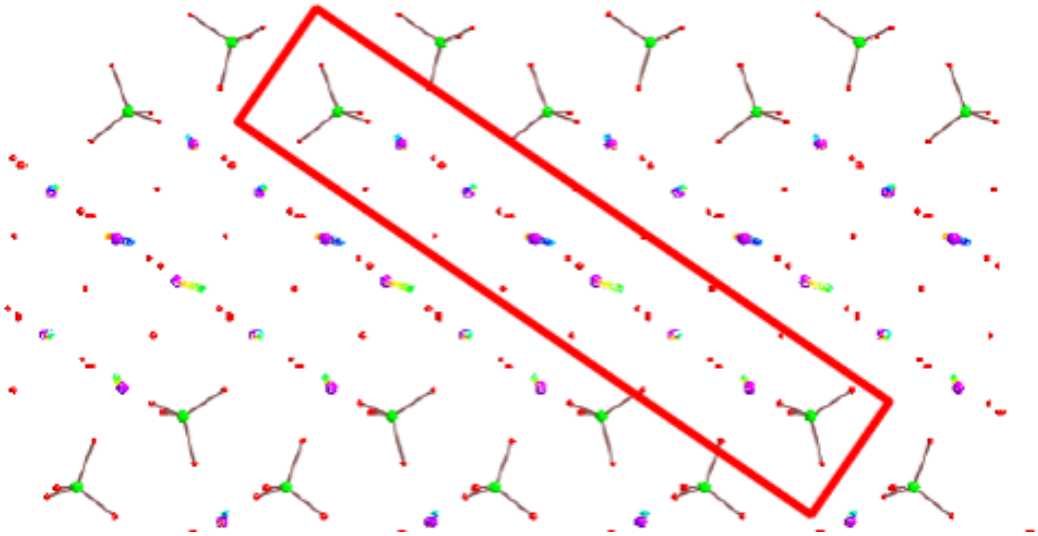

Figure 4.58.: The first CDW phase of the $MPTB_p$ member m=6 with the modulation of the W position 25 times bigger to show better the direction. The same representation of the modulation as shown in Fig. 4.57 is used with the Lissajous curves. This figure is taken from the thesis of Duverger-Nedellec [115].

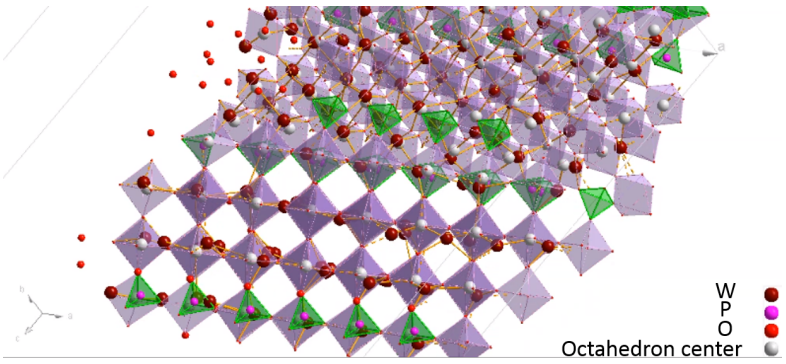

Figure 4.59.: The first CDW phase of m=8 with the modulation of the W position 5 times bigger to show better the direction. The tungsten atoms are displaced along one of the "long" W-O-W-O chain. The W atoms are in purple, whereas the centre of the octahedron is denoted by grey sphere. In addition, also a tilting of the octahedra is present.

m	**Instability in high symmetry phase**	**Structural change**
2	rigid-body motions	Tilting of octahedra/tetrahedra (max 0.4 Å)
		Displacement of W & P (max ∼0.1 Å)
6	W-O-W-O chains	Displacement of W (max 0.04 Å)
8	W-O-W-O chains	Displacement of W (max 0.4 Å)

Table 4.7.: The structural distortions happening in the structure at the CDW phase for m=2, 6 and 8.

This axis libration shows a space-time dependence along **b*** direction with a phase change related to the CDW modulation. For this member, the rigid body analysis is sufficient to describe the instabilities.

For the W-block members (m=6,7,8), the DS shows diffuse planes due to the framework instability of the empty-perovskite W-block. There are two families of planes, corresponding to the long and short W-O-W-O chains, the first more intense than the second. The planes of the same family have an intensity dependence which is not proportional by **Q**. This is due to the fact that the W-O-W-O chains have an intra- and inter-correlation.

Upon cooling, the difference between low- and high-term members start to be revealed. In m=6, the structure of the diffuse plane is lost and a fine structure is visible, which is also related to the nesting vectors and the condensation to the satellites. In m=8, no intermediate phase is visible, the diffuse planes are visible just above the T_{CDW} and, on those, the CDW satellites condense at the CDW transition. An hypothesis can be that the distortion and the framework instability are particularly intense for this member that the fine structure is covered by the intense diffuse planes. Another hypothesis can be that the Fermi surface for m=8 cannot be seen for a more complicated pattern with respect to m=6. At the CDW transition, the rearrangement of the structure is referred to a small displacement of the tungsten atoms for the low-term member (∼ 0.04 Å) and a significant rearrangement of the tungsten atoms along the long W-O-W-O chains direction (∼ 0.4 Å) for the high-term member. Probably, the W-atoms can move more freely in this direction that in the short W-chain one, explaining the difference in intensity between the two families of diffuse planes. A scheme of the diffuse patterns/CDW phases is reported in Fig. 4.60, showing more easily the differences

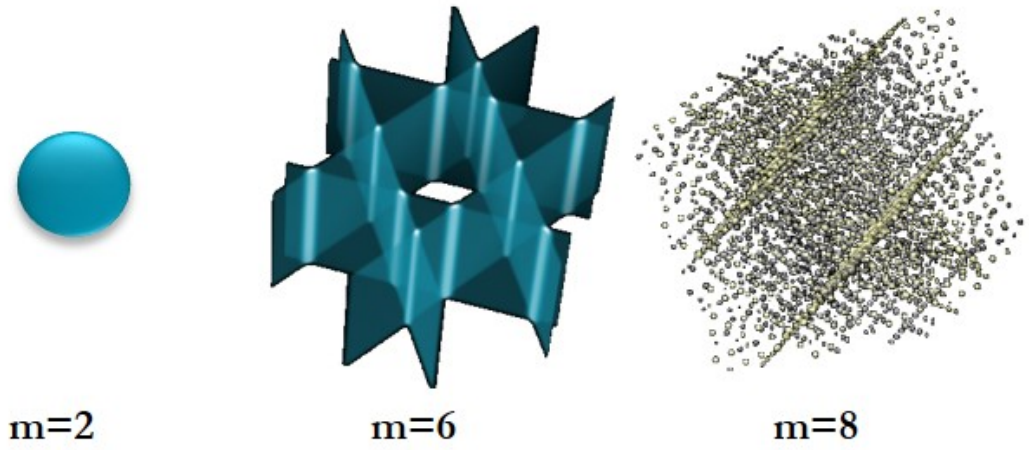

Figure 4.60.: Schemes of diffuse patterns and CDW phases for the different members. From the left, the isotropic spherical distribution of the diffuse pattern for m=2. On the center, the diffuse pattern of m=6 follows a linear features, where the condensation is at the crossing of the planes. On the right, the diffuse planes found in the high-symmetry phase of m=8 condense directly on a complex pattern of Bragg satellites, shown in the figure.

for the three members.

The lattice dynamics have similar response for the members m=6 and 8. In fact, both members present a valley of soft phonons around the $\mathbf{q}_{CDW}$ with a minimum on it. A temperature dependence is evident for m=6, whereas for m=8, no change in energy is found as a function of temperature/pressure.

A new CDW phase is discovered applying pressure on m=8. The reversible transition is around 1.2 GPa, passing from orthorhombic to monoclinic with a $\mathbf{q}$= 0.5 **a***. From the IXS results, the lattice dynamics seem not linked to the transition.

5. Antimony lattice dynamics under pressure

Rhombohedral antimony is a good example in order to illustrate the lattice instability on the base of simple geometric arguments. The rhombohedral structure (A7), common to almost all of the group Va elements, comes from small distortions with respect to a simple cube. An analysis of the pressure dependence of the structure shows that an evolution of the distortion takes place. Two different transitions from A7 are possible and they happen alternatively in Va elements: A7 to PC (primitive cubic), in which the system distortion is relaxed, or A7 to BCC (Body centred cubic), where the rhombohedral distortion is reduced but the PC structure is never reached. Antimony falls into the second category and, in this chapter, we will analyse the importance of the A7 framework instability and the lattice dynamics response to the two different transition mechanisms. The experimental approach consists of a combination of DS and IXS. The results are compared with two theoretical models: a symmetry-based phenomenological model of the phase transitions, which calculates and analyses the critical vectors related to each transition; as well as, a Density Functional Theory (DFT) based approach, which leads to a better understanding of the phonon behaviour.

5.1. Scientific background

The electronic structure and lattice dynamics model of the group Va elements have been disputed for a long time, due to their challenging structure and, in some cases, their semimetallic behaviour. The semimetals: Sb, Bi, Ar and black phosphorus (with a tunable electronic gap) are of great interest because of their electronic and optical properties, as well as possible applications [185–196].

The group Va elements, with the only exception of nitrogen, crystallise in a rhombohedral A7 structure, due to a distortion of the simple cubic structure. The distortion leads to twice as many atoms in the primitive cell, as one would expect otherwise [197]. Such effect arises due to the paired layers in the structure and it is induced by a gain in the electron energy with a connected gap opening

[198]. Hence the rhombohedral distortion causes a Jahn-Teller type of symmetry breaking which induces a metallic-semimetallic transformation, often referred to as Peierls transition [199, 200].

The electronic configuration of the group Va elements can be described in a simplified way. The general configuration has five electrons in the outermost shell, which are distributed two in the s orbitals and three unpair in p orbitals, with the anti-bonding p states empty. Both the s- and p-shells are tightly bound and there is only a small amount of s-p overlap. The bonds are in a octahedral coordination with the nearest-neighbour angle distorted away from 90°. Thus the simple cubic or its similar structures and the semimetallic phase are favoured [199, 201–203]. Despite the semimetal nature of antimony (which would not allow for the formation of true covalent bonds [201]), the very low carrier concentration leads to an electronic localization, which is similar to bond charges.

The pressure decreases the Peierls distortion and the metallic state is restored at the transition, as shown in an early X-ray diffraction experiment [204], in agreement with *ab initio* total energy calculations [198, 205]. It is also well described by Haussermann *et al.*, who calculated the DOS and showed that the electronic states are filled at the Fermi level [206]. In addition, an increase in the electron-phonon coupling and a change in the bonding properties are expected under pressure. Under such conditions, the s-p bands overlap increases, together with the bandwidths and number of nearest neighbours. As a result, the system attempts to achieve the PC structure, but it never reaches stability in Sb. The Peierls distortion and its energy gaining effect leads to a choice of a less symmetric structure at ambient temperature and pressure conditions. This leads to a diversification of the behaviour of those elements, relative to the general behaviour of pressure-induced phase transitions, on which the high symmetry structure is stabilized at lower pressure [207–209]. One must consider the Landau theory of structural phase transitions, where the high symmetry phase is called "parent" phase.

5.1.1. The crystal structure of antimony

The A7 structure [210] is derived from the simple NaCl structure, as a result of two consecutive distortions. As a first step, there is a stretching of the body diagonal, followed by a reduction of the rhombohedral angle α, as shown in Fig. 5.1a. The diagonal preserves the 3-fold symmetry and it converts in a trigonal axis. The two distortions are described through:

- the internal displacement, μ; $\tau = \mu\mathbf{d}$, where $\mu \leq \frac{1}{4}$, 2τ is the vector that separates the two interpenetrating lattices and $\mathbf{d}$ is the body diagonal. The

primitive cubic (PC) structure corresponds to $\mu = \frac{1}{4}$, while the diamond structure to $\mu = \frac{1}{8}$;

- the rhombohedral angle α which determines the stretching (60° corresponds to the PC structure).

The hexagonal description is also add, since it may be more convenient for some description. Later in the discussion, the hexagonal or the trigonal setting is used, depending on the convenience. We also use the pseudo-cubic structure (PC) derived from A7, as an "approximant" of the Peierls structure. The three structures are shown in Fig. 5.1 and their parameters are written in the Tab. 5.1. [1]

To avoid any misunderstanding, we choose the 'obverse' setting, as used in other papers, for the real lattice conversion, R_3, hexagonal-rhombohedral [213]:

$$\begin{cases} \boldsymbol{a}_H = \boldsymbol{c}_R - \boldsymbol{b}_R \\ \boldsymbol{b}_H = \boldsymbol{a}_R - \boldsymbol{b}_R \\ \boldsymbol{c}_H = \boldsymbol{a}_R + \boldsymbol{b}_R + \boldsymbol{c}_R \end{cases} \qquad \begin{cases} a_H = 2a_R \sin \frac{\alpha_R}{2} \\ c_H = \sqrt{3} a_R \sqrt{1 + 2\cos \alpha_R} \end{cases}$$

where the notation $\mathbf{a}_H$, $\mathbf{b}_H$, $\mathbf{c}_H$ is referred to the hexagonal basis vectors in the real lattice and $\mathbf{a}_R$, $\mathbf{b}_R$, $\mathbf{c}_R$ is referred to the rhombohedral basis vectors. We use bold face for the vectors and the normal face to refer to the norm of the vectors.

The conversion between hexagonal and rhombohedral settings in the reciprocal space is given by:

$$\begin{pmatrix} H \\ K \\ L \end{pmatrix}_H = \begin{pmatrix} 1 & \bar{1} & 0 \\ 0 & 1 & \bar{1} \\ 1 & 1 & 1 \end{pmatrix} \begin{pmatrix} h \\ k \\ l \end{pmatrix}_R$$

High pressure transitions

The phase diagram of antimony remained misunderstood for a long time. The first works on the system used a linear extrapolation of the rhombohedral angle, α(P), to study the phase transition [215, 216]. As the deviation, relative to the PC structure, is reduced when the pressure increases [215, 217], the system was assumed to go towards the PC structure at ∼8 GPa [215]. It was described as a “sluggish” transition because it was observed only in 6 cases out of 30 [218], raising skepticism on the actual high pressure structure [218, 219]. The following

[1] Note that the unfolded simple cubic structure reported in the literature (for example in references [211, 212]) is not the one we describe as the pseudo-cubic structure, shown in Fig. 5.1

Hexagonal	Lattice constant	a (Å)	4.3084
		c (Å)	11.2741
Rhombohedral	Lattice constant	a (Å)	4.5067
	Rhombohedral angle	α	57°11’
	Internal displacement parameter	μ	0.2336
Pseudo-cubic	Lattice constant	a (Å)	3.1962

Table 5.1.: Crystal structure parameters of Sb in each setting, from Ref. [214]: hexagonal, rhombohedral and pseudo-cubic; for the latter, our chosen system.

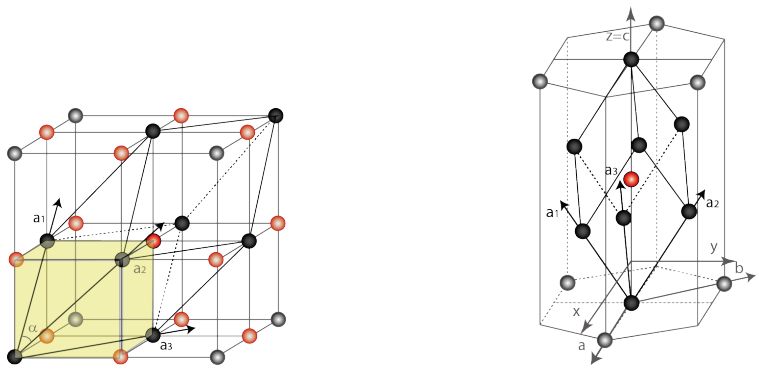

(a) (b)

Figure 5.1.: Figure (a) shows the A7 structure within the NaCl one, before the two distortions. The rhombohedral angle, α, and the lattice vectors, a_1, a_2 and a_3, of the A7 structure are indicated. With no distortions, α is equal to 60°. The faces of the pseudo-cubic structure are highlighted in yellow; Figure (b) shows the crystal structure of Sb, where the rhombohedral A7, with a_1, a_2 and a_3 vectores and the hexagonal structures, a, b and c vectors, are visible. The atoms from the second sublattices are not shown, except within the unit cell.

high-pressure phases were proposed as monoclinic, derived from an orthorhombic SnS-type structure, hexagonal close-packed with or without distortion, tetragonal based structure, etc. [215, 220, 221].

Major technical improvements in high pressure diffraction experiments, as well as the introduction of the incommensurate host-guest structures happened in the

late 90s [222–224], allowed to unpuzzle the Sb phase diagram. The high pressure structures are composed by a host and an interpenetrating guest, which is incommensurate to the former along one axis. These complex host-guest structures are not uniquely observed in Sb under pressure but also in almost all the rest of the Va elements. A summary of the high-pressure phases for group Va elements is shown in Fig. 5.2. A common trend is visible, the A7 structure eventually transforms under pressure to a BCC structure, the highest pressure structure for all Va elements, excluding molecular nitrogen. In order to reach the structure above some Va elements, such as black phosphorus and arsenic, go through the PC structure [225–228], while antimony is in an intermediate situation. Namely, in the absence of the PC structure transition the system is obliged to decompose the PC-to-BCC mechanism into two successive, monoclinic and tetragonal, host-guest structures. All the complex high-pressure phases of Va members can be described as host-guest structures, with the exception of the PIV phase, which is an incommensurate modulated structure [229].

Under pressure, the A7 structure transforms itself into a host-guest structure, SbIV, which is observed in a narrow interval of pressure 8-10 GPa, where host and guest are both body-centred monoclinic [230]. It can be described as I'2/c($q_1 0 q_3$), where q_1=0.1662 and q_3=1.33047. On further pressure increasing, the SbII phase is stabilized, which is a tetragonal structure fully determined in 2003 by Schwarz et *al*. [231]. In this work, the structure was found as an incommensurate phase, where both host and guest are body-centred tetragonals (BCT) and the latter incommensurate with the former along the tetragonal *c*-axis [231, 232]. The distortion SbIV-SbII is very small, with only a small deviation ($\sim$0.5°) of β_H from 90°. However, the transition is clearly evident from the unsplitting of the peaks, through diffraction, passing from monoclinic to tetragonal [230]. Finally at $\sim$28 GPa , a first-order phase transition takes place towards the BCC structure (SbIII), which is stable up to at least 43 GPa [233].

The A7 to BCC transition through incommensurate host-guest structures is found more energetically favourable than the transition to PC, which settles the controversy on PC and BCC for antimony [234]. In Fig. 5.3, the work of Schwarz *et al.* shows the gaining in energy thanks to the Peierls distortion at ambient conditions. When the volume decreases, the energy difference between PC and A7 structures shortens and becomes really small near the first transition. However the incommensurate phase Sb-II has a lower energy and therefore it becomes the successive phase and convenient path. Also in this case, we can describe the energy of the system with a simplified model. The total energy of the system has two components: I) the E^{band}, which is the sum over the occupied one-electron states; II) the electrostatic energy, $E^{Madelung}$, which is responsible for the repulsion of the charged ions. E^{band} favours the open-packed structure, in which the

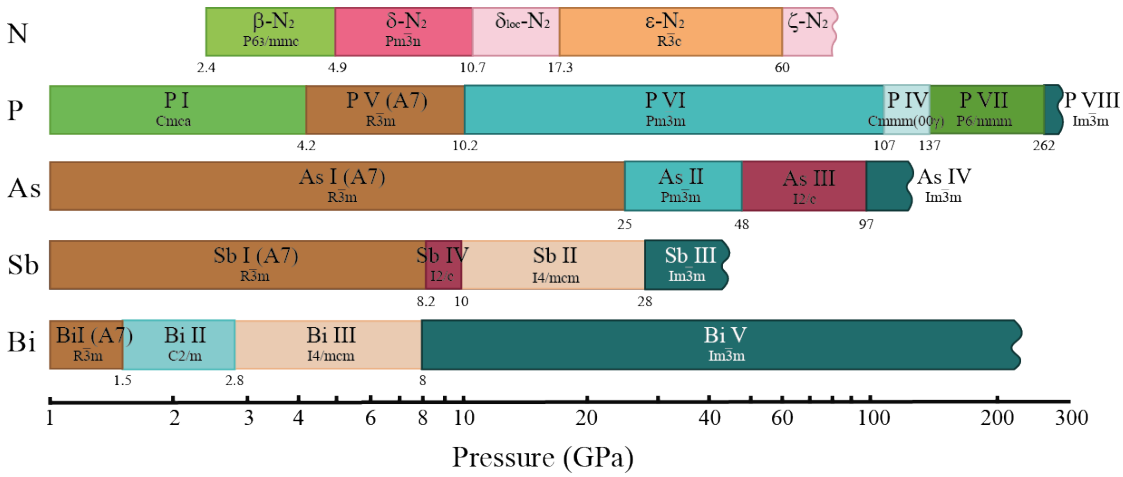

Figure 5.2.: High pressure phases in group Va elements.

atoms are closer to each other and where covalent bonding is prevalent. Thus, in our particular case, the A7 structure prevails. On the other hand, $E^{Madelung}$ is an opposite contribution with the tendency to stabilise the high-symmetry densely packed structure. BCC is the structure with the highest Madelung constant [235]. As the pressure increases, the contribution of E^{band} diminishes and $E^{Madelung}$ starts to increase. The incommensurate phase structure is a result of the interplay between such effects [206]. At a later stage, we will follow up on an explanation from the point of view of the symmetry-based phenomenological phase transition of A7-Incommensurates-BCC path, Sec. 5.2.1.

5.1.2. State of art in the lattice dynamics

The study of the lattice dynamics becomes a supplementary tool to the more direct diffraction studies in the understanding of the phase transitions. For further information, please consult published reviews [236–238].

In earlier studies, the lattice dynamics of A7 antimony were reported at ambient conditions through triple axis spectrometer INS (inelastic neutron scattering) [239, 240]. The measured directions in the reciprocal space are shown in Fig. 5.4. In the same figure are also included the lattice dynamics of bismuth, hich is one of the most similar elements in the Va group. They reveal an identical behaviour: an initial rapid rise in the lower energy frequency until the middle of the BZ, which is followed by almost flat branches until the border of the BZ. Sharp *et al.* reported that the lattice dynamics of the semimetals are governed by: I) the symmetry of the structure; II) the pseudo-covalent bonding; III) the low carriers

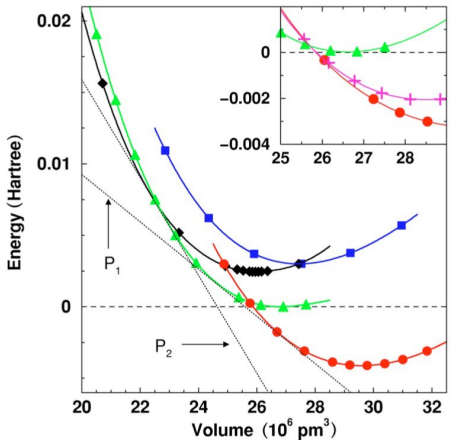

Figure 5.3.: Total energy calculations versus volume of the principal structures under investigations calculated by Schwarz et *al.* (the Sb-IV was not yet discovered). The energies are marked as circles, A7; crosses, PC; triangles, tetragonal approximant of SbII; diamonds, BCC; squares, tetragonal primitive. The dotted line corresponds to the zero energy, chosen as the energy minimum of the tetragonal approximant. Reprinted with permission from *U. Schwarz, l. Akselrud, H. Rosner, A. Ormeci. Yu. Grin and M. Hanfland, PRB* ***67*** *214101 (2003).* Copyright 2018 by the American Physical Society.

density. The Born-von Karman model calculations, where the general tensor forces were extended to the ninth-nearest neighbours, was not sufficient to reproduce the optical phonon dispersions. *Ab initio* calculations are needed to finally converge the theoretical results with the experimental one [241].

The high-pressure lattice dynamics at k=0 was studied through Raman and Brillouin scattering [211, 212, 243–245]. The rhombohedral phase has three modes, of A_{1g} and a degenerate E_g symmetries. Under pressure, they show a continuous softening ($\backsim$ 20%) over the full range of SbI up to the first transition [211, 212]. Afterwards, the phonon modes of the high-pressure phase have a hardening trend, Fig. 5.5a. The same behavior appears in arsenic and bismuth [244, 245]. The softening in the A7 phase was linked to the pressure-induced reduction of the Peierls-like distortion [198, 211]. In fact, these two modes originate from the folding of the simple cubic Brillouin zone. The triply degenerate phonon mode at R_5^+ (R=π/a(1,1,1)) of the simple cubic is folded in the observed modes.

In addition, a giant increase was observed in the Raman linewidths that was related to anharmonic decay channels and higher order terms [198, 212, 241, 244]. Finally, asymmetric Raman peaks were observed and explained as a result of phonon-phonon interaction or coupling between phonon and interband electronic transitions [246].

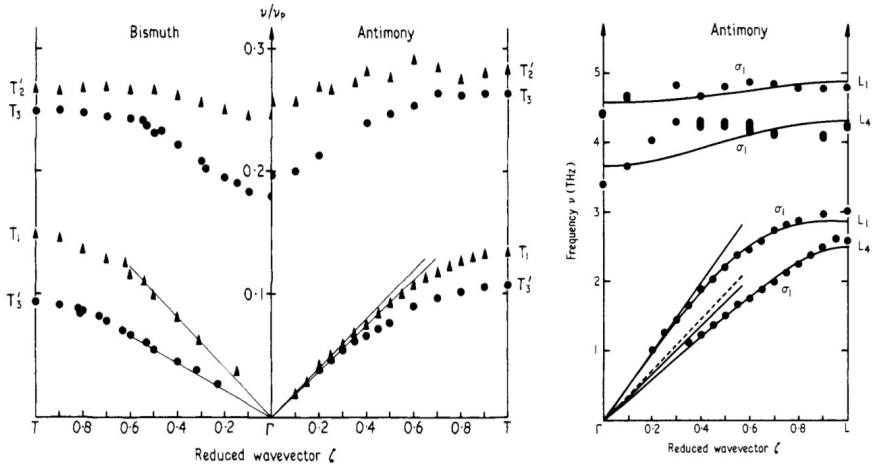

Figure 5.4.: The phonon dispersion of antimony and bismuth at ambient condition measured by INS. On the right the <111> directions. Bismuth and antimony show a similar behaviour. On the right, the <100> direction. The smooth curves are given by the result of the ninth nearest neighbour Born-von Karman. Bismuth data are taken from Ref. [242]. Reprinted with permission from *R. I. Sharp and E. Warming, J. Phys. F: Metal Phys.* ***1*** *570-587 (1971).* Copyright 2018 by the IOP science.

We should include in the discussion the Raman response of those elements facing a direct A7-PC transition, such as arsenic shown in Fig. 5.5b. In this case, near the transition, the Raman intensity decreases and the modes of the A7 structure disappear with a softening of $\sim$ 18 % for A_{1g} and a stronger softening of $E_g \sim 30$ %. Above the transition a single phonon peak is observed, in agreement with the biatomic-monoatomic transition [227, 247].

5.2. Reconstructive phase transition method, *ab initio* calculation and experimental results

The experimental survey and the analysis through the calculations and the reconstructive phase transition method is necessary to understand the contribution of the lattice dynamics in the reduction of the Peierls-like distortion and in the ultimate stabilisation of the BCC structure. In this section, all the steps for the analysis will be shown. In particular, we will focus on the A7 to PC and A7 to BCC phase transitions.

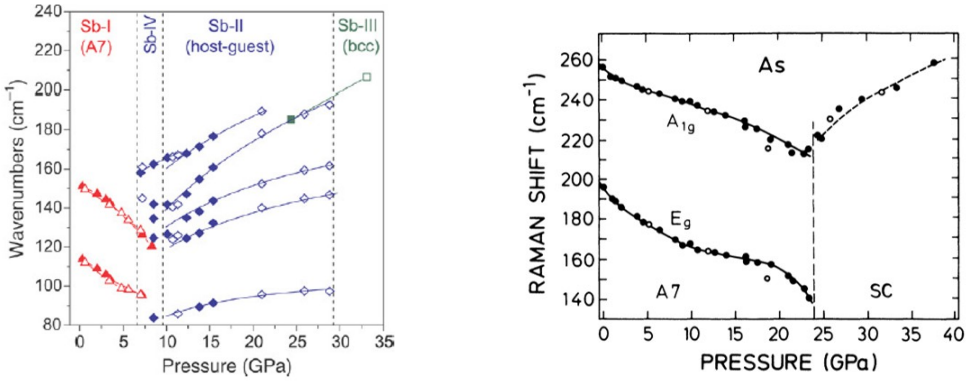

(a) (b)

Figure 5.5.: a) Raman-frequencies pressure dependence of Sb (a) and Ar (b), showing the A7-host-guest and A7-PC transitions, respectively. Vertical dashed line denotes the phase transitions. Reprinted with permission from *O. Degtyareva, V. V. Struzhkin, R. J. Hemley, Solid State Commun.* ***141*** *164-167, 2007* and *H. J. Beister, K. Strössner and K. Syassen, Phys. Rev. B* ***41*** *(9), 5535-5543, 1990.* Copyright 2018 by the IOP science and Elsevier.

5.2.1. Reconstructive phase transition method

Until 20 years ago, the phase transitions analysed with the Landau theory were mainly second-order transitions where a group-subgroup relationship between the two phases occurred. If this relationship did not exist, the phase transition was considered an uninteresting case, since an order-parameter for the transformation should be forbidden. The possibility to add the cases considered "forbidden" were done by Dmitriev *et al.* [248, 249]. Successivelly, Tolédano and Dmitriev published a book were they reported a classification of the different cases and a method to describe the leftover transitions [250]. We will briefly introduce the method, concentrating in the cases that are important for our discussion.

The Landau theory does not establish any transition. Instead, it starts from the experimental evidence and with it, it explains the nature of the microscopic characteristics of the transition. As a result, the Landau theory is a phenomenological theory. It is based on two concepts: the order-parameter and the transition free-energy. The free energy can be expanded as a Taylor series of ν, the order parameter. The second order phase transitions has an order parameter, which grows continuously from zero at the phase transition. In this case, the series is dominated by the first terms. The order parameter is the ionic displacement, $\nu_0=(\nu_x^0,\nu_y^0,\nu_z^0)$, since it varies considering temperature or pressure. Where the group-subgroup

relationship exists, a parent phase can be chosen (the most symmetric one) and here the order parameter is considered zero ν_0=0, as it would be in an equilibrium position. For this kind of transition, a phenomenological Landau theory has been elaborated [251, 252].

The analysis of the first-order phase transitions is more complicated. There are two classes where a modification of the crystal's atomic configuration happened. The first class maintains a sort of group-subgroup relationship. The two phases are associated with different subgroup to a common parent structure, from which they can be inferred through slight distortions. At the transition, the chemical bonds are broken and the displacements are of the order of 0.01-0.1 Å. In this case, the change happens both in length and in orientation. The second class is called "reconstructive" and it involves bond breaking with a drastic change of the initial structural. There is a breaking of the group-subgroup relationships, considering the two phases present completely different symmetry elements. Since the Landau theory is based on symmetry considerations, it was believed that a unifying theoretical scheme was impossible to formulate without a connection between the structures. In this case, the structures should be considered as a composition of specific configuration of sites. Deforming continuously the initial sites, one could transform a symmetry element into another. Therefore, the deformation can be described in symmetric functions and the group-subgroup relationship is not necessary [250].

The phase transition mechanisms in Va elements has already been largely explained by Katzke *et al.* [234]. We will reformulate and add to the discussion the information necessary to understand the connection between phase transition and lattice dynamics [2]. We present the mechanism of displacements in the *direct* space and we integrate to a *reciprocal* space vision, essential to understand its dynamics. In the discussion, the Peierls-distorted structure A7, R$\bar{3}$m(Z_I^P=2), is replaced with a pseudo-simple-cubic structure [(pseudo)SbI, Pm$\bar{3}$m(Z_{pI}=1)], Fig. 5.1a of the *direct* space and Fig. 5.6a of the *reciprocal* space. The latter is the structure reached by pressure by arsenic and phosphorus. The parent structure, in this phenomenological reconstruction, is chosen as the high-pressure BCC [SbIII, space group Im$\bar{3}$m(Z_{III}^P=1), A2 structure type].

In our specific case, the transformations that affect antimony are of reconstructive type with a displacive atomic mechanism. In the displacive reconstructive phase transition, the transition mechanism is described by the order-parameter and it corresponds to a deformation of the structure, described as atomic displacements. In the discussion we will consider the trio of phases " (pseudo)A7 - (SbIV - SbII)

[2]The mechanism analysis for antimony under pressure was possible thanks to the collaboration with Prof. Vladimir Dmitriev.

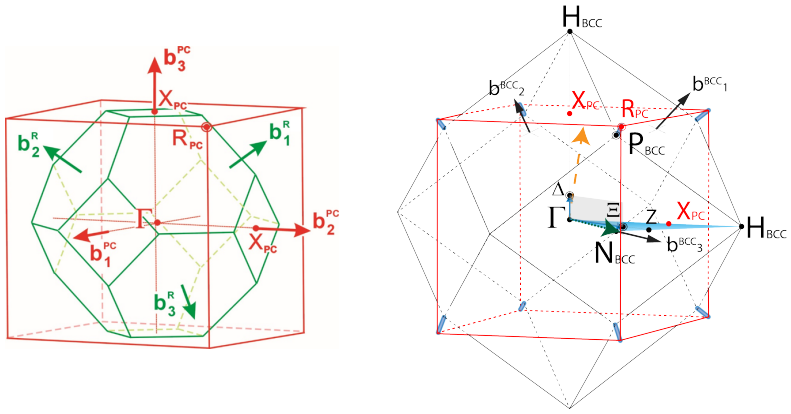

(a) (b)

Figure 5.6.: In Figure (a), it can be seen the exemplification of the distorted A7 rhombohedral structure (R) Brillouin zone (green lines and symbols) to the cubic (pseudo-PC) one (red lines and symbols); In Figure (b), it can be seen the Brillouin zones of the pseudo-cubic structure related to A7, red lines, and BCC, black lines, and their relative high symmetry points. Blurry blue lines indicate a secondary macroscopic BCC-PC lattice distortion, ∼10 %. The chosen dispersions measured under pressure are indicated: $<110>_R$ and $<121>_R$ directions, which are marked in green and yellow respectively. The related experimental results are presented in Sec. 5.2.3.

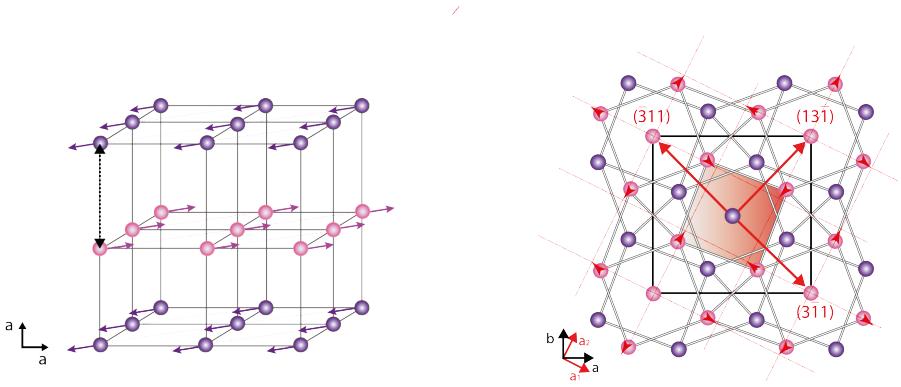

Figure 5.7.: Figure (a) shows the atomic rearrangement associated with BCC-PC transition. The arrows indicate the atomic displacements, different layers have opposite directions. The double arrow explains the compression applied on the side in order to reach the PC structure; Figure (b) shows the displacive mechanism associated with incommensurate-BCC transition. Different colours are assigned for the layers in *c*. The atomic displacement is only shown in the first layer as arrows, the other layer follows the same rule. Dashed red lines and the other red elements are referred to the new cubic unit cells.

- BCC ", where the two intermediate, incommensurate structures (tetragonal and monoclinic) are very similar and structurally interlinked by negligible distortions, thus they will be considered as a single incommensurate structure. Moreover, the A7-PC transition, the only one which is not displacive, is included in the discussion since is essential to understand the framework instability of our system and its pressure-dependence.

Considering the symmetry-base transition method, another explanation for the complex structural path under pressure (A7-Incommensurates-BCC) respect the total energy of the system is given by the need to stabilize the critical reconstructive phase transitions between pseudo-PC (A7) and BCC, [253]. The mechanism is explained like elastic properties of the crystal lattice towards a bilinear connection between critical displacement gradients and secondary strains.

PC to A7 transition

The distortions in the *direct* space, which take place in the transition, were already explained in the introduction. All those mechanisms are along the three-fold axis (or trigonal axis) [254]. The transformations between PC-A7 are:

$$\begin{cases} \boldsymbol{d}_1^R = \boldsymbol{a}_1^{PC} + \boldsymbol{a}_3^{PC} \\ \boldsymbol{d}_2^R = \boldsymbol{a}_2^{PC} + \boldsymbol{a}_3^{PC} \\ \boldsymbol{d}_3^R = \boldsymbol{a}_1^{PC} + \boldsymbol{a}_2^{PC} \end{cases}$$

where **d** and **a** are referred to the final and initial structures, respectively. In the *reciprocal* space, the corresponding **k**-critical is $\mathbf{k}_{13}=1/2(\mathbf{b}_1+\mathbf{b}_2+\mathbf{b}_3)_{PC}$, which goes until the R-point of the primitive cubic BZ, see figure Fig. 5.6a.

BCC-PC transition

The transformation between the pseudo-PC (SbI) and BCC (SbIII) is ferrodistorsive, $Z_{pI}=Z_{III}$. The two space groups are $Pm\bar{3}m(Z_{pI}=1)$ and $Im\bar{3}m(Z_{III}=1)$, respectively, thus the group-subgroup relationship is nonexistent. If one considers the real distorted structure, one should arrive at the same conclusion ($R\bar{3}m(2)$ - $Im\bar{3}m(1)$ transformation). As already explained in the introduction of this section, in order to find a phenomenological scheme, the transformation should have an intermediate phase which shares the space group [250]. The type of displacement is via antiparallel shifts of alternating $(001)_{PC}$ atomic planes in the $\pm[110]_{PC}$ directions, Fig. 5.7a. For general magnitude displacements, the shifts reduce the symmetry from cubic to orthorhombic Cmcm(2). With further special shifts, the cubic structure can be restored.

The transition in the *direct* space from PC to BCC can be described:

$$\begin{cases} \boldsymbol{d}_1^{BCC} = \boldsymbol{a}_1^{PC} \\ \boldsymbol{d}_2^{BCC} = \boldsymbol{a}_2^{PC} \\ \boldsymbol{d}_3^{BCC} = 2\boldsymbol{a}_3^{PC} \end{cases}$$

where $\mathbf{d}_1$,$\mathbf{d}_2$ and $\mathbf{d}_3$ are the final BCC cell parameters, whereas the **a** cell vectors are referred to the PC structure. The critical vector is $\mathbf{k}=\frac{1}{2}\mathbf{b}_3^{PC}$, which goes to the X-point of the primitive cubic BZ, Fig. 5.6b.

On the other way, the transformation in *direct* space from BCC to PC is given by:

$$BCC \begin{cases} \boldsymbol{a}_1(\bar{1}11) \\ \boldsymbol{a}_2(1\bar{1}1) \\ \boldsymbol{a}_3(11\bar{1}) \end{cases} \qquad \begin{cases} \boldsymbol{d}_1^{PC} = (200) = \boldsymbol{a}_2 + \boldsymbol{a}_3 \\ \boldsymbol{d}_2^{PC} = (020) = \boldsymbol{a}_1 + \boldsymbol{a}_3 \\ \boldsymbol{d}_3^{PC} = (002) = \boldsymbol{a}_1 + \boldsymbol{a}_2 \end{cases}$$

where $\mathbf{d}_1$,$\mathbf{d}_2$ and $\mathbf{d}_3$ are the final doubled cell parameters of the primitive cubic structure. The critical vector is $[\mathbf{k}_{12}^{BCC}=1/2(\mathbf{b}_1^{BCC}+\mathbf{b}_2^{BCC}-\mathbf{b}_3^{BCC})]$, until H_{BCC}-point, see Fig. 5.6b.

Phase transition	*Critical vector* (k)	*Point or direction in the BZ* [a]
PC - A7	$\mathbf{k}_{13}^{PC}$=1/2 ($\mathbf{b}_1^{PC}$+$\mathbf{b}_2^{PC}$+$\mathbf{b}_3^{PC}$)	R_{PC}
BCC - PC	$\mathbf{k}_{12}^{BCC}$=1/2 ($\mathbf{b}_1^{BCC}$+$\mathbf{b}_2^{BCC}$-$\mathbf{b}_3^{BCC}$)	H_{BCC}
BCC - SbII (SbIV)	$\mathbf{k}_1^{BCC}$=2/5 ($\mathbf{b}_1^{BCC}$-$\mathbf{b}_2^{BCC}$)-1/5 $\mathbf{b}_3^{BCC}$ and $\mathbf{k}_8^{BCC}$=μ 2/5 ($\mathbf{b}_1^{BCC}$-$\mathbf{b}_2^{BCC}$- $\mathbf{b}_3^{BCC}$)	$\Gamma - \Xi - Z$ and $\Gamma - \Delta - H_{BCC}$

[a] Direction in the Brillouin zones referred to Fig. 5.6

Table 5.2.: Critical vectors for principal phase transitions and their directions in the reciprocal space

Incommensurate phases to BCC

The displacement vectors for the two incommensurate phases (SbII and SbIV) from BCC can be explained with the transformation:

$$\begin{cases} \boldsymbol{d}_1^{Inc} = \boldsymbol{a}_1^{BCC} - \boldsymbol{a}_2^{BCC} - \boldsymbol{a}_3^{BCC} \\ \boldsymbol{d}_2^{Inc} = 2\boldsymbol{a}_2^{BCC} + \boldsymbol{a}_3^{BCC} \\ \boldsymbol{d}_3^{Inc} = \boldsymbol{a}_1^{BCC} + 2\boldsymbol{a}_3^{BCC} \end{cases}$$

where one should consider the primitive BCC cell, $\mathbf{a}_1^{BCC}$,$\mathbf{a}_2^{BCC}$ and $\mathbf{a}_3^{BCC}$. The atomic displacements are shown in Fig. 5.7b. The result is described by two reciprocal space vectors. The first is a long-periodic, commensurate vector, $\mathbf{k}_1$=2/5($\mathbf{b}_1$-$\mathbf{b}_2$)-1/5$\mathbf{b}_3$ which lies in the N_{BCC}-Γ -H_{BCC} plane. The latter is incommensurate, which is along the Γ -Δ -H_{BCC} line normal to this plane, $\mathbf{k}_8$=μ($\mathbf{b}_1$+$\mathbf{b}_2$-$\mathbf{b}_3$). The vector varies towards the H_{BCC}-point.

In conclusion, the critical vectors in the *reciprocal* space for each structural transformation are summarised in Tab. 5.2. The correlation between the pseudo-cubic and BCC Brillouin zones are drawn in Fig. 5.6b, associated with the critical vec-

tors for each transition. Thanks to this method, one may evaluate the important direction/points in the *reciprocal* space.

5.2.2. *Ab initio* calculation

Different calculations attempts were made in order to understand the electronic configuration of group Va elements [205, 239, 254–259].

The calculations were performed by Dr. Aldo Humberto Romero, who already did calculations based on the experimental Raman and Brillouin data at k=0 and the full phonon dispersion by INS [241]. He calculated with a good agreement the acoustic branches. Applying virtual pressure, a hardening in the Γ-T_H direction and a softening in the X_H-point just for the acoustic branches were found, while a hardening happened for the optic modes. Some comparing tests between our calculations and the one found in Ref. [241] were performed at a constant volume of 53.5 Å.

Thanks to our experimental results, the calculations were improved. The software package used is ABINIT [260–264]. The ambient conditions antimony electronic structure was calculated using Fritz-Haber pseudopotentials [265]. The optimization of the electronic structure was reached using a grid of 8x8x8 **k**-points in the Brillouin zone. We used low energy convergence (less than 10^{-5} eV/atom) and stress convergence criteria less than 10^{-3} GPa. An energy cutoff of 50 Ha was employed to ensure convergence. The preconditioning method was used to improve the density convergence [266]. In order to calculate under pressure, the lattice and its parameters were fully relaxed to a constant pressure between 0 and 7 GPa.

Making an interpolation of the dynamical matrices corresponding to a grid 8x8x8 **q**-points (for each pressure configuration), the phonon dispersion relations along selected high symmetry directions were obtained. These matrices were calculated within the framework of density functional perturbation theory and the linear response method [267, 268].

In order to choose the correct functionals, different calculations attempts were made, Fig. 5.8. In the figure, the experimental phonon dispersions at ambient condition are shown to compare. It is already possible to observe the consistency reached with local density approximation (LDA) . We include in the figure the functional without spin-orbit coupling, even if, as already pointed out in other papers [254, 269], in order to treat the electronic structure of those elements, the spin-orbit coupling is unavoidable.

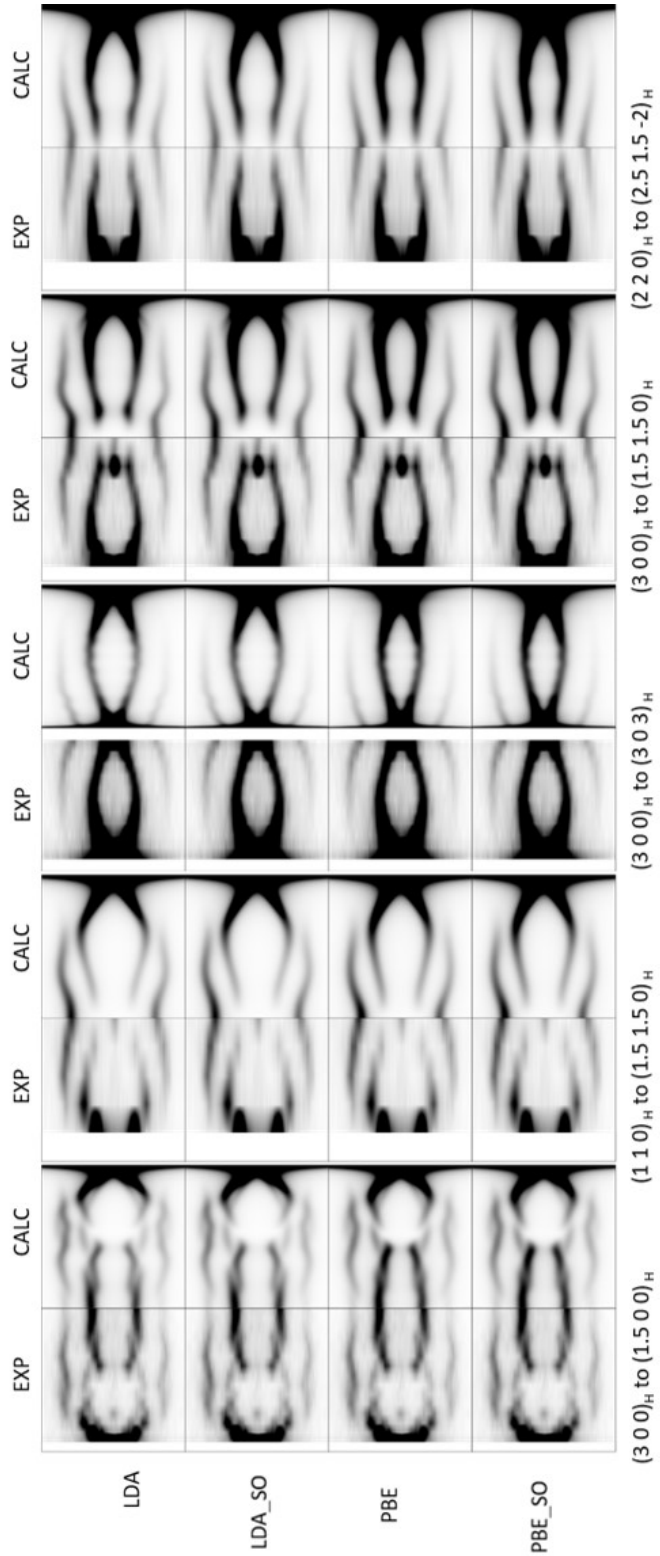

Figure 5.8.: Example of attempts with different functionals as the Perdew-Burke-Ernzerhof (PBE) functional and local density approximation (LDA) with and without spin-orbit coupling. The calculated (on the right) and experimental (on the left) phonon dispersions are compared.

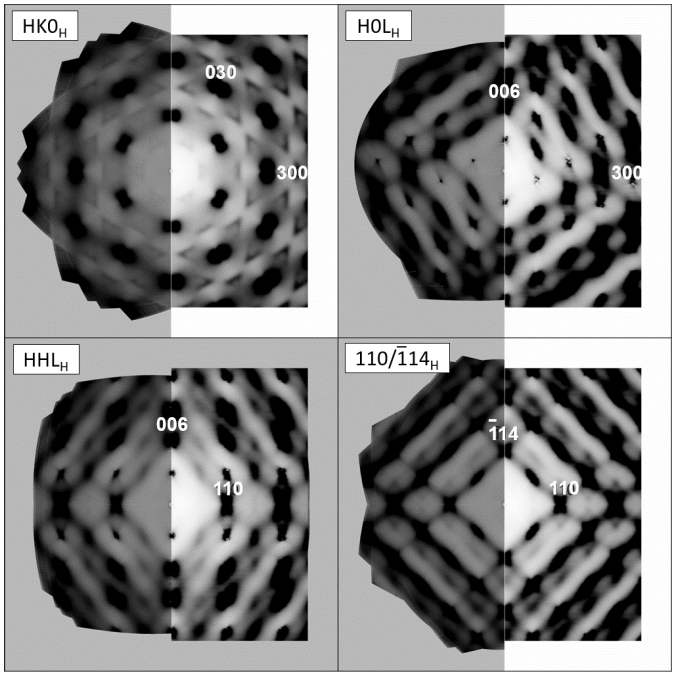

Figure 5.9.: Diffuse scattering maps, experimental on the left and calculated on the right. The indices are in hexagonal setting.

5.2.3. Diffuse scattering and inelastic X-ray scattering results

The A7 structure, as already explained, is a Peierls-distortion of a simple cubic structure. This kind of structural distortion is applied to a specific direction, the stretching of the 3-fold axis, and to a displacement of the two interpenetrated FCC in opposite directions of the same axis. This structural rearrangement can be classified in the framework instability. Since all variables are related to a specific direction, the distortion should be visible as a diffuse plane.

As a matter of fact, the DS maps of A7 antimony, as shown in Fig. 5.9, show a plethora of complicated diffuse patterns. One such prominent case are the diffuse planes in the $<110/\bar{1}14>_H$ map, resembling a 4-fold axis symmetry. The planes are identified by the $<110>_R$ direction normal to the plane or by the $<100>_{PC}$ direction of the pseudo-cubic structure. They seem to be connected to the chains displacement present as intrinsic distortion in the A7 structure. In Fig. 5.10 the A7 and simple cubic structure are oriented along the normal to $(110)_R$ and $(100)_{PC}$. The modulation in the atomic chains derived by the Peierls-distorted structure is visible and Fig. 5.10 shows which directions produce the diffuse planes pattern.

Furthermore, other pronounced features are observed in the $HK0_H$ plane: diffuse planes which intersect $HK0_H$, shown as $<120>_H$-direction lines, and V-shapes

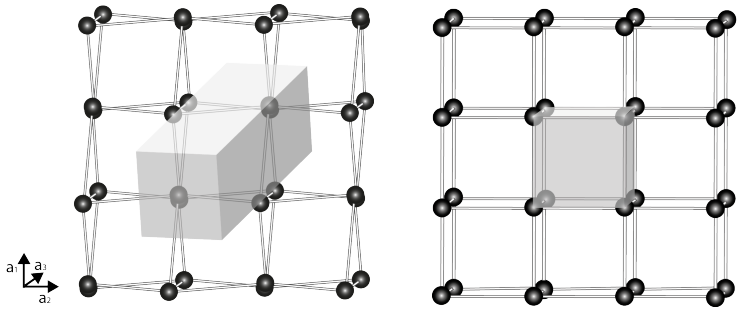

(a) (b)

Figure 5.10.: Projection in the real cell of A7 (a) and PC (b) along the normal of the diffuse planes visible in $<110/\bar{1}14>_H$ map in Fig. 5.9. A chains modulation normal to the projection is visible and clearly related to the Peierls-distortion.

component in the $<\bar{1}10>_H$ direction. Those features are related to **k**-critical that we described in Sec. 5.2.1. The first is related to the phase transition path followed by antimony "A7 - incommensurate phases - BCC". The second feature is nearby the **k**-critical of A7-PC. Thus the origin of those diffuse features should be understood with a complementary step, measuring them with a pressure-dependence energy-resolution experiment.

Fig. 5.11 summarizes the ambient pressure IXS data. Once more, the accuracy of the calculations is observed (discrepancy of less than $\pm 5\%$). Two directions were measured at 0.2 GPa in the DAC cell, $[\bar{1}10]_R$ and $[\bar{1}0\bar{1}]_R$ in Fig. 5.13. They can be add to the discussion of the lattice dynamics at ambients conditions. In general, most of the directions display a downturn of the phonon energy near the zone boundary.

Since the main goal is to understand the contribution of the lattice dynamics to the pressure induced phase transitions, the phonon dispersions should be measured along the critical-**k** vectors, Fig. 5.6, as derived from the analysis presented above in Sec. 5.2.1. Additionally, the *ab initio* calculations indicate the directions of the reciprocal space with a large pressure dependence. The calculated maps of the $HK0_H$ plane at pressures up to 4.7 GPa, Fig. 5.12, show an increasing intensity of the diffuse planes in the $< \bar{1}20 >_H$ directions ($<110>_R$ direction).

Taking into account all those considerations, Fig. 5.13 summarizes the high pressure IXS results along two main directions, in the pseudo-cubic approximation: the <121> direction depicted by the yellow arrow and the <110> direction illustrate by the green arrow in Fig. 5.6b. The former is related to the reduction of the Peierls-like distortion (A7-PC), whereas the latter lies on the plane related to the complicated PC-Incommensurate-BCC transition.

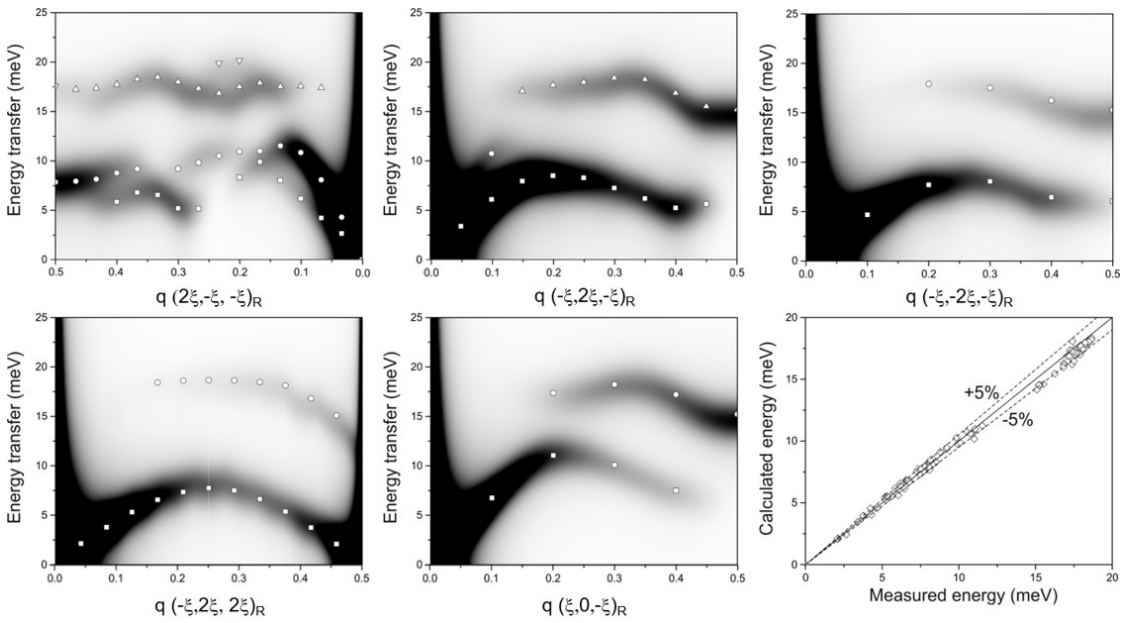

Figure 5.11.: Phonon dispersions of Sb at ambient condition. Calculations are shown in map form with IXS fit data superimposed (white dots). The deviation between the calculated and measured energy is of the order of ±5%. The agreement is excellent.

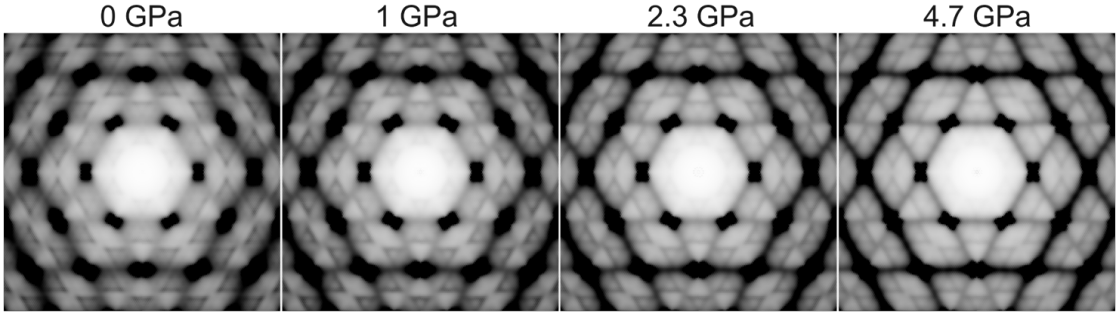

Figure 5.12.: $HK0_H$ plane theoretical predicted by *ab initio* calculations at applied pressures up to 4.7 GPa.

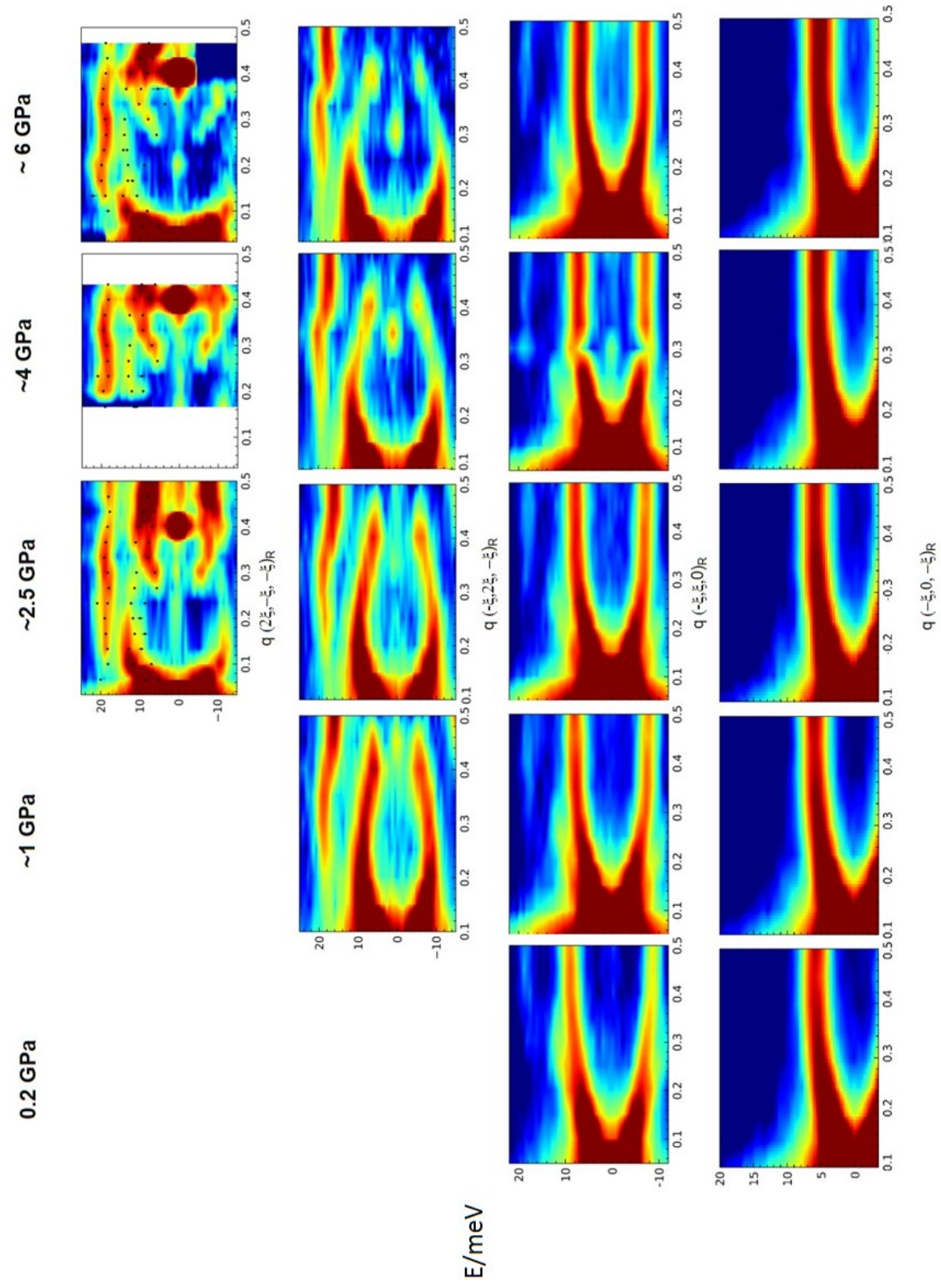

Figure 5.13.: Pressure dependence of IXS spectra in different directions. The phonon dispersions are shown as map. The first direction $[2\overline{1}\overline{1}]_R$ shows the fitted points since the phonon dispersion is difficult to read due to the multiple contributions.

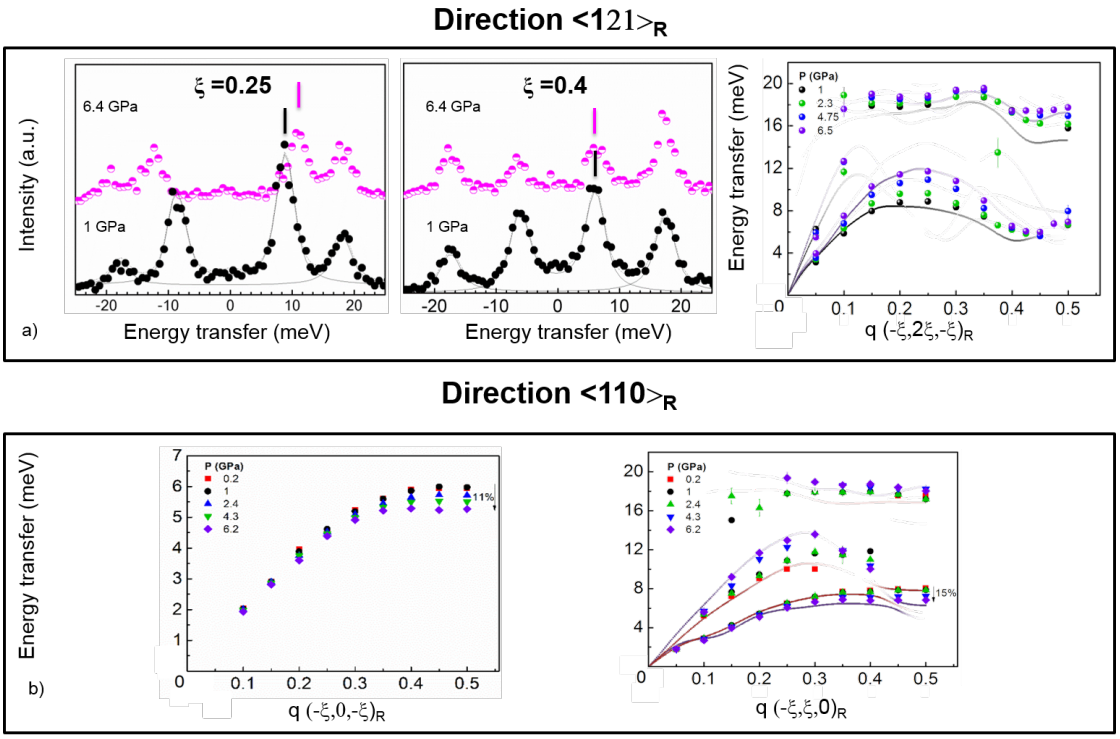

Figure 5.14.: The phonon dispersion along the direction: (a) near BCC-PC transition, $<121>_R$: from the left, IXS scans at ξ=0.25 and ξ=0.4 of 1 GPa and 6.4 GPa show the hardening and "relative" softening, respectively. On the right, the fitting data derived from IXS scans under pressure, where the experimental data (dots) and calculated dispersion (continuous lines) show the excellent agreement; (b) related to BCC-PC transition, $<110>_R$: two phonon dispersions under pressure where the directions are considered similar for the A7-PC approximation. The points correspond to the fitting experimental data, and the lines are the *ab initio* calculation at ambient condition and 6.5 GPa. Experimental results show near the zone boundary a softening of $\backsim$ 11% and $\backsim$ 15%, respectively.

The phonon dispersions in the direction $[\bar{1}2\bar{1}]_R$ display a hardening trend with increasing pressure, Fig. 5.14a. The IXS scans at ξ=0.25 at 1 GPa and 6.5 GPa provide an example of this behaviour. A hardening is shown also by the optical phonon, especially enhanced at BZ border. A relative softening (an absence of hardening) is observed in the acoustic branch near the BZ border, ξ=0.4. The IXS scans at that position are shown for 1 and 6.5 GPa, the energy of the acoustic phonon is fixed at ∼6 meV. On the contrary, the other direction, $[2\bar{1}\bar{1}]_R$ shows a more complicated pattern. Therefore, the fitting points are reported directly in the experimental map, Fig. 5.13, and no further analysis is presented.

The second direction $<110>_R$, related to the phase transitions in antimony, shows a more evident softening, Fig. 5.14b. In the $[\bar{1}0\bar{1}]_R$ direction, the transverse acoustic (TA) phonon has a continuous softening until the zone boundary of $\backsim$ 11%. The $[\bar{1}10]_R$ direction shows more components. The presence of longitudinal (LA) and transverse acoustic phonons leads to a more complicated pattern. One can recognize the different elements from the calculations. In fact, the pressure-dependence of LA (longitudinal acoustic) and TA (transverse acoustic) phonons is different. The longitudinal phonon is visible all along the BZ, with the same behaviour found in $[\bar{1}0\bar{1}]_R$ direction. At ξ=0.43, the intensity of the longitudinal phonon almost disappears due to an anticrossing between LA and TA. The LA softens by $\backsim$ 7%, whereas the TA has a hardening until ξ=0.3 and a softening of $\backsim$ 15% post ξ=0.4.

Even if the calculations seem to have a good agreement at ambient condition and they are visibly similar to the high-pressure measurements, some differences are still present. In the calculation, the $[\bar{1}2\bar{1}]_R$-direction optical phonons have a greater pressure-dependent energy, with a bigger shift to low energies. In the second direction $<110>_R$, especially $[\bar{1}10]_R$, the theoretical predicted softening of TA was $\backsim$ 20%, whereas the experimental is just a 15 %.

5.3. Conclusion

In this chapter, the lattice dynamics of the Peierls-distorted Sb structure under pressure was analysed. At ambient conditions, the framework instability of the distorted rhombohedral structure is clearly visible in the diffuse pattern manifesting as diffuse planes perpendicular to <100> pseudo-cubic directions. It can be qualitatively associated to the correlated displacement of atoms along the chains. Applying pressure, antimony follows the general trend of Va group: the pressure induces a distortion reduction. Even if the rhombohedral structure tries to fol-

low the symmetry-increased path, a more complicated phase transition pathway is energetically favourable.

In this chapter, we measured under pressure the directions along the critical vectors/planes related to the A7-PC transition and to the A7-Incommensurate-BCC transition. Nearby the first critical vector, in Γ-R direction, we observed a relative softening of the phonon dispersion ($<121>_R$-direction). Earlier Raman data [211, 212] show the two active modes with pressure-dependence frequencies, a softening of $\sim$ 30%. Those modes, as already explained, correspond to the R-point of the unfolded structure, the primitive cubic. Along the second direction, $< 110 >_R$, in the plane corresponding to the the BCC-pseudo-PC(A7) critical vector, the phonon dispersion presents an intense softening (of $\sim$ 11 % for $[\bar{1}0\bar{1}]_R$ and 15 % $[\bar{1}10]_R$]. Thus, the stronger phonon softening is related to A7-BCC transition, which is ultimately the chosen structural transition path, while complicated by the intermediate incommensurate phases. The system presents a pressure-dependence softening in each direction, also if they have a different intensity.

6. Conclusions and future perspectives

In this Thesis, the interplay between framework instability and electron-phonon coupling in the phase transition mechanism was studied in two systems from different material classes. While not encompassing the situation in its entirety, this choice allows two unique perspectives on the subject thus allowing one to form a good, if incomplete, picture of the subject matter.

This study demonstrated, once again, the productivity of using IXS, DS and first-principle calculations in conjunction. It was also shown that, even if *ab initio* lattice dynamics calculations remain beyond reach, semi-quantitative interpretation of DS may bring valuable insights into the phase transition mechanism.

We have presented work performed on monophosphate tungsten bronzes and in three members that allow a description of the general family behaviour. The lowest term, m=2, is a "model" system describing the quasi-1D electronic system of the single zig-zag chain. The CDW phase is connected with a strong correlation between octahedra tilting of different chains. The results is a classic Peierls transition with a related Kohn anomaly where the phonon reaches zero-frequency in the $\mathbf{q}_{CDW}$ at T_{CDW}. For the W-block members, the DS measurement reveals strong diffuse planes related to the instability within the perovskite building blocks, which exhibit correlated displacements of tungsten atoms along the W-O-W-O chains. IXS measurements then allow one to establish a link between the structural instability and soft valley of low-energy phonons. The latter may be described by the bipolaron theory of Aubry. In both cases, the CDW phases of m=6 and m=8 result from the interplay between the two instabilities, albeit showing different eventual behaviour. For the member m=6, the diffuse intensity distribution reveals a fine structure approaching T_C, directly linked to the hidden Fermi surface nesting. The weak intensity of the incommensurate satellite peaks reveals a modest displacement of the tungsten atoms from the octahedron centre. Simultaneously, the phonon energy at $\mathbf{q}_{CDW}$ shows a modest softening when approaching the transition from above. In contrast in the member m=8, a strong displacement of tungsten atoms occurs along the so-called "long" W-O-W-O chains, reaching a maximum amplitude of 0.4 Å. The corresponding CDW phase displays stronger

commensurate satellite peaks. The elastic component at q_{CDW} is maintained in the high-temperature phase and is associated with an energy softening of two phonons approaching the transition.

The understanding of this family cannot be considered complete. This work is the first study of the complex lattice dynamics of the family. In this regard, small terms as m=4 may present different behaviour and should be investigated. Moreover, since significant results were obtained during the high pressure study of high-term members, such as a new CDW phase of m=8 and the positive trend of dT_{CDW}/dP, the subject area warrants further study. *Ab initio* modelling of the electronic structure, still lacking, would provide important insight into the atomistic and electronic mechanisms at play.

The structure of the second system investigated, elemental antimony, also shows intrinsic instability well visible at ambient condition. In fact, the system exhibits an A7 rhombohedral structure, a Peierls-distorted structure of the parent primitive cubic (PC) phase. The diffuse intensity distribution is a clear signature of the broken symmetry. Furthermore, the instrisic instability of the system is manifested in the diffuse planes perpendicular to <100> pseudo-cubic directions. Applied pressure relaxes the distortion, however the electron-phonon coupling promotes a complex sequence of phase transitions eventually reaching a final BCC structure as opposal to a PC structure. In fact, the phonon softening in the direction of the critical vector related to A7-incommensurate-BCC transitions is significally greater than in the one related to the A7-PC transition. The results can be directly extrapolated to the case of bismuth, based on the diffuse scattering patterns. When considering the role of lattice dynamics in the high pressure phase transitions, one should enlarge the study to further Va group elements. The most pertinent of which would be arsenic and black phosphorus as they both reach a PC structure [234].

A. Appendix

Some additional results on the monophosphate tungsten bronze family are here reported.

m=2

The phonon dispersion starting from the same Bragg peak, $(01\bar{6})$ with $\mathbf{q}(0\text{-}\xi 0)$ was measured at different temperatures. The dispersion shows the longitudinal acoustic phonon. There is no temperature dependence.

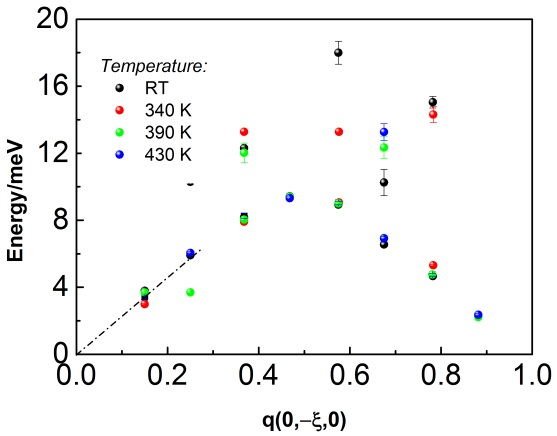

Figure A.1.: The longitudinal acoustic phonon of m=2 from the Bragg $(01\bar{6})$ in the direction $[0\bar{1}0]$ at different temperatures.

m=8

Temperature measurements

The DS maps at each temperature recorded for the sample is reported here with the a,b,c and the angles. The temperatures already reported in the main chapter are skipped here. The deformation to a monoclinic distortion from the orthorhombic high-symmetry phase is present at lower temperature passing trough the 1^{st} CDW phase going to the lower CDW phase.

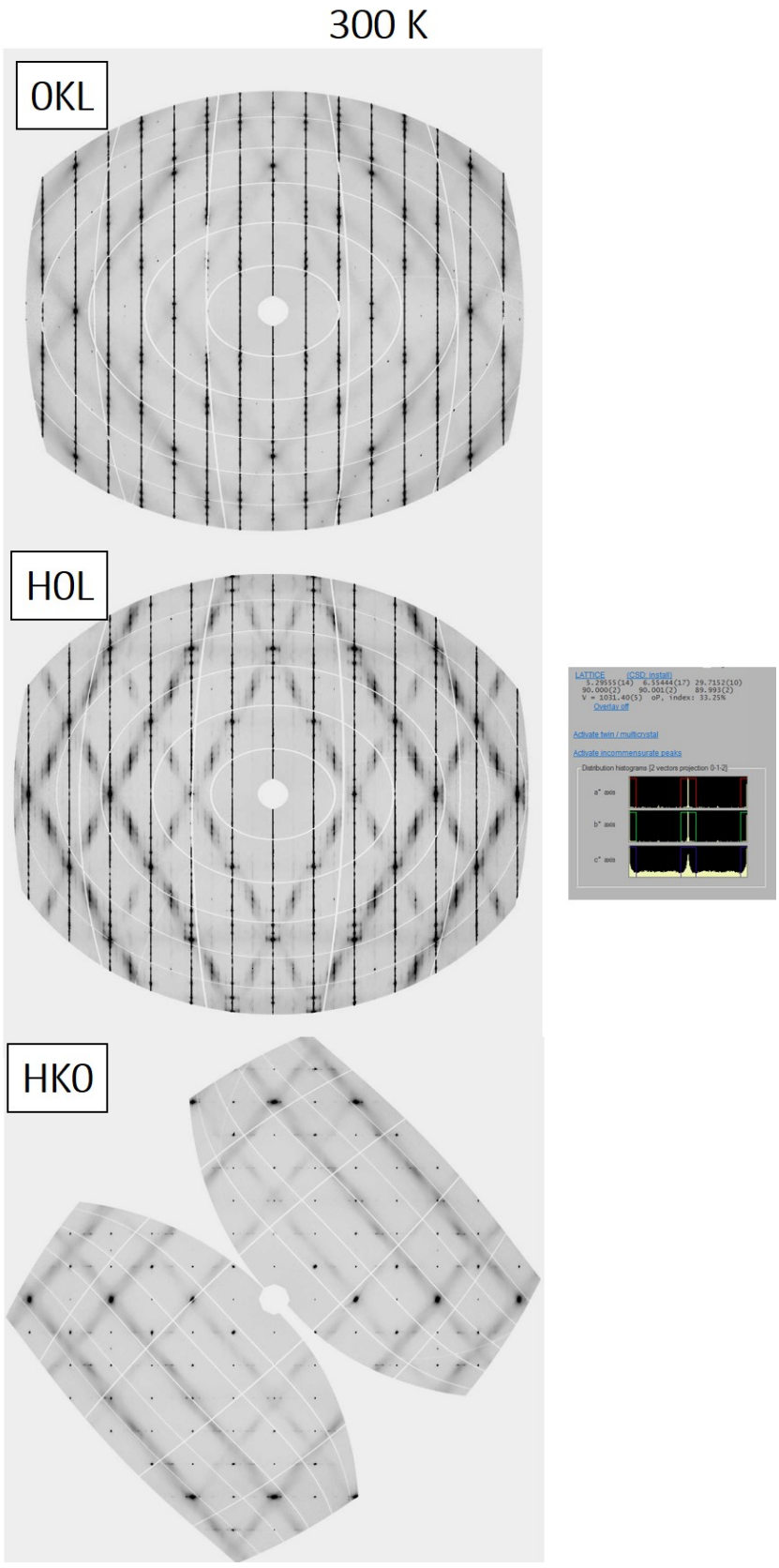

Figure A.2.: DS maps at 300 K of m=8.

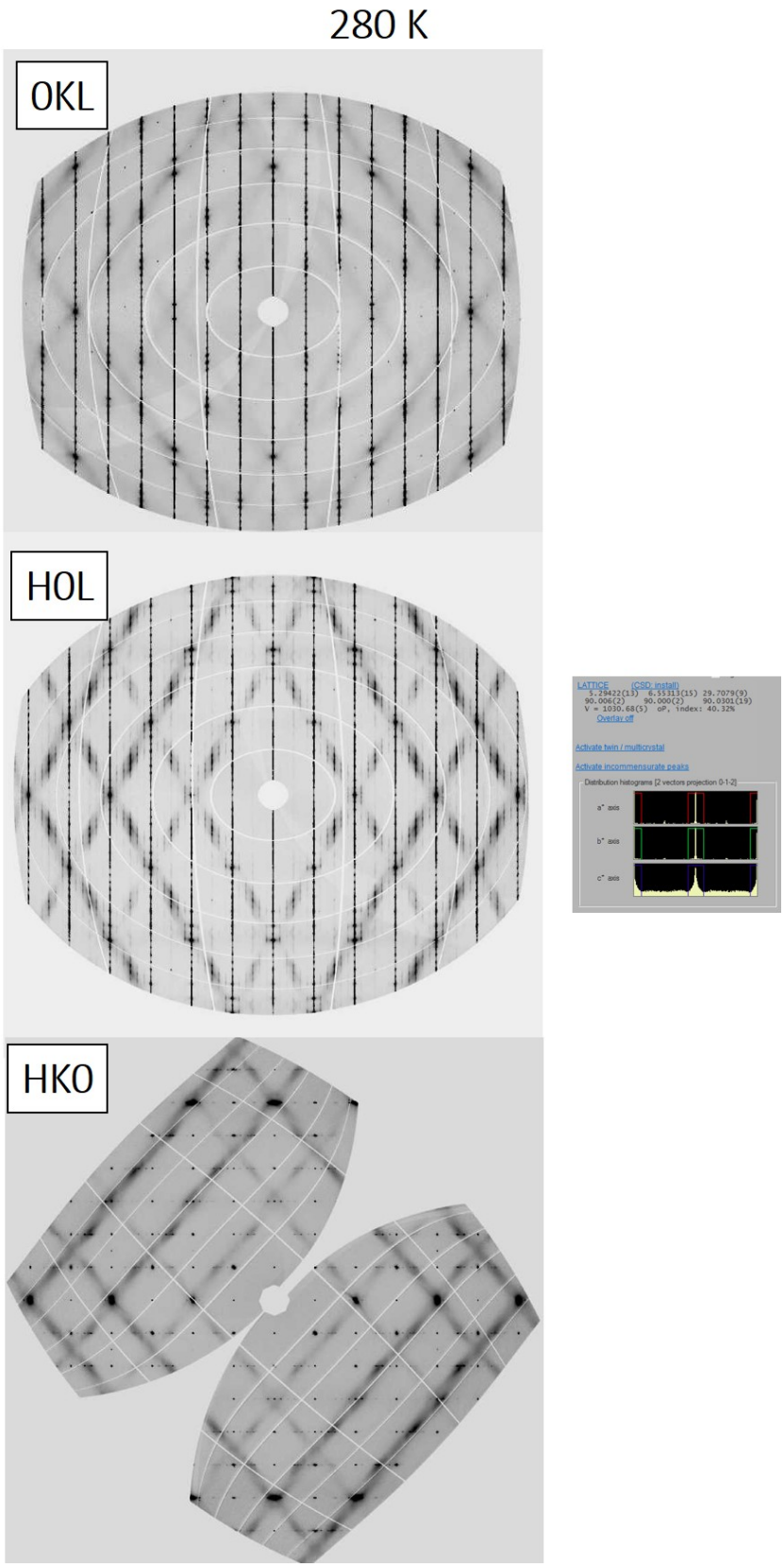

Figure A.3.: DS maps at 280 K of m=8.

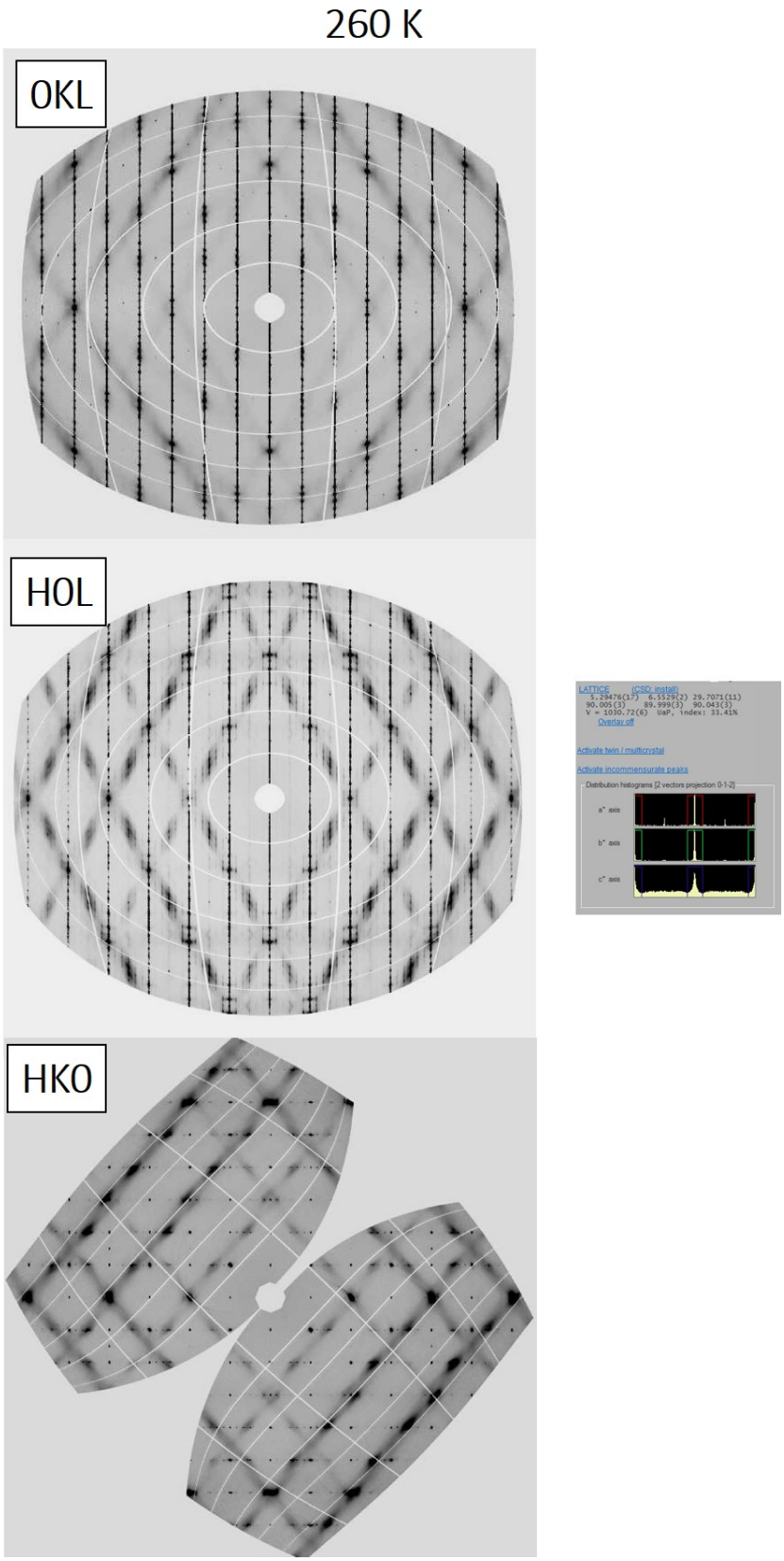

Figure A.4.: DS maps at 260 K of m=8.

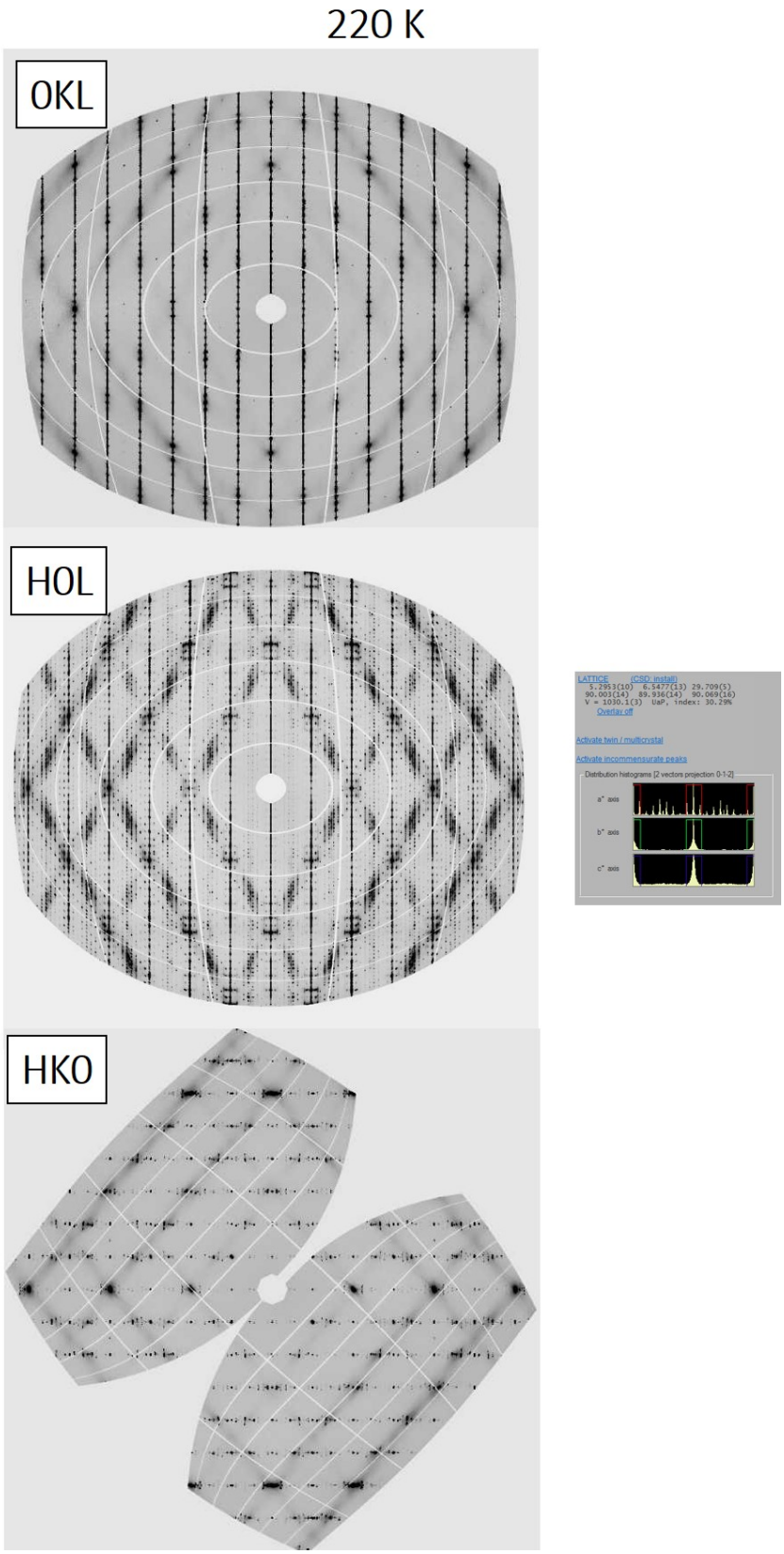

Figure A.5.: DS maps at 220 K of m=8.

Bibliography

[1] B. Wehinger. *On the combination of thermal diffuse scattering, inelastic x-ray scattering and ab initio lattice dynamics calculations*. Phd thesis, Université de Grenoble, July 2013.

[2] A Bosak, D Chernyshov, B Wehinger, B Winkler, M Le Tacon, and M Krisch. In-between bragg reflections: thermal diffuse scattering and vibrational spectroscopy with x-rays. *J. Phys. D: Appl. Phys.*, 48(50):504003, 2015.

[3] S. M. Souliou, Y. Li, X. Du, M. Le Tacon, and A. Bosak. Soft-phonon-driven orbital order in $CaMn_7O_{12}$. *Phys. Rev. B*, 94(18), 2016.

[4] R G Burkovsky, I Bronwald, D Andronikova, B Wehinger, M Krisch, J Jacobs, D Gambetti, K Roleder, A Majchrowski, A V Filimonov, A I Rudskoy, S B Vakhrushev, and A K Tagantsev. Critical scattering and incommensurate phase transition in antiferroelectric $PbZrO_3$ under pressure. *Sci. Rep.*, 2017.

[5] A. Girard, H. Taniguchi, S. M. Souliou, M. Stekiel, W. Morgenroth, A. Minelli, A. Kuwabara, A. Bosak, and B. Winkler. Competing structural instabilities in Bi_2SiO_5. *Phys. Rev. B*, 98:134102, Oct 2018.

[6] L. D. Landau. *Collected Papers of L. D. Landau*. Pergamon Press, 1995.

[7] J. Frenkel. *Wave mechanics*. 1. Oxford University Press, 1936.

[8] M. T. Dove. *Structure and dynamics: an atomic view of materials*. Oxford master series in condensed matter physics. Oxford university press, New York, 2002.

[9] M. Born and K. Huang. *Dynamical theory of crystal lattices*. Oxford Classic Texts in the Physical Sciences. Clarendon Press, 1998.

[10] M. T. Dove. *Introduction to Lattice Dynamics*, volume 4 of *Cambridge topics in mineral physics and chemistry*. Cambridge University Press, 1993.

[11] N. D. Mermin N. W. Ashcroft. *Solid state physics*. Harcourt College Publishers, 1976.

[12] C. Kittel. *Introduction to solid state physics*. Wiley, Chichester, New York, 1996.

[13] H. Böttger. *Principles of the theory of lattice dynamics*. Physik-Verlag, Weinheim, 1983.

[14] R. C. Powell B. Di Bartolo. *Phonons and resonances in solids*. Wiley, New York, 1976.

[15] S. R. Elliott. *The physics and chemostry of solids*. Wiley, Chichester, 1998.

[16] A. M. Kosevich. *The crystal lattice: phonons, solitons, dislocations, superlattices*. Wiley, Chichester, 2006.

[17] B. T. M. Willis and A. W. Pryor. *Thermal vibrations in crystallography*. Cambridge University Press, 1975.

[18] B. Berge, J. P. Bachheimer, J. Dolino, M. Vallade, , and C. Zeyen. Inelastic neutron scattering study of quartz near the inncommensurate phase transition. *Ferroelectrics*, 66:73–84, 1986.

[19] M. Vallade, B. Berge, and G. Dolino. Origin of the incommensurate phase of quartz: II. Interpretation of inelastic neutron scattering data. *J. Physique I*, 2:1481–1495, 1992.

[20] H. Grimm and B. Dorner. Mechanism of $\alpha - \beta$ phase transformation of quartz. *J. Phys. Chem Solids*, 36:407–413, 1975.

[21] M. T. Dove, V. Heine, and K. D. Hammonds. Rigid unit modes in framework silicates. *Mineral. Mag.*, 59:629–639, 1995.

[22] M. T. Dove, A. K. A. Pryde, V. Hein, and K. D. Hammonds. Exotic distributions of rigid unit modes in the reciprocal spaces of framework aluminosilicates. *J. Phys.: Condens. Matter*, 19:275209, 2007.

[23] M. T. Dove, K. O. Trachenko, M. G. Tucker, and D. A. Keen. Rigid unit modes in framework structures: Theory, experiment and applications. *Rev. Mineral. Geochem.*, 39(1):1, 2000.

[24] F. A. Kassan-Ogly and V. E. Naish. The immanent chaotization of crystal structures and the resulting diffuse scattering. I. Mathematical scheme and physical models. *Acta Cryst. B*, 42:297–306, 1986.

[25] F. A. Kassan-Ogly and V. E. Nash. The immanent chaotization of crystal structures and the resulting diffuse scattering. II. Crystallochemical conditions of perovskite chaotization. *Acta Cryst.*, B42:307–313, 1986.

[26] A. Ragulskaya, A. Bosak, D. Chernyshov, and R. Burkovsky. Phonon and phonon-like excitations in knbo3. unpublished results, Report ESRF Summer school, 2016.

[27] R. Comès, M.Lambert, and A.Guinier. Désordre linéaire dans les cristaux (cas du silicium, du quartz, et des pérovskites ferroélectriques). *Acta Cryst.*, A26:244, 1970.

[28] R. E. Peierls. *Quantum Theory of Solids*. Clarendon, Oxford, 1955.

[29] C.-W. Chen, J. Choe, and E Morosan. Charge density waves in strongly correlated electron systems. *Rep. Prog. Phys.*, 79(8):084505, 2016.

[30] T. Aruga. Surface Peierls transition on Cu(001) covered with heavier p-block metals. *Surface Science Reports*, 61:283–302, 2006.

[31] R. H. Friend and D. Jerome. Periodic lattice distortions and charge density waves in one- and two-dimensional metals. *J. Phys. C: Solid State Phys.*, 12:1441–1478, 1979.

[32] P. Monceau. Nature of the peierls transition in charge density wave systems: Strong coupling versus weak coupling. *Physica D*, 216(1):167 – 171, 2006. Nonlinear Physics: Condensed Matter, Dynamical Systems and Biophysics.

[33] R. E. Thorne. Charge-density-wave conductors. *Phys. Today*, pages 42–47, 1996.

[34] C. M. Varma and A. L. Simons. Strong-coupling theory of charge-density-wave transitions. *Phys. Rev. Lett.*, 51:138–141, Jul 1983.

[35] G. Grüner. *Density waves in solids*, volume 89. Addison-Wesley Publishing Company.

[36] G. Grüner. The dynamics of charge-density waves. *Rev. Mod. Phys.*, 60(4):1129–1181, 1988.

[37] M. D. Johannes and I. I. Mazin. Fermi surface nesting and the origin of charge density waves in metals. *Phys. Rev. B*, 77:165135, Apr 2008.

[38] K.Rossnagel. On the origin of charge-density waves in select layered transition-metal dichalcogenides. *J.Phys. Condens.Matter*, 23, 2011.

[39] Altmann S. L. *Theory of solids: introduction from the point of view of symmetry*. Oxford Science Publications, New York, 1991.

[40] R. Peierls. *More Surprises in Theoretical Physics*. Princeton University Press, 1991.

[41] P. Monceau, editor. *Electronic properties of inorganic quasi-one-dimensional compounds*. Series B: quasi-one dimensional materials. Springer Science + Business Media, 1985.

[42] J. T. Devresse, R. P. Evrard, and B. E. van Doren, editors. *Highly conducting one-dimensional solids*. Plenum Press, New York and London, 1979.

[43] M. Greenblatt, editor. *Oxide bronzes.* World Scientific [Int. J. Mod. Phys. B 7, 3973 (1993)], 1993.

[44] K. Shin. *Electronic structure and charge density waves in the rare earth (R) tellurides RTe_2 and R_2Te_5.* Phd thesis, Stanford university, 2008.

[45] M. H. Whangbo, J. Ren, W. Liang, E. Canadell, J. P. Pouget, S. Ravy, J. M. Williams, and M. A. Beno. Some general conditions for hidden fermi surface nesting. *Inorg. Chem.*, 31(20):4169–4173, 1992.

[46] M. H. Whangbo, E. Canadell, P. Foury, and J. P. Pouget. Hidden fermi surface nesting and charge density wave instability in low-dimensional metals. *Science*, 252(5002):96–98, 1991.

[47] E. Canadell and M.-H. Whangbo. Structural and electronic origin of the hidden nesting and charge density waves in transition metal oxides and bronzes. *Int. J. Mod. Phys. B*, 07(23n24):4005–4043, 1993.

[48] W. Kohn. Image of the fermi surface in the vibration spectrum of a metal. *Phys. Rev. Lett.*, 2:393–394, May 1959.

[49] E. J. Woll and W. Kohn. Images of the fermi surface in phonon spectra of metals. *Phys. Rev.*, 126(5):1693–1697, 1962.

[50] J. R. Schrieffer. *Theory of Superconductivity.* Benjamin, Inc., 1963.

[51] Tinkham. *Introduction to Superconductivity.* Dover edition, 1975.

[52] J.-P. Pouget. The peierls instability and charge density wave in one-dimensional electronic conductors. *C. R. Phys.*, 17(3):332 – 356, 2016.

[53] A. B. Migdal. Interaction between electrons and lattice vibrations in a normal metal. *Zh. Eksp. Teor. Fiz*, 34:1438–1446, 1958.

[54] A. B. Migdal. Interaction between electrons and lattice vibrations in a normal metal. *Sov. Phys. JETP*, 7:996–1001, 1958.

[55] W. L. McMillan. Microscopic model of charge-density waves in 2H-$TaSe_2$. *Phys. Rev. B*, 16(2):643–650, 1977.

[56] M. Maschek, S. Rosenkranz, R. Heid, A. H. Said, P. Giraldo-Gallo, I. R. Fisher, and F. Weber. Wave-vector-dependent electron-phonon coupling and the charge-density-wave transition in $TbTe_3$. *Phys. Rev. B*, 91:235146, 2015.

[57] F. Weber, S. Rosenkranz, J.-P. Castellan, R. Osborn, R. Hott, R. Heid, K.-P. Bohnen, T. Egami, A. H. Said, and D. Reznik. Extended Phonon Collapse and the Origin of the Charge-Density Wave in $2H-NbSe_2$. *Phys. Rev. Lett.*, 107:107403, 2011.

[58] C. Schlenker, editor. *Low dimensional electronic properties of molybdenum bronzes and oxides.* Kluwer Acad. Publ, 1989.

[59] S. Aubry, G. Abramovici, and J.-L. Raimbault. Chaotic polaronic and bipolaronic states in the adiabatic holstein model. *J. Stat. Phys.*, 67(3):675–780, May 1992.

[60] J.-L. Raimbault. *Configurations bipolaroniques et fluctuations quantiques du reseau dans les chaines de peierls incommensurables*. Phd thesis, Physique Nantes, 1990. Thèse de doctorat dirigée par Lefrant, Serge Physique Nantes 1990.

[61] Lev P. Gor'kov. Strong electron-lattice coupling as the mechanism behind charge density wave transformations in transition-metal dichalcogenides. *Phys. Rev. B*, 85:165142, Apr 2012.

[62] T. Holstein. Studies of polaron motion: Part ii. the small polaron. *Ann. Phys.*, 8(3):343 – 389, 1959.

[63] P Y Le Daeron and S Aubry. The metal-insulator transitions in the peierls chain. *J. Phys. C: Solid State Phys.*, 16(24):4827–4838, aug 1983.

[64] W. Schülke. *Handbook on Synchrotron Radiation*, volume 3. Elsevier Science Publ, 1991.

[65] E. Burkel. Phonon spectroscopy by inelastic x-ray scattering. *Rep. Prog. Phys.*, 63(2):171, 2000.

[66] D. Griffiths. *Introduction to elementary particles*. John Wiley and sons, inc, 1987.

[67] L. Van Hove. Correlations in space and time and born approximation scattering in systems of interacting particles. *Phys. Rev.*, 95(1):249–262, 1954.

[68] R. Xu and T. C. Chiang. Determination of phonon dispersion relations by x-ray thermal diffuse scattering. *Z. Kristallogr.*, 220:1009–1016, 2005.

[69] M. Born and K. Huang. *Dynamical theory of Crystal lattice*. Oxford University Press, Oxford, 1954.

[70] Lambert. *Neutron and syncrothron radiation for condensed matter studies*, volume Volume 1 Theory, Instruments and Methods. Springer-Verland & EDP Sciences, 1993.

[71] W. Morgenroth B. Winkler N. Tguyen-Thanh L. Paolasini S. M. Souliou A. Minelli D. Gambett A. Bosak A. Girard, M. Stekiel. A new diffractomere for diffuse scattering studies at the id28 beamline of the esrf. *under review*.

[72] T. R. Welberry. Diffuse x-ray scattering and models of disorder. *Rep. Prog. Phys.*, 48(11):1543, 1985.

[73] C. Brönnimann, E. F. Eikenberry, B. Henrich, I. Johnson, A. Mozzanica, C. M. Schlepütz, P. R. Willmott, and B. Schmitt. *J. Synchrotron Radiat*, 13:120, 2006.

[74] V. Dyadkin, P. Pattison, V. Dmitriev, and D. Chernyshov. A new multi-purpose diffractometer pilatus@esrf. *J. Synchrotron Radiat.*, 23(3):825–829, 2016.

[75] *Agilent. CrysAlis PRO.Agilent Technologies Ltd, Yarnton, Oxfordshire, England.*, 2014.

[76] H. Zachariasen. *Theory of X-ray Diffraction in Crystals*. Dover, New York, 1944.

[77] C. Masciovecchio, U. Bergmann, M. Krisch, G. Ruocco, F. Sette, and R. Verbeni. A perfect crystal x-ray analyser in mev energy resolution. *Nucl. Instrum. and Methods in Phys. Res. Sec. B*, 117(339):181–186, 1996.

[78] W. R. Busing and H. A. Levy. Angle calculations for 3- and 4- circle x-ray and neutron diffractometers. *Acta Cryst.*, 22:457, 1967.

[79] W. Graeff and G. Materlik. Millielectron volt energy resolution in bragg backscattering. *Nucl. Instrum. Methods*, 195:97–103, 1982.

[80] A. Bergamin, G. Cavagnero, and G. Mana. Lattice parameter and thermal expansion of monocrystalline silicon. *J. Appl. Phys.*, 82:5396, 1997.

[81] R. Verbeni, F. Sette, M. Krisch, U. Bergmann, B. Gorges, C. Halcooussis, K. Martel, C. Masciovecchio, J. F. Ribois, G. Roucco, and H. Sinn. X-ray Monochromator with 2 $\times 10^8$ Energy Resolution. *J. Synchrotron Radiation*, 3:62, 1996.

[82] F. Sette and M. Krisch. *Neutron and X-ray spectroscopy*. Springer, 2006.

[83] M. Krisch and F. Sette. *Inelastic X-Ray Scattering from Phonons*, pages 317–370. Springer Berlin Heidelberg, 2007.

[84] A. Q. R. Baron. Introduction to high-resolution inelastic x-ray scattering.

[85] B. FÅk and B. Dorner. Proceedings of the first european conference on neutron scattering phonon line shapes and excitation energies. *Physica B*, 234:1107 – 1108, 1997.

[86] K. Syassen. Ruby under pressure. *High Pressure Res.*, 28(2):75–126, 2008.

[87] A. Dewaele, M. Torrent, P. Loubeyre, and M. Mezouar. Compression curves of transition metals in the mbar range: Experiments and projector augmented-wave calculations. *Phys. Rev. B*, 78:104102, 2008.

[88] G. J. Piermarini and S. Block. Ultrahigh pressure diamond-anvil cell and several semiconductor phase transition pressures in relation to the fixed point pressure scale. *Rev. Sci Instrum.*, 46:973, 1975.

[89] H. K. Mao, J. Xu, and P. M. Bell. Calibration of the ruby pressure gauge to 800 kbar under quasi-hydrostatic conditions. *J. Geophys. Rev*, 91:4673, 1986.

[90] H. K. Mao. *Simple molecular systems at very high density*, chapter Static compression of simple molecular system in the megabar range, pages 221–236. Plenum Press, New York, 1989.

[91] https://www.surfacenet.de/.

[92] J. P. Pouget and S. Kagoshima. Evidence for a peierls transition in the blue bronzes k0.3mom3 and rb0.30moo3. *J. de Phys. Lett L*, 44:133, 1983.

[93] R. Buder, J. Devenyi, J. Dumas, J. Marcus, J. Mercier, C. Schlenker, and H. Vincent. Two-dimensional electronic properties of the purple potassium molybdenum bronze $K_{0.9}Mo_6O_{17}$. *J Phys. Lett.-Paris*, 43(2):59–65, 1982.

[94] C. Escribe-filippini, K. Konaté, J. Marcus, C. Schlenker, R. Almairac, R. Ayroles, and C. Roucau. Evidence for a charge-density-wave instability in the purple bronze k_0-$p_9mo_6o_{17}$. *Philos. Mag. B*, 50(3):321–330, 1984.

[95] P. Labbé, M. Goreaud, B. Raveau, and J. C. Monier. Etude comparative des structures M_xWO_3 de type bronze hexagonal. I. Analyse structurale des bronzes de composition $M_{0,3}0WO_3$. Stéréochimie des éléments M=RbI, TlI et InI. *Acta Crystallogr.*, B34(5):1433–1438, May 1978.

[96] P. Roussel, O. Pèrez, and Ph. Labbé. Phosphate tungsten bronze series: crystallographic and structural properties of low-dimensional conductors. *Acta Crystallogr.*, B57(5):603–632, 2001.

[97] A. Magnéli. The crystal structure of Mn_4O_{11} (η-Molybdenum Oxide). *Acta Chem. Scand.*, 2:861–871, 1948.

[98] M. Ghedira, H. Vincent, M. Marezio, J. Marcus, and G. Furcaudot. Structure cristalline du conducteur métallique bidimensionnel Mo_4O_{11}-gamma. *J. Solid State Chem.*, 56(1):66 – 73, 1985.

[99] J. P. Giroult, M. Goreaud, Ph. Labbé, and B. Raveau. $K_xP_2W_2O_{16}$: A bronze with a tunnel structure built up from PO_4 tetrahedra and WO_6 octahedra. *Journal of Solid State*, 44:407, 1982.

[100] A. Benmoussa, D. Groult, and B. Raveau. Propriétés électriques des bronzes monophosphates de sodium et de potassium A_x $(PO_2)_4$ $(WO_3)_{2m}$ (m= 4, 6, 10). *Rev. Chim. Miner.*, 21(6):710–720, 1984.

[101] M. Vujković, Z. Nedić, P. Tančić, O. S. Aleksić, M. V. Nikolić, U. Mioč, and S. Mentus. Electrochemical lithiation/delithiation kinetics and capacity of phosphate tungsten bronze and its chemically pre-lithiated derivatives in aqueous solutions. *J. Mater. Sci.*, 51(5):2481–2489, 2015.

[102] I. Holclajtner-Antunović, U. Mioč, M Todorović, Z. Jovanovic, M Davidović, D. Bajuk-Bogdanović, and Z. Laušević. Characterization of potassium salts of 12-tungstophosphoric acid. *Mater. Res. Bull.*, 45:1679–1684, 11 2010.

[103] A. Martínez de la Cruz, F.E. Longoria Rodríguez, Lucy T. González, and Leticia M. Torres-Martínez. Behavior of the monophosphate tungsten bronzes $(PO_2)_4(WO_3)_{2m}$ (m=7 and 8) in the course of electrochemical lithium insertion. *Electrochim. Acta*, 52(23):6490 – 6495, 2007.

[104] O. Pérez, L. Elcoro, J. M. Pérez-Mato, and V. Pet̀rì̀cek. Monophosphate tungsten bronzes with pentagonal tunnels: reinvestigation through the peephole of the superspace. *Acta Crystallogr.*, B69(2):122–136, 2013.

[105] W.L. Kehl, R.G. Hay, and D. Wahl. The structure of tetragonal tungsten trioxide. *J. Appl. Phys.*, 23:212, 1952.

[106] P. Roussel, Ph. Labbé, H. Leligny, D. Groult, P. Foury-Leylekian, and J. P. Pouget. $P_4W_{20}O_{68}$: A complex charge-density-wave modulated structure with an antiferroelectric-like lattice distortion. *Phys. Rev. B*, 62(1):176–188, 2000.

[107] N. F. Mott. *Metal-Insulator Transitions*. Taylor and Francis, London, 1974.

[108] J. Dumas, U. Beierlein, S. Drouard, C. Hess, D. Groult, Ph. Labbé, P. Roussel, G. Bonfait, E.Gomez Marin, and C. Schlenker. Electronic Instabilities and Localization Effects in the Quasi-Two-Dimensional Monophosphate Tungsten Bronzes $(PO_2)_4(WO_3)_{2m}$ and $K_xP_4W_8O_{32}$. *J. Solid State Chem.*, 147(1):320 – 327, 1999.

[109] N. Witkowski, M. Garnier, D. Purdie, Y. Baer, D. Malterre, and D. Groult. High-energy-resolution photoemission investigation of monophosphate tungsten bronzes. *Solid State Commun.*, 103(8):471–475, 1997.

[110] E. Canadell and M.-H. Whangbo. Charge-density-wave instabilities expected in monophosphate tungsten bronzes. *Phys. Rev. B*, 43:1894–1902, Jan 1991.

[111] E. Canadell and M H. Whangbo. Conceptual aspects of structure-property correlations and electronic instabilities, with applications to low-dimensional transition-metal oxides. *Chem. Rev.*, 91(5):965–1034, 1991.

[112] E. Sandre, P. Foury-Leylekian, S. Ravy, and J.-P. Pouget. Ab initio fermi surface calculation for charge-density wave instability in transition metal oxide bronzes. *Phys. Rev. Lett.*, 86:5100–5103, May 2001.

[113] A Rötger, C Schlenker, J Dumas, E Wang, Z Teweldemedhin, and M Greenblatt. Magnetotrasport and charge-density-wave instabilities in the quasi-2-dimensional phosphate tungsten bronzes (po2)4(wo3)2m (m = 4,6,7). *Synthetic metals*, 56(2-3):2670–2675, 1993. International conf. on science and technology and synthetic metals (ICSM 92), Goteborg, Sweden, Aug 12-18, 1992.

[114] P. Roussel, Ph. Labbé, and D. Groult. Symmetry and twins in the monophosphate tunsgten bronze series $(PO_2)_4(WO_3)_{2m}$ (2<m<14). *Acta Cryst.*, B56:377–391, 2000.

[115] Elen Duverger-Nedellec. *Transitions vers des états électroniques complexes et des structures super périodiques dans les Bronzes Mono Phosphates de Tungstène*. PhD thesis, Normadie Université, 2017.

[116] Jens Lüdecke, Andreas Jobst, Sandra Geupel, and Sander van Smaalen. Structure of the two-dimensional incommensurate charge-density wave in $(PO_2)_4(WO_3)_8$ at 20 K. *Phys. Rev. B*, 64:104105, Aug 2001.

[117] Pascale Foury. *Etude structurale des bronzes et oxydes quasi-bidimensionnels* $(PO_2)_4(WO_3)_{2m}$, $A_xMo_6O_{17}$ *(A=K,Na;x=1), gamma et eta* Mo_4O_{11} *et des quasi-unidimionsionnels* $Cs_{1-x}P_8W_8O_{40}$. PhD thesis, Centre d'Orsay, Juin 1993.

[118] C. Le Touze, G. Bonfait, C. Schlenker, J. Dumas, M. Almeda, M. Greenblatt, and Z.S. Teweldemedhin. Quantum transport in the charge density wave state of the quasi two-dimensional bronze $(PO_2)_4(WO_3)_{2m}$ (m=4,6). *J. Phys. I France*, 5:437–442, 1995.

[119] K. K. Kolincio. *Study of thermal and electronic transport properties in low dimensional oxides*. Phd thesis, Ecole doctoral S.I.M.E.M., October 2013.

[120] A. Ottolenghi, P. Foury, J.P. Pouget, Z.S. Teweldemedhin, M. Greenblatt, D. Groult, J. Marcus, and C. Schlenker. Charge density wave instabilities in the family of monophosphate tungsten bronzes: $(PO2)_4(WO_3)_{2m}$. *Synth. Met.*, 70(1):1301 – 1302, 1995. Proceedings of the International Conference on Science and Technology of Synthetic Metals.

[121] A. Ottolenghi and J.-P. Pouget. Evidence of high critical temperature charge density wave transitions in the $(PO_2)_4(WO_3)_{2m}$ family of low dimensional conductors for m>8. *J. Phys. I France*, 6:1059–1083, 1996.

[122] C. Hess, C. Le Touze, C. Schlenker, J. Dumas, D. Groult, and J. Marcus. Localisation effects in the Peierls state of the quasi two-dimensional compounds $(PO_2)_4(WO_3)_{2m}$ (m>8). *Synth. Met.*, 86(1):2419 – 2422, 1997. Proceedings of the International Conference on Science and Technology of Synthetic Metals.

[123] Enric C. and M.-H. Whangbo. On the possible electronic instability of the monophosphate tungsten bronze (wo3)4(po2)4. *J. Solid State Chem.*, 86(1):131 – 134, 1990.

[124] E. Canadell, M. H. Whangbo, and I. El I. Rachidi. Similarity of the electronic properties of the monophosphate tungsten bronzes. *Inorg. Chem.*, 29(19):3871–3875, 1990.

[125] S. Paul, A. Ghosh, T. Sato, D. D. Sarma, T. Takahashi, E. Wang, M. Greenblatt, and S. Raj. Electronic band structure and Fermi surfaces of the quasi-two-dimensional monophosphate tungsten bronze, P_4 W_{12} O_{44}. *EPL*, 105(4):47003, 2014.

[126] S. Paul, S. Kumari, and S. Raj. High-resolution angle-resolved photoemission investigation of potassium and phosphate tungsten bronzes. *J. Electron. Spectrosc. Relat. Phenom.*, 208, 2016.

[127] M. Greenblatt. *Physics and chemistry of low-dimensional inorganic*. Plenum Press, New York, 1996.

[128] P. Foury, J. P. Pouget, E. Wang, and M. Greenblatt. Charge Density Wave Transitions with Multiple Nesting in the Monophosphate Tungsten Bronzes: P_4 W_{12} O_{44} and P_4 W_{14} O_{50}. *EPL*, 16(5):485, 1991.

[129] A. Leclaire, H. Chahboun, D. Groult, and B. Raveau. The crystal structure of β-$NbPO_5$. *Z. Kristallogr.*, 177:277–286, 1986.

[130] S.L. Wang, C.C. Wang, and K.H. Lii. Crystal structure of WPO_5, the second member of the monophosphate tungsten bronze series $(WO_3)_{2m}(PO_2)_4$. *J. Solid State Chem.*, 82(2):298 – 302, 1989.

[131] N. Kinomura, M. Hirose, N. Kumada, F. Muto, and T. Ashida. Preparation of a new tungsten(V) phosphate and its polymorph. *J. Solid State Chem.*, 77(1):156 – 161, 1988.

[132] M. H. Whangbo. Structural and electronic properties of linear chain compounds and their molecular analogies. *Acc. Chem. Res.*, 16(3):95–101, 1983.

[133] M.-H. Whangbo. Mott-Hubbard condition for electron localization in the Hartree-Fock band theory. *J. Chem. Phys.*, 70(11):4963–4966, 1979.

[134] B.H. Brandow. Electronic structure of Mott insulators. *Adv. Phys.*, 26(5):651–808, 1977.

[135] Z.S. Teweldemedhin, K.V. Ramanujachary, and M. Greenblatt. Magnetic and electronic transport properties of the monophosphate tungsten bronze $(PO_2)_4(WO_3)_{2m}$, m = 2. *J. Solid State Chem.*, 95(1):21 – 28, 1991.

[136] P. Foury-Leylekian and J.-P. Pouget. Peierls transition in two-dimensional metallic monophosphate tungsten bronzes. *Solid State Sci.*, 4(3):387 – 396, 2002.

[137] P. Foury, J. P. Pouget, Z. S. Teweldemedhin, E. Wang, and M. Greenblatt. Quasi one dimensional charge density wave instabilities in the family of monophosphate tungsten bronzes: $(PO_2)_4(WO_3)_{2m}$. *Synth. Met.*, 55-57:2605–1610, 1993.

[138] C. Hess, C. Schlenker, J. Dumas, M. Greenblatt, and Z. S. Teweldemedhin. Magnetotransport and thermopower properties of the quasi-two-dimensional charge-density-wave compounds $(PO_2)_4$ $(WO_3)_{2m}$ (m=4,6). *Phys. Rev. B*, 54:4581–4588, Aug 1996.

[139] Z.-T. Zhu, J. L. Musfeldt, Z. S. Teweldemedhin, , and M. Greenblatt. Vibrational Properties of Monophosphate Tungsten Bronzes $(PO_2)_4(WO_3)_{2m}$ (m = 4, 6). *Chem. Mater.*, 13(9):2940–2944, 2001.

[140] A. Rötger. *Etude par magnétotransport de l'état d'onde de densité de charge dans les bronzes oxygénés quasi-bidimensionnels* KMo_6O_{17} *et* $(PO_2)_4(WO_3)_{2m}$. Phd thesis, Université Joseph Fourier, February 1993.

[141] B. Domengès, M. Hervieu, B. Raveau, and R. J. Tilley. The monophosphate tungsten bronzes with pentagonal tunnels (mptb). *J. Solid State Chem.*, 54:10–28, 1984.

[142] P. Labbé, M. Goreaud, and B. Raveau. Monophosphate tungsten bronzes with pentagonal tunnels $(PO_2)_4(WO_3)_{2m}$: Structure of two even-m members $P_4W_{12}O_{44}$ (m = 6) and $P_4W_{16}O_{56}$ (m = 8). *J. Solid State Chem.*, 61(3):324 – 331, 1986.

[143] C. Hess. *Propriétés de transport des bronzes oxygénés quasi-bidimensionnels à ondes de densité de charge,* $(PO_2)_4(WO_3)_{2m}$ *(m=4 à 14).* Phd thesis, Université Joseph Fourier - Grenoble I, July 1997.

[144] C. Schlenker G. Bonfait E. Gomez Marin D. Groult J. Dumas, C. Hess and J. Marcus. *Eur. Phys. J.*, B 14:73–82, 2000.

[145] C. Schlenker, C. Le Touze, C. Hess, A. Rötger, J. Dumas, J. Marcus, M. Greenblatt, Z. S. Teweldemedhin, A. Ottolenghi, P. Foury, and J. P. Pouget. Transport properties of the charge density wave quasi two-dimensional compounds $(PO_2)_4(WO_3)_{2m}$. *Synth. Met.*, 70:1263, 1995.

[146] P. M. Chaikin and T. C. Lubensky. *Principles of condensed matter physics.* Cambridge University Press, 1995.

[147] J. F. Scott. Soft-mode spectroscopy: Experimental studies of structural phase transitions. *Rev. Mod. Phys.*, 46:83–128, Jan 1974.

[148] G. Kresse and J. Hafner. Ab initio molecular dynamics for liquid metals. *Phys. Rev. B*, 47:558–561, 1993.

[149] G. Kresse and J. Hafner. Ab initio molecular-dynamics simulation of the liquid-metal-amorphous-semiconductor transition in germanium. *Phys. Rev. B*, 49:14251–14269, 1994.

[150] G. Kresse and J. Furthmüller. Efficiency of ab-initio total energy calculations for metals and semiconductors using a plane-wave basis set. *Comp. Mater. Sci.*, 6(1):15 – 50, 1996.

[151] G. Kresse and J. Furthmüller. Efficient iterative schemes for ab initio total-energy calculations using a plane-wave basis set. *Phys. Rev. B*, 54:11169–11186, 1996.

[152] D. F. Shao, R. C. Xiao, W. J. Lu, H. Y. Lv, J. Y. Li, X. B. Zhu, and Y. P. Sun. Manipulating charge density waves in $1T-TaS_2$ by charge-carrier doping: A first-principles investigation. *Phys. Rev. B*, 94:125126, Sep 2016.

[153] B.S. Yizhi Ge. *First-principle study of charge density waves, electron-phonon coupling, and superconductivity in transition-metal dichalcogenides*. Phd thesis, Faculty of the Graduate school of arts and sciences of Georgetown university, 2013.

[154] D. L. Duong, M. Burghard, and J. C. Schön. Ab initio computation of the transition temperature of the charge density wave transition in $TiSe_2$. *Phys. Rev. B*, 92:245131, Dec 2015.

[155] H. Kim and M. Kaviany. Effect of thermal disorder on high figure of merit in PbTe. *Phys. Rev. B*, 86:045213, Jul 2012.

[156] V. Calandrini, P. Calligari, K. Hinsen, and G. R. Kneller. *nMOLDYN: User's Guide*, 2006.

[157] Pettersen E.F., Goddard T.D., Huang C.C., Couch G.S., Greenblatt D.M., Meng E.C., and Ferrin T.E. Ucsf chimera–a visualization system for exploratory research and analysis. *J Comput Chem.*, 25(13):1605–12, Oct 2004.

[158] R. Comès, M. Lambert, and A. Guinier. The chain structure of $BaTiO_3$ and $KNbO_3$. *Solid State Commun.*, 6(10):715 – 719, 1968.

[159] Hans-Martin Eiter, Michela Lavagnini, Rudi Hackl, Elizabeth A. Nowadnick, Alexander F. Kemper, Thomas P. Devereaux, Jiun-Haw Chu, James G. Analytis, Ian R. Fisher, and Leonardo Degiorgi. Alternative route to charge density wave formation in multiband systems. *Proceedings of the National Academy of Sciences*, 2012.

[160] P. Quémerais. Theory of charge density wave depinning by electromechanical effect. *EPL*, 117:57004, 2017.

[161] M. F. Collins. *Magnetic Critical Scattering*. Oxford University Press, New York-Oxford, 1989.

[162] M. Stekiel, T.Nguyen-Thanh, A. Girard, W.Morgenroth, and B. Winkler. unpublished results.

[163] S. Ravy, J.-P. Itié, A. Polian, and M. Hanfland. High-pressure study of x-ray diffuse scattering in ferroelectric perovskites. *Phys. Rev. Lett.*, 99:117601, Sep 2007.

[164] G. A. Samara, T. Sakudo, and K. Yoshimitsu. Important generalization concerning the role of competing forces in displacive phase transitions. *Phys. Rev. Lett.*, 35:1767–1769, Dec 1975.

[165] R. J. Donohoe, S. P. Love, M. A. Y. Garcia, and B. I. Swanson. *Frontiers of High-Pressure Research*, volume 286 of *Series B: Physics*. 1991.

[166] D Jerome and LG Caron. *Low-Dimensional Conductors and Superconductors*. NATO ASI series, 1987.

[167] J Beille, U Beierlein, J Dumas, C Schlenker, and D Groult. Pressure effect on the charge density wave instabilities in the quasi-two-dimensional conductors $(PO_2)_4(WO_3)_{2m}$ (m = 4, 5, 6) and ν-Mo_4O_{11}. *J. Phys.: Condens. Matter*, 13(7):1517, 2001.

[168] A. Rötger, J. Beille, J.M. Laurant, and C. Schlenker. Pressure dependence of the Peierls transition in the quasi two-dimensional purple bronze KMo_6O_{17}. *Solid State Commun.*, 87(10):913 – 916, 1993.

[169] J. Beille, A. Rötger, J. Dumas, and C. Schlenker. Effect of hydrostatic pressure on the resistivity of the charge-density-wave compound KMo_6O_{17}. *Philos. Mag. Lett.*, 64(4):221–226, 1991.

[170] A. Briggs, P. Monceau, M. Nunez-Regueiro, J. Peyrard, M. Ribault, and J. Richard. Charge density wave formation, superconductivity and Fermi durface determination in $NbSe_3$: a pressure study. *J. Phys. C: Solid St. Phys.*, 13:2117–30, 1980.

[171] S. Ôhara, M. Koyano, H. Negishi, M. Sasaki, and M. Inoue. Effect of Pressure on the Charge Density Wave Transitions in μ-Mo_4O_{11} Crystal. *Physica Status Solidi B*, 164(1):243–252, 1991.

[172] J. Chaussy, P. Haen, J. C. Lasjaunias, P. Monceau, and G. Waysand. Phase transitions in $NbSe_3$. *Solid State Commun.*, 20:759, 1976.

[173] P. Haen, G. Waysand, G. Boch, A. Waintal, P. Monceau, N. P. Ong, and M. Portis. Effect of pressure and electric field on CDW induced resistitivity anomalies in $NbSe_3$. *J. Phys.*, 37:C4–179, Oct 1976.

[174] R. H. Friend, R. F. Frindt, D. Jérome, and A. J. Grant. The effect of pressure on the charge density wave transitions in $4H_b$ TaS_2. *Il nuovo cimento*, 38(2), 1977.

[175] M. Ido, K. Tsutsumi, T. Sambongi, and N. Môri. Pressure dependence of the metal-semiconductor transition in TaS_3. *Solid State Commun.*, 29(4):399 – 402, 1979.

[176] C. Berthier, P. Molinié, and D. Jérome. Evidence for a connection between charge density waves and the pressure enhancement of superconductivity in 2H-$NbSe_2$. *Solid State Commun.*, 18(9):1393 – 1395, 1976.

[177] T F Smith, R N Shelton, and R E Schwall. Superconductivity of TaS_{2-x} Se_x layer compounds at high pressure. *J. Phys. F: Met. Phys.*, 5(9):1713, 1975.

[178] C. Escribe-Filippini, J. Beille, M. Boujida, J. Marcus, and C. Schlenker. Pressure effect on the transport properties of superconducting $Li_{0.9}Mo_6O_{17}$ bronze. *Physica C*, 162-164:427 – 428, 1989.

[179] M. Inoue, S. O'hara, S. Horisaka, M. Koyano, and H. Negishi. Transport Properties of Quasi-Two-Dimensional Mo_4O_{11} Crystals. *Physica Status Solidi B*, 148(2):659–671, 1988.

[180] H Fujishita, C Murayama, N Mori, and M Sato. Pressure dependence of the charge-density wave of sodium molybdenum purple bronze. *J. Phys.: Condens. Matter*, 2:8751–8754, 1990.

[181] J. Dumas, C. Escribe-Filippini, J. Marcus, J. Mercier, D. Salomon, C. Schlenker, and F. Razavi. Electronic transition under pressure in the two-dimensional purple bronze $K_{0.9}Mo_6O_{17}$. *Physica B+C*, 117-118:602 – 604, 1983.

[182] R. H. Friend, D. Jérome, D. M. Schleich, and P. Molinié. Pressure enhancement of charge density wave formation in VSe_2; the role of coulomb correlations. *Solid State Commun.*, 27:169–173, 1978.

[183] M. Hoesch, G. Garbarino, C. Battaglia, P. Aebi, and H. Berger. Evolution of the charge density wave superstructure in $ZrTe_3$ under pressure. *Phys. Rev. B*, 93:125102, 2016.

[184] C. Le Touze. *Etude des propriétés associées aux ondes de densité de charge dans les bronzes oxygénés quasi-bidimensionnels* $(PO_2)_4(WO_3)_{2m}$. Phd thesis, Université Joseph Fourier, Octobre 1996.

[185] P. Haier, B.A. Hermann, N. Esser, U. Pietsch, K. Lüders, and W. Richter. Influence of the deposition rate on the structure of thin metal layers. *Thin Solid Films*, 318(1-2):223 – 226, 1998.

[186] R. Hunger, N. Blick, N. Esser, M. Arens, W. Richter, V. Wagner, and J. Geurts. Growth of Sb on Si(111) studied by Raman scattering. *Surf. Sci.*, 307-309, Part B:1061 – 1065, 1994. Proceedings of the European Conference on Surface Science.

[187] R. D. Bringans. Arsenic passivation of Si and Ge surfaces. *Crit. Rev. Solid State*, 17:353, 1992.

[188] D. H. Rich, T. Miller, G. E. Franklin, and T. C. Chiang. Sb-induced bulk band transitions in Si(111) and Si(001) observed in synchrotron photoemission studies. *Phys. Rev. B*, 39:1438–1441, Jan 1989.

[189] D. A. Prishchenko, V. G. Mazurenko, M. I. Katsnelson, and A. N. Rudenko. Gate-tunable infrared plasmons in electron-doped single-layer antimony. *ArXiv*.

[190] S. Cho, X. DiVenere, G. K. Wong, J. B. Ketterson, J. R. Meyer, and C. A. Hoffman. Thermoelectric power of MBE grown Bi thin films and Bi/CdTe superlattices on CdTe substrates. *Solid State Commun.*, 102:673–676, 1997.

[191] J. Wasserfall and W. Ranke. Arsenic interaction with vicinal Si(001) surfaces. *Surf. Sci.*, 315(3):237 – 247, 1994.

[192] J. Kim, S. S. Baik, S. H. Ryu, Y. Sohn, S. Park, B.-G. Park, J. Denlinger, Y. Yi, H. J. Choi, and K. S. Kim. Observation of tunable band gap and anisotropic Dirac semimetal state in black phosphorus. *Science*, 349(6249):723–726, 2015.

[193] N. Youngblood, C. Chen, S. J. Koester, and Mo Li. Waveguide-integrated black phosphorus photodetector with high responsivity and low dark current. *Nature photonics*, 9:247–252, 2015.

[194] Z. Wang, A. Islam, R. Yang, X. Zheng, and P. X.-L. Feng. Environmental, thermal, and electrical susceptibility of black phosphorus field effect transistors. *J. Vac. Sci. Technol. B*, 33(5):052202, 2015.

[195] J. Pang, A. Bachmatiuk, Y. Yin, B. Trzebicka, L. Zhao, L. Fu, R. G. Mendes, T. Gemming, Z. Liu, and M. H. Rummeli. Applications of phosphorene and black phosphorus in energy conversion and storage devices. *Adv. Energy Mater.*, 8(8):1702093, 2017.

[196] Z. Yang and J. Hao. Recent progress in black-phosphorus-based heterostructures for device applications. *Small Methods*, 2(2):1700296, 2017.

[197] R.W. James and Norman Tunstall. XXVI. The crystalline structure of antimony. *Philos. Mag.*, 40(236):233–239, 1920.

[198] K. J. Chang and M. L. Cohen. Rhombohedral phase stability of the group-VA elements. *Phys. Rev. B*, 33:7371–7374, May 1986.

[199] M. H. Cohen, L. M. Falicov, and S. Golin. Crystal Chemistry and Band Structures of the Group V Semimetals and the IV-V-VI Semiconductors. *IBM J. Res. Dev.*, 8(3):215–227, July 1964.

[200] P. B. Littlewood. Structure and bonding in narrow gap semiconductors. *Crit. Rev. Solid State Mater. Sci.*, 11(3):229–285, 1983.

[201] M. Cohen. Interatomic interactions in metals. *J. Phys. Radium*, 23:643–647, 1962.

[202] L. Pauling. *The nature of the chemical bonds.* Cornell University Press, Ithaca, 1960.

[203] A. Ormeci and Helge R. Electronic structure and bonding in antimony and its high pressure phases. *Z. Kristallogr.*, 219(6):370–375, 2004.

[204] H. Iwasaki and T. Kikegawa. Pressure-induced phase transition in antimony at elevated temperatures. *Physica B+C*, 139-140:259 – 262, 1986.

[205] A. B. Shick, J. B. Ketterson, D. L. Novikov, and A. J. Freeman. Electronic structure, phase stability, and semimetal-semiconductor transitions in Bi. *Phys. Rev. B*, 60:15484–15487, Dec 1999.

[206] U. Haussermann, K. Saderberg, and R. Norrestam. Comparative Study of the High-Pressure Behavior of As, Sb, and Bi. *J. Am. Chem. Soc.*, 124(51):15359–15367, 2002.

[207] H. Katzke and P. Tolédano. Competition between Burgers mechanism and Bain deformation in alkaline-earth metals: Host-guest structures of barium and strontium. *Phys. Rev. B*, 75:174103, May 2007.

[208] H. Katzke, U. Bismayer, and P. Tolédano. Theory of the high-pressure structural phase transitions in Si, Ge, Sn, and Pb. *Phys. Rev. B*, 73:134105, Apr 2006.

[209] H. Katzke and P. Tolédano. Structural mechanisms and order-parameter symmetries for the high-pressure phase transitions in alkali metals. *Phys. Rev. B*, 71:184101, May 2005.

[210] R. W. G. Wyckoff. *Crystal structure*, volume 1. Interscience Publishers, New York, 1960.

[211] O. Degtyareva, V. V. Struzhkin, and R. J. Hemley. High-pressure Raman spectroscopy of antimony: As-type, incommensurate host-guest, and bcc phases. *Solid State Commun*, 141(3):164 – 167, 2007.

[212] X. Wang, K. Kunc, I. Loa, U. Schwarz, and K. Syassen. Effect of pressure on the Raman modes of antimony. *Phys. Rev. B*, 74:134305, Oct 2006.

[213] T. Hahn, editor. *International tables for crystallography,*, volume Volume A: Space-group symmetry. 2002.

[214] Jette E. R. and Foote F. Precision determination of lattice constants. *J. Chem. Phys.*, 3, 1935.

[215] Kolobyanina T. N., Kabalkina S.S., Vereshchagin L.F., and Fedina L. V. Investigation of the crystal structure of antimony at high pressures. *Sov. Phys. JETP*, 28:88, 1969.

[216] P.W. Bridgman. Linear compressions to 30,000 kg/cm^2, including relatively incompressible substances. *Proc. Am. Acad. Arts Sci*, 56:211, 1949.

[217] D. Schiferl. 50 kilobar gasketed diamond anvil cell for single-crystal x-ray diffractometer use with the crystal structure of sb up to 26 kilobars as a test problem. *Rev. Sci. Instrum.*, 48(1):24–30, 1977.

[218] D. Schiferl, D. T. Cromer, and J. C. Jamieson. Structure determinations on Sb up to 85 $\times$ 10^2 MPa. *Acta Crystallogr.*, B37(4):807–810, Apr 1981.

[219] D. B. McWhan. The pressure variable in materials research. *Science*, 176:751–758, May 1972.

[220] S. S. Kabalkina, T. N. Kolobyanina, and L.F. Vereshchagin. Investigation of the crystal structure of the antimony and bismuth high pressure phases. *Sov. Phys. JETP*, 31:259, 1970.

[221] M.J. Duggin. A high-pressure phase in arsenic and its relation to pressure-induced phase changes in group 5B elements. *J. Phys. Chem. Solids*, 33(6):1267 – 1271, 1972.

[222] R. J. Nelmes, D. R. Allan, M. I. McMahon, and S. A. Belmonte. Self-Hosting Incommensurate Structure of Barium IV. *Phys. Rev. Lett.*, 83:4081–4084, Nov 1999.

[223] V. Heine. Crystal structure: As weird as they come. *Nature*, 403:836–837, Feb 2000.

[224] S. K. Reed and G. J. Ackland. Theoretical and computational study of high-pressure structures in barium. *Phys. Rev. Lett.*, 84:5580–5583, Jun 2000.

[225] T. Kikegawa and H. Iwasaki. An x-ray diffraction study of lattice compression and phase transition of crystalline phosphorus. *Acta Crystallogr. B*, 39(2):158–164, 1983.

[226] J. C. Jamieson. Crystal structures adopted by black phosphorus at high pressures. *Science*, 139(3561):1291–1292, 1963.

[227] H. J. Beister, K. Strössner, and K. Syassen. Rhombohedral to simple-cubic phase transition in arsenic under pressure. *Phys. Rev. B*, 41:5535–5543, Mar 1990.

[228] O. Degtyareva. Crystal structure of simple metals at high pressures. *High Pressure Res.*, 30(3):343–371, 2010.

[229] H. Fujihisa, Y. Akahama, H. Kawamura, Y. Ohishi, Y. Gotoh, H. Yamawaki, M. Sakashita, S. Takeya, and K. Honda. Incommensurate Structure of Phosphorus Phase IV. *Phys. Rev. Lett.*, 98:175501, Apr 2007.

[230] O. Degtyareva, M. I. McMahon, and R. J. Nelmes. Pressure-induced incommensurate-to-incommensurate phase transition in antimony. *Phys. Rev. B*, 70:184119, Nov 2004.

[231] U. Schwarz, L. Akselrud, H. Rosner, Alim Ormeci, Yu. Grin, and M. Hanfland. Structure and stability of the modulated phase Sb-II. *Phys. Rev. B*, 67:214101, Jun 2003.

[232] M. I. McMahon, O. Degtyareva, and R. J. Nelmes. Ba-IV-Type Incommensurate Crystal Structure in Group-V Metals. *Phys. Rev. Lett.*, 85:4896–4899, Dec 2000.

[233] K. Aoki, S. Fujiwara, and M. Kusakabe. New phase transition into the b.c.c. structure in antimony at high pressure. *Solid State Commun.*, 45(2):161 – 163, 1983.

[234] H. Katzke and P. Tolédano. Displacive mechanisms and order-parameter symmetries for the A7-incommensurate-bcc sequences of high-pressure reconstructive phase transitions in Group Va elements. *Phys. Rev. B*, 77:024109, Jan 2008.

[235] D. G. Pettifor. *Bonding and structure of molecules and solids.* Clarendon Press, Oxford, 1995.

[236] H. Olijnyk. Raman scattering in metallic Si and Ge up to 50 GPa. *Phys. Rev. Lett.*, 68:2232–2234, Apr 1992.

[237] H. Olijnyk, W. A. Grosshans, and A. P. Jephcoat. Lattice vibrations and electronic transitions in the rare-earth metals: Praseodymium under pressure. *Phys. Rev. Lett.*, 93:255505, Dec 2004.

[238] A. F. Goncharov, V. V. Struzhkin, H.-K. Mao, and R. J. Hemley. Spectroscopic evidence for broken-symmetry transitions in dense lithium up to megabar pressures. *Phys. Rev. B*, 71:184114, May 2005.

[239] R. I. Sharp and E. Warming. The lattice dynamics of antimony. *J. Phys. F: Met. Phys.*, 1(5):570, 1971.

[240] J. Sosnowski, E. F. Maliszewski, S. Bednarski, and A. Czachor. Phonon dispersion relations in antimony. *Physica Status Solidi B*, 44(2):K65–K68, 1971.

[241] J. Serrano and A. H. Romero. Lattice dynamics of antimony at high pressure: an ab initio study. *High Press. Res.*, 28(4):477–481, 2008.

[242] J. L. Yarnell, J. L. Warren, R. G. Wenzel, and S. H. Koenig. Phonon dispersion curves in bismuth. *IBM J. Res. Dev.*, 8(3):234–240, 1964.

[243] G. A. Saunders and Yogurtcu Y. K. Third-order elastic constants and acoustic-mode vibrational anharmonicity of antimony. *Phys. Rev. B*, 30:5734–5741, 1984.

[244] H. Olijnyk, S. Nakano, and K. Takemura. First- and second order Raman scattering in Sb and Bi at high pressure. *Phys. Status Solidi B*, 244(10):3572–3582, 2007.

[245] Richter W., Fjeldly T., Renucci J., and Cardona M. Hydrostatic pressure dependence of the zone-center phonons in group Vb Materials: As, Sb, Bi. In M. Balkanski, editor, *Proceedings of the international conference on lattice dynamics*, page 104, Paris, France, Flarion, Paris, 1978.

[246] M. L. Bansal and A. P. Roy. Raman study of phonons and intraband electronic excitations in antimony. *Phys. Rev. B*, 33:1526–1528, Jan 1986.

[247] R. N. Zitter. *The Physics of Semimetals and Narrow Gap Semiconductors*, volume p. 285. Pergamon, Oxford, 1971.

[248] V. P. Dmitriev, S. B. Rochal, Y. M. Gufan, and P. Tolédano. Definition of a transcendental order parameter for reconstructive phase transitions. *Phys. Rev. Lett.*, 60:1958, 1988.

[249] V. P. Dmitriev, S. B. Rochal, Yu. M. Gufan, and P. Tolédano. Reconstructive transitions between ordered phases: The martensitic fcc-hcp and the graphite-diamond transitions. *Phys. Rev. Lett.*, 62:2495–2498, May 1989.

[250] P. Tolédano and V. Dmitriev. *Reconstructive phase transitions: in crystals and quasicrystals*. Word Scientific Publishing, Singapore, 1996.

[251] J. C. Tolédano and P. Tolédano. *The Landau Theory of Phase Transitions*. Word Scientific Publishing, Singapore, 1987.

[252] A. Izyumov Yu and V. N. Syromyatnikov. *Phase Transitions and Crystal Symmetry*. Kluwer, Dordrecht.

[253] A. L. Korzhenevskii and V. Dmitriev. Strain induced incommensurate structures in vicinity of reconstructive phase transitions. *J. Phys.: Condens. Matter*, 27(37):375401, 2015.

[254] L. M. Falicov and S. Golin. Electronic Band Structure of Arsenic. I. Pseudopotential Approach. *Phys. Rev.*, 137:A871–A882, Feb 1965.

[255] L. M. Falicov and P. J. Lin. Band Structure and Fermi Surface of Antimony: Pseudopotential Approach. *Phys. Rev.*, 141:562–567, Jan 1966.

[256] S. Golin. Band structure of bismuth: Pseudopotential approach. *Phys. Rev.*, 166:643–651, Feb 1968.

[257] L. F. Mattheiss, D. R. Hamann, and W. Weber. Structural calculations for bulk As. *Phys. Rev. B*, 34:2190–2198, Aug 1986.

[258] R. J. Needs, R. M. Martin, and O. H. Nielsen. Total-energy calculations of the structural properties of the group-V element arsenic. *Phys. Rev. B*, 33:3778–3784, Mar 1986.

[259] R. J. Needs, R. M. Martin, and O. H. Nielsen. Revised results for the structural properties of arsenic. *Phys. Rev. B*, 35:9851–9852, Jun 1987.

[260] The ABINIT code. Université catholique de louvain, corning inc.

[261] X. Gonze, J.-M. Beuken, R. Caracas, F. Detraux, M. Fuchs, G.-M. Rignanese, L. Sindic, M. Verstraete, G. Zerah, F. Jouet, M. Torrent, A. Roy, M. Mikami, P. Ghosez, J.-Y. Raty, and D. C. Allan. First-principles computation of material properties: an abinit software project. *Comput. Mat. Sci*, 25:487–492, 2002.

[262] X. Gonze, G.-M. Riganese, M. Verstraete, J. Betiken, Y. Pouillon, R. Caracas, F. Jollet, M. Torrent, G. Zerah, M. Mikami, P. Ghosez, M. Veithen, J.-Y. Raty, V. Olevano, F. Bruneval, L. Reining, R. Godby, G. Onida, D. R. Hamann, and D. C. Allan. A brief introduction to the abinit software package. *Z. Kristallogr.*, 220:558–562, 2005.

[263] Xavier Gonze, François Jollet, F Abreu Araujo, Donat Adams, Bernard Amadon, Thomas Applencourt, Christophe Audouze, J-M Beuken, Jordan Bieder, A Bokhanchuk, et al. Recent developments in the abinit software package. *Comput. Phys. Commun.*, 205:106–131, 2016.

[264] X. Gonze, B. Amadon, P-M Anglade, J-M Beuken, F. Bottin, P. Boulanger, F. Bruneval, D. Caliste, R. Caracas, M. Côté, et al. Abinit: First-principles approach to material and nanosystem properties. *Comput. Phys. Commun.*, 180(12):2582–2615, 2009.

[265] M. Fuchs and M. Scheffler. Ab initio pseudopotentials for electronic structure calculations of poly-atomic systems using density-functional theory. *Comput. Phys. Commun.*, 119(1):67–98, 1999.

[266] P-M Anglade and X. Gonze. Preconditioning of self-consistent-field cycles in density-functional theory: The extrapolar method. *Phys. Rev. B*, 78(4):045126, 2008.

[267] X. Gonze and C. Lee. Dynamical matrices, Born effective charges, dielectric permittivity tensors, and interatomic force constants from density-functional perturbation theory. *Phys. Rev. B*, 55(16):10355, 1997.

[268] S. Baroni, S. De Gironcoli, A. Dal Corso, and P. Giannozzi. Phonons and related crystal properties from density-functional perturbation theory. *Rev. Mod. Phys.*, 73(2):515, 2001.

[269] Y. Liu and R. E. Allen. Electronic structure of the semimetals Bi and Sb. *Phys. Rev. B*, 52:1566–1577, 1995.

List of Figures

List of Tables

Acknowledge

I would like to thank all the people involved in my project and contributed to its success. A special thanks goes to the ESRF, the UGA and all the other institutions which let me do my work in the best possible environment.

In primis, I would like to start with a big thank to my supervisor/boss/mentor Alexeï Bosak who spent the last three years in a desperate attempt to teach me something. It was an honour to have the opportunity to work with a scientist with such huge scientific competence. I hope that I have learned his critical perspective and took some of his baggage of knowledge with me, despite my Gold fish memory.

Thanks to the President, the referees and the members of the committee to have kindly accepted to review this Thesis and to have participated at the *viva*. I hope this is a moment of reciprocal learning and of interest for all of you.

I would also like to thank the other persons involved in my project as Marc de Boissieu, who pushed me to analyse in a very careful way my results, Alain Pautrat and Olivier Perez. It was an honour and a pleasure to work with all of you. I am also very grateful to Elen Duverger-Nedellec, who was a scientific and moral support in the difficult task to reach the Bronzes truth and for the high-quality of the samples. I would also like to thank Patrick Rosa. Your presence and help during the high-pressure beamtime were very precious. It was a pleasure to work with Marek Mihalkovic and spend two weeks in the beautiful Bratislava. It was very important for me, in order to understand how to overcome issues in calculations and simulations. Thanks to Anna Efimenko, Marco Moretti, Christoph Sahle and Matteo Rossi for the RIXS experiments on the bronzes.

I would also like to thank Prof. Vladimir Dmitriev for a very fruitful collaboration and not only that. From your very patient discussion and explanation about the phase transition theory, I understood that yours is not just a professor title.

Michaela Souliou, I would like to thank you to be my office mate and have patiently taught and listened in every situation. Without you, the antimony part would still be a chaos. Thank you.

Thank you Sasha Chumakov for providing beam time for the diffuse scattering experiments, without this I would have been completely lost during the first months.

Thank you very much Björn Wehinger, your lectures on the *ab initio* calculations were really important for me. It was a pleasure to work with you, especially in the anatase project. It was a very important opportunity to learn more about high-pressure techniques, IXS and DS. I hope there will be more possibilities to work again together.

Thanks to Jeroen Jacobs, your DACs are still held hostage by me but I will give them back to you. I promise. For the high pressure technique, I would like to thank Gaston Garbarino. You were very kind and patient in every situation.

A big thanks to all ID28 beamline. At first, to Luigi Paolasini, who warmly welcomed me from the first days, giving me a "roof" and being a friend. Thanks for the infinite times you helped me and I hope, in some way, I returned it. Thanks to Denis Gambetti, Thanh Tra Nguyen, Adrien Girard, MichałStekieł, you all helped me during my beamtime and my stressful experiments. Thanks also to Dan Chaney and Edoardo Mariani, you stayed fewer months, but this does not mean you were less important. Hope I have in some way give back all the kindness and friendship and I hope we will still be in touch in the future. I wish you all the best.

Thanks to Alexeï, Marc, Michaela, Gigi, Danilo, Dan and Gaetan for the careful proofreading and comments on my manuscript.

I would like to thank all the other students and post-docs (and not only) at the ESRF and UGA, for the nice moments spent together: Matteo (Giusy), Silvia, Oonagh, two Andreas, Edoardo, Anastasia, Ruggero, Alberto, Valerio, Enorme, Orazio, two Alessandros, Sant, Micaela, two Lauras, Marila, Vanni, Tomas, Jorge, Raquel and I am sure that I am forgetting someone, I am sorry for that.

Last but not least, thanks to all my friends in Grenoble and elsewhere and thanks to my family (my parents, my sister and her precious husband, my cousins, my uncles and aunts, my grandmothers and "my" Andrea).